sid.inpe.br/mtc-m21c/2021/10.22.19.22-TDI

STUDY OF MAGNETIC ACCRETION IN INTERMEDIATE POLARS AND SW SEXTANTIS STARS

Isabel de Jesus Lima

Doctorate Thesis of the Graduate Course in Astrophysics, guided by Dra. Cláudia Vilega Rodrigues, approved in November 03, 2021.

URL of the original document:
<http://urlib.net/8JMKD3MGP3W34R/45LE9G8>

INPE
São José dos Campos
2021

PUBLISHED BY:

Instituto Nacional de Pesquisas Espaciais - INPE
Coordenação de Ensino, Pesquisa e Extensão (COEPE)
Divisão de Biblioteca (DIBIB)
CEP 12.227-010
São José dos Campos - SP - Brasil
Tel.:(012) 3208-6923/7348
E-mail: pubtc@inpe.br

DIGITAL LIBRARY:

Dr. Gerald Jean Francis Banon

Clayton Martins Pereira - Divisão de Biblioteca (DIBIB)

DOCUMENT REVIEW:

Simone Angélica Del Ducca Barbedo - Divisão de Biblioteca (DIBIB)

André Luis Dias Fernandes - Divisão de Biblioteca (DIBIB)

ELECTRONIC EDITING:

Ivone Martins - Divisão de Biblioteca (DIBIB)

André Luis Dias Fernandes - Divisão de Biblioteca (DIBIB)

sid.inpe.br/mtc-m21c/2021/10.22.19.22-TDI

STUDY OF MAGNETIC ACCRETION IN INTERMEDIATE POLARS AND SW SEXTANTIS STARS

Isabel de Jesus Lima

Doctorate Thesis of the Graduate Course in Astrophysics, guided by Dra. Cláudia Vilega Rodrigues, approved in November 03, 2021.

URL of the original document:
<http://urlib.net/8JMKD3MGP3W34R/45LE9G8>

INPE
São José dos Campos
2021

Cataloging in Publication Data

Lima, Isabel de Jesus.
L628s Study of magnetic accretion in intermediate polars and SW sextantis stars / Isabel de Jesus Lima. – São José dos Campos : INPE, 2021.
xxiv + 164 p. ; (sid.inpe.br/mtc-m21c/2021/10.22.19.22-TDI)

Thesis (Doctorate in Astrophysics) – Instituto Nacional de Pesquisas Espaciais, São José dos Campos, 2021.
Guiding : Dra. Cláudia Vilega Rodrigues.

1. Binaries stars. 2. Cataclysmic variables. 3. White dwarf stars. 4. Dwarf novae. I.Title.

CDU 524.354.7

MINISTÉRIO DA
CIÊNCIA, TECNOLOGIA
E INOVAÇÕES

INSTITUTO NACIONAL DE PESQUISAS ESPACIAIS
Serviço de Pós-Graduação - SEPGR

DEFESA FINAL DE TESE DE ISABEL DE JESUS LIMA
BANCA Nº 271/2021, REG 130052/2016

No dia 03 de novembro de 2021, as 09h, por teleconferência, o(a) aluno(a) mencionado(a) acima defendeu seu trabalho final (apresentação oral seguida de arguição) perante uma Banca Examinadora, cujos membros estão listados abaixo. O(A) aluno(a) foi APROVADO(A) pela Banca Examinadora, por unanimidade, em cumprimento ao requisito exigido para obtenção do Título de Doutora em Astrofísica. O trabalho precisa da incorporação das correções sugeridas pela Banca Examinadora e revisão final pelo(s) orientador(es).

Título: “Study of magnetic accretion in intermediate polars and SW Sextantis stars"

Membros da banca:
Dr. José Carlos Neves de Araujo - Presidente - INPE
Dra. Cláudia Vilega Rodrigues - Orientadora - INPE
Dr. Francisco José Jablonski - Membro Interno - INPE
Dr. Flávio D'Amico - Membro Interno - INPE
Dr. Gerardo Juan Manuel Luna - Membro Externo - IAFE/CONICET
Dra. Karleyne Medeiros Gomes da Silva - Gemini Observatory/NOIRLAB

Documento assinado eletronicamente por **Francisco Jose Jablonksi**, **Pesquisador**, em 03/11/2021, às 15:22 (horário oficial de Brasília), com fundamento no § 3º do art. 4º do Decreto nº 10.543, de 13 de novembro de 2020.

Documento assinado eletronicamente por **José Carlos Neves de Araújo**, **Pesquisador**, em 03/11/2021, às 15:33 (horário oficial de Brasília), com fundamento no § 3º do art. 4º do Decreto nº 10.543, de 13 de novembro de 2020.

Documento assinado eletronicamente por **Cláudia Vilega Rodrigues**, **Pesquisadora**, em 03/11/2021, às 16:59 (horário oficial de Brasília), com fundamento no § 3º do art. 4º do Decreto nº 10.543, de 13 de novembro de 2020.

Documento assinado eletronicamente por **Flavio D Amico**, **Pesquisador**, em 03/11/2021, às 19:17 (horário oficial de Brasília), com fundamento no § 3º do art. 4º do Decreto nº 10.543, de 13 de novembro de 2020.

A autenticidade deste documento pode ser conferida no site http://sei.mctic.gov.br/verifica.html, informando o código verificador **8317901** e o código CRC **152537A0**.

Referência: Processo nº 01340.007338/2021-37 SEI nº 8317901

ABSTRACT

In this PhD thesis, we study the magnetic accretion in cataclysmic variables using two approaches. On one hand, we applied the CYCLOPS code to observational data of V405 Aur, an intermediate polar, a sub-class of magnetic cataclysmic variables. On the other hand, we performed a search of magnetic accretion in SW Sex objects, a class of objects in which the magnetic accretion is not definitely established. Magnetic cataclysmic variables are binary systems in which mass transfer occurs from a low-mass star onto a magnetic white dwarf. The accretion forms a shock near the white dwarf, and the compressed material – the post-shock region – is responsible for the circular polarization in optical and infrared light detected in some intermediate polars and SW Sex stars. This region also emits high energies mainly by bremsstrahlung and line emission. The CYCLOPS code was developed by our group in order to model multi-wavelength data of magnetic cataclysmic variables. In its present version, it solves the shock structure and calculates the cyclotron and free-free emission from a three-dimensional and non-homogeneous accretion structure (post- and pre-shock region), in terms of density, temperature and magnetic field. To our knowledge, the CYCLOPS code is the only one currently available with these approaches. This manuscript shows the first CYCLOPS application for intermediate polars. The X-ray spectrum and light curve data of V405 Aur was fitted and illustrates the degeneracy problem described by our group. We confirmed that the X-ray spectrum requires a mass accretion rate in the range of $10^{-9} - 10^{-10}$ $M_\odot$ year^{-1}, as previously reported in the literature. While the X-ray spectrum constrains physical parameters such as the white-dwarf mass and the accretion rate, the modulated optical emission strongly restricts the geometrical parameters. However, the optical light curves in UBVRI photometry and polarimetry of V405 Aur fitted by CYCLOPS code did not provide us a good model. We suggest that results could be related to presence of two accretion columns symmetrically opposite coming from two threading regions. So far, the CYCLOPS code has only considered one threading region, therefore a new implementation in our code may be conducted to model intermediate polars. In the second part of this thesis, we searched for signs of magnetic accretion in six SW Sex systems (BO Cet, SW Sex, V442 Oph, V380 Oph, LS Peg, and UU Aqr) such as circular polarization and/or periodic flux variability that can be associated with the white-dwarf spin period. We interpreted the periods found from circular polarization such as the spin period of BO Cet at 11.1 min, SW Sex at 41.2 min, and UU Aqr at 25.7 min. Possible candidates were V442 Oph, whose period of 19.4 min is below the FAP level of 1% as well as V380 Oph whose period is 22.0 min. We also confirmed the detection of circular polarization in LS Peg, whose spin period at 18.8 min, differs from the literature. Considering the entire group of SW Sex systems, we reported that 15% have direct evidence of magnetic accretion.

Keywords: binaries stars. cataclysmic variables. white dwarf stars. dwarf novae.

ESTUDO SOBRE ACREÇÃO MAGNÉTICA EM POLARES INTERMEDIÁRIAS E ESTRELAS DO TIPO SW SEXTANTIS

RESUMO

Nesta tese de doutorado, estudamos a acreção magnética em variáveis cataclísmicas usando duas abordagens. Por um lado, aplicamos o código CYCLOPS aos dados observacionais de V405 Aur, uma polar intermediária, subclasse de variáveis cataclísmicas magnéticas. Por outro lado, realizamos uma busca por acreção magnética em estrelas do tipo SW Sex, uma classe de objetos em que a acreção magnética não está definitivamente estabelecida. Variáveis cataclísmicas magnéticas são sistemas binários nos quais a transferência de massa ocorre de uma estrela de baixa massa para uma anã branca magnética. A acreção forma um choque próximo à anã branca, e o material comprimido - a região pós-choque - é responsável pela polarização circular na luz óptica e infravermelha detectada em alguns polares intermediárias e em estrelas do tipo SW Sex. Esta região também emite altas energias principalmente por bremsstrahlung e linhas de emissão. O código CYCLOPS foi desenvolvido por nosso grupo para modelar dados em múltiplos comprimentos de onda de variáveis cataclísmicas magnéticas. Em sua versão atual, o código resolve a estrutura de choque e calcula emissão cíclotron e bremsstrahlung de uma estrutura de acreção tridimensional e não homogênea (região pós e pré-choque), em termos de densidade, temperatura e campo magnético. Até onde sabemos, o código CYCLOPS é a única ferramenta disponível atualmente com essas abordagens. Este manuscrito mostra a primeira aplicação do CYCLOPS para polares intermediárias. O espectro e a curva de luz em raios X de V405 Aur foram ajustados e ilustram o problema de degenerescência descrito por nosso grupo. Confirmamos que o espectro de raios-X requer uma taxa de acréscimo de massa de $10^{-9} - 10^{-10}$ $M_\odot$ ano^{-1}, conforme relatado anteriormente na literatura. Enquanto o espectro de raios-X restringe os parâmetros físicos, como a massa da anã branca e a taxa de acreção, a emissão óptica modulada restringe fortemente os parâmetros geométricos. No entanto, as curvas de luz óptica UBVRI em fotometria e polarimetria de V405 Aur modeladas com CYCLOPS não forneceram um bom modelo. Nos sugerimos que isso está relacionado à presença de duas colunas de acreção, simetricamente opostas, provenientes de duas regiões de acoplamento. Já que até o momento, o código CYCLOPS considera apenas uma região de acoplamento, portanto, demonstramos que uma nova implementacao no CYCLOPS seria necessaria se queremos usar o codigo para descrever variáveis cataclísmicas magnéticas e não somente polares. Na segunda parte desta tese, procuramos por sinais de acreção magnética em seis sistemas do tipo SW Sex (BO Cet, SW Sex, V442 Oph, V380 Oph, LS Peg e UU Aqr), como polarização circular e/ou variabilidade períodica do fluxo que pode estar associada ao período de rotação da anã branca. Interpretamos os períodos encontrados a partir da polarização circular, como o período de rotação de BO Cet em 11,1 min, SW Sex em 41,2 min e UU Aqr em 25,7 min. Os possíveis candidatos foram V442 Oph, cujo período de 19,4 min está abaixo do nível de FAP de 1%, bem como V380 Oph, cujo período é de 22,0 min. Nós também confirmamos a detecção de polarização circular em LS Peg, cujo período de rotação é 18,8 min, diferentemente da literatura. Considerando todo o grupo de sistemas do tipo SW Sex, relatamos que 15% têm evidências diretas de acreção magnética.

Palavras-chave: estrelas binárias. variáveis cataclísmicas. anãs brancas. novas anãs.

“The mind that opens up to a new idea
never returns to its original size.”

ALBERT EINSTEIN

To Maria Wilma de Jesus Conceição, my mother.

ACKNOWLEDGEMENTS

I would like to thank God, the Universe.

I would like to thank my advisor, professor Dr. Cláudia Vilega Rodrigues for all her help, dedication, patience, guidance and understanding and in particular, for her friendship. Her phrase “you already have the *NO* answer” changed my life.

This study was supported by Fundação de Amparo à Pesquisa do Estado de São Paulo (FAPESP) grants #2018/05420-1, #2015/24383-7, #2013/26258-4. Thanks to FAPESP for the funding and investment in science.

I acknowledge Dr. V. Piirola for providing optical data, Dr. P. A. Evans, Dr. C. Hellier for clarifying some aspects of V405 Aur X-ray data, and Dr. Diogo Belloni for providing the updated version of the CYCLOPS code.

I am extremely thankful to Dr. Francisco José Jablonsky, in my research with SW Sex stars and Dr. Paula Szkody, my supervisor in the internship visiting program at the University of Washington.

I am also very appreciative of having been able to attend the following schools: Vatican Observatory Summer School on Stellar variability in the era of large surveys; ESO/NEON Observing School at La Silla; COSPAR Capacity Building Workshop: Latin American X-ray school for different astrophysical scenarios. - Data analysis of the XMM-Newton, Chandra and NuStar missions.

I am eternally grateful to my family; my mother Wilma, my sister Raquel and my uncles Wilson and Wedison and my aunts Wilza, Wrani and Wnira.

I would also like to thank my colleagues Aysses and Lorena who supported me throughout this long journey.

I am grateful to the many people involved in my research work. In particular, I would like to extend my thanks to the professors and employees of the Astrophysics Division at INPE.

LIST OF FIGURES

LIST OF TABLES

Page

LIST OF ABBREVIATIONS

APEC	Astrophysical Plasma Emission Code
APED	Astrophysical Plasma Emission Database
ARF	Ancillary Response File
ASCA	Advanced Satellite for Cosmology and Astrophysics
CCD	Charge-coupled device
CGS	Centimetre–Gram–Second
CV	Cataclysmic variables
EPIC	European Photon Imaging Camera
FAP	False-alarm probability
GTI	Good Time Interval
HST	Hubble Space Telescope
IDL	Interactive Data Language
IP	Intermediate polar
ISM	Interstellar medium
IUE	International Ultraviolet Explorer
LS	Lomb-Scargle
MCV	Magnetic cataclysmic variables
MEKAL	Mewe-Kaastra-Liedahl
MHD	Magneto-hydrodynamic
MOS	Metal Oxide Semi-conductor
ODF	Observation Data File
OM	Optical Monitor
PSF	Point-Spread Function
PSR	Post-Shock Region
QPO	Quasi-periodic oscillation
RGS	Reflection Grating Spectrometers
RMF	Redistribution Matrix File
RXTE	Rossi X-ray Timing Explorer
SED	Spectral Energy Distribution
SNR	Signal-to-noise ratio
UV	Ultraviolet
WD	White dwarf

LIST OF SYMBOLS

a – Binary separation
B – Magnetic field strength
B_{lat} – Latitude magnetic field axis
B_{long} – Longitude magnetic field axis
β – Colatitude angle
c – Velocity of light
δ_{long} – Longitude direction of threading region
δ_R – Radius direction of threading region
G – Gravitational constant
H – Disk height
h – Plank's constant
i – Inclination
L_{acc} – Accretion luminosity
L_{dic} – Disk luminosity
m – Mass of the electron
M_1 – Mass of the primary
M_2 – Mass of the secondary
M_{WD} – White dwarf mass
$\dot{M}$ – Accretion rate
$N(H)$ – Hydrogen column density
P – Binary period
P_{beat} – Beat period
P_{pres} – Pressure
P_{orb} – Orbital period
P_{spin} – Spin period of the white dwarf
q – Mass ratio secondary to primary
$\overrightarrow{r}$ – Test particle position
$\overrightarrow{r_1}$ – Position vector of the primary
$\overrightarrow{r_2}$ – Position vector of the secondary
r_{circ} – Circularization radius
r_μ – Magnetosphere radius
R_{disc} – Disk radius
υ – Kinematic viscosity
υ_k – Keplerian velocity
υ_s – Speed of sound
ω – Angular velocity
μ – Magnetic moment
ρ – Density
ν – Velocity of matter

CONTENTS

Page

1 INTRODUCTION

1 INTRODUCTION

This chapter reviews cataclysmic variables and their subclasses, intermediate polars and SW Sextantis stars. In Section 1.1, we introduce the definition of the cataclysmic variables (hereafter referred to as CVs) along with some fundamental concepts such as Roche lobe geometry. SW Sextantis stars are introduced in Section 1.2 while Section 1.3 discusses some properties of intermediate polars (IPs). Finally, the objective of this study is presented in Section 1.4.

1.1 Cataclysmic variables

CVs are compact binary systems in which a white dwarf (WD) primary accretes material from a low-mass late-type main-sequence component (the secondary) via Roche lobe overflow. The secondary rotation is synchronized with the orbital translation due to tidal forces. Reviews of CVs have been carried out by Warner (1995) and Hellier (2001).

Generally, CVs are classified according to their optical light curves in the presence or absence of eruptions, their amplitude and the duration of these eruptions. In a second dimension, CVs can also be classified as being magnetic or non-magnetic, depending on the importance of the WD magnetic field in the accretion dynamics (OSAKI, 1996; SINGH, 2013, e.g.). The main non-magnetic CV types are:

- **Dwarf Novae** show outbursts of amplitudes of 2–6 magnitudes interpreted as being due to accretion disk instabilities. Dwarf Novae are further subdivided into:
    - **SU UMa** – These systems show two distinct outbursts: a short one lasting a few days and a longer superoutburst of around two weeks;
    - **Z Cam** – These systems occasionally display standstill periods, with an intermediate level between the maxima and minima outbursts;
    - **U Gem** – These systems exhibit regular quasi-periodic outbursts. Depending on the star, the eruptions occur at intervals of 30 to 500 days and usually last from 5 to 20 days.

  There are some classes of CVs whose systems may be magnetic or non-magnetic. They are:

- **Novae**, which show only one observed large eruption of approximately 6–9 magnitudes due to a thermonuclear burning of matter accumulated on the surface of the WD;

- **Recurrent Novae**, systems that present more than one nova eruption;
- **Nova-likes**, which do not exhibit outbursts, contrary to that observed in dwarf novae. Some nova-like subclasses are:
  - **VY Scl stars**, which are bright systems that occasionally undergo a fall in brightness of more than one magnitude;
  - **SW Sex stars**, these systems have spectroscopic particularities, which places them in a specific class. These are discussed in Section 1.2.

Dwarf novae eruptions are commonly explained by the accretion disk instability model. In this scenario, the outbursts are due to the propagation of heating and cooling fronts that are favoured by an increase in disk viscosity, while during quiescence the disk remains in a low-viscosity regime and refills the mass lost during a previous outburst. In the standard model proposed by Osaki (1996), the mass transfer rate is assumed to be constant during the whole outburst cycle. However, in recent versions of the disk instability model this assumption has been abandoned (BUAT-MÉNARD et al., 2001, e.g.). On the other hand, the nova-like systems are not subject to such instabilities because they have a high enough mass transfer rate to keep the disk in a stable state of high viscosity.

The accretion is an efficient method to extract potential gravitational energy and convert it into radiation. In fact, Equation 1.5 shows that the luminosity is derived from the accretion. Half of this luminosity is from the disk and the other half has still to be released very close to the star, in the so-called boundary layer (FRANK et al., 2002).

In non-magnetic CVs, the accretion occurs via an accretion disk. CVs in which the WD magnetic field is strong enough to disrupt the inner accretion disk or even prevent disk formation altogether are called magnetic cataclysmic variables (MCVs). The accretion flow of MCVs is magnetically controlled by the field lines, resulting in accretion columns/curtains near the WD surface (LAMB; MASTERS, 1979), see Section 1.3. Near the WD, the material reaches a supersonic velocity, and a shock front is formed. The region between the shock front (pre-shock region) and the WD surface is called the post-shock region (PSR), see Section 1.3.2. This region emits high energies mainly by bremsstrahlung and line emission and circular polarization in optical and infrared light.

MCVs have been classified into two distinct classes, the IPs or DQ Her type, and the polars or AM Her type, see Figure 1.1. The WD spin period (P_{spin}) in polars is synchronized to the orbit period (P_{orb}), whereas the WDs in IPs are asynchronous. The polars accrete without an intervening accretion disk owing to the intense WD surface magnetic field ($10-250$ MG) (SCHMIDT et al., 1996, e.g.). The ballistic stream from L_1 point is funneled by the WD magnetic field and accretes preferentially near the magnetic pole(s). Cropper (1990) provides a comprehensive review of polars.

MCVs offer a great opportunity to study interactions of the accretion flow with the WD magnetosphere. Furthermore, the orbital periods of the binaries (hours) and the spin periods of the WD ($\sim$10 min in IPs) result in variations in easy-to-observe timescales (HELLIER, 2014).

Figure 1.1 - Illustration of the geometries of a polar (left) and an intermediate polar (right).

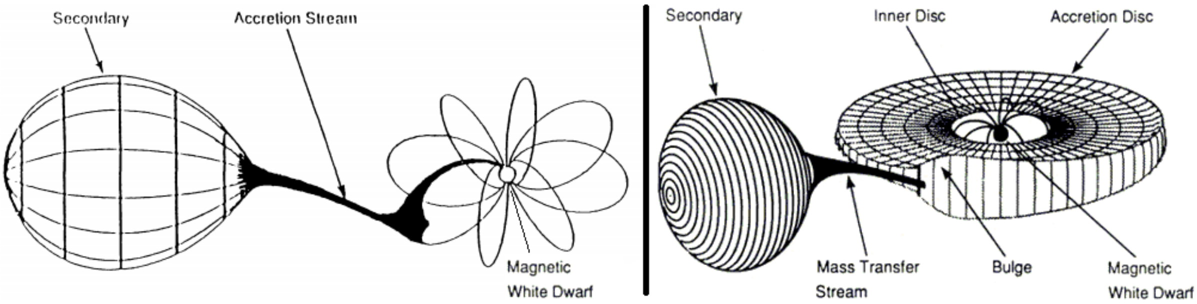

SOURCE: Cropper (1990) and NASA (2006).

1.1.1 Roche geometry

The Roche geometry is useful to represent compact binary systems. In CVs, the secondary shape is usually approximated by its Roche lobe. The Roche potential considers the orbit of a test particle in the gravitational potential of a binary stellar system. This is known as a simplified three-body problem. The Roche lobe approach assumes that the two stars are point masses and a non-inertial coordinate system rotating with the binary. The Roche potential, $\phi_R(\overrightarrow{r})$, is given by Equation 1.1 (FRANK et al., 2002).

$$\phi_R(\overrightarrow{r}) = -\frac{GM_1}{|\overrightarrow{r} - \overrightarrow{r_1}|} - \frac{GM_2}{|\overrightarrow{r} - \overrightarrow{r_2}|} - \frac{1}{2}(\omega \wedge \overrightarrow{r})^2, \tag{1.1}$$

where G is a gravitational constant, M_1 and M_2 are the primary and secondary masses, respectively, $\overrightarrow{r}$ is the test particle position, $\overrightarrow{r_1}$ and $\overrightarrow{r_2}$ are the position vectors of the centers of the two stars, and ω is the angular velocity, the frequency of the revolution of the binary about its center of mass.

Figure 1.2 illustrates the Roche lobe potential in the orbital plane for a mass ratio equal to 0.25. The Lagrange points (L_n) are the positions where the gravitational forces of the two stars exactly balance the centrifugal force undergone by the test particle.

Figure 1.2 - The Roche lobe geometry and equipotential surfaces. ϕ_R constant for a binary system with mass ratio equal to 0.25. M_1 is the primary, M_2 the secondary. The L_n are the Lagrangian points.

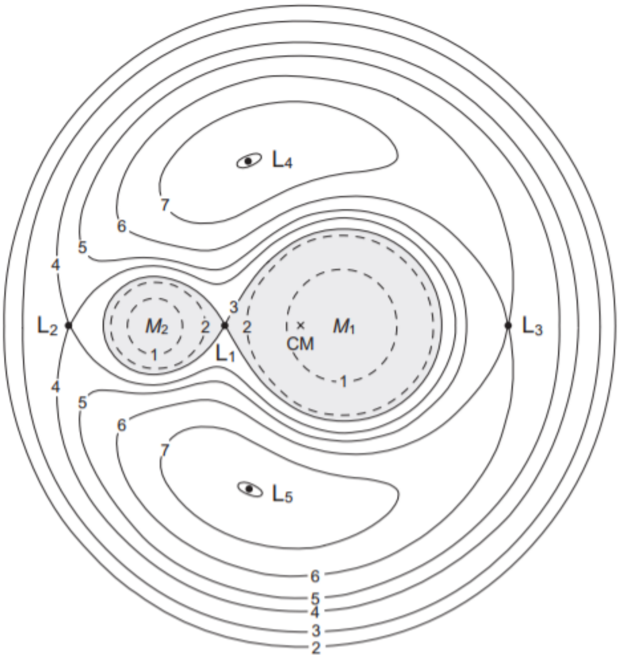

SOURCE: Frank et al. (2002).

The shape of the equipotentials is governed entirely by the mass ratio ($q = M_2/M_1$), while the overall scale is given by the binary separation, a. The relationship between these quantities is given by Kepler's third law, Equation 1.2.

$$a^3 = \frac{GMP^2}{2\pi^2}, \tag{1.2}$$

where P is the binary period, and $M = M_1 + M_2$.

1.1.2 Accretion geometry: disks and magnetic columns

In non-magnetic CVs and some IPs, an accretion disk is formed. This occurs because the stream material that leaves the Roche lobe of the secondary from the L_1 point has too much angular momentum to accrete directly onto the primary. So, it outlines non-circular orbits around the WD, which entangle themselves and by friction the material loses energy and reaches the circular orbit of lowest energy. The matter rotates in a circular orbit referred to as the circularization radius (r_{circ}). The annulus rotates at the local Keplerian velocity, $v_k = \sqrt{GM_1/r}$. Thus, the matter closer to the primary orbits faster than that further away and the viscosity acting on the gas rotating near r_{circ} will tend to heat it and spread it into a disk. For the purpose of conserving the total angular momentum, part of the material transfers the angular momentum to the outer parts of the disk. This results in a disk extended further out from the primary star.

$$r_{circ} = a(1+q)[0.500 - 0.227\ log\ q]^4, \tag{1.3}$$

where a is the separation of stars and q is the mass ratio.

In IPs, the central parts of accretion disks are destroyed by the WD magnetic field within its magnetosphere with radius r_μ, Equation 1.4. The magnetosphere extension depends on the strength of the field and the accretion rate, although it also depends on whether the material is confined to a stream or spreads out into a disk (HELLIER, 2001, e.g.). A review of the conditions for the existence and the formation of partial accretion disks is given by King and Lasota (1991), in which the authors concluded that depending on the mass ratio some IPs with $P_{spin} = 0.1 \times P_{orb}$ are near the limit of the partial disk formation. In polars, the magnetosphere radius is greater than the circularization radius preventing the disk formation and the matter in ballistic trajectory follows the magnetic field lines towards the WD surface.

$$r_\mu = 9.9 \ \times \ 10^{10} \mu_{34}^{4/7} M_1^{-1/7} \dot{M}_{16}^{2/7} \ \ cm, \tag{1.4}$$

where μ is the magnetic moment in units of 10^{34} $G\ cm^3$. M_1 is the primary mass. $\dot{M}$ is the accretion rate in units of 10^{16} $g\ s^{-1}$. The accretion luminosity is also function of M and $\dot{M}$, which in a steady state is given by Equation 1.5 (HELLIER, 2001, e.g.).

$$L_{disk} = \frac{G M_1 \dot{M}}{2 R_1} = \frac{1}{2} L_{acc}, \tag{1.5}$$

where L_{acc} is the accretion luminosity, R_1 is the primary radius.

Shakura and Sunyaev (1973) described a useful parametrization of our ignorance regarding the viscosity problem: the famous α-prescription. The turbulence is assumed to provide the relevant source of viscosity. This prescription assumes a geometrically thin disk, i.e the disk radius (R_{disk}) is much larger than the disk height (H). The kinematic viscosity (υ) at a given radius is taken to be $\upsilon \ = \ \alpha \ v_s \ H$, where v_s is the speed of sound, and the parameter α is expected to be less than 1, where 0 corresponds to no viscosity A null viscosity corresponds to no accretion (FRANK et al., 2002). The mechanism usually attributed to being the physical origin of the viscosity is the magneto-rotational instability, as proposed by Balbus and Hawley (1991).

1.1.3 Evolution of CVs

The main observable for understanding the evolution of CVs is the distribution of the number of objects per orbital period (Figure 1.3). This graph has many important properties, one of them is the decrease in the number of objects with periods between 2 and 3 h, which is called the period gap.

During the evolution of the CVs, the orbital period decreases due to angular momentum loss through two types of mechanisms: the magnetic braking, which is efficient over longer orbital periods; and gravitational waves, which is effective over shorter periods. A review of the standard evolution model can be found in Knigge et al. (2011). In the period gap, the standard model suggests that the magnetic braking process is switched off and the transfer of matter is interrupted, hence CVs are not observed owing to the decrease in their luminosity.

Figure 1.3 shows that IPs are located between 3 h and 6 h and polars are concentrated between 1.3 h and 3 h. The lack of dwarf novae in orbital periods between 3 and 4 hours and an increase in SW Sex systems in the same area is evident. This distribution could indicate that SW Sex stars evolve into polars. Indeed, Patterson et al. (2002) suggest that the magnetic fields in SW Sex stars are comparable in strength to the highly magnetic polars, but the high accretion rate in SW Sex objects would result in small magnetospheres and asynchronous WD rotation periods (see Figure 1.4).

Figure 1.3 - The distribution of the number of CVs as a function of orbital period. The distributions for some CV classes compiled by Ritter and Kolb (2003, v7.24-2015) and Hoard et al. (2003, v5.3.0-2016) are also displayed. The lines indicate the limits of the period gap.

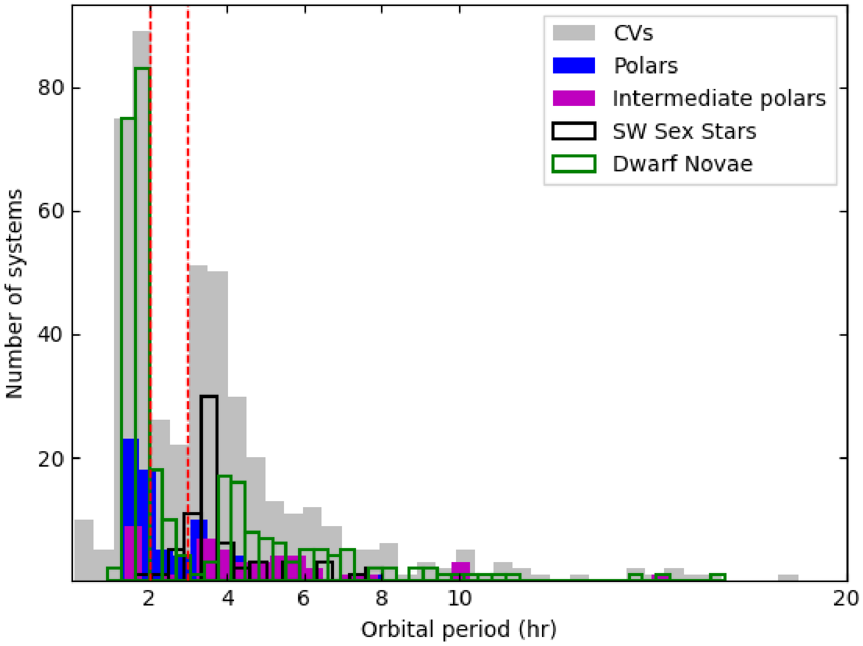

SOURCE: The author.

1.2 SW Sex stars

SW Sex objects are a class of nova-like CVs. Nova-likes are characterized by an approximately steady brightness caused by a disk that is always in a high-viscosity regime due to a high mass accretion rate. Some SW Sex stars reduce their brightness. These low states are irregular and are probably associated with a variation of the mass accretion rate. Because of this, these systems were originally called anti-dwarf nova systems. Historically, the SW Sex-type objects are defined by certain peculiar observational properties. The main SW Sex stars characteristics are listed below (HONEYCUTT et al., 1986; SZKODY; PICHE, 1990; THORSTENSEN et al., 1991; HOARD et al., 2003; RODRÍGUEZ-GIL et al., 2007; DHILLON et al., 2013, e.g.):

- their spectra exhibit single-peaked emission lines rather than the double-peaked lines. This occurs even in eclipsing systems, for which the double-peaked lines are expected from near-edge-on disks;
- the Balmer and He I emission lines are only shallowly (or not at all) eclipsed compared to the continuum. This implies emission originating above the orbital plane;
- the emission line radial velocities are shifted in phase compared to expectations from a simple model of the binary system;
- the emission lines show high-velocity S-waves extending up to 4000 km/s, with maximum blueshift near phase 0.5;
- flux modulation in the optical emission-line wings (emission-line flaring) and kilo-second quasi-periodic oscillations (QPOs);
- orbital periods of 3 – 4.5 hr, slightly above the period gap (2 – 3 hr). The period gap is mainly populated by magnetic systems.

Not all SW Sex stars display all these observational features. Actually, some objects have certain properties at certain times. In order to explain the observational features of SW Sex stars, several physical models have been proposed. Some scenarios, not mutually exclusive, are described below (HONEYCUTT et al., 1986; HELLIER, 1996; TOVMASSIAN et al., 2014; WILLIAMS, 1989; CASARES et al., 1996; DHILLON et al., 2013, e.g.):

- a disk overflow together with an accretion wind that fills in the double-peaked line profile from the accretion disk;
- an optically thick disk and an extended hot spot region, which is responsible for the single-peaked emission lines;
- magnetic accretion.

MCVs exhibit a range of observational signatures. The optical and X-rays light curves show variability synchronized with the WD spin period, and the optical spectra can show cyclotron harmonics, intense Balmer and He II emission lines. However, since several of these observational properties are shared with other classes of objects, the only observation that unambiguously confirms magnetic accretion is circular polarization (MEGGITT; WICKRAMASINGHE, 1982b, e.g.). Polarized light from cyclotron emission can be completely circularly polarized when the magnetic field lines are parallel to the line-of-sight, and maximum linear polarization occurs when the magnetic field lines are perpendicular to the line of sight. LS Peg was the first SW Sex star with direct evidence of circular polarization (RODRÍGUEZ-GIL et al., 2001). In comparison with IPs, there are also others possible signs of magnetism in SW Sex stars such as the flaring in optical emission lines in time scales of tens of minutes, superhumps (periodic brightening), and QPOs (PATTERSON et al., 2002; RODRÍGUEZ-GIL; MARTÍNEZ-PAIS, 2002, e.g.).

Figure 1.4 - Distribution of CVs types in the white dwarf's magnetic moment (μ) and accretion rate ($\dot{M}$) space. AM Her stars are above the upper line, and non-magnetic CVs are below the lower line. DQ Her and SW Sex stars are in between the lines.

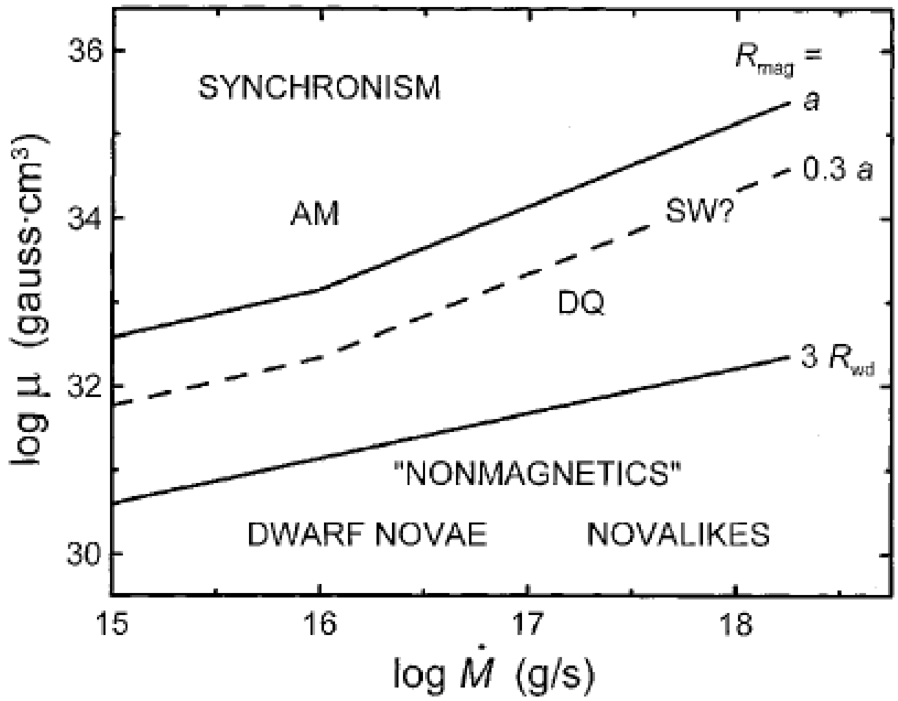

SOURCE: Patterson et al. (2002).

1.3 The Intermediate Polars

The first IP, DQ Her, was reported with a periodic 71 s variation in its light curve (WALKER, 1955). Optical pulses of 33 s were detected in AE Aquarii by Patterson (1979) and other CVs also revealed rapid periodical variations, much smaller than the orbital period. By analogy, with the discovery of X-ray pulsars and the development of models for rotating neutron stars, the DQ Her behavior was associated with the presence of a rotating magnetized WD (LAMB, 1974).

Historically, IPs and DQ Her systems were considered to be different classes due to their spin periods: the slower rotators, having spin periods of $\sim$ 1000 s, were classified as IPs, while the objects with spin of around 50 s were considered as being DQ Her type. The increase in the number of known objects demonstrates that the period distribution is continuous between 0.001 $P_{orb} < P_{spin} < 1$ P_{orb}, showing a concentration of periods around 0.1 P_{orb}. Thus, IPs and DQ Her became synonymous for most authors (HELLIER, 2001). Figure 1.5 shows the distribution of WD rotation periods as a function of the orbital period for MCVs.

Figure 1.5 - The distribution of spin period versus orbital period for MCVs. The triangles are polars and the squares are IPs.

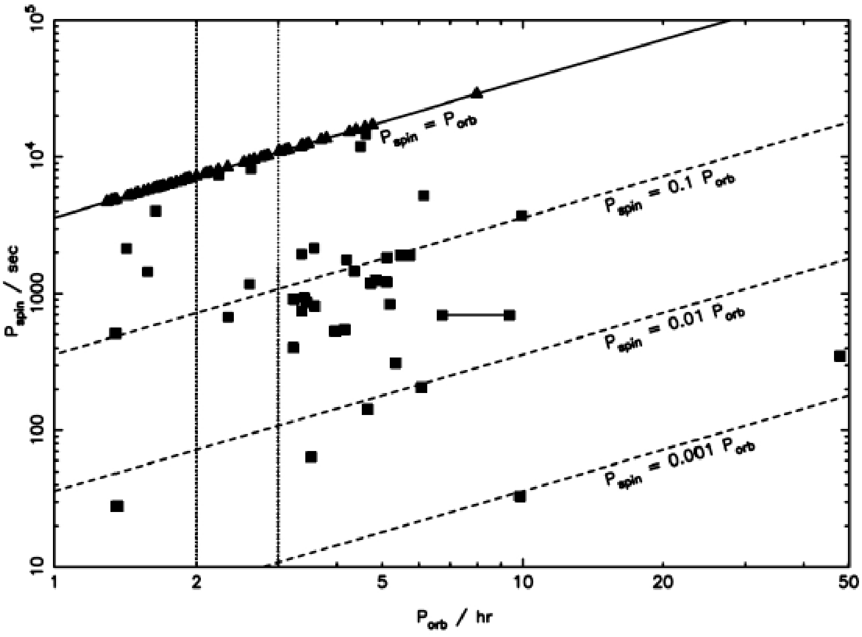

SOURCE: Norton et al. (2004).

The number of known CVs exceeds one thousand systems. The Ritter and Kolb (2003)'s catalog, in its version 7.24, lists 1425 CVs, of which 120 objects are polars and 60 objects are IPs (see Figure 1.3) corresponding to 20 – 25% of MCVs. An IP list can be found in Ferrario et al. (2015, their Table 3). Recently, Pala et al. (2020) defined a complete volume sample of 42 CVs within a distance of 150 pc from GAIA of which 36% have a magnetic WD corresponding to a space density of $1.3^{+0.3}_{-0.4} \times 10^{-6}$ pc^{-3}, which is consistent with previous estimates (WICKRAMASINGHE; FERRARIO, 2000, e.g.,).

Most polars have been discovered using soft X-ray surveys such as ROSAT (BEUERMANN, 1999), whereas IPs are harder X-ray sources and a large number of systems have been discovered by INTEGRAL (LUTOVINOV et al., 2020) and SWIFT (BARLOW et al., 2006; BAUMGARTNER et al., 2013). Optical synoptic sky surveys have also contributed to the MCV census, such as SDSS (SZKODY et al., 2002; SZKODY et al., 2003; SZKODY et al., 2004; SZKODY et al., 2005; SZKODY et al., 2006; SZKODY et al., 2007; SZKODY et al., 2009; SZKODY et al., 2011; OLIVEIRA et al., 2017; SZKODY et al., 2018; OLIVEIRA et al., 2020; SZKODY et al., 2020, e.g.), CRTS (OLIVEIRA et al., 2017; SZKODY et al., 2018; OLIVEIRA et al., 2020; SZKODY et al., 2020, e.g.), ZTF (SZKODY et al., 2020, e.g.). The forthcoming e-Rosita X-ray survey and Vera Rubin Observatory's survey will likely increase these numbers (ZAZNOBIN et al., 2021, e.g.,). The MCV census is important because it provides a better understanding of CV (and MCVs) evolution and the CV contribution to the stellar population and luminosity in optical and X-ray wavelengths (PALA et al., 2020; BELLONI et al., 2020, e.g.).

The main characteristics of IPs (PATTERSON, 1994; HELLIER, 2001; NORTON et al., 2004; HELLIER, 1993, e.g) are listed below and some of them are discussed in the following section.

- The presence of a stable and coherent period in light curves and/or spectra in X-ray and/or optical data different from the orbital one. This flaring period is associated with the WD rotation or the beat period between orbital and rotation periods. This modulation is distinguishable from other signals such as quasi-periodic oscillations and flickering. Detailed studies of spin-phase resolved spectroscopy of IPs have been carried out by Marsh and Duck (1996, FO Aqr) and Bloemen et al. (2010, DQ Her).

- Optical spectrum of high ionization as evidenced by He II 4686Å line.

- In some IPs, optical and infrared light contains a contribution by cyclotron emission from the accretion region and is therefore polarized.

- The magnetic field of WD is in the order of 10^6 G.
- Hard X-ray emission and signatures of absorption in soft X-ray.
- The inner disk is truncated by the magnetosphere radius. In extreme instances, the disk can be fully disrupted.

There is evidence that in V2400 Oph there is no accretion disk (HELLIER; BEARDMORE, 2002). Therefore, the accretion occurs via stream-fed mode, in other words the matter follows a stream from the L_1 point to the magnetosphere/threading region and then falls onto the magnetic WD such as polars. In IPs that have accretion disks, the geometry of the magnetic accretion can be complex, forming accretion columns or arc-shaped curtains, referred to as disk-fed accretion. This complexity arises because the region in which the material is captured by the WD magnetic field is not synchronized with the WD rotation. Moreover, some IPs show evidence of disk-overflow mode, in which the accretion can switch between both scenarios disk-fed and stream-fed (NORTON et al., 1997).

1.3.1 IPs observational properties

An important observational property of IPs is the variation of the flux and its spectral dependence along the rotation cycle. This can be observed as much through phase diagrams from X-ray data, whose amplitude and shape depend on the range of energy, as the spectra that vary with time phase. The flux modulation with spin arises from the WD rotation by means of two processes: the recurrent occultation of the PSR behind the WD or absorption/scattering of the PSR emission by the intervening higher accretion column. The "pulses" of the light curves may have a sinusoidal or irregular shape as shown in Figure 1.6.

The magnetic field regulates the geometry of the flow of matter. The emission of the PSR at high energies can be reprocessed by the material in the pre-shock region generating wide profiles in the emission lines in X-rays and ultraviolet, UV (LUNA et al., 2015, e.g.). A discussion of the interpretation of variability in geometrical terms is presented by Hellier (1999) and Belloni et al. (2021).

The X-ray spectra of IPs are featured by hard X-ray emission originating from PSRs. A soft blackbody emission observed in some systems is understood to arise from the heated WD surface around the accretion footprints (EVANS; HELLIER, 2007, e.g.).

The temperature of the post-shock matter depends on the WD mass and, therefore, the X-ray spectra of IPs can be used for WD mass determination (ISHIDA; TAKEUTI, 1991; SULEIMANOV et al., 2005, e.g.). However, there is an important degeneracy in this determination using only the X-ray spectrum, as recently shown by Belloni et al. (2021). In fact, the WD masses can be estimated by fitting hard X-ray continuum spectra using the structure of the PSR (see Section 1.3.2). The X-ray continuum of IPs in the range < 20 keV is modified by interstellar and intrinsic absorption, and by a possible reflection component. The intrinsic absorption is still not well understood due to the possible inhomogeneous and complex geometry of the accretion flow.

Figure 1.6 - Examples of IPs phase diagrams in three X-ray energy bands. The XMM-Newton data are shown in red and the NuSTAR data are in black.

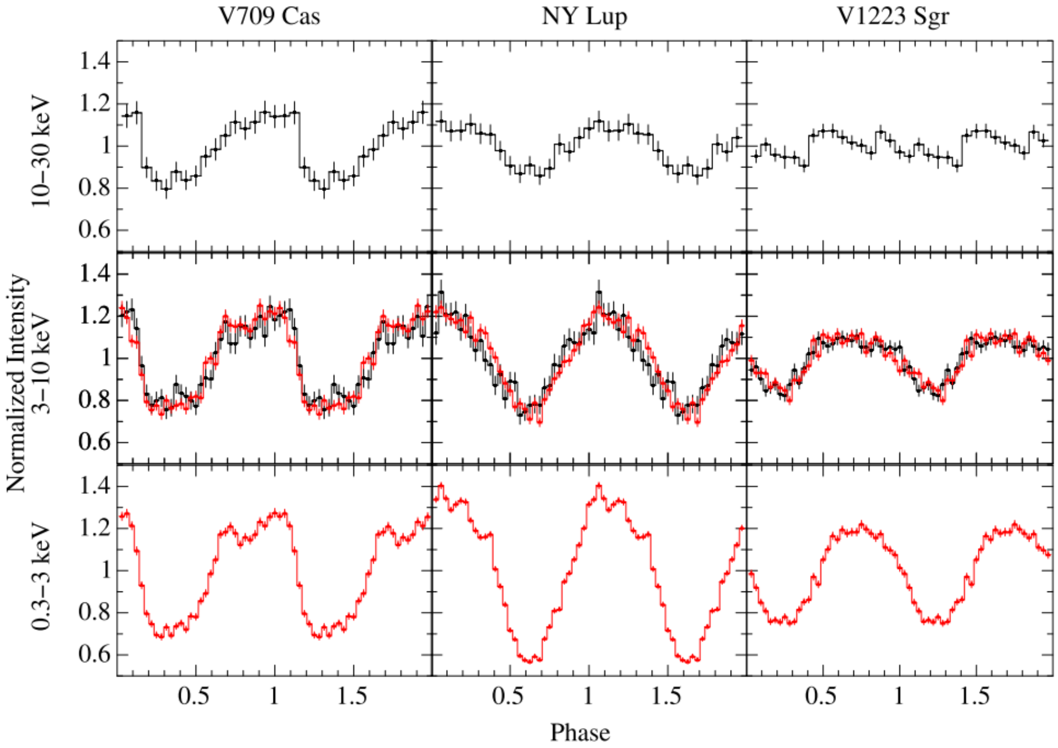

SOURCE: Mukai et al. (2015).

Typically, the optical light curves of IPs show signatures of the orbital period, WD spin period, and the beat frequency, which can be the result of accretion via the "stream-fed" model or the reprocessing of X-rays. Some IPs present low states, whose magnitude can vary 1 – 1.5 mag such as AO Psc and AE Aqr systems (KENNEDY et al., 2017). The cause of these low states is currently suspected to be star spots passing over the L_1 point on the surface of the companion star, temporarily halting mass transfer (HILL et al., 2016). The IP optical spectra can exhibit intense Balmer and He II λ4686 emission lines.

IPs exhibit circular polarization when magnetic fields are in the range of 1 – 10 MG with levels around 1 – 2% (Table 4.1 shows IPs with circular polarization different from zero). The null circular polarization is attributed to the dilution of the polarized light from the PSR by the emission of the disk. However, some authors suggest that a high accretion rate may decrease the high magnetic field on the surface of WD (CUMMING, 2004, e.g.). An example of an object with a positive detection of circular polarization is BG Canis Minoris. Its polarization is -1.74 ± 0.26% in the 1.10-1.38 μm wavelength range and provides direct evidence of magnetic fields controlling the dynamics of accretion in IPs. In particular, it indicates $B \sim 4 \times 10^6$ G (PATTERSON, 1994). On the other hand, cyclotron emission is not confirmed in other IPs such as AE Aqr (FERRARIO et al., 2015; PATTERSON, 1994; PATTERSON et al., 1988, e.g.). Butters et al. (2009) present a list of IPs observed using circular polarimetry, but not all of them have had polarization detected.

1.3.2 Structure of the post-shock region

As said before, the PSR is located between the shock front and the WD surface (Figure 1.7). The PSR physics in polars and IPs is very similar. In PSRs, the pre-shock kinetic energy is converted into thermal energy with temperatures of the order of tens keV. The compressed material in the PSR mainly cools by bremsstrahlung, emission lines and cyclotron. This produces an increase in density from the WD to the shock front. The temperature has the opposite behavior, see Figure 1.8. This is commonly called shock structure.

Aizu (1973) is a seminal work for accretion onto WD. He solves the shock structure, i. e. the density and temperature dependence with the height of the PSR and also calculates the emission from the homogeneous region, considering a pure cooling by optically thin bremsstrahlung. His study also shows that the temperature of the PSR is a function of the WD mass and that the density and height of the region – and therefore its luminosity – are determined by the accretion rate. The PSR structure in an accretion column according to the Aizu (1973) model is shown in Figure 1.8.

King and Lasota (1979) and Lamb and Masters (1979) considered the cooling via bremsstrahlung and cyclotron emission, which quantitatively explains the observational properties of MCVs. Then, Wu et al. (1994), Wu (1994) using both cooling processes, one-dimensional plane-parallel PSR, and disregarding gravitational forces inside the column analytically calculated the temperature and density profiles. Thus, multitemperature spectra can be calculated and compared to observed X-ray spectra in order to determine fundamental properties of the MCVs, such as the WD mass.

Figure 1.7 - The illustration of the accretion column. The PSR is produced when the accretion flow coming from the threading region reaches supersonic velocities. In the PSR, radiation processes cool matter and shape the density and the temperature profiles.

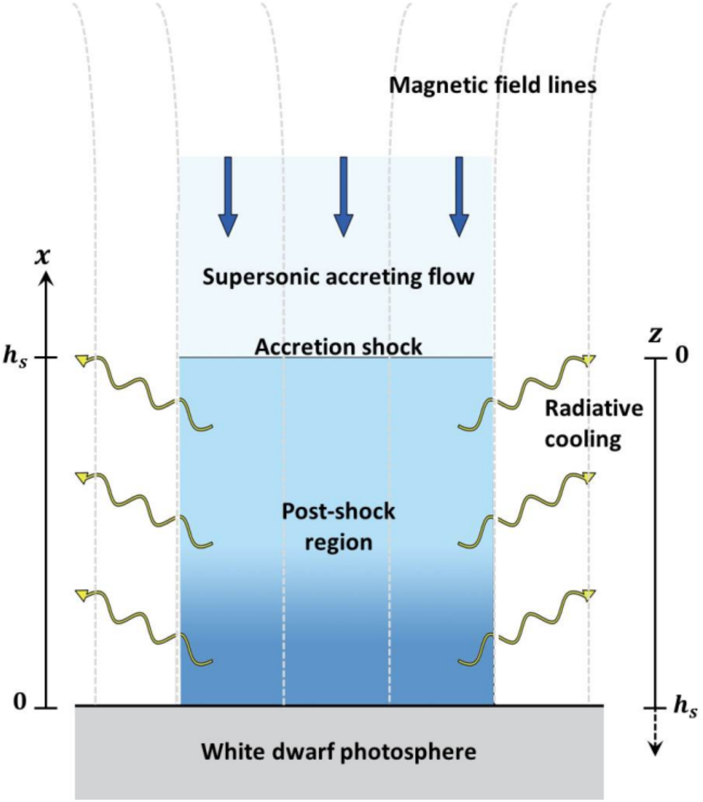

SOURCE: Som et al. (2018)

Cropper et al. (1999) were the first to include the effects of a radially varying gravitational acceleration on the PSR. In other words, they took into account non-negligible shock heights. The effect of the gravitational potential is more significant in the case of the pure bremsstrahlung cooling which results in a larger shock height in comparison with models that also include the cyclotron cooling. In addition, the shock temperature is lower than that calculated from the Aizu model, because the pre-shock velocities at this height are less than those at the surface of the WD. When the gravitational potential is included and the cyclotron cooling is also used, the correction is not so significant because shock height is lower. Using Cropper's model, the WD mass of polars and IPs was estimated using data from different X-ray satellites such as GINGA/LAC (japanese for 'galaxy' – the energy range is 1.5 – 500 keV) by Ishida and Takeuti (1991), ASCA (Advanced Satellite for Cosmology and Astrophysics – ranging 0.4 to 10 keV) by Ezuka and Ishida (1999a), RXTE (Rossi X-ray Timing Explorer – ranging 2 to 250 keV) by Suleimanov et al. (2005).

Figure 1.8 - Shock structure in an accretion column by Aizu (1973). Relative temperature (solid black, left axis) and density (dashed blue, right axis) of the post-shock region.

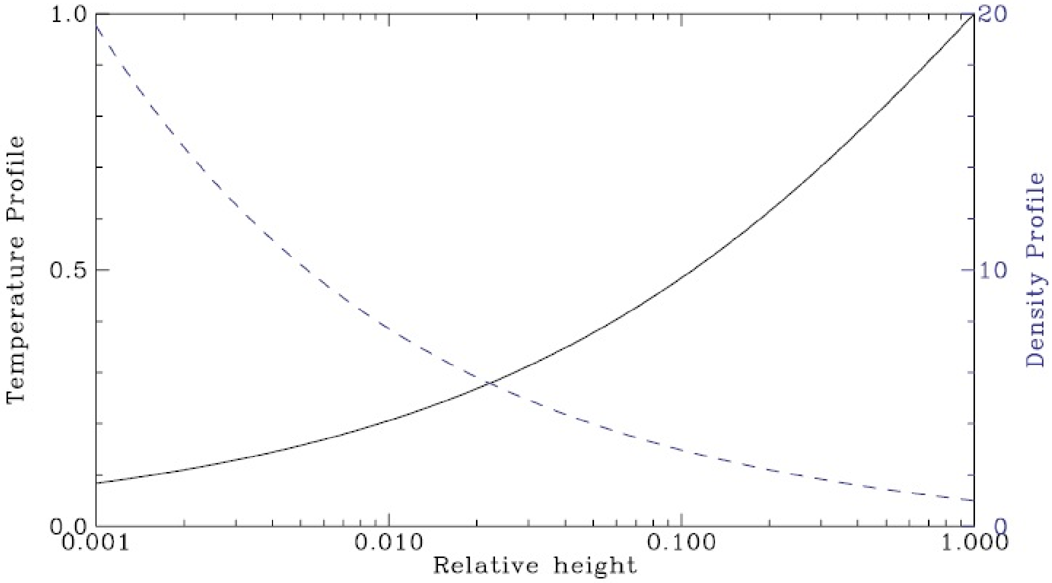

SOURCE: Mukai (2017).

Canalle et al. (2005) added one more ingredient to the PSR structure calculation. They considered the dipole-field geometry in which the accretion flow is considered non-radial. In fact, the hydrodynamics in funnel flow and in radial are qualitatively different, especially for tall post-shock columns where the variation of the gravitational potential is significant. The authors also considered the electrons and ions in thermal equilibrium (one-temperature plasma). However, Saxton et al. (2007) showed that for high mass systems a two-temperature gas/plasma treatment is more accurate and predicts harder X-ray spectra.

The effect of the specific accretion rate ($\dot{m}$), in other words, the mass accretion rate per unit area was discussed by Yuasa et al. (2010). The authors used as comparison, the Cropper model, which has $\dot{m}$ fixed at 1.0 g cm^{-2} s^{-1}, and showed that the estimated WD mass is affected by less than 30% when varying $\dot{m}$ in the range of 1.0 – 10 g cm^{-2} s^{-1} if the WD is less massive than 1.2 $M_{\odot}$, which is true for most WDs. In this context, Hayashi and Ishida (2014a) modified the Cropper model to better deal with the more massive WD of IPs. Specifically, they used dipole geometry, non-equilibrium between ions and electrons, and the parameter $\dot{m}$ from 0.0001 to 100 g cm^{-2} s^{-1}. Their modeling indicated that the temperature and density profiles depend on the specific accretion rate. In particular, the Cropper model is not valid if the specific accretion rate is below a critical $\dot{m}$, which ranges from about 5 to 100 g cm^{-2} s^{-1} for 0.7 and 1.2 $M_{\odot}$ WD, respectively, or when the height of the PSR reaches about 1% of the WD radius.

The effect of the gravitational potential was recently studied by Som et al. (2018), who showed that gravity can be neglected for shock height less than 0.01 R$_{WD}$, whereas it is essential for larger heights. Also, the inclusion of gravity reduces the shock height and produces harder X-ray spectra.

In Belloni et al. (2021), we calculated the PSR temperature and density profiles assuming the equipartition between ions and electrons, the WD gravitational potential, the finite size of the magnetosphere and a dipole-like magnetic field geometry. We also considered the cooling by bremsstrahlung and cyclotron radiative processes. Our model is the only one that solves the radiative transfer using a 3D approach. For mode details see Section 2.12. An overview of the assumptions of some PSR models from literature is shown in Table 1.1.

1.3.3 IPs emission models

Cyclotron emission is not always observed in IPs and most of the IP modeling only uses X-ray data. Although the first X-ray spectrum models represented the PSR as a homogeneous region in temperature (EZUKA; ISHIDA, 1999b), the correct interpretation of the spectra should be performed considering the shock structure and the absorption produced by material in the pre-shock column.

Table 1.1 - Summary of shock solution of PSR from literature.

Model	Gravitational potential	Specific accretion rate (g cm^2 s^{-1})	Magnetic field (MG)	Geometry	Different ion and electron temperatures
Aizu (1973)	Not included	>0.01	0	Cone	Not included
Wu et al. (1994)	Not included	4	30	Cylindrical	Not included
Cropper et al. (1999)	Included	1	30	Cylindrical	Not included
Canalle et al. (2005)	Included	1	0	Dipole	Not included
Yuasa et al. (2010)	Included	Parametrized	0	Cylindrical	Not included
Hayashi and Ishida (2014a)	Included	Parametrized	0	Dipole	Included
Som et al. (2018)	Included	1	10	Cylindrical	Not included
Belloni et al. (2021)	Included	Parametrized	Parametrized	Dipole	Not included

Bremsstrahlung is an important component of the high-energy emission of IPs and in the hottest regions of the PSR, it can be the dominant emission process. Figure 1.9 shows a bremsstrahlung fitting for IGR J00234+6141 with a temperature of 10.8 ± 2.1 keV. For some systems, however, the contribution of emission lines in soft X-rays from cold parts of the PSR can not be neglected (BEARDMORE et al., 2000; CROPPER et al., 1999). Compton scattering can be dominant in spectrum with temperatures above 10 keV (MUKAI, 2017), for example Suleimanov et al. (2008) show that for V709 Cas, it is important to take the Compton scattering into account (Figure 1.10).

Mukai et al. (2003) classify the MCV spectra into two types: cooling flow and photoionized. The first refers to the standard WD accretion model in which the cooling is dominated by free-free emission. It is valid for some IPs and non-magnetic CVs. Luna et al. (2015) applied this model to a high-resolution X-ray spectrum of EX Hya, a low luminosity IP, and concluded that this model needs additional ingredients to modify the temperature structure in order to reproduce the continuum and the lines. The photoionization model applies to V1223 Sgr, AO Psc, and GK Per, for instance. Their X-ray spectra are characterized by a hard, power law-like continuum in the $0.5-8$ keV range that is too flat to be reproduced by the cooling flow model modified by a simple absorber. However, their X-ray spectra above 10keV are well fit by cooling flow type models (MUKAI, 2011; MUKAI, 2017, e.g.).

PSR emission in MCVs can be affected by photo-absorption in the pre-shock accretion column. Norton and Watson (1989) also used the X-ray light curves of all IPs detected by EXOSAT conclude that the pulse profiles can be explained by a combination of absorption by the pre-shock region and PSR self-occultation by the WD. Also, Norton and Watson (1989) reproduced the BY Cam spectra considering an ad hoc absorption prescription, variable with WD spin phase, but without a consistent accretion geometry. The height of the accretion column is also an important ingredient to reproduce the observed modulation. A PSR that extends to non-negligible height in comparison to the WD radius has several consequences. PSR self-occultation by WD is decreased and may not exist for higher PSR regions (which are warmer, but less dense). For a same geometry, the increase in the height of the PSR results in a decrease of the pre-shock region and, consequently a lower absorption (BELLONI et al., 2021). Moreover, the amplitude of the reflection in WD would also be very small (HELLIER, 1999, e.g.).

Figure 1.9 - IP spectrum fitting using only bremsstrahlung . The temperature is approximately 11 keV.

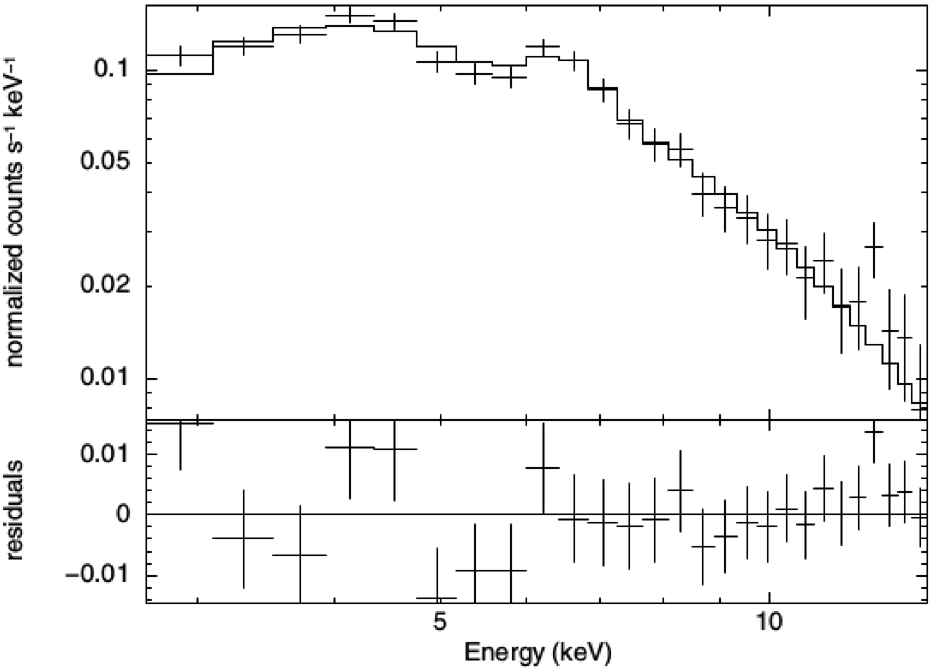

SOURCE: Butters et al. (2011).

The photo-absorption effect can be considered in XSPEC (X-Ray Spectral Fitting Package), see Section 3.1, using a partial covering absorber model called *pcfabs* or a simple absorber model such as *phabs* and *wabs* (ANZOLIN et al., 2008, e.g.). In Figure 1.11, we compare the spectra from XSPEC using the *bremss* and *bremss* modified by *phabs* models with the same temperature (T = 10 keV). The difference of the models is the attenuated emission in soft X-rays due to absorption in the pre-shock accretion column.

IP spectra may present many iron lines such as H-like (6.97 keV), He-like (6.68 keV), 6.4 keV fluorescent lines and also K-shell lines from medium-Z elements. Ezuka and Ishida (1999a), using an sample from ASCA satellite, interpreted that the 6.4 keV line comes from the reflection off the WD surface.

Figure 1.10 - V709 Cas spectrum and the best-fit spectral model of the PSR. The crosses represent the data from RXTE and INTEGRAL. The solid line is the total spectrum of the PSR model with Compton scattering and the dashed without Compton scattering. The dotted curve represents the Gaussian iron line.

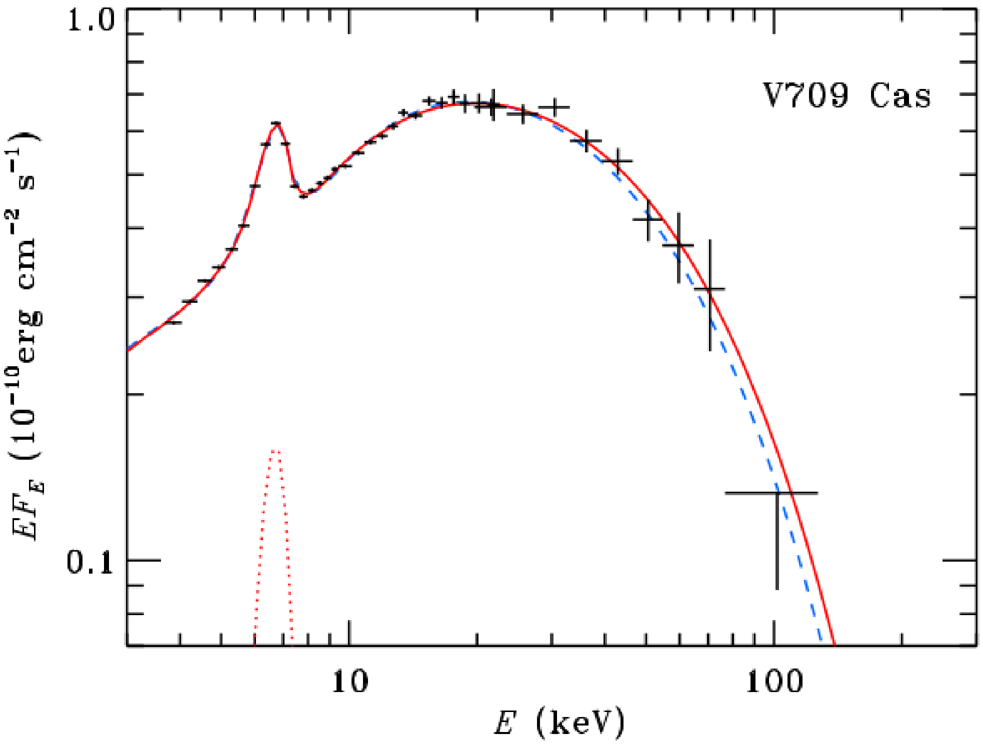

SOURCE: Suleimanov et al. (2008).

The traditional partial covering models do not include the dependence of absorption on geometry. The lines-of-sights to different parts of the X-ray emission region go through differing amounts of matter. To solve this problem, Done and Magdziarz (1998) proposed the *pwab* model, which fits multi-temperature emission, reflection model, and a power law that approximately represents a distribution of covering fractions by several discrete values of the hydrogen column density ($N(H)$). This could represent a physical situation where the column is blobby. Mukai (2017) advertises the development of a new version of a complex absorber model with an ionized absorber. The difference is shown in Figure 1.12. However, absorption models may not be applicable to all IPs, for example, EX Hya displays little evidence of simple or complex absorption.

Figure 1.11 - The XSPEC fitted with *bremss* model is the blue line and *bremss* modified by *phabs* model is the red line. We used T = 10 keV, norm = 1, and N(H) = 5.133 × 10^{+20} cm^3.

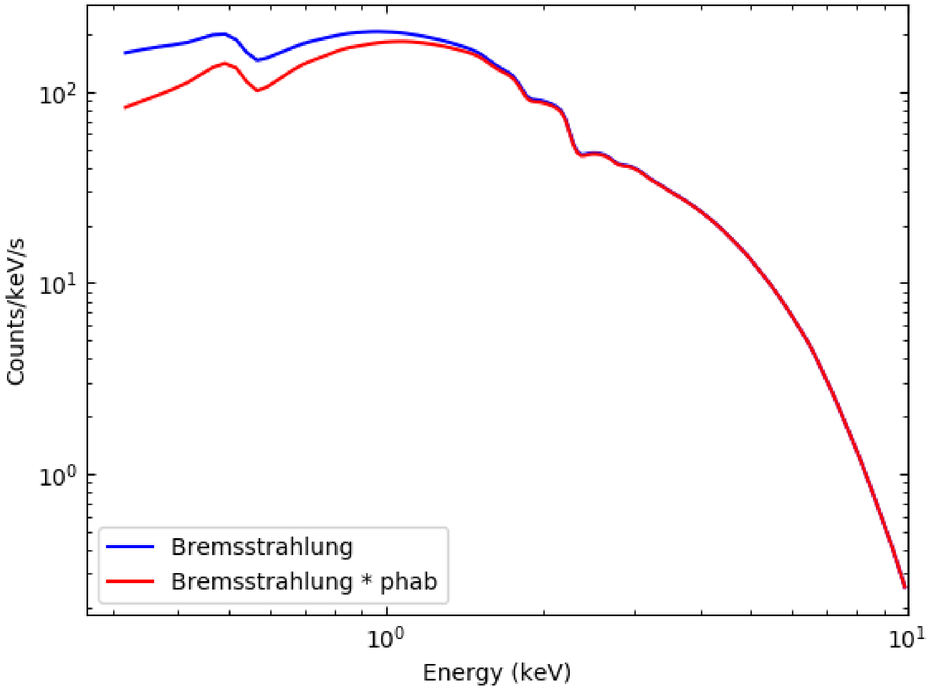

SOURCE: The author.

1.4 The goals of the thesis

The general goal of this thesis is to study magnetic accretion from CVs. Specifically, we performed two different projects: one related to SW Sex stars and the other regarding IPs.

Figure 1.12 - Spectral fitting with XSPEC models of V1223 Sgr. The blue model is the *mkcflow* modified by *pwab* and the red model is the new version *pwab* carried on by Mukai (2017).

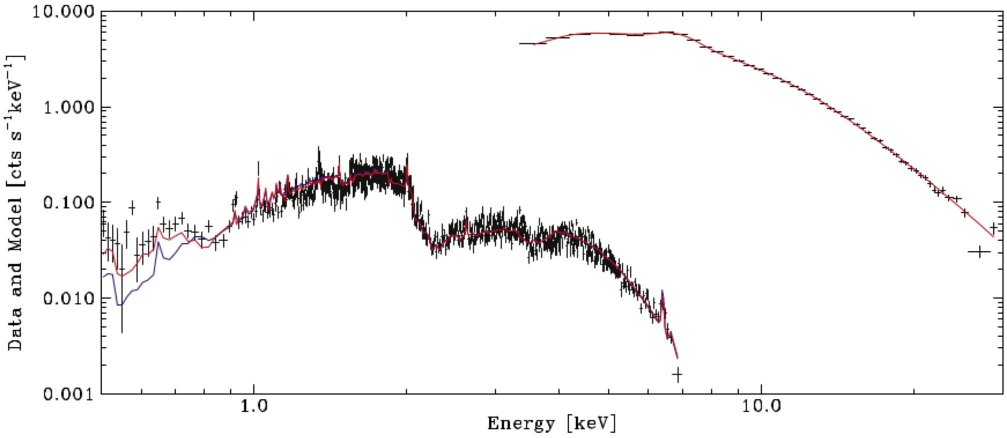

SOURCE: Mukai (2017).

The study of SW Sex systems was initiated during my master's degree, but more observational campaigns were developed during this PhD along with the analysis of the results and their eventual dissemination in Lima et al. (2021). This project sought observational evidence of magnetic accretion in six objects of the SW Sex class: BO Cet, SW Sex, V442 Oph, V380 Oph, LS Peg, and UU Aqr.

The modeling of the IP V405 Aur using the CYCLOPS code was performed in order to apply our code to IPs for the first time, because heretofore CYCLOPS code applications were restricted to polars. In fact, the CYCLOPS code is a suitable and competitive tool to study magnetic accretion in IPs because the PSRs do not care if the material comes from a stream or a courtain accretion. The code is unique because it adopts a 3D approach and calculates the radiative transport of cyclotron and bremsstrahlung processes in the PSR structure. Besides, CYCLOPS is not limited to optically thin regimes.

The structure of the thesis is as follows. Chapter 2 describes the CYCLOPS code. Chapter 3 provides a general introduction to the XSPEC code and a comparison with CYCLOPS. Chapter 4 presents the selection of the IP type as our initial choice for the modeling of V405 Aur. UU Col is another case where this is a good option for the modeling. Chapter 5 discusses the fitting of V405 Aur photometric and polarimetric UBVRI optical data besides its spectrum and light curve in X-rays. Chapter 6 shows the results of our search for magnetic accretion in SW Sex stars.

2 THE CYCLOPS CODE

This chapter introduces the CYCLOPS code. A short history of the code is presented in Section 2.1 while the radiative transport for optical and X-ray data is described in Section 2.2. In Section 2.3 the geometrical and physical input parameters are enumerated and the way the code works along with the main routines are presented in Section 2.4. Section 2.5 describes how the input files of CYCLOPS should be used while Section 2.6 exhibits the optimization procedure used in our code. The figure of merit is discussed in Section 2.7 and Sections 2.8, 2.9, 2.10, and 2.11 present additional information on how the code deals with the interstellar extinction, the absorption and scattering by the interstellar medium and internal to the binary, and multifrequency modeling, respectively. The shock solution of PSR implemented in the code, namely the 2020 version is described in Section 2.12. Finally, the code without the shock solution, that is, the version prior to 2020 is discussed in Section 2.13.

2.1 History

CYCLOPS – an acronym for the CYCLOtron emission of PolarS – is a code to model the continuum optical, infrared, and X-ray emission from the PSR by cyclotron and bremsstrahlung emission. The code considers a three-dimensional and non-homogeneous accretion column. The temperature and density are represented by radial profiles and the magnetic field varies in a 3D space following a dipolar recipe (COSTA; RODRIGUES, 2009; SILVA et al., 2013).

In the initial version, the CYCLOPS code considered only the cyclotron emission and enabled the simultaneous fit of two optical light curves (COSTA; RODRIGUES, 2009). As part of her thesis, Silva (2013) modified the code to include any number of optical light curves and X-ray spectra. Recently, the X-ray light curves have been implemented (Belloni et al. (2021) and this thesis).

The numerical solution of the hydro-thermodynamic equations that describe the temperature and density profiles in the PSR was added to the code replacing the arbitrary functions described by Silva et al. (2013). The solution was implemented by Dr. Diogo Belloni (BELLONI et al., 2021).

Figure 2.1 shows an example of the PSR geometry of the eclipsing polar MLS110213: 022733 +130617 as modeled by the CYCLOPS code. In particular, this geometry is consistent with the observed eclipse (SILVA et al., 2015).

Figure 2.1 - Geometric representation of the emitting region on the WD surface using the CYCLOPS code. The blue line represents the walls of the PSR, the red curve is the magnetic field line that passes through the PSR center and, the green line is the magnetic axis.

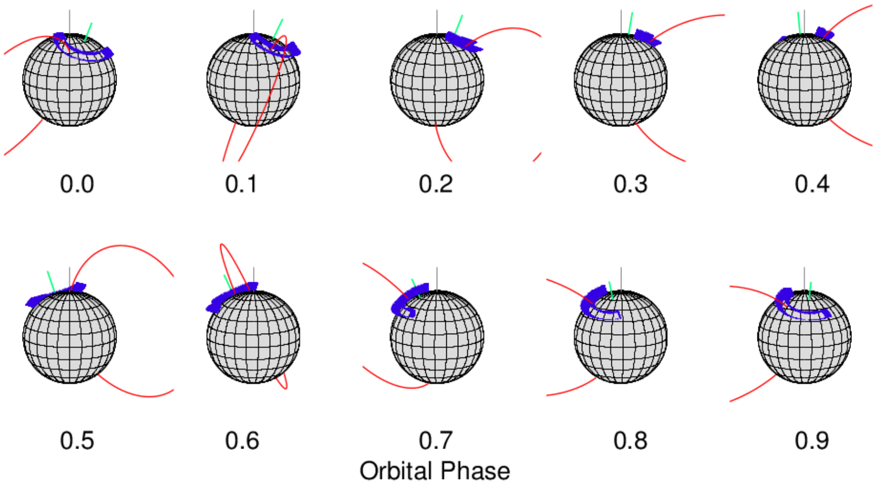

SOURCE: Silva et al. (2015).

2.2 Radiative transfer

The CYCLOPS code uses a reference system with the origin at the WD center, in which the z-axis is the observer direction, i.e. the direction of the radiation propagation, the x-axis is in the orbital plane, and the y-axis completes the coordinate system for each phase. The emitting region is composed of N × N × M cells, a rectangular prism, where N is the resolution in the sky plane and M is the is the resolution along the line-of-sight. Initially, the code uses N × N × N cells, however, the code requires to have at least ten steps in the radiative transfer in the line-of-sight direction. Therefore, if N is not high enough to fulfill this condition, the resolution in the line-of-sight direction is increased to M. CYCLOPS calculates the radiative transfer in each cell. The density, temperature and magnetic field in each cell are assumed to be constant, but they vary from cell to cell. The first cell is the input to second cell and so on. The flux is obtained in each of the Stokes parameters in each rotation phase step by integrating the intensities in all line-of-sights. Therefore, the radiative transfer is performed for each rotation resolution step (COSTA; RODRIGUES, 2009).

The CYCLOPS code calculates the radiative transport solution of Pacholczyk and Swihart (1975) and Meggitt and Wickramasinghe (1982a) for the intensities of the four Stokes parameters for the cyclotron process, which is relevant for MCVs in the optical and infrared regime. In X-rays, only the total intensity produced by the bremsstrahlung process for any optical depth is calculated. Also, the photo-absorption is implemented in CYCLOPS owing to the dominant radiative process in the pos- and pre-shock accretion column, respectively. The radiative transfer solution was solved for each line-of-sight considering the emission and absorption (SILVA et al., 2013). The convolution between the instrumental responses and the model is performed by the package for interactive analysis of line emission *PINTofALE* code (KASHYAP; DRAKE, 2000).

2.3 Geometrical and physical parameters

The geometry of the magnetic accreting column in the CYCLOPS code is illustrated by Figure 2.2. The emitting region is located near the WD, denoted by the red circle. The input parameters of a CYCLOPS model are listed below.

Geometrical parameters:

- i – the inclination of the MCV orbital plane relative to the observer. The WD rotation axis is assumed to be normal to the orbital plane;
- β – the central PSR colatitude, in other words, the angle between the WD rotation axis and the center of the PSR region on the WD surface;
- $B_{\rm lat}$ and $B_{\rm long}$ – define the latitude and longitude of the magnetic axis with respect to the orbital plane and the line connecting the WD and the donor centers, respectively;
- $\Delta_{\rm long}$ and $\Delta_{\rm R}$ – define the threading region size and are the semi-amplitude in the longitudinal and radial directions, respectively. $\Delta_{\rm R}$ is represented as a fraction of the distance of the threading region center to the WD center.

Physical parameters:

- $M_{\rm WD}$ – the WD mass;
- B – the WD magnetic field strength at the WD magnetic pole;
- $\dot{M}_{\rm WD}$ – the mass accretion rate.

Figure 2.2 - Geometry accretion used by the CYCLOPS code. The PSR on the surface of the WD is shown as a white region, highlighted by a red circle. The threading region is defined by Δ_{long} and Δ_R parameters. β is the colatitude angle of the center of the PSR and the B line represents the magnetic axis.

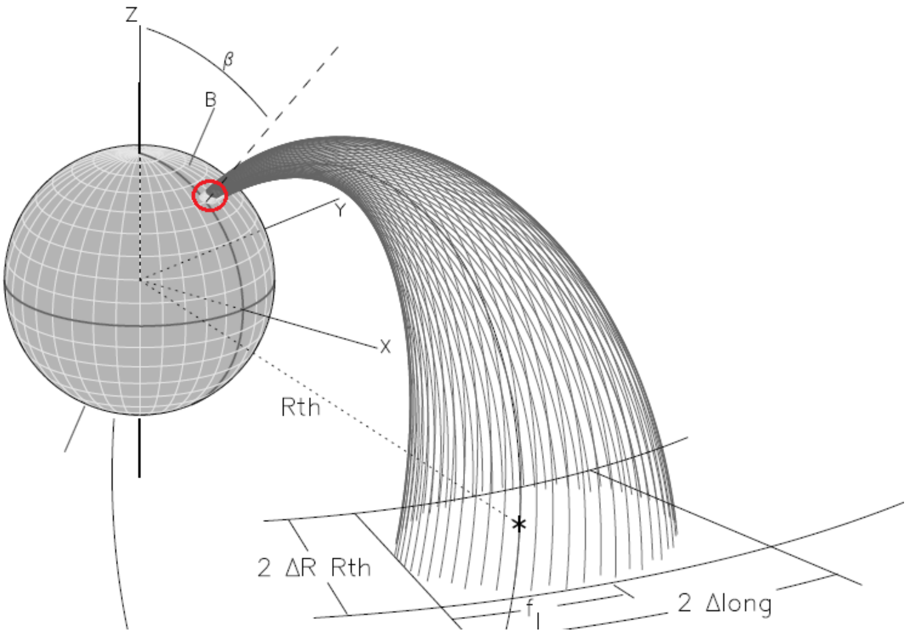

SOURCE: Costa and Rodrigues (2009).

The accretion geometry is defined from the threading region (see Figure 2.2). Currently, the same threading region in CYCLOPS produces two PSRs: one in the northern hemisphere and another in the southern hemisphere. Given a PSR emission model calculated by the CYCLOPS code, we can identify some external factors that can modify the observed emission. The interstellar extinction is one example. To compare data and model, it may also be necessary to define other kinds of non-intrinsic PSR parameters such as the difference of phase between the model and the observations or the flux level.

In the X-ray fitting, the distance of the source, which may be provided by the accurate parallaxes from Gaia satellite for many sources, can be considered in CYCLOPS in order to calculate the absolute flux levels. In Section 3.2, we demonstrate that CYCLOPS spectra in absolute physical units are consistent with those obtained using XSPEC .

2.4 Main routines

The CYCLOPS code consists of several IDL (*Interactive Data Language*) and C++ routines. In general terms, the code can be divided into three blocks: the model calculation; the comparison between a model and an observational data set; the fitting of an observational data set. The code has optical and/or X-ray data files as inputs along with a file containing the geometrical and physical parameters to calculate a model or to perform the optimization algorithm (see Section 2.6). Regarding the calculation of a model, the first step is to calculate and save the geometry of the WD, the PSR, and the pre-shock region. Then, the differential hydro-thermodynamic equations and boundary conditions of PSR are numerically solved and the PSR grid is filled with density, temperature, and magnetic fields values. Next, the code calculates the radiative transfer based on the the cyclotron and bremsstrahlung emissivities and their absorption cross sections for each line-of-sight of PSR. This is performed for each WD rotation step since the grid changes as a function of the observed line-of-sight. When comparing a given model with observations, the interstellar extinction are also taken into account. This includes the photoelectric absorption in X-rays and reddening in the optical range. If the model refers to X-rays, the convolution with the instrumental response is performed as an option.

A model is calculated for a given number of WD rotational phases (defined by an input parameter), which can be different from the number of data phases. Thus, the code interpolates or bins the flux in phase. The number of optical curve phases may be different from the number of X-ray curve phases.

If the code is running a fitting procedure, the chi-square (χ^2) of each model is calculated and concatenated in a single file. Finally, we identify the minimum χ^2 and graphically compare the model with the data.

The main routines of the CYCLOPS code are listed below.

polar_pikaia.pro , performs the optimization algorithm in order to search for the best model;

model_inhomog_c.pro , calculates an emission model of PSR based on geometrical and physical parameters. The geometry includes the WD, the PSR , and pre-shock region;

transfer_2d.pro , this routine performs the radiative transfer on all lines-of-sight in the emitting region;

bremss_trans.pro , calculates the bremsstrahlung emission and absorption coefficients;

gyro_trans.pro , calculates the cyclotron emission and absorption coefficients;

PSRsolver.c , numerical solution of the PSR based on hydro-thermodynamic equations and boundary conditions. The solution is the result of the Runge-Kutta-Fehlberg numerical method associated with adaptive step-size control;

calc_chi.pro , calculates the χ^2 of the models with respect to the data;

xanalise.pro , this routine allows the user to produce graphs comparing the data with a model.

2.5 Input files of CYCLOPS

The CYCLOPS code considers one input file for each optical band. For example, one file represents the B band, another the V band, and so on. These files should use the extension ".olc". They should contain a set of frequencies (in Hz) and their respective weights to represent a spectral band response. The limit case of only one frequency is allowed.

The harmonic number of the cyclotron emission varies throughout the region because the magnetic field changes in space due to the dipolar geometry. So, to fit broadband observational data it is advisable to understand the importance and effects of the frequency choice. Ideally, CYCLOPS should use a large number of frequencies to correctly map the spectral response in one band. However, as the radiative transfer is done frequency by frequency, there is a high price in terms of computational time. Our experience shows that UBVR bands are well represented by one frequency in the fitting algorithm. However, the R and I bands need at least three frequencies due to their width and also because the cyclotron emission tends to have a larger optical depth for low frequencies (see Section 2.11).

The optical input data are the flux density, in Jansky or a unit proportional to it, circular polarized fraction, linear polarized fraction, and polarization angle as a function of the WD rotation phase. The conversion of magnitudes into flux density in a particular X band (f_X) is given by Equation 2.1.

$$f_X(m_X) = f_X(m_X = 0) \times 10^{-m_X/2.5}, \tag{2.1}$$

where $f_X(m_X = 0)$ is the flux corresponding to $m_X = 0$ and m_X is the object magnitude in the X band.

CYCLOPS fits absolute optical fluxes in each band, which is equivalent to a fit of the spectral energy distribution. Therefore, a correct calibration of optical magnitudes is essential for optical multiband fitting. Otherwise, the incorrect wavelength dependence of the observed emission can produce a bias in the fitted parameters.

The input files for X-ray data are spectrum and their instrumental responses, and light curves. The calculation of light curves requires the input of one spectrum data file. The instrumental responses and the spectrum are created using the tools adequate for the observatory. During the X-ray data reduction, we obtained two files: the detector redistribution matrix file (RMF), which is a file containing the mapping matrix from the detector channel into the photon energy, and the ancillary response file (ARF), the vector of the effective area of the detector as a function of the energy (ZUHONE et al., 2014). The spectrum input file for CYCLOPS must have the ".xsp" extension. The unit of the abscissa should be given in energy (keV) and the counts of an individual channel in counts/keV/s.

2.6 The optimization procedure

In order to determine the parameters of the model that best fit the data, the optimization algorithms PIKAIA and AMOEBA were implemented in the CYCLOPS code. Both of them have public domain implementation software codes. To perform a search in a broad range of parameters, we used the PIKAIA genetic algorithm (CHARBONNEAU, 1995). Then, we used the AMOEBA subroutine (PRESS et al., 1992) to refine the search for a given model in a limited domain portion.

PIKAIA is appropriated for large numbers of input parameters. This genetic algorithm belongs to a class of search techniques inspired by the biological process of evolution by natural selection. In the space of parameters, the algorithm forces the figure of merit minimization by crossover probability and a maximum mutation rate. Some parameters of PIKAIA are as follows (CHARBONNEAU, 1995): (i) *nger*, defines the number of the generations used; (ii) *nd*, defines the number of significant digits retained in chromosomal encoding; and (iii) *pmut*, initial mutation rate, which is the probability of one gene locus mutating in one generation.

AMOEBA or downhill simplex method was proposed by Nelder and Mead (1965). The minimization of a function of n variables depends on the comparison of function values at the $(n+1)$ vertices of a general simplex, or a geometrical figure such as a triangle or a tetrahedron, followed by the replacement of the vertex with the highest value by another point. In other words, if P_o is the initial starting point, the other N points are given by Equation 2.2.

$$P_i = P_o + \lambda e_i, \tag{2.2}$$

where the e_i's are N unit vectors, and λ is a constant, which is your guess of the problem's characteristic length scale.

2.7 The figure of merit

To determine the model parameters that best fit the observational data set, we used the χ^2 as the figure of merit in CYCLOPS. The input data (photometry, circular polarimetry, linear polarimetry, polarization angle, X-ray spectrum, and X-ray light curve) can differ numerically by orders of magnitudes. For this reason, the user may want to attribute different weights to prioritize the fitting of a given observational set. Hence, the code considers the weights given for each type of data (see Equation 2.3). It is calculated by Equation 2.3, which takes into account simultaneously optical data (χ^2_{opt}) and X-ray data (χ^2_{xr}).

$$\chi^2_{total} = \sum_i \omega_i \chi^2_i, \tag{2.3}$$

where ω_i is the weight chosen by the user for each i kind of input data, which $i = 1$ is the photometry, $i = 2$ is the circular polarimetry, $i = 3$ is the linear polarimetry, $i = 4$ is the polarization angle, $i = 5$ is the X-ray spectrum, and $i = 6$ is the X-ray light curve.

The χ^2 of the photometry data is calculated by Equation 2.4, the χ^2 of the polarimetric data is given by Equation 2.5 while the χ^2 of the X-ray data is determined by Equation 2.6.

$$\chi^2_{E_{opt}} = \sum_{E_{opt}} \sum_{E_{ph}} [d_{E_{opt,ph}} - (f_{cyc} F_{opt,ph} + f^{np}_{E_{opt}})]^2, \tag{2.4}$$

$$\chi^2_{E_{opt}} = \sum_{E_{opt}} \sum_{E_{ph}} (d_{E_{opt,ph}} - f_{cyc} F_{opt,ph})^2, \tag{2.5}$$

$$\chi^2_{E_{xr}} = \sum_{E_{xr}} \sum_{j} [d_{E_{xr,j}} - (f_{xr} F^{conv}_{E_{xr,j}})]^2, \tag{2.6}$$

where E_{opt} and E_{xr} are the energies in optical and X-rays wavelengths, respectively, $d_{E_{opt,ph}}$ and $d_{E_{xr,j}}$ are the fluxes observed in terms of optical (ph) and high energies (j) phase-dependent. $F_{opt,ph}$ is the optical flux calculated using the core of the code, f_{cyc} is the multiplicative value used to normalize optical models and allow a comparison between the χ^2 values, $F^{np}_{E_{opt}}$ is the additive constant, which represents the unpolarized optical flux. f_{xr} is the multiplicative value for X-ray data applied to fit absolute flux, and $F^{conv}_{E_{xr,j}}$ is the X-ray flux convolved with the instrumental responses (ARF and RMF).

We used the IDL routine *conv_rmf* from *PINTofALE* in order to convolute the original flux from CYCLOPS, $F_{xr,ph}$, with the response matrices to obtain the flux for observation:

$$F^{conv}_{E_{xr,j}} = ARF \times (F_{xr,ph} \times RMF). \tag{2.7}$$

2.8 Optical interstellar extinction

The optical interstellar extinction is the light attenuation along the propagation path in the interstellar medium (ISM). The extinction occurs due to absorption and scattering by dust in the ISM. Extinction by interstellar dust affects most astronomical observations and it is not equally effective for all wavelengths: the shorter the wavelength, the higher the extinction. This phenomenon causes an object to appear redder than it really is. The extinction for a given wavelength, λ, in units of magnitude is usually defined as $A(\lambda)$. The extinction can also be quantified by the color excess ($E_{\lambda-V}$), with respect to the V band, a reference passband (LARSON; WHITTET, 2005, e.g.), see Equation 2.8.

$$E(\lambda - V) = (m_\lambda - V) - (m_\lambda - V)_o, \tag{2.8}$$

where $(m_\lambda - V)$ and $(m_\lambda - V)_o$ are the observed and the intrinsic values of the color index, respectively.

In the Johnson system, the extinction is usually parameterized by R_V [$\equiv A(V)/E(B-V)$], the ratio of total to selective extinction. Theoretically, R_V characterizes the size distribution of the dust grains being larger in regions with larger grains. In the diffuse ISM, R_V has been shown to be constant and approximately 3.05 ± 0.15 (WHITTET, 1992, e.g.).

The wavelength dependence of the extinction can be represented by the ratio $A(\lambda)/A(V)$. Cardelli et al. (1989) studied the extinction in many Galactic lines-of-sight and concluded that this ratio is well represented by a function of R. The optical reddening correction in CYCLOPS uses their recipe, which is shown in Figure 2.3 for certain values of R. CYCLOPS adopts the extinction curve of Cardelli et al. (1989) using $R_V = 3.1$ (SCHLAFLY; FINKBEINER, 2011).

The CYCLOPS code calculates the absolute value of the extinction in a given band based on the hydrogen columnar density, $N(H)$, an input parameter of CYCLOPS. First of all, CYCLOPS calculates $A(V)$ from the gas-to-dust ratio, $N(H)/A(V)$ of Zhu et al. (2017, Equation 2.9). If the data is not in the V band, CYCLOPS uses the Cardelli et al. (1989) relation to calculate $A(\lambda)$ from $A(V)$.

$$N(H) = (2.08\ \pm\ 0.02) \times 10^{21} A(V) [H\ cm^{-2}\ mag]. \tag{2.9}$$

2.9 Absorption in X-rays

In X-rays, the photons emitted by the PSR can undergo interaction with matter inside the binary, the circumbinary matter, and the ISM. Photoelectric absorption is the dominant process for X-rays below 10 keV (HOFFMAN; DRAINE, 2016). CYCLOPS takes into account the absorption from the ISM and from the pre-shock region. This was implemented by Silva et al. (2013). The ISM optical depth (τ^{XR}_{ISM}) is determined using the package *bamabs* from *PINTofALE*. In wavelengths less than 91.2 nm, $\tau^{XR}_{ISM}(\lambda)$ is expressed by Equation 2.10 (KASHYAP; DRAKE, 2000).

$$\tau^{XR}_{ISM} = \sum_i \sigma^{abs}_i(\lambda) N_i, \tag{2.10}$$

where σ^{abs}_i is the photo-absorption cross-section of species i and N_i is the column density of species i in the ISM, as seen from Earth.

Figure 2.3 - Interstellar extinction implemented in the optical regime of the CYCLOPS code from Cardelli et al. (1989). The blue line corresponds to $R_V = 2.75$, the red for $R_V = 3.52$, and the green for $R_V = 5.30$. The CYCLOPS code adopts $R_V = 3.1$.

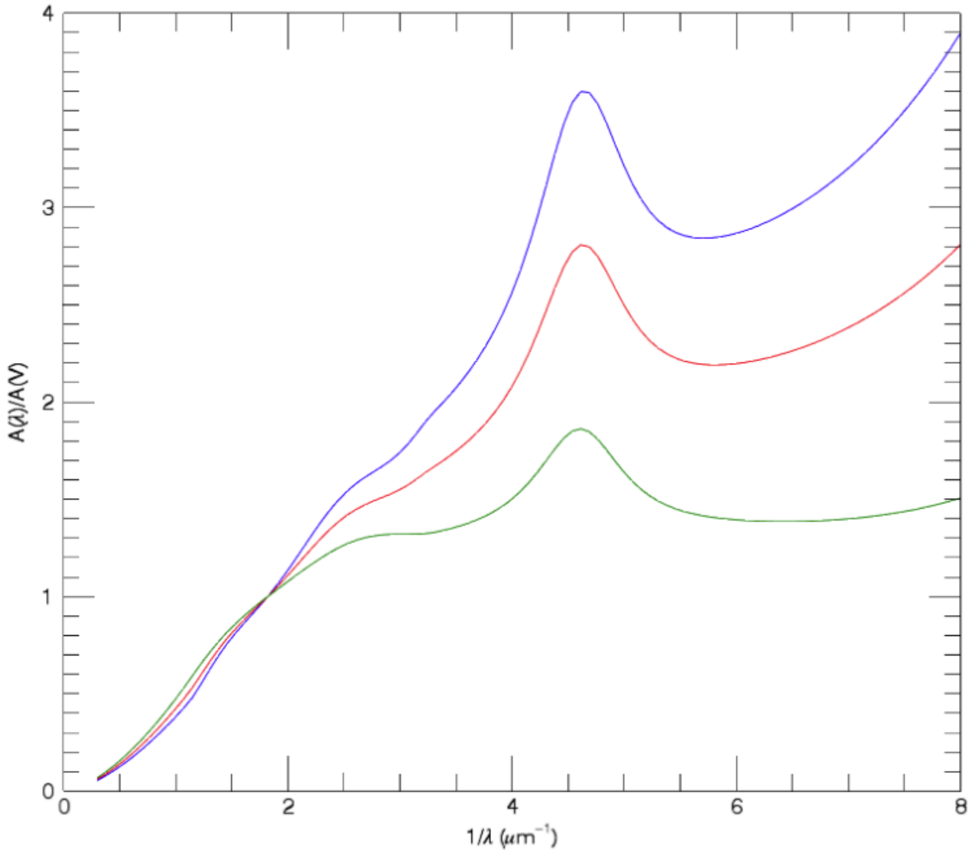

SOURCE: The author.

As already mentioned, the fluxes are calculated for each WD rotational phase, ph: $F_{E,ph}$. In each phase, the total flux emitted by the PSR is calculated by the sum of the fluxes from all lines-of-sight (pixels) that compose the projection of the PSR in the plane of sky. The photo-absorption produced by the pre-shock region is calculated individually for each line-of-sight and applied to the PSR emission of the respective line-of-sight. The absorption in each line-of-sight is proportional to the length of the pre-shock region.

The observed flux attenuation is due to interstellar photo-absorption given by Equation 2.11 and by the scattering in the pre-shock columns (Section 2.10).

$$F_{E,ph} = e^{-B\tau_{ISM}} \sum_{l} F_{E,l,ph} e^{-\tau_{pre}(l)}, \tag{2.11}$$

where τ_{ISM} and $\tau_{pre}(l)$ are given by Equations 2.12 and the 2.13, the variable B ranges from 0 and 1 and can be constant or can be fitted to provide the minimum value of χ^2.

$$\tau_{ISM} \ = \ \sigma_{ph} \ N_{col}^{ISM}, \tag{2.12}$$

where σ_{ph} is the photo-absorption cross-section and N_{col}^{ISM} is the interstellar column density of hydrogen discussed in Section 2.8.

$$\tau_{pre}(l) \ = \ k_l \ s \ \sigma_{ph} \ N_e^{pre}, \tag{2.13}$$

where k_l is the number of cells in the pre-shock region, s is the optical path corresponding to one cell length, σ_{abs} is the photo-absorption cross-section, and N_e^{pre} is the PSR density given by Equation 2.14

$$N_e^{pre} = A * 0.25 * 0.5 * N_e^{min}, \tag{2.14}$$

where A is a variable fraction between 0 and 1; the factor 0.25 comes from the Hankine-Hugoniot conditions, which represent a discontinuity in the plasma near the top of the shock front and the WD photosphere, i.e., the density in the shock front decreases by a factor of 4 from the pre-shock region to the PSR; the factor 0.5 comes from the assumption that the ionized fraction of the material in the pre-shock region is 50%. N_e^{min} is the PSR minimum density, which occurs at exactly the shock front at the top of the PSR.

The optical depth of the pre-shock region is defined by the number of cells and the optical path length in each line-of-sight as well as the density of PSR. In each line-of-sight that composes the PSR image in a given rotation phase, the maximum optical depth of the pre-shock region is defined by the number of cells, the optical path length of each cell as well as the pre-shock density and the cross section (Equation 2.13). In CYCLOPS , the pre-shock density is assumed to be a constant value, N_e^{pre}.

2.10 Scattering in the pre-shock column

The scattering of radiation from electrons in the pre-shock region is considered by CYCLOPS code for optical and X-ray modeling. In optical wavelengths, the classical case of Thomson scattering is used. The differential Thomson cross section for unpolarized incident radiation is given by Equation 2.15. In X-rays emission, CYCLOPS uses the Compton scattering calculated by the Klein–Nishina formula (RYBICKI; LIGHTMAN, 1979, Equation 2.16).

$$\sigma_T = 6.6525 \;\times\; 10^{-25} cm^2, \tag{2.15}$$

$$\sigma = \sigma_T \frac{3}{4} \left\{ \frac{1+x}{x^3} \left[\frac{2x(1+x)}{1+2x} - ln(1+2x) \right] + \frac{1}{2x} ln(1+2x) - \frac{1+3x}{(1+2x)^2} \right\}, \tag{2.16}$$

where $x \;\equiv\; h\nu/mc^2$, which h being Plank's constant = 6.625 x 10^{-27} erg s, ν is the wave frequency, m is the electron mass, c is the free space velocity of light.

In CYCLOPS, the pre-shock region is considered to be partially ionized with an arbitrary value of 0.5 of the ionized fraction.

2.11 Multifrequency modeling

The cyclotron radiation is known to be circularly and linearly polarised and wavelength-dependent (WEST et al., 1987). Figure 2.4 shows an example of the observed spectrum and a cyclotron emission model of polar RX J1938.6-4612 using three different phases as a function of the angle between the magnetic field lines and the line-of-sight (φ), temperatures, and magnetic field. This figure shows the theoretical and observational cyclotron emission variation as a function of wavelength. Thus, the multifrequency correction leads to harmonic cyclotron deviations.

In its present version, the CYCLOPS code allows the user to consider an arbitrary number of frequencies to represent a band . In previous versions, the effective wavelength midpoint of the filters was fixed to the Johnson system (SILVA et al., 2013). This approach prevented the fitting of data observed in other photometric systems. We have implemented a generalized multifrequency approach to represent a data set.

Figure 2.4 - The normalized cyclotron spectra in different phases, temperature, magnetic field, and projection angle (angle between line-of-sight and magnetic field). From top to bottom: ϕ = 0.06 ,0.19, 0.73, kT = 10, 5, 5 keV, B = 47, 70, 70 MG, φ = 80°, 40°, 80°.

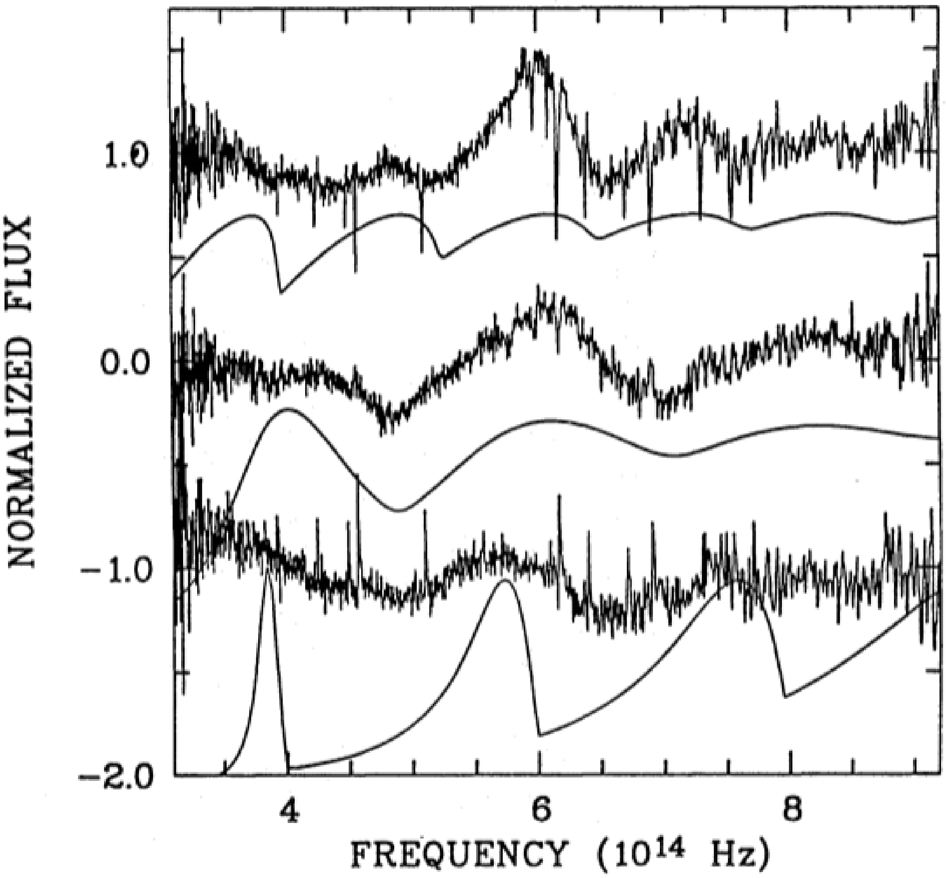

SOURCE: Schwope et al. (1995).

2.12 CYCLOPS with shock solution

The CYCLOPS code solves the PSR density and temperature profiles assuming: (i) stationary one-dimensional hydro-thermodynamic differential equations (WU et al., 1994, e.g.); (ii) dipole-like geometry (CANALLE et al., 2005, e.g.) and (iii) equipartition between ions and electrons (HAYASHI; ISHIDA, 2014a, e.g.). For a review of these models see Section 1.3.2. The shock in magnetic CVs is produced when the supersonic flow along the magnetic accretion has to settle down at the surface of the WD. In MCVs, the ionized gas from the threading region follows the magnetic field lines to the surface of the WD. When it reach supersonic velocities, the abrupt stopping of the inflow near the surface of the WD leads to the formation of a shock, which heats the inflowing material (AIZU, 1973; FABIAN et al., 1976; KING; LASOTA, 1979; LAMB; MASTERS, 1979).

Figure 2.5 - Geometry of the PSR model from CYCLOPS. Λ_{cyc} and Λ_{brem} are the cyclotron and bremsstrahlung cooling functions, respectively. S_b is the accretion area of the PSR on the WD surface and B_b is the magnetic field strength at the PSR bottom. The shock position is given by $z = z_{sh} = R_{WD} + H_{sh}$, where H_{sh} is the shock height with respect to the WD surface. The accretion area and magnetic field vary through the PSR in the z-axis.

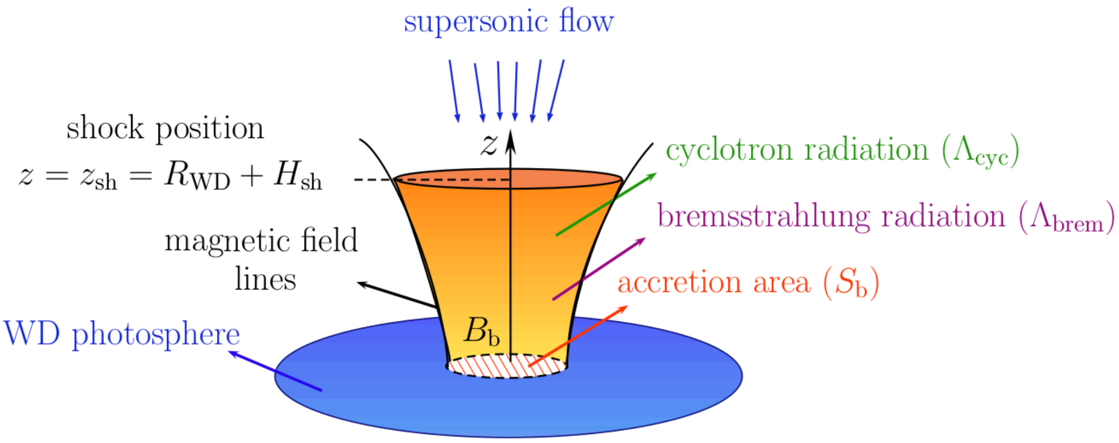

SOURCE: Belloni et al. (2021).

In the PSR, radiation processes cool matter and shape the density and the temperature profiles, which are obtained by solving numerical hydrodynamic equations. These differential equations with gravity and assuming steady state, without viscosity and conduction effects are (WU et al., 1994; HAYASHI; ISHIDA, 2014b; SOM et al., 2018, e.g.): (i) the mass continuity equation, Equation 2.17; (ii) the momentum equation, Equation 2.18; and (iii) the energy equation, Equation 2.19.

$$\frac{d}{dz}(\rho v S) = 0, \tag{2.17}$$

$$\frac{d}{dz}(\rho v^2 + P) + \frac{\rho v^2}{S}\frac{dS}{dz} + g_{WD}\,\rho = 0, \tag{2.18}$$

$$\upsilon\frac{dP}{dz}+\gamma P\frac{d\upsilon}{dz}+(\gamma-1)\left(\Lambda-\frac{\rho\upsilon^3}{2S}\frac{dS}{dz}\right)=0, \tag{2.19}$$

where z is the spatial coordinate, ρ is the density, υ is the flow velocity, S is the cross-section of the PSR (Equation 2.20), P is the pressure for an ideal gas (Equation 2.22), g_{WD} is the WD gravitational field (Equation 2.23), $\gamma = 5/3$ is the adiabatic index, and Λ is the cooling function.

$$S = S_b\left(\frac{z}{R_{WD}}\right)^n, \tag{2.20}$$

where S_b is the area of the bottom of the PSR. In the above equation, n corresponds to the type of accretion geometry, in which n = 0 is cylindrical and n = 3 is dipolar. R_{WD} is the WD radius given by Nauenberg (1972, Equation 2.21).

$$R_{WD} = 7.8\times10^8\left[\left(\frac{M_{WD}}{1.44M_\odot}\right)^{-2/3}-\left(\frac{M_{WD}}{1.44M_\odot}\right)^{2/3}\right]^{1/2} cm, \tag{2.21}$$

where M_{WD} is the WD mass.

$$P=\frac{\rho k_b T}{\mu_i m_H}, \tag{2.22}$$

where $k_b = 1.380658\times10^{-16}$ erg K^{-1} is the Boltzmann constant, T is the temperature, $\mu_i = 0.615$ is the mean molecular mass of a fully ionized gas with solar metallicity, and $m_H = 1.673525\times10^{-24}$ g is the atomic hydrogen mass.

$$g_{WD}=\frac{GM_{WD}}{z^2}, \tag{2.23}$$

where G is the gravitational constant.

The hot subsonic PSR flow settles gradually onto the WD, and cools via emitting bremsstrahlung and lines X-rays and optical/infrared cyclotron radiation. The cooling function is given by Equation 2.24.

$$\Lambda=\Lambda_{bremss}+\Lambda_{cycl}, \tag{2.24}$$

where optically thin bremsstrahlung (Λ_{bremss}) is given by Equation 2.25 and cyclotron (Λ_{cycl}) is given by Equation 2.26 (SOM et al., 2018).

$$\Lambda_{bremss} = 5.01 \times 10^{6} \left(\frac{\rho}{10^{-9} g \cdot cm^{-3}}\right)^{2} \left(\frac{T}{10^{8} K}\right)^{0.5} erg \cdot cm^{-3} \cdot s^{-1}. \tag{2.25}$$

$$\Lambda_{cycl} = 7.15 \times 10^{7} \left(\frac{S}{10^{15} cm^{2}}\right)^{-0.425} \left(\frac{B}{10 MG}\right)^{2.85} \left(\frac{\rho}{10^{-9} g \cdot cm^{-3}}\right)^{0.15} \left(\frac{T}{10^{8} K}\right)^{2.5} erg \cdot cm^{-3} \cdot s^{-1}, \tag{2.26}$$

where B is the magnetic field in the column.

Equations 2.17, 2.18, and 2.19 were reduced into the two-dimensional system of ordinary differential equations shown in Equations 2.27 and Equations 2.28:

$$\frac{dv}{dz'} = \frac{g(z')}{v} - \frac{1}{\dot{m}} \frac{dP}{dz'}, \tag{2.27}$$

$$\frac{dP}{dz'} = \frac{(\gamma - 1)(\Lambda - \frac{\rho v^{3}}{2S} \frac{dS}{dz'})\dot{m} + g(z')\gamma P(\dot{m}/v)}{\gamma P - \dot{m} v}, \tag{2.28}$$

where z' is the independent variable given by $z' = z_0 - z$, where z_0 is the shock coordinate, $\dot{m}$ is the specific accretion rate, and $g(z')$ is Equation 2.23 in z' coordinate.

The hydrodynamic solution of Equations 2.27 and 2.28 depends on the boundary conditions. The initial value problem is solved with the $4 - 5$th order Runge-Kutta-Fehlberg numerical method assuming the Rankine-Hugoniot conditions of an adiabatic shock in terms of density and velocity given by Equations 2.29 and 2.30, respectively.

$$\rho_2 = 4\rho_1, \tag{2.29}$$

$$\nu_2 = \frac{1}{4}\nu_1, \tag{2.30}$$

where the indexes 1 and 2 indicate the variables before and after the shock, respectively.

The shock height was extracted from $z' = z_{sh} - z$ $(z' = 0)$ to $z' = H_{sh}$ (height of shock) in the boundary conditions (SULEIMANOV et al., 2005, Equations 2.31, 2.32, 2.33, and 2.34):

$$\upsilon_{sh} = 0.25\sqrt{2GM_{WD}(1/z_{sh} - 1/R_{th})}, \tag{2.31}$$

$$\rho_{sh} = \dot{m}/\upsilon_{sh}, \tag{2.32}$$

$$P_{sh} = 3\dot{m}\upsilon_{sh}, \tag{2.33}$$

$$T_{sh} = 3\mu_i m_H \upsilon_{sh}^2/k_b, \tag{2.34}$$

Finally, the whole boundary value problem is solved using the shooting algorithm based on the Newton-Raphson root finding method. The comparison between the shock solution results from CYCLOPS and some previous models such as Cropper (1990), Yuasa et al. (2010), Hayashi and Ishida (2014a), and Som et al. (2018) is shown in Figure 2.6. In comparison with Cropper (1990), the top left of the first panel, the temperature profile from CYCLOPS calculated with B = 0, $\dot{m}$ = 1 g s^{-1} cm^{-2}, M$_{WD}$ = 1.0 $M_\odot$ and λ = 0.615, cylindrical model, and R$_{th}$ > R$_{WD}$ exhibits the same behavior as that proposed by the authors. In comparison with Som et al. (2018), the top right of the second panel, the CYCLOPS model using B = 10 MG (fixed), $\dot{m}$ = 1 g s^{-1} cm^{-2}, M$_{WD}$ = 0.8 $M_\odot$, λ = 0.5, cylindrical model, and R$_{th}$ > R$_{WD}$ shows a good agreement. In comparison with Hayashi and Ishida (2014a), the middle left of the first and middle right of the second panels, CYCLOPS models considered both cylindrical and dipolar geometry using B = 0, M$_{WD}$ = 0.7 $M_\odot$, λ = 0.615, R$_{th}$ > R$_{WD}$, and $\dot{m}_b$ = 10^{-4} g s^{-1} cm^{-2} (left), $\dot{m}_b$ = 10^{-2} g s^{-1} cm^{-2} (right). All these results are consistent. Compared with Yuasa et al. (2010), the top left of the first panel, in which CYCLOPS used $\dot{m}$ = 10 g s^{-1} cm^{-2}, M$_{WD}$ varies from 0.2 to 1.4 $M_\odot$, and cylindrical model, CYCLOPS is also consistent using the same conditions. The bottom right of the second panel shows the CYCLOPS results compared to Hayashi and Ishida (2014a) model using M$_{WD}$ = 1.2 $M_\odot$ on the plot of the height shock as a function with $\dot{m}$ varying from 10^{-4} to 10^{2} g s^{-1} cm^{-2} and we obtain the same conclusion regarding the consistency of our code. The maximum difference in the shock height obtained using CYCLOPS and the previous models is around 10%.

Probably this discrepancy is related to the distinct bremsstrahlung cooling prescriptions and numerical techniques used to solve the boundary value problem associated with the PSR structure.

Figure 2.6 - The temperature profiles from CYCLOPS compared with some previous models.

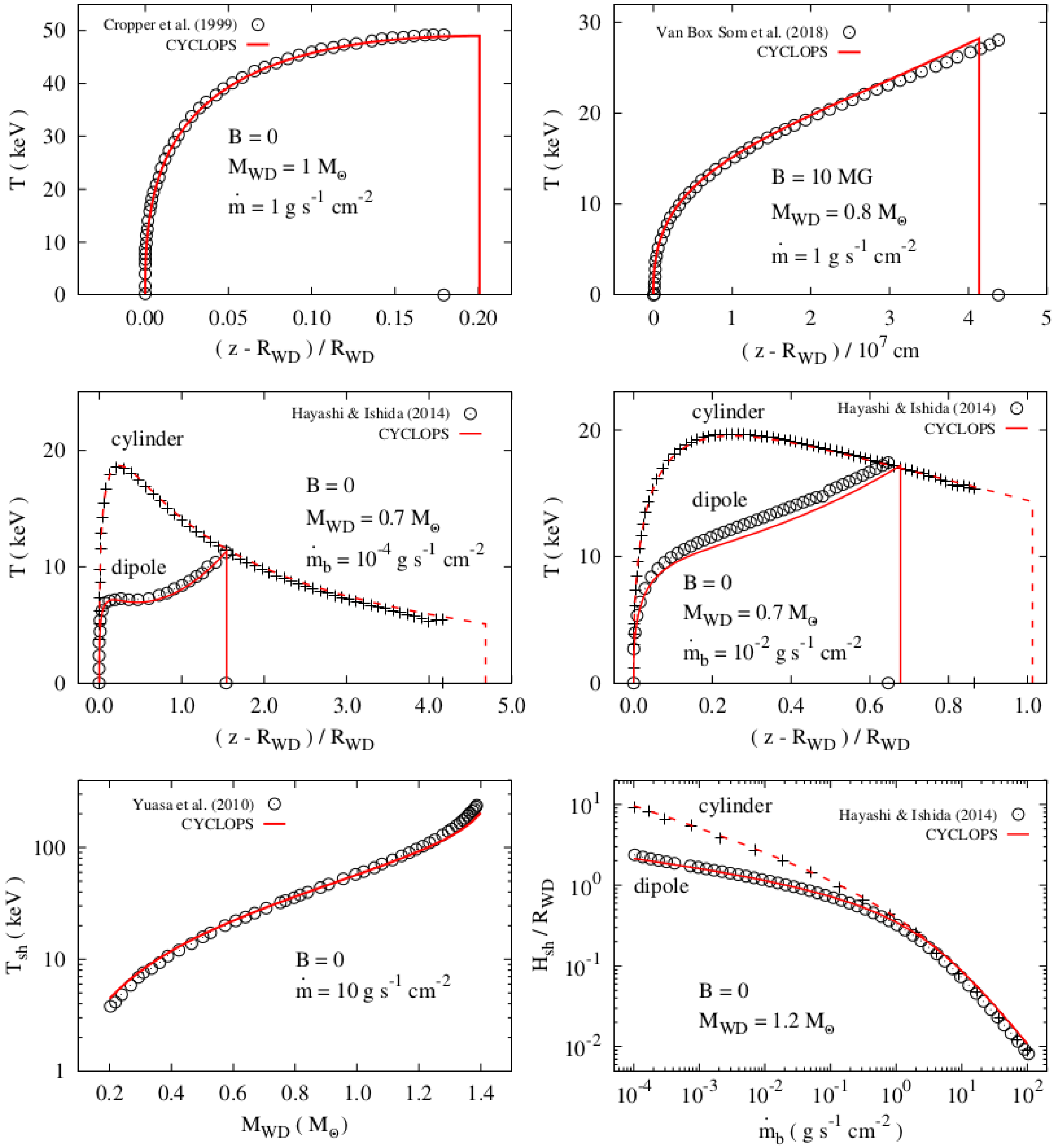

SOURCE: Belloni et al. (2021).

2.13 CYCLOPS without shock solution

The CYCLOPS code without the shock solution will be quickly described here in order to allow us to discuss some results of V405 Aur obtained using the earlier version of the code. Previously, the CYCLOPS code considered the temperature and density profiles as arbitrary functions varying in radial and/or tangential directions. In the tangential direction, the temperature and density were assumed to be constant or decreasing exponentially from a reference point to the border of the PSR following Equations 2.35 and 2.36.

$$T(d) = T(h_{cell})e^{-\sqrt{d}}, \tag{2.35}$$

$$N(d) = N(h_{cell})e^{-\sqrt{d}}, \tag{2.36}$$

where d is the least distance from the cell to the reference point. This reference point contains the reference magnetic field line that passes through the anchor point - see Costa and Rodrigues (2009).

The temperature and density profiles are calculated as a function of height of a given cell, h_{cell} (SILVA et al., 2013). They were given by Equation 2.37 and 2.38:

$$T(h_{cell}) = T_{max}\ exp\left[2.5\left(\frac{h_{cell}}{h} - 1\right)\right], \tag{2.37}$$

$$N_e(h_{cell}) = N_{max}\ exp\left[-2.5\sqrt{\frac{h_{cell}}{h}}\right], \tag{2.38}$$

where T_{max} and N_{max} are the maximum values or maxima of the electron temperature and density, respectively, and h is the height of emitting region in WD radius units.

3 THE XSPEC CODE

This chapter presents the XSPEC code used for X-ray spectral analysis. This code allows one to model X-ray observational data using typical additive and multiplicative models. As mentioned in Chapter 2, the CYCLOPS code also models X-ray data using bremsstrahlung. However, we should emphasize that while CYCLOPS considers the optically thin and thick regimes, XSPEC is only used for the optically thin regime. In addition, CYCLOPS is implemented with the radiative transfer in a 3D emitting region while the XSPEC models are 1D. The general aspects of XSPEC are discussed in Section 3.1. A comparison between CYCLOPS and XSPEC is outlined in Section 3.2.

3.1 XSPEC package

XSPEC is a widespread X-ray analysis package, which allows spectral fitting with many models. It was developed at Cambridge University as a mission-independent general analysis program for X-ray spectral data by Arnaud (1996). The observed source spectrum, $C(I)$, as a function of energy channels (I), through a convolution between the incident spectrum and the instrument response is given by Equation 3.1 (ARNAUD, 1996; DORMAN; ARNAUD, 2001).

$$C(I) = \int_0^\infty f(E)\ R(I,E)\ dE, \tag{3.1}$$

where $f(E)$ is the spectrum of the source and $R(I,E)$ is the instrumental response and is proportional to the probability that an incoming photon of energy E will be detected in channel I.

Ideally, it is possible to determine the source spectrum $f(E)$ by deriving $f(E)$ for a given set of $C(I)$. However, this operation is not possible, because the inversion tends not to be unique nor stable for small changes in $C(I)$. In practice, the procedure performed is to choose the best model spectrum as a function of parameters f(E,p1,p2,...) by fitting the data obtained by the spectrometer. Thus, for each $f(E)$, the count $C_p(I)$ is estimated using the instrumental response and compared to the observed data, $C(I)$. A figure of merit is then calculated to evaluate the proposed model (ARNAUD, 1996). In statistical terms, the chi-squared test (χ^2) is the most commonly used figure of merit, Equation 3.2.

$$\chi^2 = \Sigma \, \frac{(C(I) - C_p(I))^2}{\sigma^2(I)}, \tag{3.2}$$

where $\sigma^2(I)$ is the error for channel I.

The main files for spectral fitting with XSPEC are (ARNAUD, 1996; DORMAN; ARNAUD, 2001; ARNAUD et al., 2011, e.g.):

- a set of one or more observed spectra: D(I);
- background measurements: B(I);
- instrumental responses: R(I,E);
- a set of model spectra: M(I);

The observed spectrum C(I) is obtained by Equation 3.3, in units of counts per second.

$$C(I) = \frac{D(I)}{a_{D(I)}t_D} - \frac{b_{D(I)}}{b_{B(I)}} \, \frac{B(I)}{a_{B(I)}t_B}, \tag{3.3}$$

where t_D and t_B are the exposure times in the data and background files; $b_{D(I)}$ and $b_{B(I)}$, $a_{D(I)}$ and $a_{B(I)}$ are the background and area scaling values from the spectrum and background, respectively.

The steps performed in XSPEC to obtain the best-fit spectrum are described in Figure 3.1.

X-ray spectroscopic models are usually built up from individual components. These can be thought of as two basic types: (1) additive, an emission component or; (2) multiplicative, something which modifies the emission (additive) component (ARNAUD, 1996). Some additive emission models are: (i) blackbody; (ii) thermal bremsstrahlung; (iii) power-law; and (iv) collisional plasma such as MEKAL – Mewe-Kaastra-Liedahl (MEWE et al., 1985; MEWE et al., 1986b; KAASTRA, 1992; LIEDAHL et al., 1995), APEC – Astrophysical Plasma Emission Code (SMITH et al., 2001). Examples of multiplicative models are: (i) photoelectric absorption; and (ii) cyclotron absorption lines.

Figure 3.1 - Flowchart of the steps for X-ray spectral analysis with XSPEC.

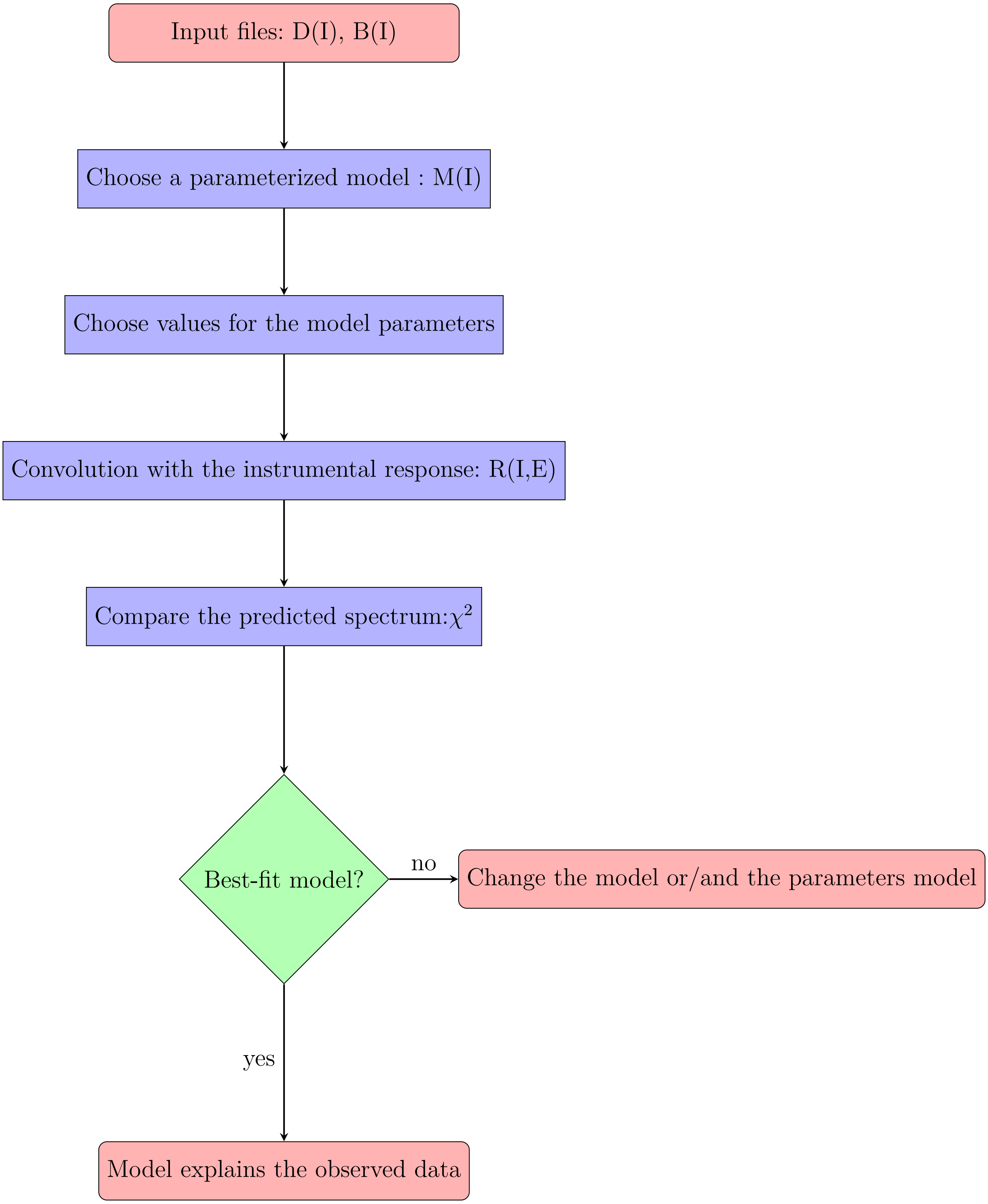

SOURCE: Arnaud (1996).

3.2 CYCLOPS versus XSPEC

As already mentioned, XSPEC is the most widely used tool to analyze X-ray data. The X-ray data analysis is performed by fitting models to observational data according to the physical properties of the source. The libraries can be accessed by HEASARC[1] with one hundred theoretical models available.

The X-ray analysis performed by CYCLOPS considers the bremsstrahlung emission, which is the most important radiative process in the PSR within a 2 – 10 keV energy range. At constant temperature, the code can be directly compared with XSPEC. An agreement between CYCLOPS and XSPEC gives us confidence that CYCLOPS does not have relevant errors in the bremsstrahlung emission implementation. This procedure has already been performed by Silva (2013), for a previous CYCLOPS version, and Belloni et al. (2021). However, they do not take into account the convolution with the instrumental response.

CYCLOPS can consider the PSR homogeneous in terms of electronic density and/or temperature. In this case, these parameters have the same values in all cells. The intensity of bremsstrahlung emission on CYCLOPS is given by Equation 3.4.

$$j_{E,k} = 1.032 \times 10^{-11} N_e^2 E^{-1} T^{-0.5} e^{-1.16\times10^{-7}\frac{E}{T}} g, \tag{3.4}$$

The XSPEC *bremss* model calculates the continuum emission of a thermal bremsstrahlung model. Its emissivity is given by Equation 3.5 based on Kellogg et al. (1975) with polynomial fits proposed by Karzas and Latter (1961). The He abundance is assumed to be 8.5% of H by number.

$$j_E = 1.42 \times 10^{-27} Z^2 N_e E^{-1} T^{0.5} e^{\frac{E}{T}} g, \tag{3.5}$$

where N_e is the electron number density, E is the energy, T is the temperature, and g is the non-relativistic Gaunt factor. Z is the ion charge number.

The normalization constants of *bremss* and *meka* models, which were applied to XSPEC data to obtain correct physical units, are given by Equation 3.6 and Equation 3.7, respectively.

---

[1] XSPEC is available in: `https://heasarc.gsfc.nasa.gov/xanadu/xspec/`

$$normalization = \frac{3.02 \times 10^{-14}}{4\pi D^2} \int n_e n_I dV, \tag{3.6}$$

$$normalization = \frac{10^{-14}}{4\pi [D(1+z)]^2} \int n_e n_H dV, \tag{3.7}$$

where D is the distance (cm), n_e and n_I are the electron and ion densities (cm^{-3}), respectively. z is the redshift value and n_H is the H density.

Figure 3.2 - Comparison of the bremsstrahlung emission of a homogeneous plasma with a density of 10^{16} cm^{-3} and temperatures of 1 keV (circle) and 100 keV (triangle) using the CYCLOPS code for a distance of 100 pc (blue color) and XSPEC using *bremss* model (green color) and *meka* model (pink color). The instrumental response function was not considered.

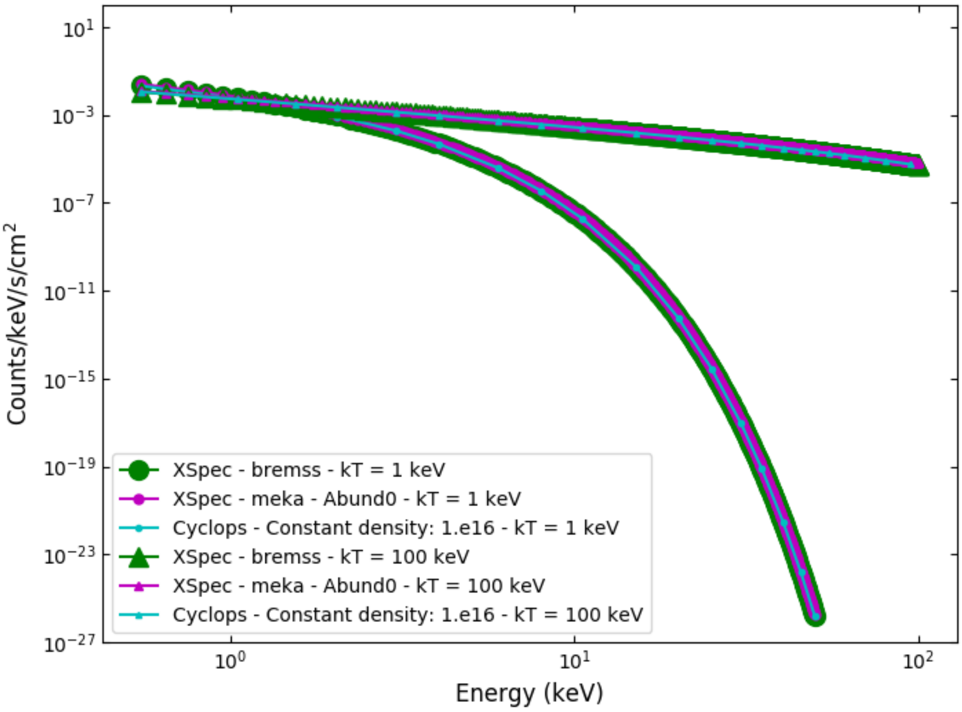

SOURCE: The author.

The X-ray luminosity is primarily determined by the accretion rate. In X-ray spectrum, the absolute flux level was implemented in CYCLOPS. Then, if the object distance is known, the fitting can be performed considering the observed count rate and not just the spectral shape. Figure 3.2 shows the comparison of CYCLOPS and XSPEC using *bremss* and *meka* models where we adopted an arbitrary distance of 100 pc and non-instrumental response function. We considered the *meka* model without emission lines (abundance = 0), because CYCLOPS does not model emission lines. In CYCLOPS, the homogeneous density was 10^{16} cm^{-3}. The flux intensities of the CYCLOPS code are in a good agreement with XSPEC at different temperatures of 1 keV and 10 keV. The differences between XSPEC and CYCLOPS are less than 10% independent of the energy and the temperature assumed (BELLONI et al., 2021).

Figure 3.3 - Comparison of bremsstrahlung emission of a homogeneous density of 10^{17} cm^{-3} and temperatures of 1 keV (circle) and 100 keV (triangle) using the CYCLOPS code for a distance of 658 pc (blue color) and XSPEC using the *bremss* model (green color) and *meka* model (pink color). The instrumental response function was considered for this test.

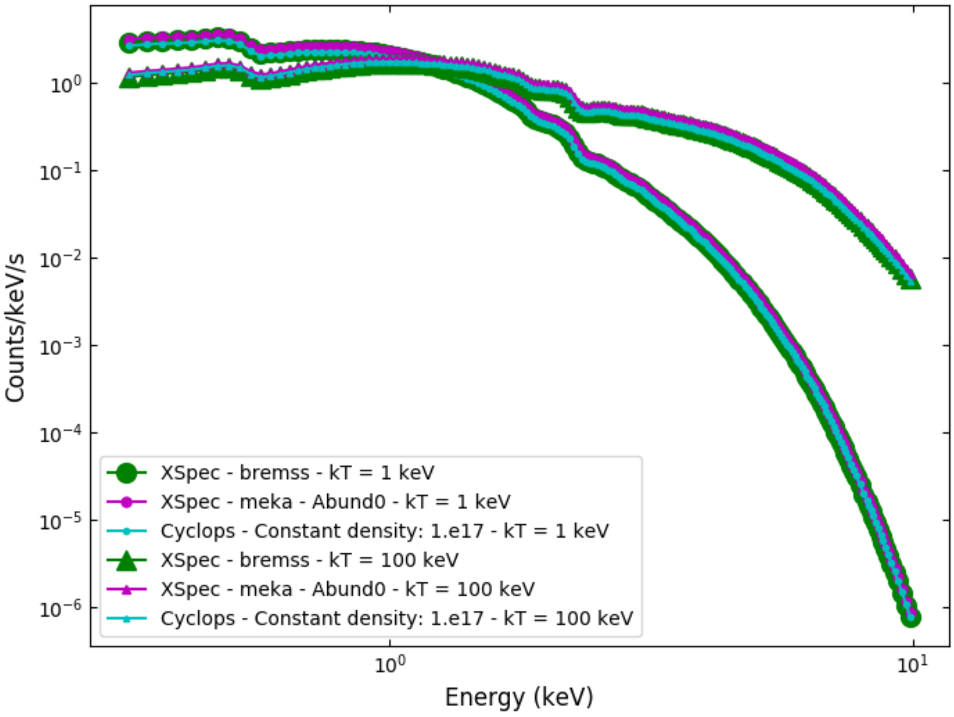

SOURCE: The author.

Figure 3.3 shows the comparison between CYCLOPS and XSPEC using the instrumental response function. We used the instrumental responses (ARF and RMF) files from our reduction of V405 Aur XMM-Newton data, which energy ranging 0.1 to 10 keV (see Section 5.3). The same ARF and RMF files were used in CYCLOPS and XSPEC. In CYCLOPS, the convolution of the model with the instrumental response was performed using routines from the *PINTofALE* package (KASHYAP; DRAKE, 2000). We performed the spectrum calculation in CYCLOPS using a homogeneous density of 10^{17} cm^{-3} and a distance of 658 pc and in the *meka* model from XSPEC non-abundance. Temperatures of 1 keV and 100 keV were considered for both codes. As we can see in Figure 3.3, there are slight differences between both codes which are of the order of 5% to 15%. These results indicate that CYCLOPS and XSPEC are quite similar to each other.

The final test was to compare both codes including the interstellar extinction. Figure 3.4 shows this result assuming a temperature of 1 keV and two different values of hydrogen column density of $5.13 \times 10^{+20}$ cm^{-2} (plus) and $5.13 \times 10^{+21}$ cm^{-2} (diamond). The *bremss* and *meka* models from XSPEC were modified by photoelectric absorption (*phabs* model).

The photoelectric absorption in CYCLOPS is performed using the *PINTofALE* routines. Again, a little difference between the codes and the hydrogen column density can be seen. This only affects energies lower than ∼2 keV. The CYCLOPS code seems to be more absorbed in comparison with the combinations performed in XSPEC .

For all tests performed in this study, we used the optically thin regime, which is the only case currently implemented in the XSPEC code. On the other hand, the CYCLOPS code solves the radiative transfer without any approximation, as it also deals with the usually optically thick cyclotron emission, which occurs in optical wavelengths (BELLONI et al., 2021). Furthermore, for this test we used a non-eclipsing system, but our code is able to calculate the partial or total eclipse of the PSR by the WD non-emissivity during the eclipse while the XSPEC is not.

The comparison between CYCLOPS and XSPEC using the instrumental and non-instrumental response function proves that the distance-dependent flux, the interstellar extinction, and the convolution procedure in the CYCLOPS code are correctly calculated. In other words, the X-ray spectral modeling by CYCLOPS is in excellent agreement with the widely used XSPEC code. Moreover, the slight differences between both codes can be related to bremsstrahlung emissitivies as shown by Equations 3.6 and 3.7.

Figure 3.4 - Comparison of bremsstrahlung emission of a homogeneous density of 10^{17} cm^{-3}, temperature of 1keV, and hydrogen column density of $5.13 \times 10^{+20}$ cm^{-2} (plus) and $5.13 \times 10^{+21}$ cm^{-2} (diamond) using the CYCLOPS code for a distance of 658 pc (blue color) and XSPEC using the *bremss * phab* model (green color) and the *meka * phab* model (pink color). The instrumental response function and interstellar extinction are considered for this test.

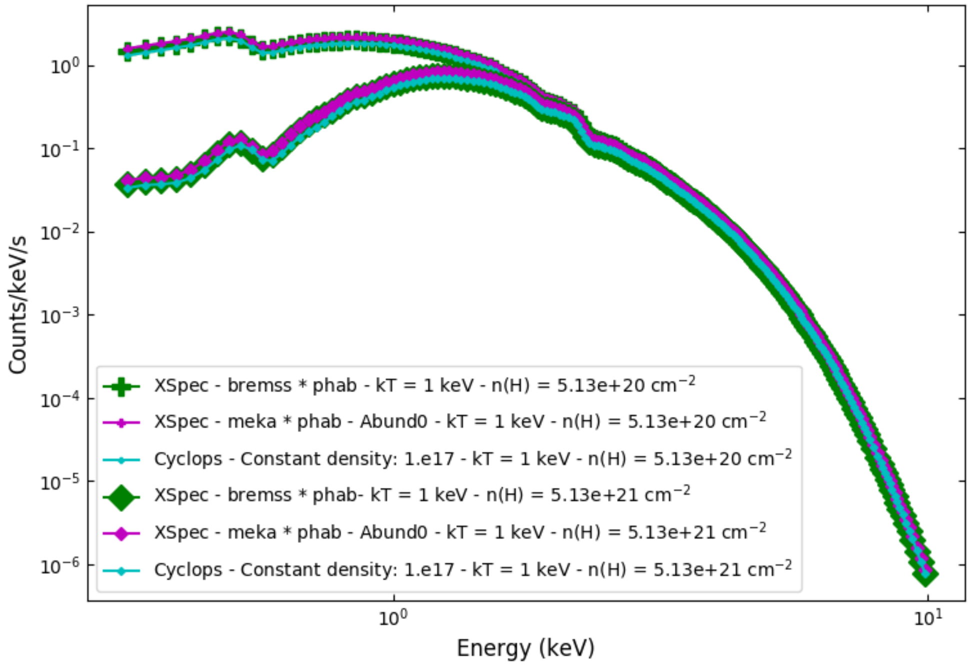

SOURCE: The author.

The Gaunt factor is a parameter that can determine the value of the emissivity. The bremsstrahlung emissitivity depends on the Gaunt factor. In fact, we can attribute the difference between the CYCLOPS and XSPEC model results of around 5% to 15% to be due to differences in this factor/quantity parameter. CYCLOPS adopts the Gaunt factor from Mewe et al. (1986a) (Equations 3.8 and 3.9). This factor is in good agreement with recent calculations proposed by Sutherland (1998) and Itoh et al. (2000) as shown in Figure 3.5. This figure compares CYCLOPS (blue continuous line) and Sutherland (1998) and Sutherland (1998) (black dashed lines) adopting cosmic abundance and ionization balance of Bryans et al. (2009). Both tests use temperatures ranging from 0.0086 and 86.1733 keV.

$$log\ G_{ff} = 0.355\lambda^{-0.06} log\ \lambda + 0.3\lambda^{-0.066} - log\ \frac{T}{100} + 0.0043\ \ (T > 1MK), \quad (3.8)$$

$$log\ G_{ff} = 0.48\lambda^{-0.08} log\ \lambda + (0.133\ log\lambda - 0.2) log\ T - 0.538\ \ (T \leqslant 1MK), \quad (3.9)$$

where λ is the wavelength and T is the temperature.

Figure 3.5 - Comparison of Gaunt factor of Mewe et al. (1986a) from CYCLOPS (blue continuous line and Sutherland (1998) and Itoh et al. (2000) (black dashed lines).

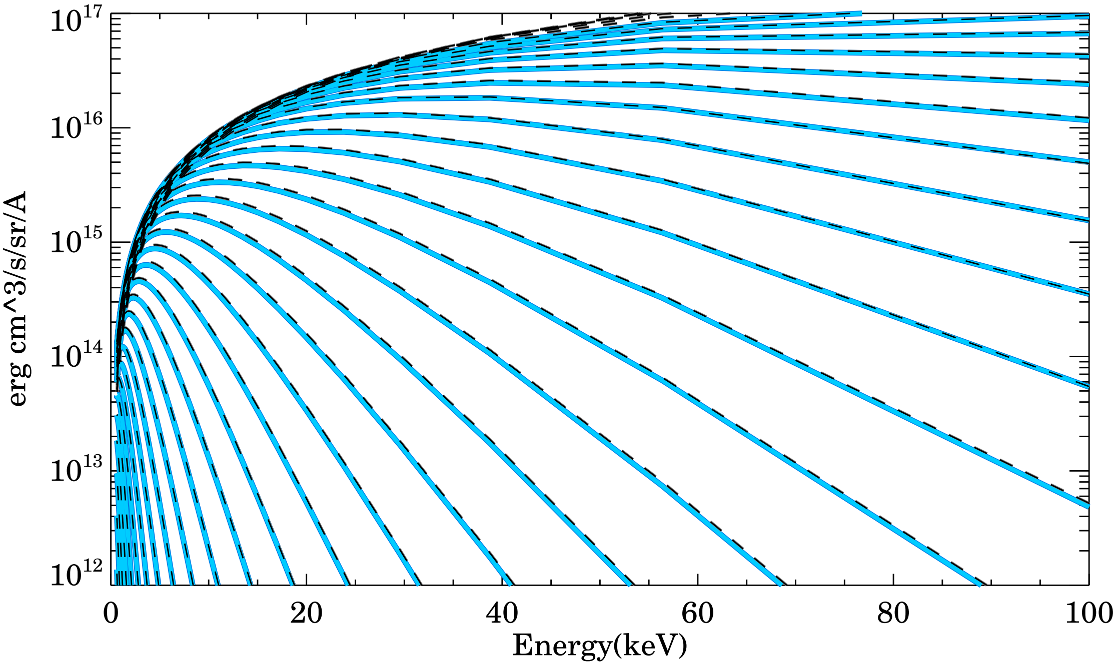

SOURCE: The author.

4 SELECTION OF IPS FOR CYCLOPS MODELING

One aim of this PhD thesis is to model IPs using the CYCLOPS code. This chapter describes the first step in this direction; a selection of IPs with adequate observational data for a proper CYCLOPS modeling.

4.1 Selection of objects

The CYCLOPS code can model IPs using optical and/or X-ray data. Both sets of data used simultaneously can restrict the geometry and the physical properties of a given system (OLIVEIRA et al., 2020). Hence, we searched for IPs with non-null circular polarization and modulated with the WD spin, preferably in different bands, and data in X-ray preferentially also modulated with the spin period of the WD. In Table 4.1, we present 9 candidates selected from the catalog of Mukai (2014), which have these data available from the literature. The distances were obtained by Gaia DR3[1] (BAILER-JONES et al., 2021).

Table 4.1 - IPs suitable for modeling with CYCLOPS code. The periods and orbital inclinations were obtained from the Mukai (2014) compilation. The distances were obtained by Gaia DR 3 (BAILER-JONES et al., 2021).

Object	P_{orb} (h)	P_{spin} (min)	P_{beat} (min)	Inclination (^{o})	Distance (pc)
UU Col	3.45	14.39	15.58	–	2545.5 (-392.7, +448.2)
V405 Aur	4.16	9.09	–	–	658.2 (-8.5, +8.5)
BG CMi	3.23	15.22?	14.12?	∼ 65 (?)	866.9 (-24.3, +26.4)
PQ Gem	5.19	13.89	14.5	–	733.6 (-14.2, +16.2)
IGR J15094-6649	5.89	13.49	14.03	–	1090.9 (-22.8, +24.5)
NY Lup	9.87	11.55	–	25-58	1265.7 (-29.9, + 34.8)
V2400 Oph	3.43	15.46	16.72	∼ 10 (?)	699.7 (-10.8, +9.7)
V2306 Cyg	4.35	24.45	26.45	–	1252.8 (-41.9, +51.3)
RX J2133.7+5107	7.14	9.52	–	<45	1371.9 (-35.0,+38.8)

From this sample, the best object for CYCLOPS modeling is V405 Aur. This system presents circular polarization curves in the UBVRI bands modulated with the spin period of the WD. Two different geometries are proposed in the literature to explain this based on polarimetric and X-ray data (more details in Section 5.1). As the CYCLOPS code permits simultaneous modeling of the cyclotron and bremsstrahlung

---

[1] Gaia DR3 is found in `https://cdsarc.u-strasbg.fr/viz-bin/Cat?Gaia`.

emissions, this analysis could clarify the dilemma between the two different proposed accretion geometries. Chapter 5 is devoted to this object. Another object that also has suitable data for CYCLOPS modeling is UU Col. The following section presents further information on this object.

4.2 UU Columbae

RX J0512.2–3241 (UU Col) is an IP discovered by ROSAT survey (BURWITZ et al., 1996). The orbital and spin periods of the accreting WD are equal to 3.45 ± 0.03 h and 863.3 ± 1.4 s, respectively (MARTINO et al., 2006).

The X-ray spectrum from XMM-Newton indicates a soft blackbody component. Martino et al. (2006) reported a blackbody temperature of 49.7^{+20}_{-9} eV including a partial covering absorber multiplicative model. However, using the same data and the same model, Evans and Hellier (2007) fitted a blackbody with a temperature of $73^{+5.6}_{-2.9}$ eV, as shown in Figure 4.1.

Figure 4.1 - XMM-Newton spectrum of UU Col. The solid line fitted the hard data, and the broken line fitted the blackbody.

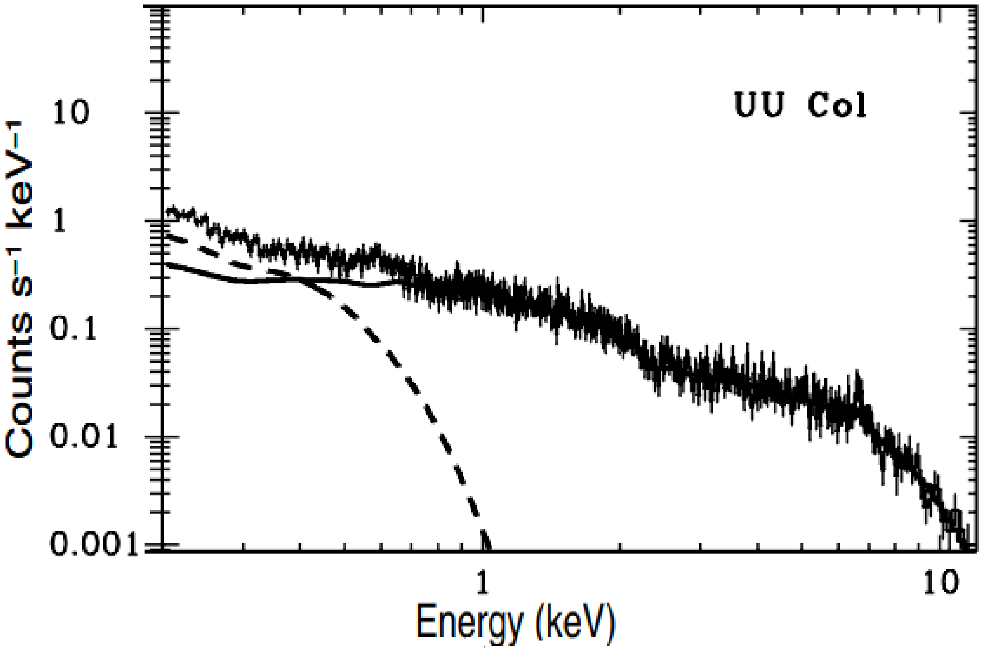

SOURCE: Evans and Hellier (2007).

The phase diagram as a function of the WD rotation period is shown in Figure 4.2. The energy dependence of the spin modulation seen in the XMM-Newton data suggests contribution from absorbing components. The spin pulse is observed with fractional amplitudes (half-amplitude) of 27 ± 2% in 2 – 5 keV, 37 ± 2% in 1 – 2 keV, and 33 ± 2% in 0.5 – 1 keV. This is probably due to photo-electric absorption. In the soft 0.2 – 0.5 keV band, an additional maximum at the minimum of the hard pulse indicates there is a substantial soft X-ray contribution from a secondary PSR (MARTINO et al., 2006).

Figure 4.2 - Phase diagrams in selected energy bands at the spin period of UU Col from XMM-Newton satellite.

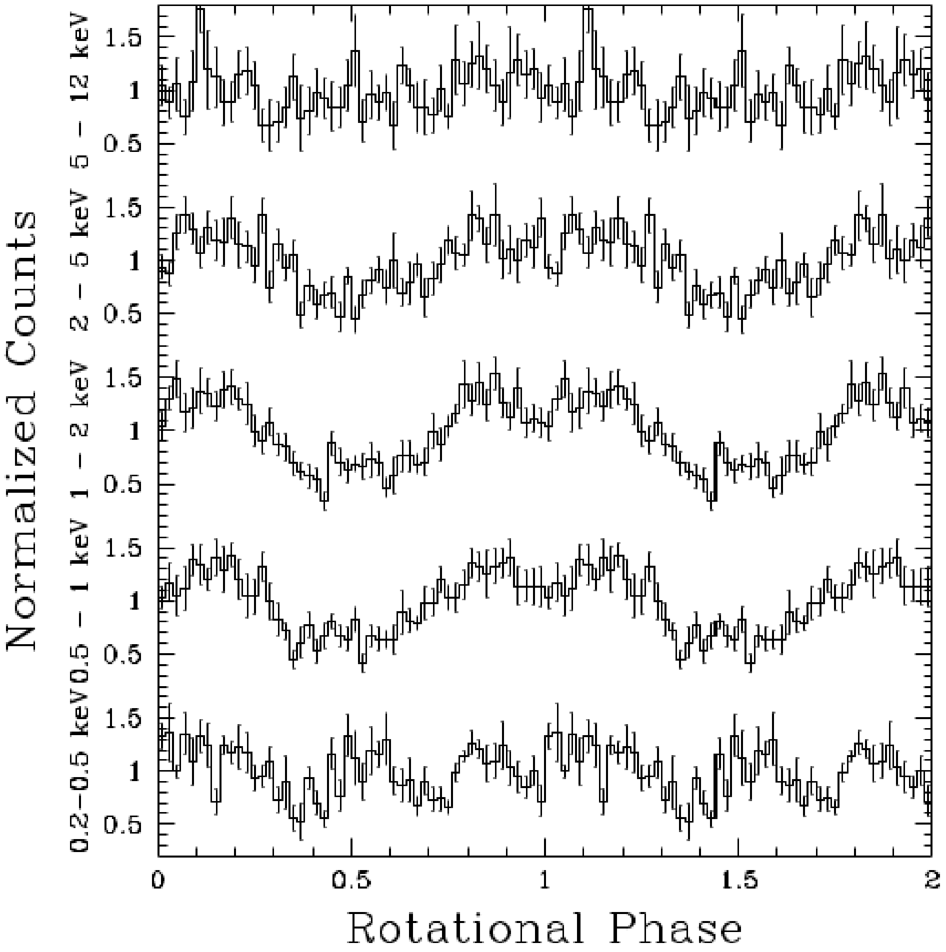

SOURCE: Martino et al. (2006).

Circular polarization data were obtained using the Very Large Telescope (VLT) and FORS1 instrument by Katajainen et al. (2010). They carried out photopolarimetric observations during two periods: 2005 December 11, and 2006 March 17 and 18 (see Figure 4.3). In 2005 December, B-band circular polarization varied between +0.7% ± 0.1% and -0.4% ± 0.1%, in other words, consistent with zero. In 2006 March, UU Col was observed with significantly better signal-to-noise ratio (SNR) in I band. The circular polarization curve was mostly negative, the minimum value was reached at phase 0.3. A positive peak of +0.6% was seen at spin phase 0.0. Zero crossing from positive to negative polarization was at phase 0.07 right (KATAJAINEN et al., 2010).

Figure 4.3 - Light curves of UU Col in the B band on the left and phase-diagrams as function of spin period on the right in the I band. Top: circular polarimetric data. Bottom: differential photometric data.

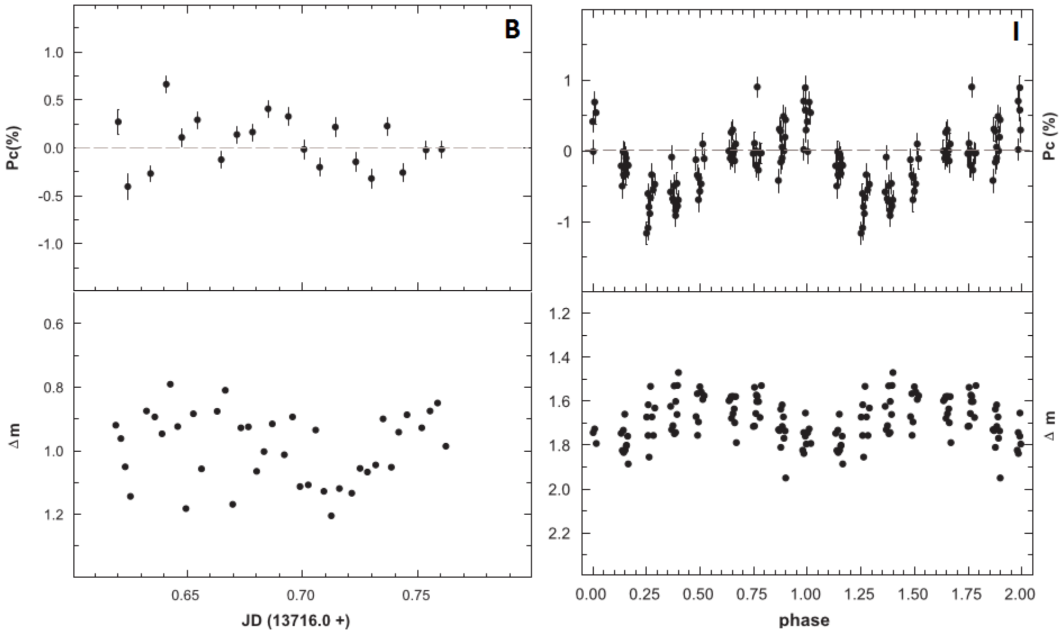

SOURCE: Katajainen et al. (2010).

From circular polarization data, Katajainen et al. (2010) proposed that the magnetic dipole has a high inclination, in such a way that cyclotron emission comes from two accretion regions simultaneously. However, Evans and Hellier (2007) suggested from X-ray data that the upper magnetic pole is visible and the lower one is only seen when it is closest to us.

5 V405 AURIGAE

V405 Aur is the first IP to be modeled using the CYCLOPS code. The literature review of this object is found in Section 5.1. Section 5.2 and Section 5.3 show details of the optical data and the X-ray data of V405 Aur, respectively. The modeling results are displayed in Section 5.4. Finally, our results are discussed in Section 5.5.

5.1 Introduction

V405 Aur (RX J0558.0+5353) was discovered by ROSAT All-Sky Survey (0.1 – 2.5 keV) and classified as an IP by Haberl et al. (1994). Initially, the WD spin period was proposed to be 272.74 s from the soft X-ray flux modulation. However, Allan et al. (1996) concluded that the true spin period is 545.45 s (Table 4.1), twice that previously proposed. The optical and soft X-ray light curves are dominated by a modulation at the first harmonic of the spin period. The optical spectroscopy yields an orbital period of about 4.15 h (SKILLMAN, 1996).

Parker et al. (2005) using observations from ASCA and RXTE satellites showed that the amplitude modulation decreases with increasing X-ray energy. Absorption in IP disks had already been invoked by Kim and Beuermann (1995). This absorption is interpreted as an extended structure at the outer edge of the accretion disk resulting from the impact of the stream thrown up at the disk. This process causes orbital modulation in X-ray emission (NORTON; MUKAI, 2007).

The UV spectra of V405 Aur from IUE (International Ultraviolet Explorer, 1150 – 3200 Å) and HST (Hubble Space Telescope) observatories show C IV 1550 Å and He II 1640 Å emission lines (SANAD, 2015). The author attributed the variations of line fluxes to the variations of both density and temperature as a result of a changing rate of mass transfer from the secondary star to the WD based on the assumption that the UV radiation comes from one pole. They also estimated the temperature of the accretion stream of $\sim$ 4100 K.

V405 Aur has a strong component in soft X-rays as shown in Figure 5.1. Probably, this emission arises from the WD surface near the accretion footprints which are heated by harder X-ray emission (PATTERSON et al., 1980, e.g.). Figure 5.2 shows the phase diagram X-ray emission from XMM-Newton in the $E \leq 0.7$ keV energy band with double-peaked modulation at WD spin period, and in the $E > 0.7$ keV energy band, which displays a single-peaked modulation (EVANS; HELLIER, 2004). The single-peaked pulsation in harder X-rays was interpreted as a result of opacity in the accretion curtains. However, the high dipole inclination means that the accretion curtains are nearly in the plane of the sky. Thus, the outer regions of the curtains do not cross the line-of-sight to the accretion footprints, explaining the absence of the deep absorption dip, which is a feature of many IPs. The sawtooth profile of this pulsation requires that the magnetic axis be offset from the WD center. The double-peaked pulsation has been explained as being the result of two magnetic poles in a system with large angle between the spin and magnetic axes, in other words, the curtains are brighter when one of the poles points towards us and fainter when both are at quadrature or vice versa as shown by illustration of emitting regions and the magnetic poles at phases in Figure 5.2 (ALLAN et al., 1996; EVANS; HELLIER, 2004).

Figure 5.1 - The X-ray spectra of V405 Aur from XMM-Newton showing models and the contributions from each component.

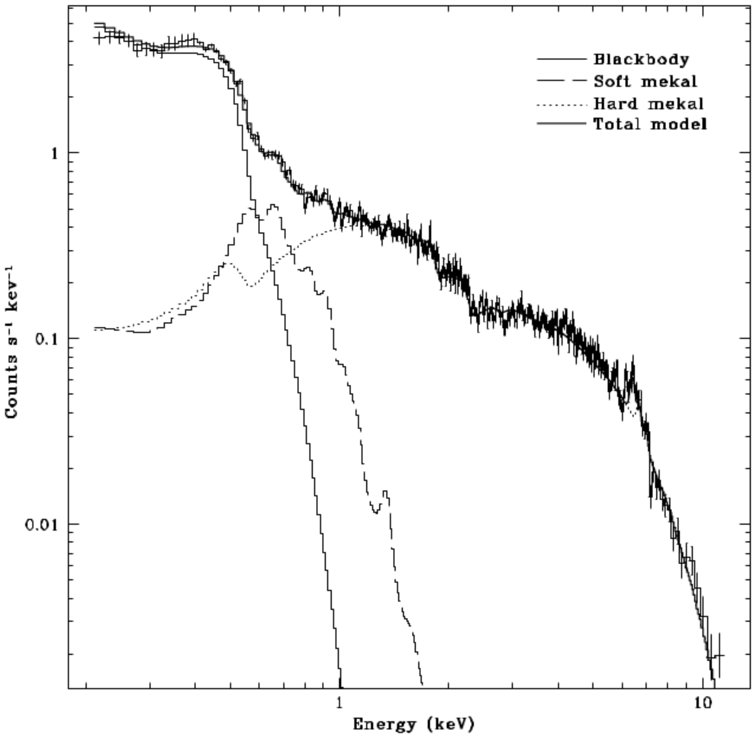

SOURCE: Evans and Hellier (2004).

Figures 5.3 and 5.4 show the simultaneous UBVRI photometry and polarimetry observations obtained by Piirola et al. (2008). They interpreted these data in a scenario with typical behavior in cyclotron emission seen in polars. When the line-of-sight is nearly along the magnetic field lines, the phase diagrams folded at the WD spin period show minimum values at 0.25 and 0.75 phases and maximum values at 0.0 and 0.5 phases when the line-of-sight is perpendicular to the magnetic field from photometry curves. On the other hand, the UBVRI circular polarimetry curves show maximum cyclotron emission intensity at 0.25 and 0.75 phases and decreases to zero at 0.0 and 0.5 phases.

Figure 5.2 - Phase diagram of V405 Aur from the X-ray spin pulse for E $\leq$ 0.7 keV and E $>$ 0.7 keV energy bands, respectively. The illustration shows emitting regions and the magnetic poles at selected phases. The arc-shaped regions are the blackbody emission and the straight lines due to the magnetic field lines.

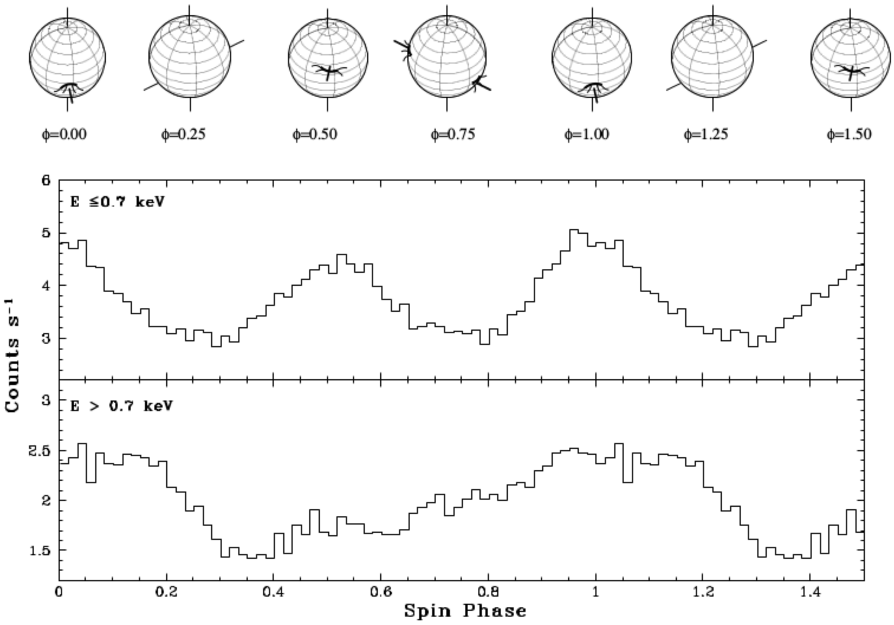

SOURCE: Evans and Hellier (2004).

In Figure 5.4, the UBVRI circular polarimetric curves are sinusoidal and symmetric. The extreme values are ± 3% in the B and V bands and ± 2% in the R band. The low percentage of the polarized emission may be due to the dilution by the disk. The excursions between positive and negative values were interpreted as the detection of two opposite magnetic poles, one accretion from the north part of WD and another accretion from the south, accreting at a similar rate in V405 Aur. The two-accretion scenario was previously reported by Evans and Hellier (2004), as mentioned above.

Piirola et al. (2008) modeled UBVRI photometric and circular polarimetric data using a geometric model involving extended emission strips on the WD surface and a viewing angle dependent of the cyclotron flux polarization and intensity from Wickramasinghe and Meggitt (1985). This modeling procedure is quite distinct from the approach adopted in the present thesis. However, the results found allow us make a comparison with the results from X-ray. Those authors proposed that the orbital inclination and colatitude of the magnetic dipole in V405 Aur are 30 - 50° and ∼90°, respectively, in a configuration illustrated in Figure 5.6. Evans and Hellier (2004) also determined a geometry of accretion from model fits to X-ray spectra. Their inclination and colatitude parameters were ∼65° and ∼60° respectively, as shown in the illustration of Figure 5.5. A comparison between X-rays and optical models shows that the geometry accretion of V405 Aur arises from two accretion regions near the opposite magnetic poles of the spinning WD (again see Figures 5.2 and 5.6). However, the orbital inclinations and colatitudes found from the two modelings differ from each other.

From low resolution circular spectropolarimetry, Piirola et al. (2008) estimated that the magnetic field intensity of V405 Aur is 31.5 ± 0.8 MG, which is of the same order of magnitude as found in polars. They used transient features which can be fitted by cyclotron harmonics of n = 6, 7, and 8. V405 Aur may be a candidate for a polar progenitor with an evolutionary timescale of ∼1 Gyr. The synchronism of spin period and orbital period is still far from being achieved, the ratio of spin to orbital period is 0.0365 (SING et al., 2004, e.g.).

One important conclusion drawn by Piirola et al. (2008) is that the prediction of the constant temperature cyclotron model was not confirmed by the broadband circular spectropolarimetry. Therefore, the authors suggest that any attempt at modeling the cyclotron spectrum should consider the physical parameters of the source region, i.e., temperature, electron number density and the magnetic field, as inhomogeneous. For this reason, the CYCLOPS code is a good approach to model V405 Aur.

Figure 5.3 - Simultaneous UBVRI photometry of V405 Aur on November 27, 1997, and September 22, 2003, left-hand and right-hand panels respectively.

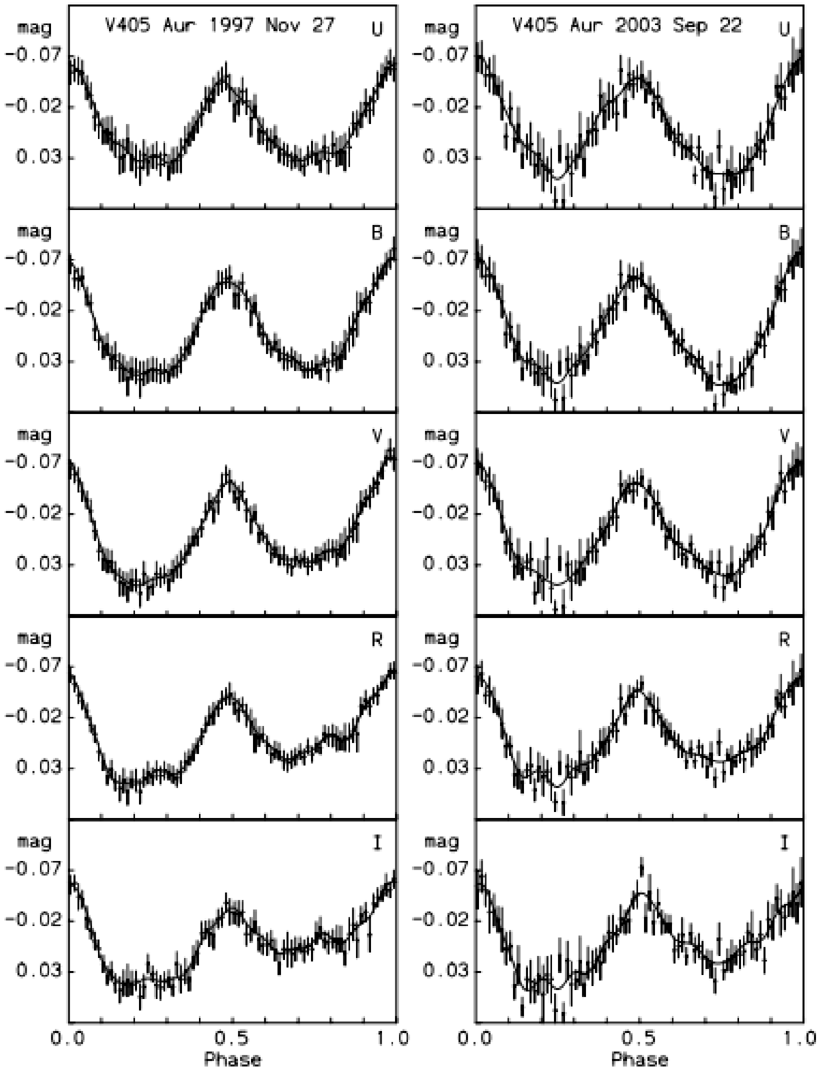

SOURCE: Piirola et al. (2008).

Figure 5.4 - Simultaneous UBVRI circular polarimetry of V405 Aur on November 27, 1997, and September 22, 2003, left-hand and right-hand panels respectively.

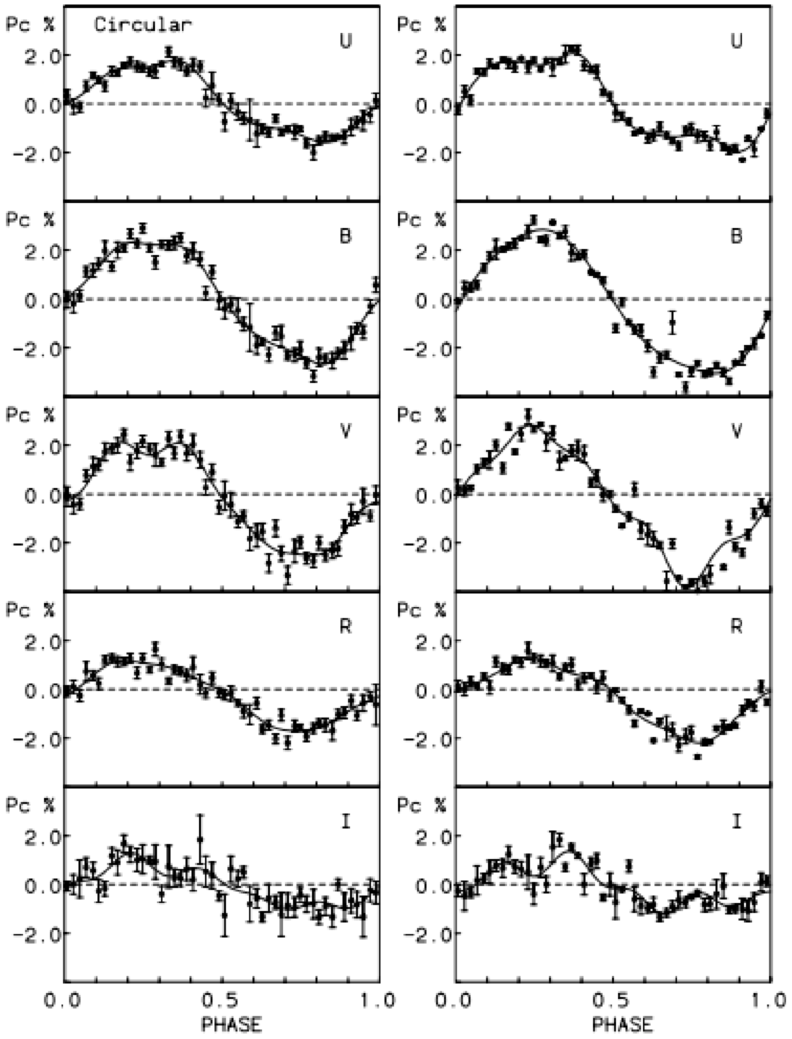

SOURCE: Piirola et al. (2008).

Figure 5.5 - Illustration of the model suggested by Evans and Hellier (2004) to explain the X-ray spectrum of V405 Aur. The orbital inclination is ~65° and the magnetic dipole angle is ~60°.

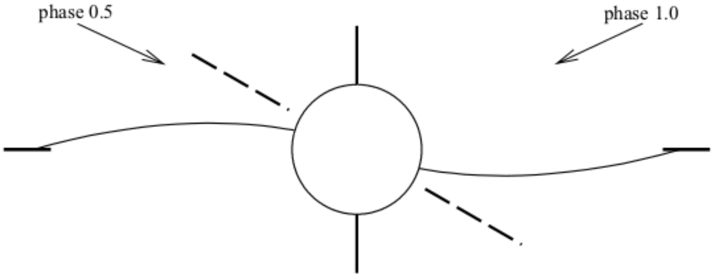

SOURCE: Evans and Hellier (2004).

Figure 5.6 - Illustration of the model suggested by Piirola et al. (2008) to explain the optical circular polarization and light curves of V405 Aur. The orbital inclination is $i = \sim 38°$ and the magnetic dipole angle is $\beta = \sim 82°$.

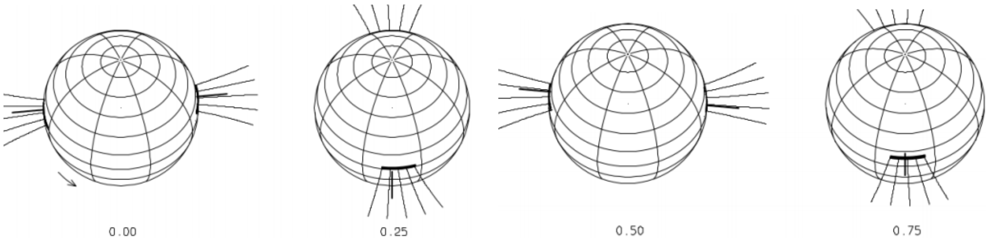

SOURCE: Piirola et al. (2008).

5.2 The optical data used in the modeling

The optical data set used in this modeling was provided by Dr. Vilppu Piirola from Piirola et al. (2008). The UBVRI circular polarimetry and photometry were obtained using the 2.5 m Nordic Optical Telescope (NOT) at Roque de los Muchachos Observatory in La Palma with the TurPol instrument, which performs simultaneous broadband multicolor polarimetry. The data were collected on September 22, 2003 and corresponds to the right-hand panels in Figures 5.3 and 5.4.

The UBVRI photometry data were provided as differential magnitudes relative to the mean magnitude (PIIROLA, 1973; PIIROLA, 1988). In order to obtain the fluxes, we adopted a mean magnitude for V405 Aur in each band. For this, we used the UBVRI magnitudes in the Johnson system found in Shakhovskoj and Kolesnikov (1997). These values are: U = 13.29 mag; B = 13.98 mag; V = 13.91 mag; R = 13.49 mag; and I = 13.31 mag. Historical light curves of V405 Aur, Figure 5.7, show variability of about 3 mag in the V band, however, most of the time, the magnitude is within the interval of 13.5 − 14.5 mag. Therefore, the adopted mean magnitudes are compatible with historical magnitudes from AAVSO[1].

Figure 5.7 - Historical light curves of V405 Aur.

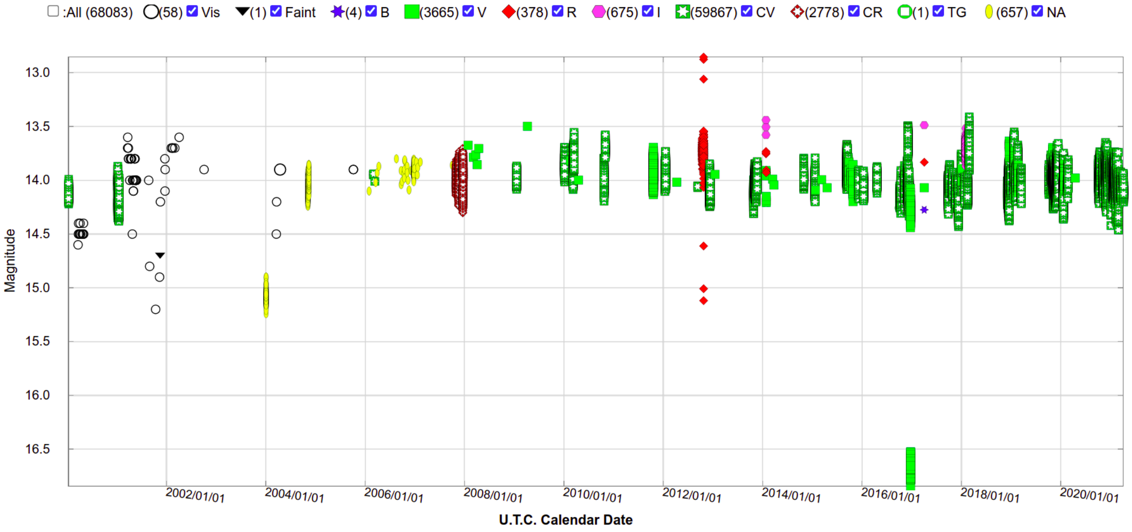

SOURCE: AAVSO (2021).

5.2.1 Input to the CYCLOPS code

The passbands of the Turpol instrument are close to the standard UBVRI system, which are centered at 0.36, 0.44, 0.54, 0.69, and 0.83 μm, respectively. The zero points corresponding to these bands are given by Bessell (1979): U = 1810 Jy; B = 4260 Jy; V = 3640 Jy; R = 3080 Jy; and I = 2550 Jy.

The effective transmission of the Turpol UBVRI bands is slightly different from the Johnson system, mainly the B and R bands (Figure 5.8). In this figure, the

---

[1] See `https://www.aavso.org/LCGv2/index.htm?DateFormat=Calendar&RequestedBands=&view=api.delim&ident=V405Aur&fromjd=2451486&tojd=2453312.163&delimiter=@@@`

red points are the selected wavelengths used in CYCLOPS in order to fit the data (see Section 2.11). Table 5.1 shows the frequencies used in the input data for each filter. The central frequency (maximum wavelength) has weight equal to 100% while the next closer points have weights of 74%, and the following neighbor points have weights of 50%. This latter frequency is only used for the R and I bands (see Section 2.5).

Figure 5.8 - The effective transmission of the UBVRI bands of the TURPOL instrument. The red points are the wavelengths used for multifrequency modeling with CYCLOPS.

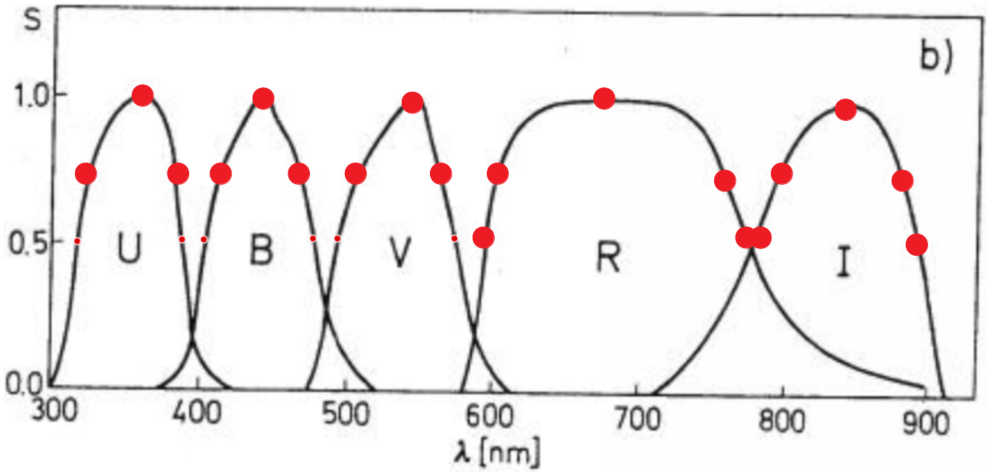

SOURCE: Piirola (1988).

In V405 Aur, the interstellar extinction, $A(\lambda)$, is not negligible. In the V band, the interstellar extinction is 0.568 mag (SCHLEGEL et al., 1998). As mentioned in Section 2.8, the hydrogen column density is the parameter used to quantify the interstellar extinction. In V405 Aur modeling, this value is $N_H = 5.133 \times 10^{20}\ cm^{-3}$, Equation 5.1. The color excess (E(B-V) = 0.09 ± 0.02) was estimated via the 3D extinction maps[2] using the distance obtained by GAIA DR 3 catalog, $658.200^{+8.465}_{-8.462}$ pc (BAILER-JONES et al., 2021).

$$N_H = 5.70 \times 10^{21} \times E(B-V)\ . \tag{5.1}$$

---

[2] The 3D extinction maps: `http://argonaut.skymaps.info/`

Table 5.1 - Frequencies and weights used in V405 Aur in input data for modeling with the CYCLOPS code.

Filter	Frequencies (x 10^{+14} Hz)	weights
U	8.33	1.0
	9.47	0.5
	7.75	0.5
B	6.81	1.0
	7.47	0.5
	6.32	0.5
V	5.45	1.0
	6.11	0.5
	5.26	0.5
R	4.47	1.0
	5.08	0.5
	3.91	0.5
	5.20	0.74
	4.00	0.74
I	3.61	1.0
	5.08	0.5
	3.41	0.5
	3.82	0.74
	3.45	0.74

5.3 The X-ray data

V405 Aur was observed by the XMM–Newton satellite on October 5, 2001 (Obs.ID: 0111180501, PI: Watson, Michael). This date correspond to two years before the optical data from (PIIROLA et al., 2008). Further information regarding the XMM-Newton Observatory is supplied by Jansen et al. (2001). This satellite consists of two RGS spectrometers (Reflection Grating Spectrometers), RGS1 and RGS2, which provide high resolution spectroscopy across the 0.33 – 2.5 keV (HERDER et al., 2001), the Optical/UV Monitor Telescope – OM (MASON et al., 2001), and three EPIC (European Photon Imaging Camera) cameras: two MOS (Metal Oxide Semi-conductor), and one PN (p-n charge-coupled device - CCD). The EPIC cameras can be operated independently in different modes with the following properties for different fields-of-view, integration times, and magnitudes of the object (TURNER et al., 2001):

Full frame and extended full frame, all CCD pixels are read out;

Partial window, MOS camera can be operated in a different mode of science data acquisition. In the PN camera, only half the area is read out;

Timing, the imaging is performed in one dimension only, along the column axis. The PN camera offers very high time resolution.

As described in Section 2.5, the input files for CYCLOPS in X-rays are the spectrum, the instrumental files (ARF and RMF), and optionally the phase diagrams. To obtain all these files, it is necessary to reduce the X-ray data. This procedure is described below.

We reduced the V405 Aur X-ray data using EPIC-MOS camera data in timing mode in order to obtain spectra as well as light curves [3]. We also obtained spectra from RGS. However, the EPIC-PN camera was not in operation and the source was outside of the OM detector during the observations. In summary, the X-ray data from V405 Aur are two spectra and two light curves from EPIC/MOS-1 and EPIC/MOS-2, and two spectra from RGS. The EPIC/MOS-1 and EPIC/MOS-2 spectra are very similar. We used the EPIC/MOS-2 data for the CYCLOPS modeling because of the smaller error bars (see Figure 5.10).

We performed the standard procedures of X-ray reduction using the XMM-SAS version 16.0.0. First, we extracted the uncalibrated files in the Observation Data File (ODF) for each instrument separately. Secondly, we obtained the calibration files and concatenated event lists using source-specific filter criteria. Then, we filtered the EPIC data for periods of high background flaring activity. Next, we performed the recipes to extract spectra and light curves individually. To obtain the source spectra, we selected and extracted the source and background regions as well as the ancillary (ARF) and redistribution (RMF) files (see Section 2.5). For light curves, we carried out a barycentric correction due to sets of data with short periods separated by long intervals of time. We then selected and extracted the source and background regions. As light curves can be affected by vignetting, bad pixels, we applied a SAS task, *epiclccorr*, which performs all of these corrections at once. Figure 5.9 shows a flowchart for the reduction steps for the EPIC timing mode data. We also obtained the spectra from the RGS detector, the reduction followed the step-by-step recipe from the XMM-Newton data analysis threads [4].

---

[3] I am grateful to COSPAR for my participation in "Latin American X-ray school for different astrophysical scenarios. - Data analysis of the XMM-Newton, Chandra and NuStar missions" (2017), which helped me in the reduction of XMM-Newton data

[4] The tools and steps to reduce the XMM-Newton data are available on: `https://www.cosmos.esa.int/web/xmm-newton/sas-threads`.

Following Evans and Hellier (2004), we removed a spurious signal at low energies from 315 columns in the EPIC/MOS-2 data and extracted the background light curves from offset circular regions on adjacent chip (CCD3), because of the limited coverage of the timing mode window. However, our instrumental responses are updated versions with respect to the ones used by the above-mentioned authors.

Figure 5.9 - Flowchart of the data reduction steps of the timing mode in XMM-Newton satellite.

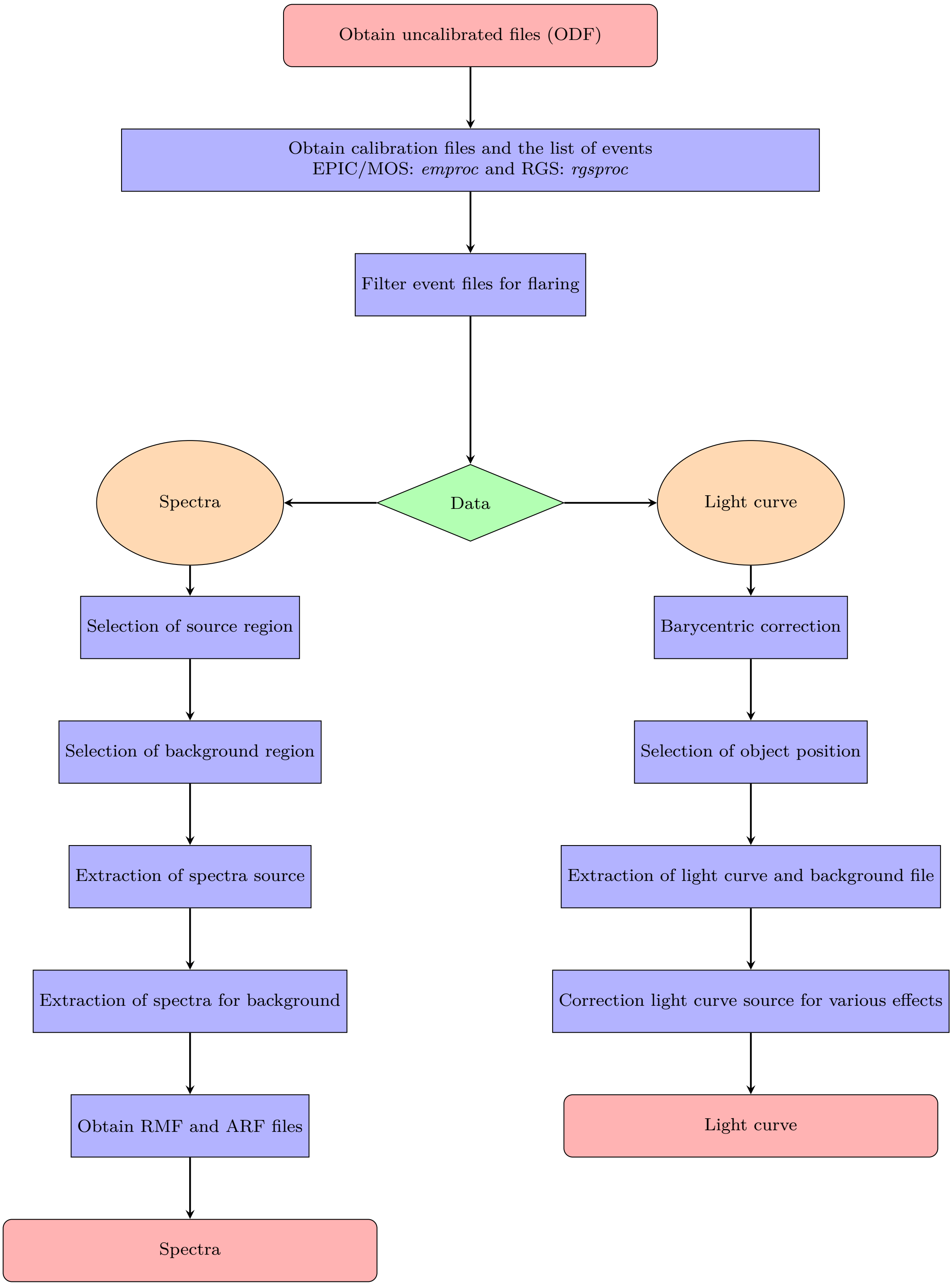

SOURCE: ESA (2021).

5.4 Results

This section describes our results regarding V405 Aur modeling. Initially, we present the X-ray spectra fitting using XSPEC in Subsection 5.4.1. In Section 5.4.2, we show a timing analysis in X-ray light curves. In Subsection 5.4.3, we present the X-ray fit using the CYCLOPS code. Subsection 5.4.4 describes the inclusion of the optical data in modeling using the CYCLOPS code. Our previous result without shock solution (prior to 2020) is presented in Section 5.4.5.

5.4.1 X-ray fitting: XSPEC code

The X-ray data obtained by XMM-Newton have energies from 0.1 to 10 keV. The integrated X-ray spectra using data from RGS-1, RGS-2, EPIC/MOS-1, and EPIC/MOS-2 detectors are shown in Figure 5.10. Evans and Hellier (2004) reported clear calibration discrepancies below 0.4 keV between the two EPIC-MOS instruments, however we did not notice it in our data, probably because we used updated instrumental responses.

The XSPEC code was used to simultaneously fit all X-ray data obtained from XMM-Newton. The models and their parameters are reported in Table 5.2. We followed the modeling prescription of Evans and Hellier (2004), however unlike them, we used RGS-1 and RGS-2 data, which are soft X-ray data. We modeled the V405 Aur spectra using two *APEC* models instead of two *MEKAL* models as proposed by Evans and Hellier (2004). Both models are used for hot plasma with collisionally-ionized diffuse gas. The *MEKAL* code is based on the bremsstrahlung model modified for the inclusion of the Fe-L line (MEWE et al., 1985; KAASTRA, 1992; LIEDAHL et al., 1995) and the *APEC* is an updated version of *MEKAL* calculating the plasma model spectra using *APED* (Astrophysical Plasma Emission Database), which contain wavelengths, radiative transition rates, and electron collisional excitation rate coefficients (SMITH et al., 2001). While our best-fitted temperatures are ∼0.2 and 64 keV, Evans and Hellier (2004) used 0.2 and 9 keV. Also, our metal abundances (*APEC* uses He fixed at cosmic and elements such as C, N, O, Ne, Mg, Al, Si, S, Ar, Ca, Fe, Ni) are an order of magnitude greater than those of Evans and Hellier (2004).

In addition, we also used the following models: (i) two simple and one partial-covering absorption owing to a large soft excess in V405 Aur. PSR absorption is commonly found in IPs as explained in Section 1.3.3. The values of N(H) are in the same order of magnitude as the results obtained by Evans and Hellier (2004) as well as our value used in the CYCLOPS modeling stated in Section 5.2.1; (ii) a blackbody component in order to model the soft emission, our temperature was very similar to the 3.97×10^{-2} keV from Evans and Hellier (2004); and (iii) a narrow Gaussian component at the 6.4 keV iron fluorescence line. Finally, the best-fit reduced χ^2 found for all models was equal to 1.15.

Figure 5.10 - The XMM-Newton V405 Aur spectra fitted using XSPEC models given in Table 5.2. Black is used for EPIC/MOS-1 data and model, red for EPIC/MOS-2, blue for RGS-1, and green for RGS-2. In the upper panel, crosses represent the data and the models are the continuum lines.

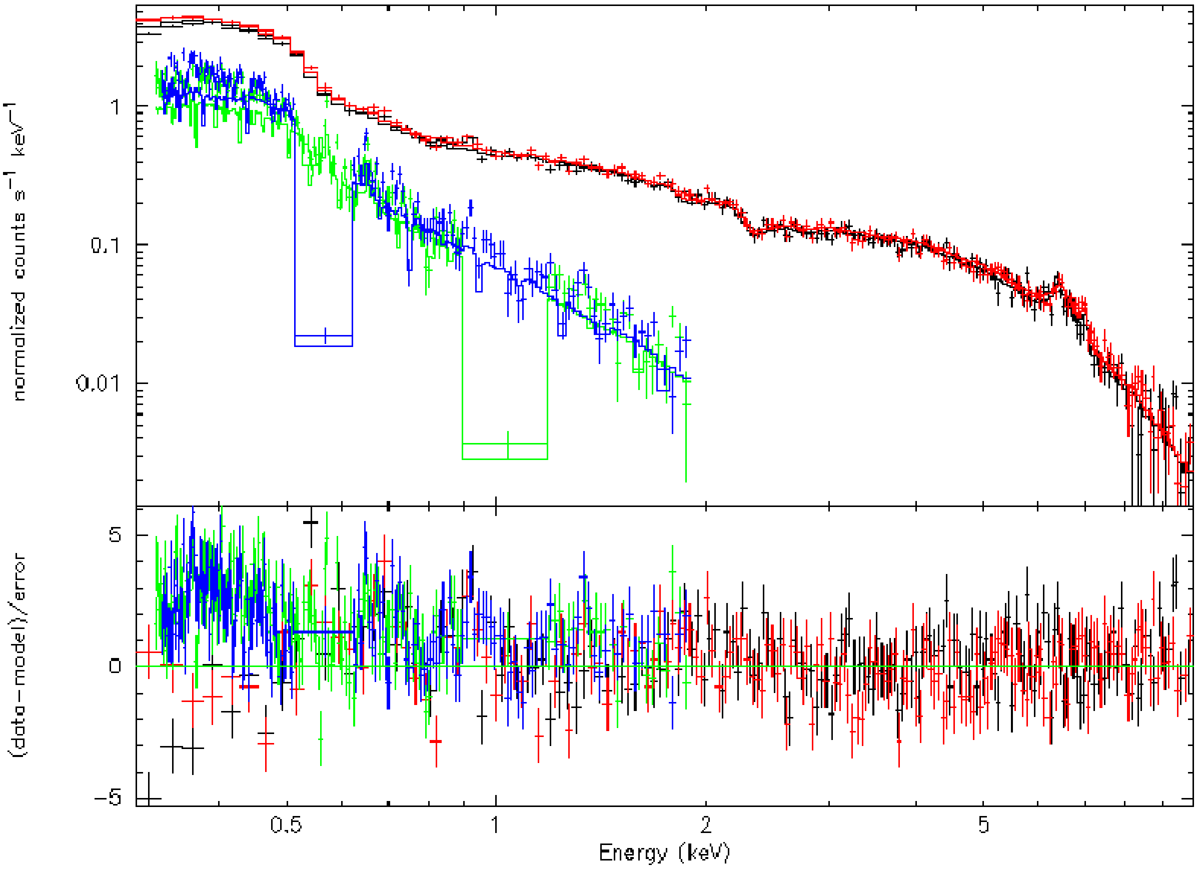

SOURCE: The author.

Table 5.2 - Model components and parameters used to fit the spectra of V405 Aur.

Component	Parameter (Units)	Value	Error
phabs	nH (cm^{-2})	6.951 x 10^{21}	(+0.028,-0.022)
bbody	kT (keV)	5.274 x 10^{-2}	(+0.003,-0.007)
	Normalization	1.461 x 10^{-3}	(+0.002,-0.001)
phabs	nH (cm^{-2})	2.642 x 10^{21}	(+0.009,-0.008)
pcfabs	nH (cm^{-2})	6.345 x 10^{21}	(+1.649,-1.064)
	CvrFract	0.46	
gaussian	Energy (keV)	6.480	(+0.056,-0.045)
	Eq. Width (keV)	0.196	(+0.078121,-0.059)
	Normalization	7.176 x 10^{-5}	(+1.871 x 10^{-5},-1.564 x 10^{-5})
APEC	kT (keV)	0.173	(+0.018,-0.0216)
	Abundance	3.744 x 10^{-3}	(+0.003,-0.002)
	Normalization	0.162	(+0.116,-0.047)
APEC	kT (keV)	64.0	(+0.64,-0.82)
	Abundance	0.283 x 10^{-3}	(+1.087,-1.021)
	Normalization	1.334 x 10^{-2}	(+0.001,-0.001)
χ^2		1.15	

5.4.2 Timing analysis

The X-ray light curves were also obtained from EPIC/MOS-1 and EPIC/MOS-2. The power spectra of the combined data set are shown in Figure 5.11, where they are divided into E $\leq$ 0.8 keV and E $>$ 0.8 keV energy bands. These energy intervals correspond to the current calibration of EPIC-MOS matrices, therefore different from the Evans and Hellier (2004) energy intervals. We found the periods of 272.7 s in the E $\leq$ 0.8 keV data and 545.5 s from the E $>$ 0.8 keV data, respectively. These periods are the first harmonic of the spin period and the spin period. The same results were reported by Allan et al. (1996) using the ROSAT satellite and Evans and Hellier (2004). Figure 5.12 shows the X-ray phase diagrams in these energy bands, which have the same behavior found by Evans and Hellier (2004), in other words, the soft emission has a double-peaked modulation at the WD spin period and the hard emission has only one.

Figure 5.11 - Power spectra of the X-ray data (EPIC/MOS-1 and EPIC/MOS-2) in the E $\leq$ 0.8 keV (left-hand panel) and in the E $>$ 0.8 keV (right-hand panel) energy bands. The prominent periods are 272.7 s and 545.5 s, respectively.

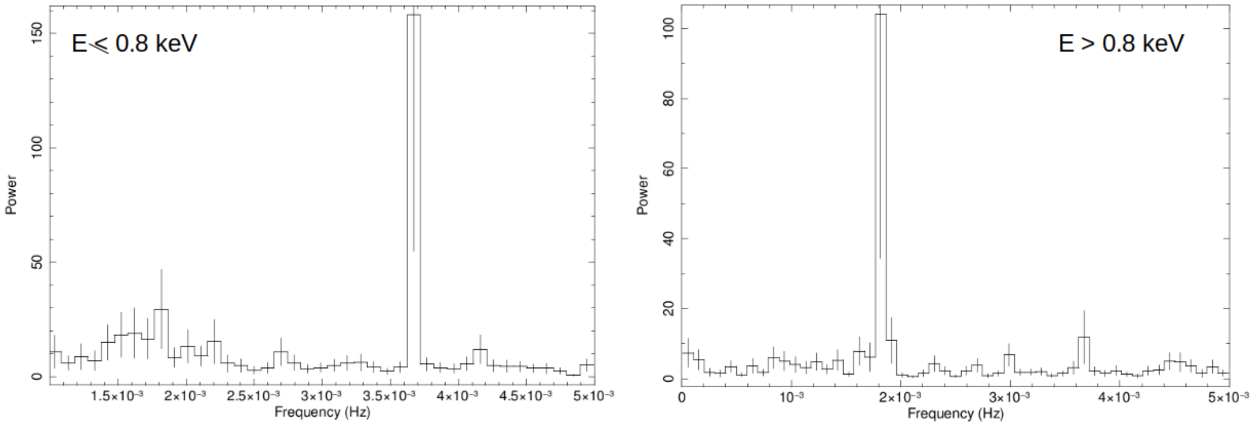

SOURCE: The author.

We could not reproduce the phase zero value of HJD 2452187.55904 proposed by Evans and Hellier (2004) using the higher peak of the soft X-rays light curve. Actually, our ephemeris using the same fiducial characteristic is given by Equation 5.2. In particular, we are using barycentric dynamic time (BJD_{TDB}), which is obtained after conversion of local satellite frame to Barycentric Julian Date.

$$BJD_{TDB}^{max} = 2452187.57416(4) + 0.0063137E \ . \tag{5.2}$$

Figure 5.12 - X-ray phase diagram folded on spin period (545.5 s) in E $\leq$ 0.8 keV (top panel) and E $>$ 0.8 keV (bottom panel) energy bands.

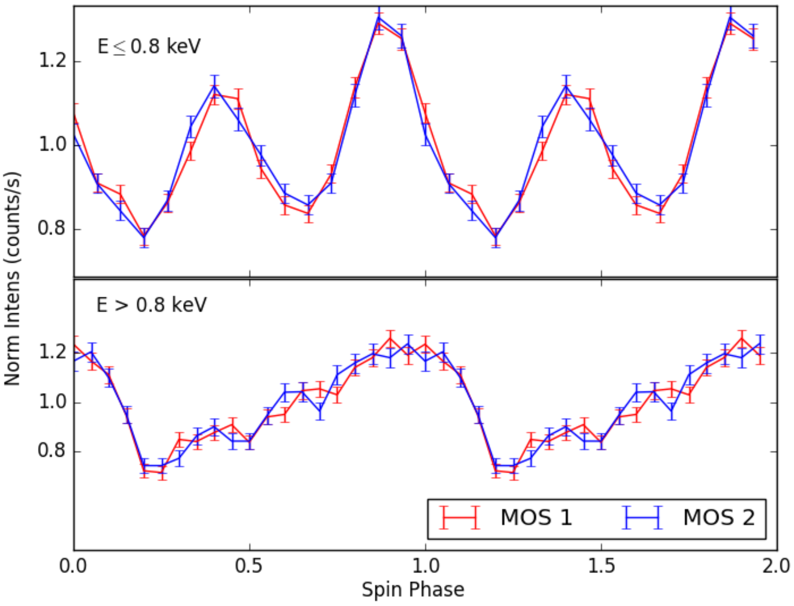

SOURCE: The author.

5.4.3 X-ray fitting: CYCLOPS code

As mentioned before, the CYCLOPS code is able to simultaneously fit optical data and X-ray spectrum and light curve data using the optimization algorithms. The total number of parameters for the CYCLOPS code is 14, a challenge for any fitting algorithm. On top of that, there is an intrinsic model degeneracy in the X-ray spectrum modeling, as discussed by Belloni et al. (2021). One way to deal with this large number of parameters in the CYCLOPS code is to perform the fitting in stages. That is, we can initially perform the fitting using a single data set to try to define some of the input parameters. Then, we fix the parameters found and include additional data to define the other parameters.

The modeling of V405 Aur using the CYCLOPS code has proved to be quite complex. One of the reasons is that we have ten optical light curves and two kinds of X-ray observables (spectrum and light curves), in total twelve input data, to fit about 14 code parameters. In this context, our strategy in order to estimate the parameters was to separate the fit procedure into X-ray spectrum data, X-ray spectrum and light curve data, one band of photometric and polarimetric optical data, X-ray data and one band of photometric and polarimetric optical data, X-ray data and two band of photometric and polarimetric optical data and so on.

We emphasize that CYCLOPS does not model emission lines yet, thus to model the V405 Aur spectrum, we removed the Kα iron emission line region from the X-ray data blend at 6.0 – 7.2 keV. We also removed E < 2.0 keV to avoid the soft blackbody component present in V405 Aur (see Section 5.1). Suleimanov et al. (2005) argued that most of the emission lines have energies less than 3 keV (with the exception of a line blend at 6–7 keV). Their modeling of V405 Aur from RXTE satellite used a broad Gaussian line to fit the iron emission line as shown in Figure 5.13.

Figure 5.13 - Spectra of V405 Aur obtained from the RXTE and NuSTAR observatories in left and right-hand panels, respectively. In the RXTE spectrum, the crosses denote PCA data, open circles – HEXTE data and the solid lines show the best fit model. In the NuSTAR spectrum, the crosses are data and red lines show the best fit model.

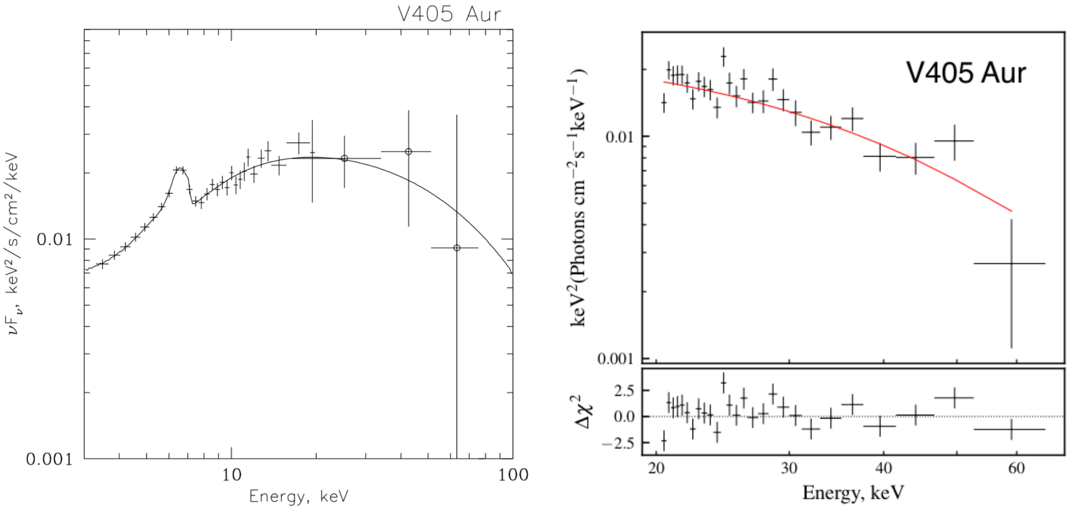

SOURCE: Suleimanov et al. (2005) and Suleimanov et al. (2019).

We used a coarse grid in CYCLOPS (PIKAIA algorithm), so we refined the search for parameters to a finer grid (AMOEBA algorithm). Initially, V405 Aur modeling was performed considering only the normalized X-ray spectrum, which means that we fitted only the shape of the spectrum and not its absolute level. We only fixed the parameters related to magnetic axis, $B_{\mathrm{lat}} = 90°$ and $B_{\mathrm{long}} = 0°$. This modeling indicates the existence of degenerate parameters, as expected. Figure 5.14 shows two models, for example, with physical and geometrical parameters presented in Table 5.3. Both models are in good agreement with the X-ray data and display almost the same behavior. However, the fitted parameters are distinct. For example, the orbital inclination of model 1 is 70.1°, while for model 2 it is 20.4°. The mass accretion rates are also very different: 10^{-8} $\mathrm{M}_{\odot}$ year^{-1} in model 1 and 10^{-7} $\mathrm{M}_{\odot}$ year^{-1} in model 2. However, both models show high WD mass values, probably a consequence of the relatively hard X-ray spectrum, which demands a hot PSR. This is discussed in greater detail below.

In both models, the temperatures (average and weighted with density squared) are as large as those found in our modeling with XSPEC using APEC (64 keV), and significantly larger than those found by Evans and Hellier (2004) using the *MEKAL* model (T = 9 keV). At this point, it is relevant to recall that *MEKAL* and *APEC* fitting considered an isotermic gas, contrary to CYCLOPS that adopts a temperature distribution. These higher temperatures in V405 Aur are related to the hardness of the X-ray spectra. The potential energy in falling gas is converted into kinetic energy until it reaches the shock, where density and temperature are enhanced. Then, the greater the gas velocity at the shock, the higher the temperature, and the more energetic the bremsstrahlung emission in the PSR. Therefore, the harder the X-ray spectrum, the greater the temperature in the PSR. We can also associate the mass of the WD with the temperature in a first approximation (SULEIMANOV et al., 2005). This means, the greater the temperature in the PSR, the greater the WD mass. Suleimanov et al. (2005) and Suleimanov et al. (2019) calculated the WD mass of V405 Aur based on the harder X-ray spectrum from the RXTE and NuSTAR observatories, respectively, these values were 0.90 ± 0.10 $\mathrm{M}_{\odot}$ and 0.73 ± 0.03 $\mathrm{M}_{\odot}$ (see Figure 5.13). We can improve those results taking into account some features that only the CYCLOPS code considered in the modeling such as absolute flux level of the X-ray spectrum (see Section 3.2) and X-ray light curve (see Section 2.5).

Figure 5.14 - V405 Aur normalized spectrum modeling by CYCLOPS.

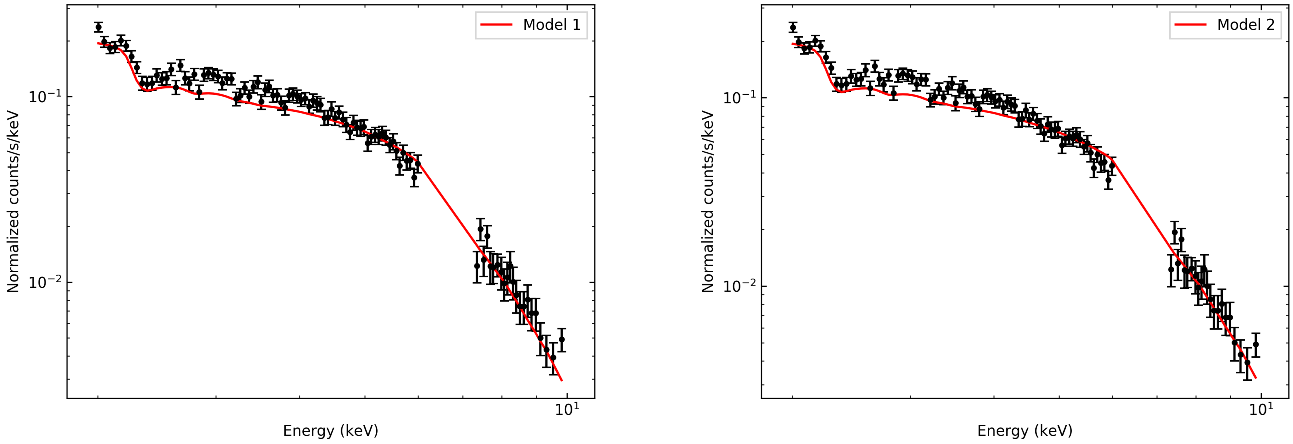

SOURCE: The author.

Table 5.3 - Physical and geometrical properties of V405 Aur using normalized X-ray spectrum fitted by CYCLOPS.

CYCLOPS input parameters	Model 1	Model 2
M_{WD} ($M_\odot$)	1.25	1.04
$\dot{M}_{\rm WD}$ ($M_\odot$ year^{-1})	10^{-8}	10^{-7}
B (G)	1.9×10^7	1.3×10^7
$B_{\rm lat}$	90°	90°
$B_{\rm long}$	0°	0°
i	70.1°	20.4°
β	7.3°	11.7°
$\Delta_{\rm long}$	23°	39°
$\Delta_{\rm R}$	0.09	0.17
CYCLOPS model associated and resulting quantities	value	value
Height of the PSR (R_{WD})	0.0015	0.0013
Average shock temperature (keV)	88.2	46.7
Weighted shock temperature (keV)	75.7	39.7
Shock electronic number density (cm^3)	4×10^{18}	2×10^{18}
Distance of the threading region to the WD centre (R_{WD})	62	24

As mentioned above, CYCLOPS was implemented with absolute flux level of the X-ray spectrum, which is expected to contribute to breaking the degeneracy. In other words, the identical normalized spectra could be distinguished using the accurate distance in the fitting procedure. However, Belloni et al. (2020) pointed out that even including the distance as well as the pre-shock region, the degeneracy could still persist.

In fact, the modeling of V405 Aur using non-normalized X-ray spectrum, in other words, the absolute emission level, indicated three good families with different parameters. Table 5.4 shows the parameters found for models 3, 4, and 5, for example. These models are in good agreement with the data shown in Figure 5.15.

When we analyzed all the models obtained in the non-normalized X-ray spectrum, we noted that the good spectrum models tend to have high WD mass and more restricted mass accretion rates with values ranging from 10^{-9} to 10^{-10} $M_{\odot}$ year^{-1}. The typical mass accretion rate value for a large fraction of IPs is 10^{-9} $M_{\odot}$ year^{-1}, which is consistent with that expected from CV secular evolution modeling, providing their orbital periods (usually, $\gtrsim$ 3 hr) and their (usually) negligible WD magnetic moments (BELLONI et al., 2020, e.g.). In fact, Suleimanov et al. (2005) and Suleimanov et al. (2019) proposed for V405 Aur from RXTE and NuSTAR data that the mass accretion rates were 0.4×10^{-9} $M_{\odot}$ year^{-1} and 0.1×10^{-10} $M_{\odot}$ year^{-1}, respectively. In this context, our results are in good agreement with the literature, different from our previous models 1 and 2. Therefore, we can use this information in order to constrain the search interval for this parameter and decrease the computation time.

Table 5.4 - Physical and geometrical properties of V405 Aur using absolute X-ray spectrum fitted by CYCLOPS.

CYCLOPS input parameters	Model 3	Model 4	Model 5
M_{WD} ($M_{\odot}$)	1.04	1.20	0.90
$\dot{M}_{\rm WD}$ ($M_{\odot}$ year^{-1})	10^{-9}	10^{-9}	10^{-10}
B (G)	7.8×10^{6}	2.3×10^{7}	1.3×10^{7}
$B_{\rm lat}$	90°	90°	90°
$B_{\rm long}$	0°	0°	0°
i	54.7°	19.7°	57°
β	6.5°	5.8°	12.5°
$\Delta_{\rm long}$	5°	11°	13°
$\Delta_{\rm R}$	0.07	0.13	0.02
CYCLOPS model associated and resulting quantities	value	value	value
Height of the PSR (R_{WD})	0.0015	0.0063	0.0053
Average shock temperature (keV)	48.1	72.9	33.5
Weighted shock temperature (keV)	41.0	61.9	28.6
Shock electronic number density (cm^{3})	1.5×10^{18}	6.7×10^{17}	2.3×10^{17}
Distance of the threading region to the WD centre (R_{WD})	78	98	21

Figure 5.15 - V405 Aur absolute spectrum modeling by CYCLOPS.

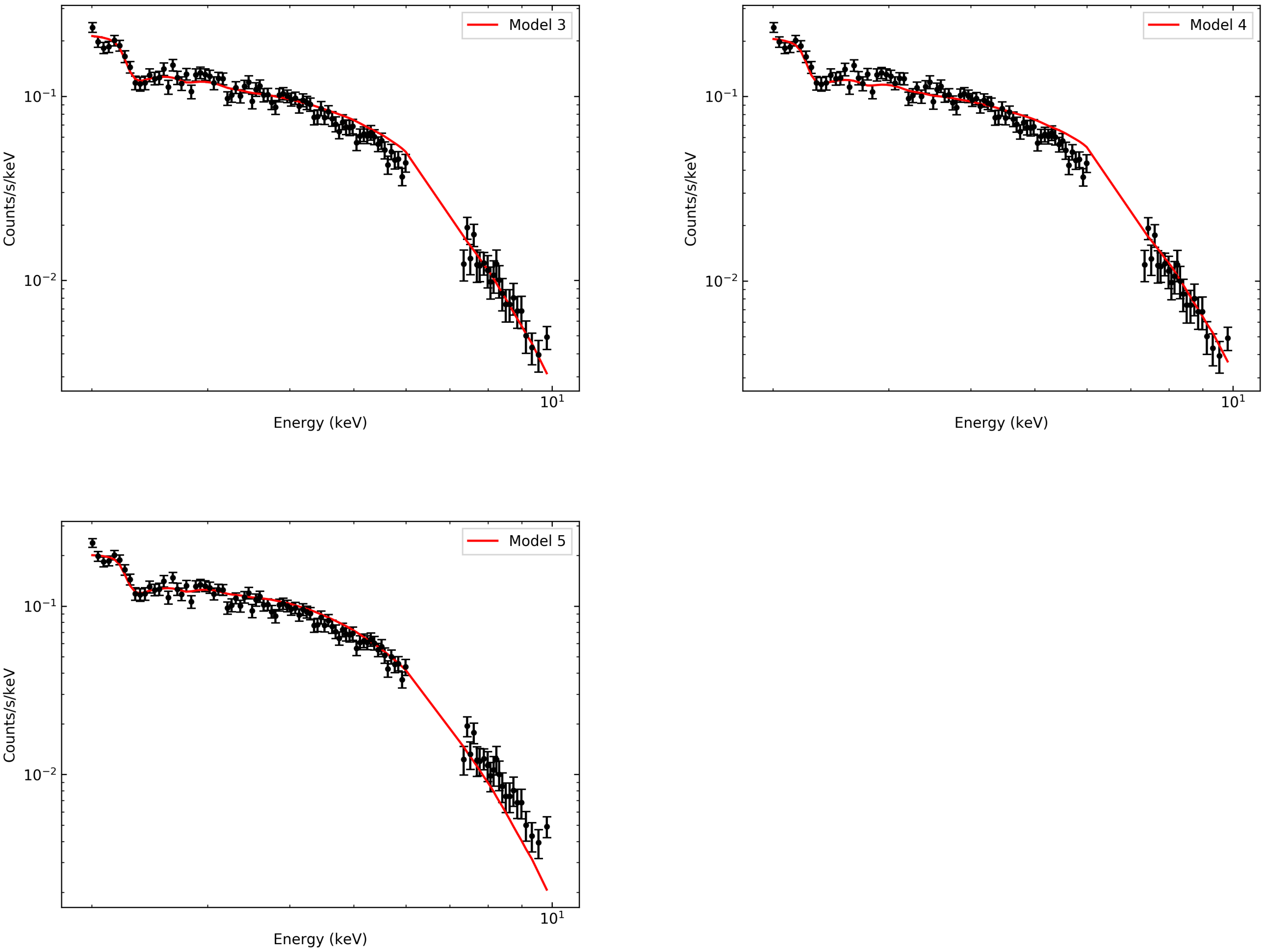

SOURCE: The author.

To break the degeneracy of the X-rays spectrum fitting, which exists even in the fitting of absolute level counts, we added the phase diagram as an additional constraint. We could not find a good fit using the magnetic axis parallel to the rotation axis, in other words, $B_{\rm lat} = 90°$ and $B_{\rm long} = 0°$ because this configuration always produces phase diagrams that are symmetric relative to phase 0.5. When fitting the X-ray observations letting the magnetic axis vary, we found good models. All results show that the best models tend to reasonably fit the light curve, but the spectrum is softer than observed.

Figure 5.16 presents a good fit of our CYCLOPS modeling using absolute X-ray spectrum and light curve. The parameters for this model are shown in Table 5.5.

We found different families in this fit, but model 6 displays the best figure of merit as well as the best visual aspect. The degeneracy problem can be solved using light curves in different energy ranges. In other words, X-ray light curves are a fruitful way out of this problem as reported by Belloni et al. (2020). This makes the CYCLOPS code the only one currently available able to handle this kind of analysis.

The magnetic field at the pole provided by model 6 is 3.7×10^7 G. This value is quite similar to the value proposed by Piirola et al. (2008), 30 MG, which can confirm that V405 Aur is the IP with the largest magnetic field. The weighted temperature is 43.2 keV, which is due to the hardness spectrum as previously mentioned. The WD mass found was 1.14 $M_\odot$, which is larger than that obtained by Suleimanov et al. (2019) using NuSTAR. In fact, the first estimates of the average WD mass in the IP population indicate relatively low masses of about 0.5–0.7 $M_\odot$ (YUASA et al., 2010, e.g.). In addition, a recent investigation using NuSTAR observations found an average WD mass close to the value ∼0.9 $M_\odot$, typical for the nearby CVs population (SULEIMANOV et al., 2019).

We tried using model 6 to fit all UBVRI optical data in order to verify if this model can simultaneously model optical and X-ray data. When we analyzed the results, which are not shown here, we concluded that it was not possible. Therefore, to include optical data it will be necessary to fit these data using CYCLOPS again. The following section will discuss the attempt to model V405 Aur.

Figure 5.16 - V405 Aur absolute spectrum and light curve modeling by CYCLOPS.

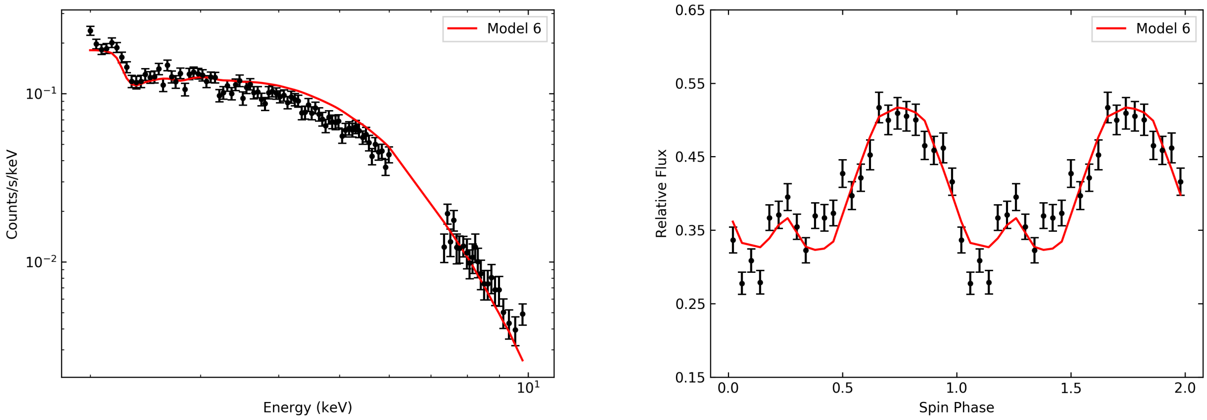

SOURCE: The author.

Table 5.5 - Physical and geometrical properties of V405 Aur using absolute X-ray spectrum and light curve fitted by CYCLOPS.

CYCLOPS input parameters	Model 6
M_{WD} ($M_\odot$)	1.14
$\dot{M}_{\rm WD}$ ($M_\odot$ year^{-1})	10^{-10}
B (G)	3.7×10^7
$B_{\rm lat}$	83°
$B_{\rm long}$	0°
i	40°
β	12.5°
$\Delta_{\rm long}$	11.5°
$\Delta_{\rm R}$	0.19
CYCLOPS model associated and resulting quantities	value
Height of the PSR (R_{WD})	0.0080
Average shock temperature (keV)	54.2
Weighted shock temperature (keV)	43.2
Shock electronic number density (cm^3)	2.0×10^{17}
Distance of the threading region to the WD centre (R_{WD})	107.2

5.4.4 Optical and X-ray fitting

The optical modeling of V405 Aur was also performed in steps. First, we looked for a good model using the photometric and polarimetric data per band in order to figure out if individual bands could be fitted and if the model could be part of the same family, then we added other bands one by one. In parallel, we performed the same procedure with the inclusion of the X-ray data. In general, we did not restrict the geometry of the system in favor of any values pre-established by Evans and Hellier (2004) and Piirola et al. (2008). The search for models were determined initially by PIKAIA and restricted with the AMOEBA algorithm. We carried out a variety of searches: (i) using the same weight for all points and bands and adopting a heavier weight for the circularly polarized flux relative to the total flux; (ii) using only UBVRI circular polarimetric data in order to model just the cyclotron emission; (iii) using one PSR and after including two (north and south) PSRs. In this context, just our best results are presented in this manuscript.

As mentioned above, a good model was found using only the the U band. We then searched using other individual bands and also found good results. The problem is that these results do not indicate parameters belonging to the same family. In fact, they are quite different from each other, especially between the U and I bands. These individual UBVRI models were not shown here. Although the previous results revealed a difficulty in finding a good model in all bands, we performed a simple test: we tried to check if the best model found in the U band fits the other bands as well. Therefore, we applied the same U band model, whose parameters are presented in Table 5.6 (model 7-a), in BVRI individually, in other words, non-simultaneous. The photometric and polarimetric curves of UBVRI bands using the non-simultaneous U band are shown in the top panel in Figure 5.17.

The orbital inclination and colatitude found in model 7-a were ∼26° and 73°, respectively. These geometrical parameters are similar to those proposed by Piirola et al. (2008) ($i = 30° - 50°$, and $\beta = 90°$). This model seems to indicate that two PSRs are located in geometrically opposite regions. However this model has the flux emission of the one PSR. In other words, only one PSR effectively contribute to emission (this was not shown in Figure 5.17). This can be related with the CYCLOPS approach of considering the accretion of matter from the same threading region (see discussion in Section 5.5).

We applied model 7-a using simultaneously UBVRI optical photometry and polarimetry curves and X-ray spectrum and light curve, denominated model 7-b (bottom in Figure 5.17). Surprisingly, we noticed that if model 7-a is applied to each band individually (top in Figure 5.17), we obtained better results than simultaneously modeling on all bands together (model 7-b). In fact, when we searched for a model using simultaneous V405 Aur data, we did not obtain good results using one or two PSRs. So far, we only found a reasonable model for UBV polarimetry curve with a contribution of two PSRs, the RI bands data are not well modelled. In this context, the photometry data can be contaminated by emission from the accretion disk, which does not fit the spectral energy distribution (SED). This model does not include X-ray data. Therefore, these results are not shown here.

Table 5.6 - Physical and geometrical properties of V405 Aur optical photometry and polarimetry in the U band fitted by CYCLOPS.

CYCLOPS input parameters	Model 7-a	Model 7-b
M_{WD} ($M_\odot$)	1.32	1.32
$\dot{M}_{\rm WD}$ ($M_\odot$ year^{-1})	10^{-9}	10^{-9}
B (G)	5.2×10^6	5.2×10^6
$B_{\rm lat}$	27°	27°
$B_{\rm long}$	0°	0°
i	26 °	26 °
β	73°	73°
$\Delta_{\rm long}$	23°	23°
$\Delta_{\rm R}$	0.791	0.791
CYCLOPS model associated and resulting quantities	value	value
Height of the PSR (R_{WD})	0.0520	0.2967
Average shock temperature (keV)	20.4	75.1
Weighted shock temperature (keV)	16.2	54.7
Shock electronic number density (cm^3)	3.3×10^{15}	3.5×10^{15}
Distance of the threading region to the WD centre (R_{WD})	4.366	6.496
Phase shift applied to the model	-0.288	-0.288

Figure 5.17 - A good model of V405 Aur for the U band applied for individual bands (top panel) and the same model simultaneous applied in UBVRI light and polarization curves and X-ray data (bottom).

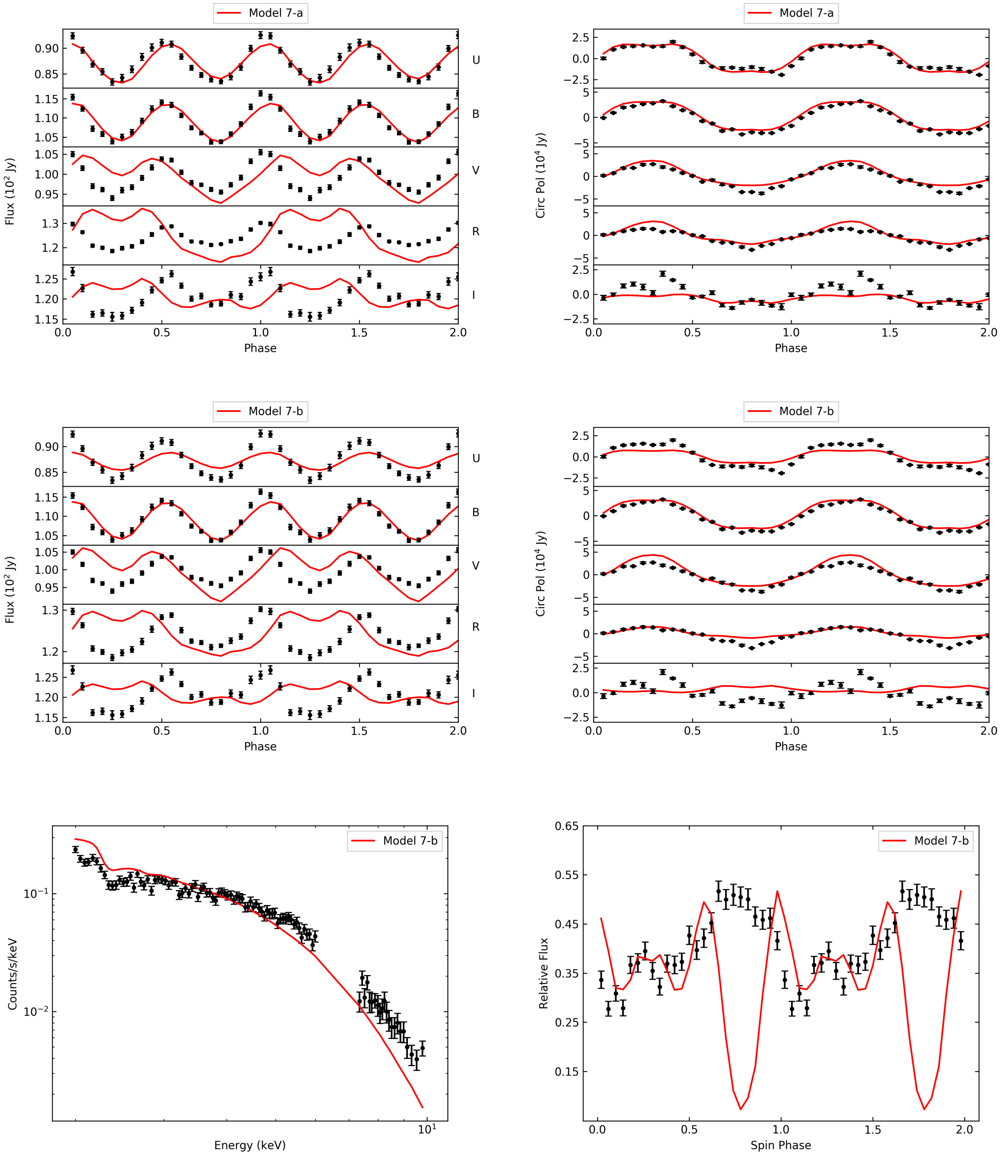

SOURCE: The author.

The CYCLOPS code was not able to find a good model that would answer our questions, such as: what is the geometry of accretion of V405 Aur? In order to figure out a possible reason that explains the lack of good models to fit our simultaneously data, we proposed to fit one PSR using half of the data. In other words, we used the data from the interval of 0 - 0.5 phase or 0.5 - 1 phase, as the data are symmetric it makes no difference which we choose. We are interested in knowing if we can model one PSR from one threading region. So far, the only model obtained is shown in Figure 5.18 (model 8), whose parameters are presented in Table 5.7. This model simultaneous fitted one photometry and polarimetry curves in the V band and X-ray spectrum and light curve. However, we do not have good results using our all data set yet. This might indicate the need for two threading regions (see Section 5.5).

Table 5.7 - Physical and geometrical properties of V405 Aur using the V band optical and absolute X-ray spectrum and light curve fitted for the range 0 - 0.5 phase by CYCLOPS .

CYCLOPS input parameters	Model 8
M_{WD} ($M_\odot$)	1.16
$\dot{M}_{\rm WD}$ ($M_\odot$ year^{-1})	10^{-10}
B (G)	8.0×10^6
$B_{\rm lat}$	72°
$B_{\rm long}$	4°
i	36.5°
β	21.5°
$\Delta_{\rm long}$	34.3°
$\Delta_{\rm R}$	0.086
CYCLOPS model associated and resulting quantities	value
Height of the PSR (R_{WD})	0.0080
Average shock temperature (keV)	54.2
Weighted shock temperature (keV)	43.2
Shock electronic number density (cm^3)	2.0×10^{17}
Distance of the threading region to the WD centre (R_{WD})	107.2
Phase shift applied to the model	-0.246

Figure 5.18 - A good model of V405 Aur for the V band and X-ray data for the range 0 - 0.5 phase using CYCLOPS.

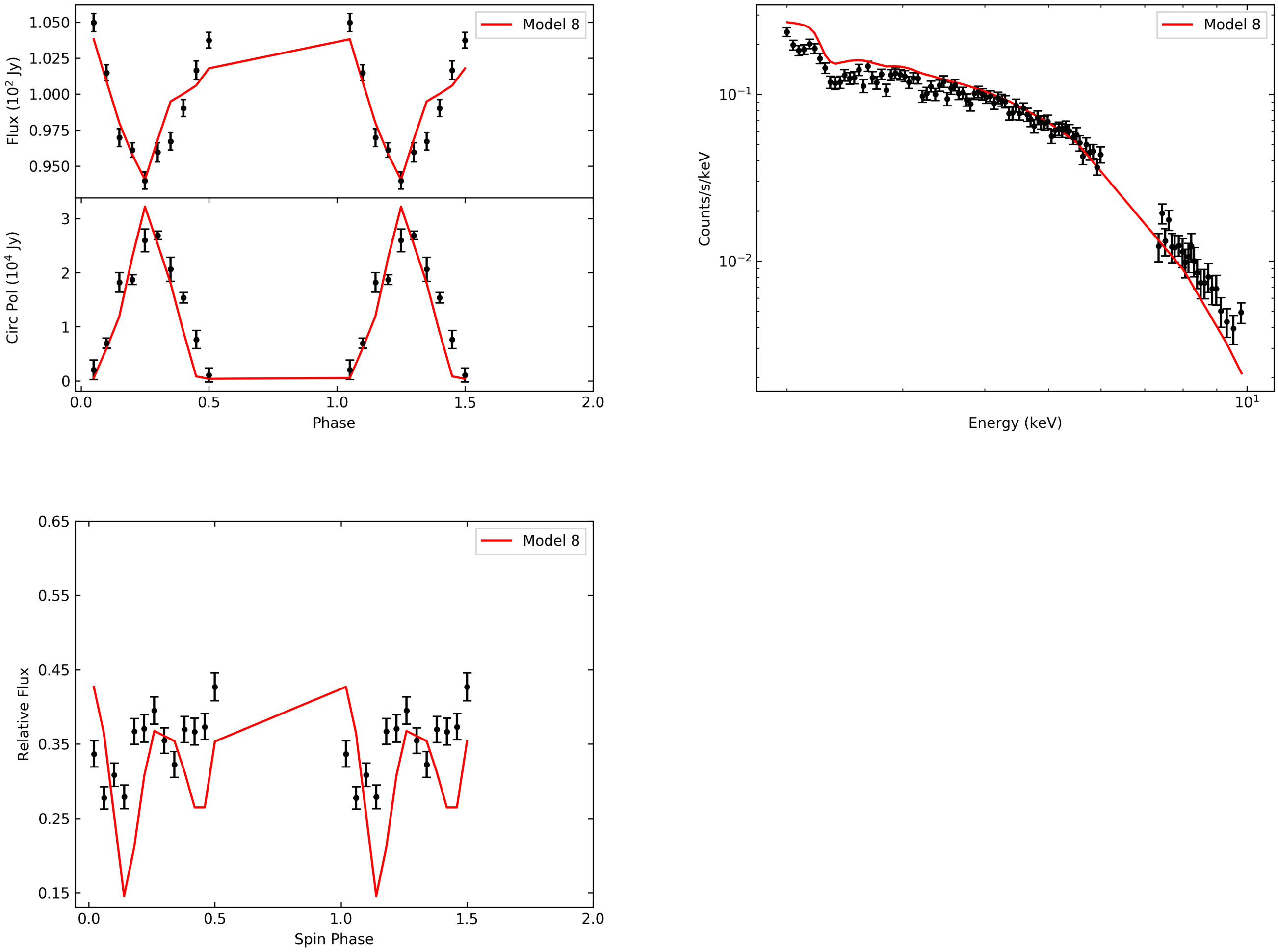

SOURCE: The author.

5.4.5 Before CYCLOPS 2020

We mentioned in Section 2.12 that CYCLOPS was implemented with the shock solution in 2020. Before this upgrade, the code used arbitrary functions for temperature and density profiles (see Section 2.13). In this section, we will present this preliminary study in order to comment on some aspects of V405 Aur modeling.

The best model of V405 Aur using CYCLOPS prior to 2020 was found using the X-ray data (removing 6.0 – 7.2 keV and E $<$ 2.0 keV). Then, we continued to had good results when applied it to simultaneous UBVRI optical photometry and polarimetry, X-ray spectrum, and X-ray light curve data. The best model using one PSR is presented in Table 5.8 and Figure 5.19. The magnetic field is B = 36 MG. This value has the same order of magnitude as that proposed by Piirola et al. (2008).

Table 5.8 - Best-fitting model parameters of V405 Aur using the CYCLOPS version prior to 2020.

CYCLOPS input parameters	Model
M_{WD} ($M_\odot$)	1.14
$\dot{M}_{\rm WD}$ ($M_\odot$ year^{-1})	10^{-10}
B (G)	3.6×10^7
$B_{\rm lat}$	67°
$B_{\rm long}$	37°
i	45.3°
β	59.1°
$\Delta_{\rm long}$	64.5°
$\Delta_{\rm R}$	0.05
Average shock temperature (keV)	358.5
Weighted shock temperature (keV)	165 keV
Shock electronic number density (cm^3)	2.0×10^{17}
CYCLOPS model associated and resulting quantities	**value**
Height of the PSR (R_{WD})	0.53
Weighted shock temperature (keV)	165
Shock electronic number density (cm^3)	12.26×10^{17}
Phase shift applied to the model	0.720

The best fitting shows the inclination equal to 45.3°. It is within the inclination range estimated from X-ray data (30° – 50°). The colatitude (∼59°) is approximately the value given by the data in the optical band, β = 60°. We highlight that the value of the shock temperature found was 358.5 keV. This is the result of the shock structure used in this CYCLOPS version which is a poor approximation. Therefore, the current version of CYCLOPS post 2020 solves the shock structure providing a more realistic shock temperature.

Figure 5.19 - A good model of V405 Aur obtained by a simultaneous fitting of UBVRI light and polarization curves (top), X-rays spectrum, and hard X-ray light curve (bottom) using the CYCLOPS version prior to 2020.

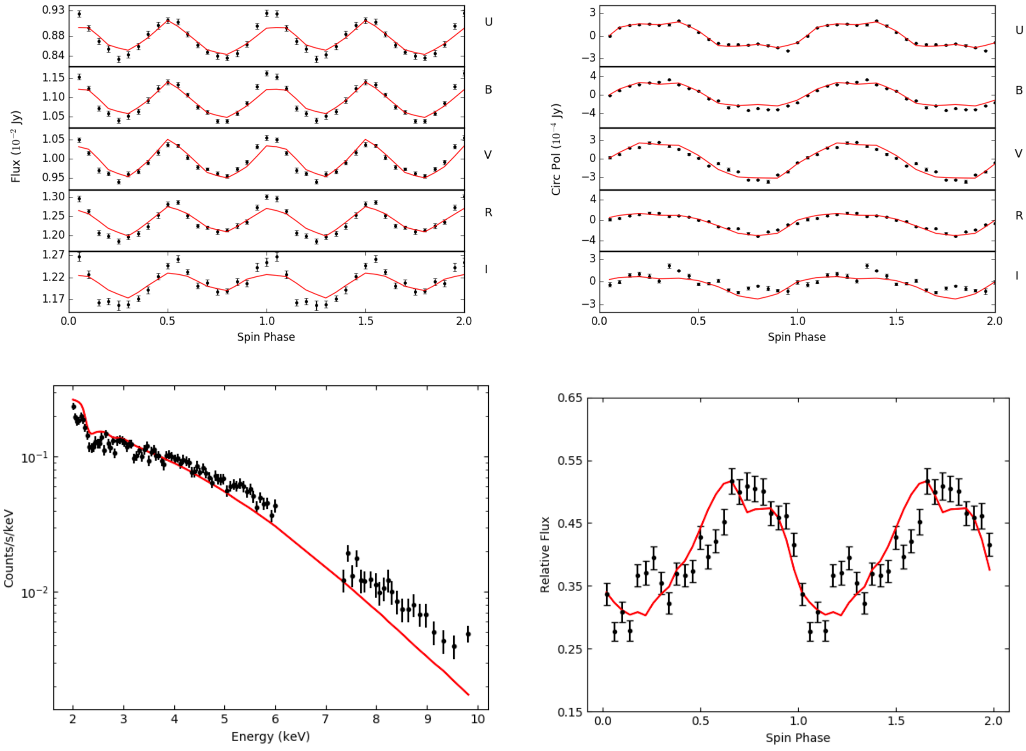

SOURCE: The author.

5.5 Discussion

The X-ray spectra of V405 Aur shows a blackbody component in the soft X-ray emission originating from the heated WD surface around the accretion footprints. This phenomenon is present in only 15 IPs. Most of them have non-zero circular polarization. This high incidence of soft X-ray emission could be correlated to the detection of circular polarization in IPs. In fact, the soft emission arising from heated WD surface around the accretion footprints, which is nearly always seen in the polars, it is only seen in some IPs with geometries where the PSRs are in line-of-sight.

X-ray spectra of V405 Aur fitted by the XSPEC code presents the hydrogen column density value of the same order of magnitude of that available in Evans and Hellier (2004) (10^{21} cm^{-3}). In this modeling, we used two *APEC* models to fit the multi-temperature emission, which are 0.17 keV and 64 keV. Although these values are not in good agreement with the results found by Evans and Hellier (2004), they are consistent with the higher average temperature weighted by the squared density ($\langle T \rangle$) found in our models using CYCLOPS as shown in Table 5.9. These temperatures are related to the hardness of the V405 Aur X-ray spectrum.

In IPs, the X-ray radiation of a PSR has been used to estimate some physical parameters such as the WD mass, the WD magnetic field strength, the accretion rate, and the threading region radius. For this, the emissivity distribution of the PSR structure is calculated and the X-ray spectra is fitted (SULEIMANOV et al., 2005; HAYASHI; ISHIDA, 2014a, see Section 1.3.2). In these estimates, however, large uncertainties are present due to degeneracy, for example, which is related to many of the parameter combinations producing identical X-ray spectra.

In order to break the degeneracy, some shock structures have been used with negligible cyclotron emission, finite but not well defined magnetospheric radius, and other simplified approaches. In other words, they decreased the number of parameter space. However, these restrictions when applied to PSR were not enough to solve the degeneracy problem (SULEIMANOV et al., 2016, e.g.). Belloni et al. (2021) proposed that the inclusion of more constraints such as adding light curves data in the modeling approach could be a possible solution. In fact, we obtained the inevitable degeneracy fitting only synthetic X-ray continuum spectra with energy up to 100 keV in four parameters: the WD mass; the WD magnetic field strength; the specific accretion rate and the threading region radius using the CYCLOPS code. When, we included the X-ray light curves in different energy ranges the degeneracy was broken.

In the modeling using X-ray spectrum and light curves (model 6), we found a WD mass of 1.1 $M_\odot$. This value is in a good agreement with values previously proposed considering the error bar (Table 5.9). Also, we were able to restrict the mass accretion rate using this model for an interval ranging from 10^{-9} – 10^{-10} $M_\odot$ year^{-1}, which is consistent with the results obtained by Suleimanov et al. (2005) and Suleimanov et al. (2019).

The magnetic field intensity of V405 Aur is estimated as being ~31.5 ± 0.8 MG from simultaneous UBVRI circular polarimetry proposed by Piirola et al. (2008) In all of our modeling, the magnetic strength has the same order of magnitude (see Table 5.9). For those authors, it indicates that V405 Aur is a likely candidate to be a polar progenitor.

While the X-ray spectrum constrains physical parameters such as the white-dwarf mass and the accretion rate, the modulated optical emission strongly restricts the geometrical parameters. This occurs because the cyclotron emission, which is the primarily responsible for the optical modulation, is very anisotropic causing an important dependence on the observer position relative to the emitting region.

Despite our efforts to simultaneously model UBVRI photometry and polarimetry data including or not including the X-ray data to propose a geometry of accretion for V405 Aur and define other physical parameters using the CYCLOPS code, we were not able to find a good model. One possible reason is discussed in the following paragraphs.

Table 5.9 - Some parameters of V405 Aur obtained by modeling its X-ray data.

Models	M_{WD} ($M_\odot$)	$\dot{M}_{\rm WD}$ ($M_\odot$ year^{-1})	B (G)	$\langle T \rangle$ (keV)
Suleimanov et al. (2005)	0.90 ± 0.10	0.4×10^{-9}	–	–
Suleimanov et al. (2019)	0.73 ± 0.03	0.1×10^{-10}	$2.2 \pm 0.05 \times 10^{6}$	–
Model 1	1.25	10^{-8}	1.9×10^{7}	75.7
Model 2	1.04	10^{-7}	1.3×10^{7}	39.7
Model 3	1.04	10^{-9}	7.8×10^{6}	41.0
Model 4	1.20	10^{-9}	2.3×10^{7}	61.9
Model 5	0.90	10^{-10}	1.3×10^{7}	28.6
Model 6	1.10	10^{-10}	3.7×10^{7}	43.2

A summary of our optical and X-ray data is shown in the phase diagram of Figure 5.20 using the ephemeris proposed by Piirola et al. (2008) in BJD_{TDB}, which is given by $BJD_{TDB} = 2449681.464617 + 0.0063131476E$. The comparison of these data show that the maximum point of circular polarimetry is the minimum of the photometry in V band. The relationship between these sets of optical data is expected for polars, and is related to the cyclotron beaming effect.

Figure 5.20 - X-ray and optical light curves for V405 Aur folded on the optical ephemeris. From top to bottom, soft and hard X-ray data, photometry and circular polarimetry in V band.

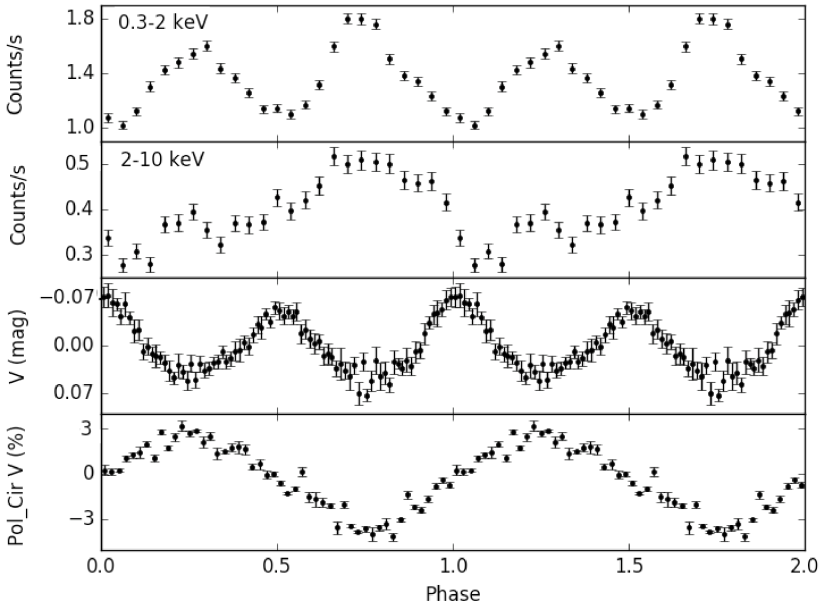

SOURCE: The author.

The sign of the circular polarization (positive and negative shown in Figure 5.20) suggested a configuration in which the magnetic field points to the observer in two columns of accretion (PIIROLA et al., 2008). The double-peaked profile from soft emission and the single-peaked in sawtooth modulation in hard emission is explained by the high dipole inclination, where the outer parts of the accretion curtains never cross the line-of-sight (EVANS; HELLIER, 2004). This can also be confirmed by the symmetry presented in the circular polarization curve.

The CYCLOPS code, initially written for polar modeling, does not have two threading regions. When we use two accretion regions for V405 Aur modeling as shown in Section 5.4.4, we consider two PSR from the same threading region (see top illustration in Figure 5.21). IPs can have different PSR threading regions. This is not taken into account by CYCLOPS. It could explain why we are not able to simultaneously model UBVRI optical data and X-ray light curve. Another threading region at 180° is one of the procedures that must be applied to the CYCLOPS code for modeling IPs, bottom in Figure 5.21. This can be verified if we find a good model using our all data set from the interval of 0 - 0.5 phase in order to model one PSR (discussed in model 8).

Figure 5.21 - Illustration of accretion geometry in IP showing one threading region currently used by CYCLOPS (top) and two threading regions which need to be implemented in the code (bottom).

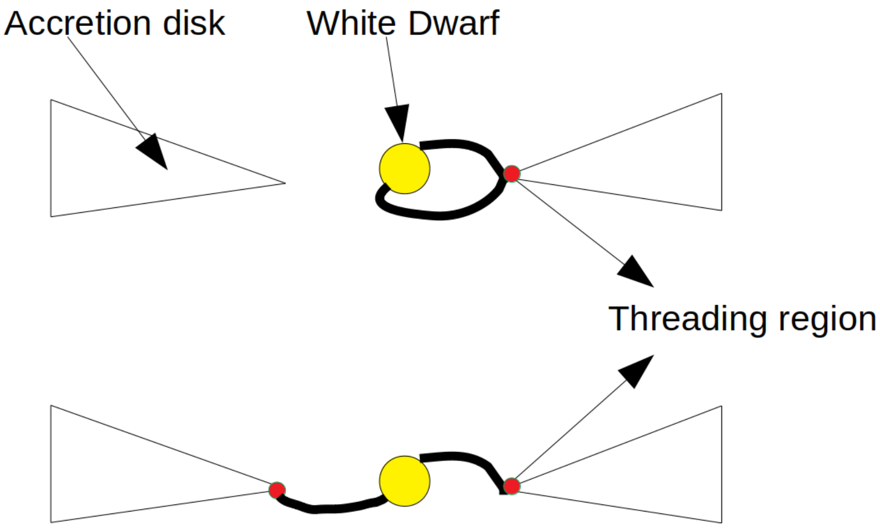

SOURCE: The author.

In order to improve the CYCLOPS code some new implementations must be performed. The second threading region is important to obtain the final modeling of V405 Aur. The future developments of CYCLOPS are described in Belloni et al. (2020), some of them are:

- the inclusion of line emission, one possibility is include APEC;
- inclusion of other radiative processes in CYCLOPS such as Compton scattering in order to fit the spectrum with energy above 10 keV, although it is expected to change the temperature and density profiles in the PSR only very slightly (SULEIMANOV et al., 2005).

We plan to simultaneously fit the X-ray light curves with optical data and X-ray absolute spectrum and light curve of V405 Aur. We expect to find a good model and figure out the best geometry which explains cyclotron and X-ray emissions. We also intend to model other IPs, in particular UU col, our second system with good features for modeling with the CYCLOPS code.

6 MAGNETIC ACCRETION IN SW SEXTANTIS STARS

This chapter briefly presents the main results of a search for magnetic accretion in SW Sextantis systems conducted by the author. The entire study is described in a paper (LIMA et al., 2021), which is reproduced in Appendix A. It was not possible to include the paper as a chapter in this thesis owing to INPE regulations.

6.1 Search for periodicities

SW Sex stars were originally identified due to a number of common enigmatic properties – most notably, single-peaked emission lines in high-inclination systems (see Section 1.2). Some of these characteristics indicate that part of the matter is out of the orbital plane, which is in line with a magnetically-channeled accretion (HOARD et al., 2003, e.g.). In this scenario, SW Sex is likely to be an IP with high mass-transfer rate. In this regard, some features of IPs must be present in SW Sex stars as well.

The polarized optical/infrared emission is the clearest sign of magnetic accretion. Polarization has been detected in only 15% of IPs, with amplitude levels ranging from 1 – 2% (see Table 4.1). These low polarization values probably result from the dilution of the PSR by the disk as well as the bright spot, and the secondary star. In comparison with IPs, we expect to find a small fraction of the SW Sex stars with detectable circular polarization.

The first confirmed system with non-null circular polarization is LS Peg. Rodríguez-Gil et al. (2001) found a modulation with an amplitude (peak-to-peak) of ∼0.3% and a periodicity of 29.6 ± 1.8 min using spectropolarimetric data. Prior to Lima et al. (2021), the number of definite SW Sex stars with circular polarimetry detected based on information presented in "The Big List of SW Sextantis Stars"[1] was five objects, however the observation of V533 Her is still uncertain (STOCKMAN et al., 1992). If we include AO Psc, usually classified as an IP, this number rises to six objects. Table 8 in Lima et al. (2021) shows a summary of circular polarization measurements.

As mentioned in Section 1.3, the power spectra of IPs are characterized by signals at the spin frequency, the orbital frequency, and the beat frequency in its power spectra. IPs can also present other periodicities such as QPOs with time scales of 1000 s, flaring emission lines, and superhumps, which present periods slightly

---

[1] D. W. Hoard's Big List of SW Sextantis Stars at `https://www.dwhoard.com/biglist`, see Hoard et al. (2003), which is updated until 2016.

longer or shorter than the orbital period, usually attributed to the precession of an eccentric accretion disk or disk warping (PATTERSON et al., 2002, e.g). Therefore, periodic signals can be interpreted as the rotation of a magnetic WD, originating from the cyclotron emission of the PSR.

In order to search for evidence of magnetic accretion in SW Sex class, we performed an observational campaign using the IAGPOL polarimeter to look for periodic variability of polarization and flux that can be associated with the rotation of the WD. Six objects were chosen: BO Cet, SW Sex, V442 Oph, V380 Oph, LS Peg, and UU Aqr (LIMA, 2016). We were also interested in discovering other periodicities such as beat periods that could indicate a sign of magnetic accretion as mentioned earlier.

6.2 Results

We performed the circular polarimetry of SW Sex stars observations at 1.6-m Perkin-Elmer telescope of the OPD–LNA coupled with the IAGPOL polarimeter (MAGALHÃES et al., 1996), which was equipped with a quarter-wave retarder plate and a Savart plate (RODRIGUES et al., 1998). We used the Lomb-Scargle (LS) periodogram (LOMB, 1976; SCARGLE, 1982) to construct the power spectra from photometric, circular and linear polarimetric in order to analyze our data. We scrambled the y-coordinates of the correspondent time series, without repetition for calculate the uncertainty of a signal detected with the LS periodogram. Then we injected a signal centered at the detected frequency, but randomly distributed around a few frequency resolution elements and with a random reference epoch between $0 - 2\pi$. We ran this simulation 1,000 times. For each realization, it was calculated the difference between injected and recovered periods. the false-alarm probability (FAP) levels of 1%, 0.1%, and 0.01%, calculated according to Scargle (1982). A more detailed description regarding the observations, data reduction, and literature of each object can be found in Lima et al. (2021). The following sections present some selected results.

6.2.1 BO Cet

Bo Cet was observed over seven nights during the 2010, 2016, and 2019 campaigns with mean magnitudes of 14.4 mag in R_C and 14.3 mag in V band with a decrease of 1 mag on October 11, 2010.

In photometric data, we found a significant period of 50.9 ± 0.5 min possibly associated with a continuum radiation source located in the inner disk region. Other periods found were 15.3 min and 19.7 min: the latter was previously reported by Rodríguez-Gil et al. (2007) from the radial velocities of the Hα line wings. In circular polarimetric data, we found a periodic signal at 11.1 ± 0.08 min (see top panel in Figure 6.1). The modulation in circular polarization (P_C) data is around 0.2% peak-to-peak (see the solid blue line in the third panel). Periods of 9 min and 14 min were also present in the circular polarimetric data and they are consistent with the positive and negative beats with the 50.9 min period. The presence of the beat periods between the main photometric and polarimetric peaks supports the reality of these periods. Therefore, we suggest that the WD spin period of BO Cet is 11.1 min, while 19 min could be related to the flaring emission line diluted by continuum emission.

6.2.2 SW Sex

We observed the prototype of the class, SW Sex, during a single night for 3.9 h covering one complete orbital cycle and one total eclipse. The magnitude in R_C was 14.66 mag with reduction of 1.6 mag during the eclipse. The system was in a high brightness state (GROOT et al., 2001).

The photometric power spectrum, after we removed the points associated with the eclipse and subtracted the orbital modulation, revealed a period at 22.6 ± 1.4 min above the 0.01% false-alarm probability (FAP) line as shown in in the left-hand column Figure 6.2. The periodogram of circular polarization showed a peak at 41.2 ± 8.5 min (see the right-hand column in Figure 6.2). The folded diagram shows a semi-amplitude of 0.2% in the circular polarimetric data (third panel) and the linear polarization shows a relatively well organized modulation (fourth panel). Considering the uncertainties, the photometric period is half that of the polarimetric one, therefore consistent with the first harmonic. We noted an increase in the polarization during the eclipse. It can be understood if part of the unpolarized component is occulted, this increases the circular polarization. Hence, this can support the presence of a magnetic WD rotating at around 41 min in SW Sex.

6.2.3 V442 Oph

V442 Oph was observed over two nights during 2014 in the R_C and V bands showing magnitudes of 13.37 mag and 13.60 mag, respectively. These values correspond to the high state of V442 Oph (PATTERSON et al., 2002).

Figure 6.1 - Circular polarimetry of BO Cet. The power spectrum is located on in the top panel, the magnitude, the percentage of circular polarization (P_C) and the percentage of linear polarization (P) folded diagrams with the period of 11 min are displayed in the second, third, and fourth panels. The dashed orange lines represent the FAP levels of 1%, 0.1%, and 0.01%. The blue lines correspond to a central-moving average considering the points inside an interval of 0.05 in phase.

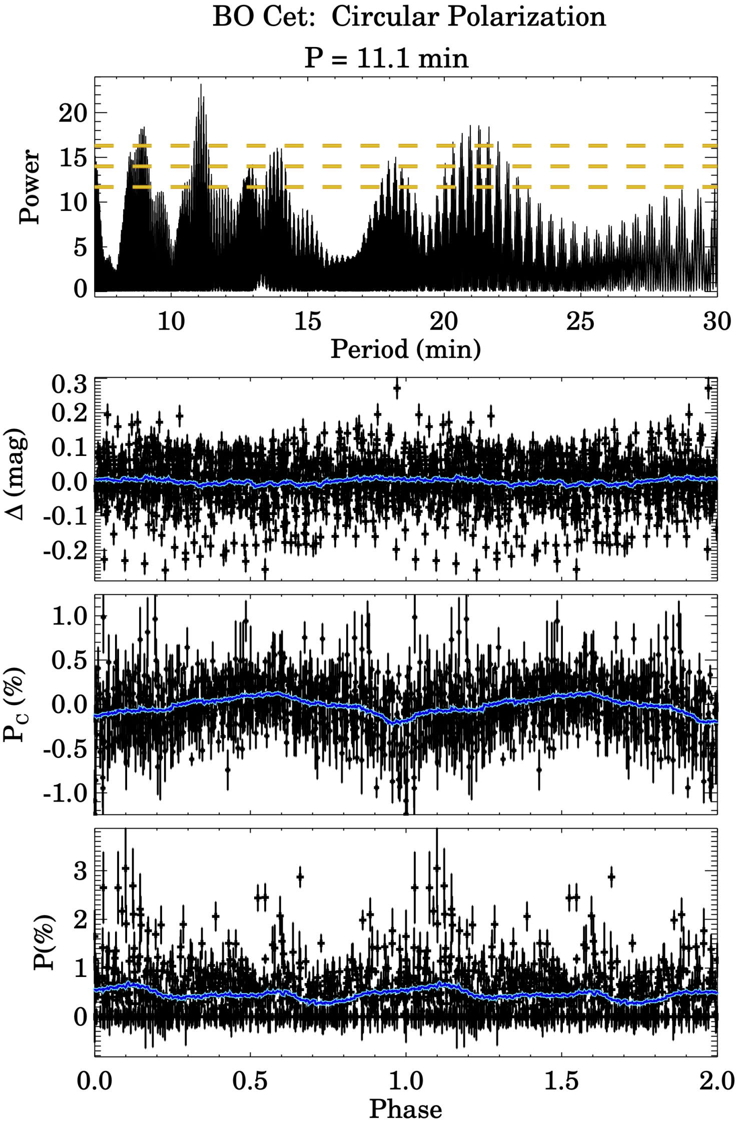

SOURCE: Lima et al. (2021).

Figure 6.2 - Photometry and circular polarimetry of SW Sex in the left and right-hand columns, respectively. The power spectra show a period at 22.6 min from photometric data and 41.2 min from polarimetric data. The phase diagrams folded at these periods in flux, P_C, and P are shown in the second, third, and fourth panels.

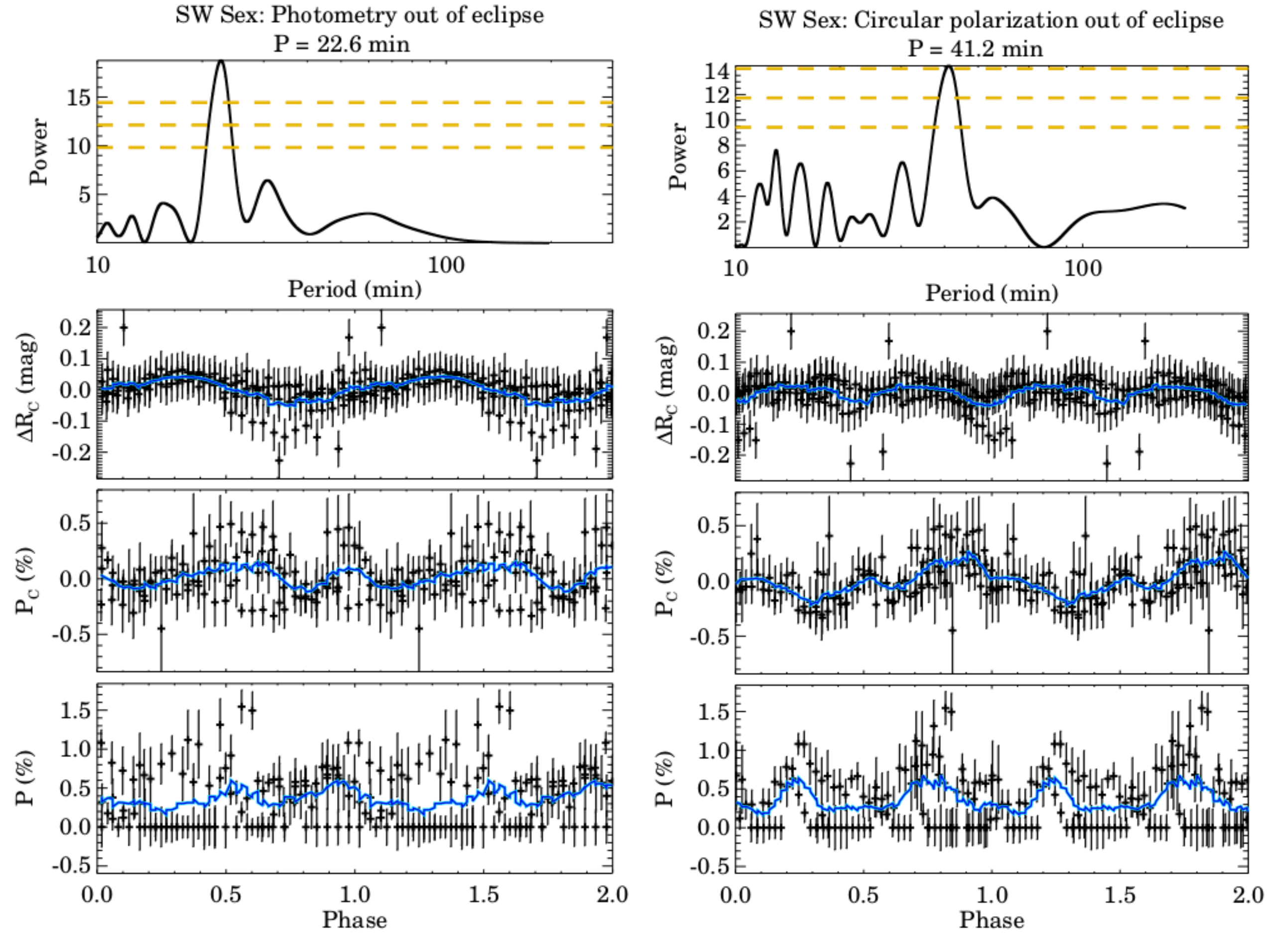

SOURCE: Lima et al. (2021).

From the photometric data we found a period of 12.4 ± 0.09 min prominent in the power spectrum and a second peak at 19.9 min with 0.1% false-alarm probability. The folded diagram at 12.4 min shows a sinusoidal photometry curve with a semi-amplitude around 0.04 mag and the circular polarimetry with slight modulation with an amplitude of around 0.1%. However, we could not explain this modulation as a beat between other periodicities of the system. The power spectra of the circular and linear polarization show peaks below the FAP lines of 0.1% at 19.4 ± 0.4 and 18.3 ± 1.1 min, respectively, as shown in Figure 6.3. A periodic variability in phase diagrams is not evident in any dataset from any data (second, third, and fourth panels). Although the 19 min period is not reliable in our observations, it was previously detected by Patterson et al. (2002). For this reason, we suggested that the 19.4 min modulation found in V442 Oph is due to the WD rotation. However, more observations are necessary to confirm this.

6.2.4 V380 Oph

We performed the observation of V380 Oph on a single night, 2014 July 19, in the V band with a magnitude of 14.5 mag for a total time span of ∼2.7 h. In addition, long photometric data obtained from SOS/SAS observatories during 2002 to 2016 were provided by Shugarov et al. (2016) in the B, V, and R_C bands.

The power spectra of the V and R_C bands from SOS/SAS did not show any clear signal in minutes, which is expected for WD spin period, only a timescale of days even after applying the CLEAN technique (ROBERTS et al., 1987). In the *B* band periodogram, a period around 55 min is found. However, the short time span of these observations, of around 2 h, makes it very uncertain. After removing the orbital modulation, a peak at 12.4 ± 0.66 min is also present in these data below a FAP of 1%. Interestingly, the circular and linear polarimetry curves folded at 12.4 min show a coherent modulation (see the left-hand column of Figure 6.4).

The OPD data shows a power spectrum from photometry with a peak at 47.4 ± 4.9 min imposed by the total time span of the observation. Coincidentally, ∼47 min was reported by Rodríguez-Gil et al. (2007) from flaring emission line. Circular polarimetry periodogram shows a peak at 22.0 ± 1.2 min with a level similar to the 0.1% FAP. After removing the orbital modulation a period of ∼12 min above the 0.01% FAP was found. These periods from polarimetry are not statistically significant, therefore more observational data are necessary.

Figure 6.3 - Circular and linear polarimetry of V442 Oph. The power spectra show periods at 19.4 min from circular and 18.3 min from linear polarimetry. The phase diagram folded at these periods in flux, P_C, and P are shown in the second, third, and fourth panels.

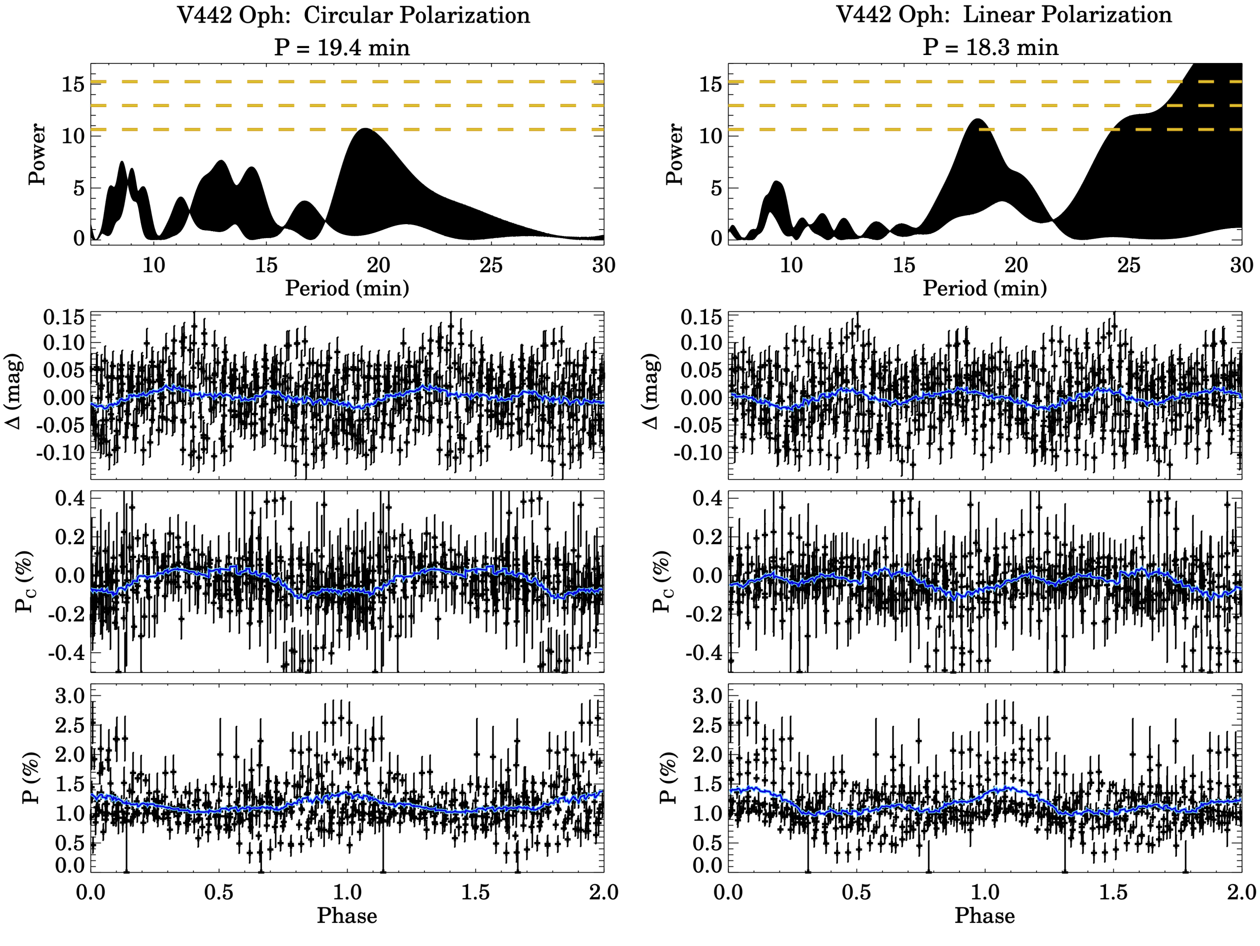

SOURCE: Lima et al. (2021).

Due to the complexity of the periodicities found, we did not conclude if this system presents a coherent period that could be associated with the WD spin rotation. We were not able to interpret the photometric 47 min period as a spin or beat period, but as it is also a flaring period, a phenomenon associated with IPs, it could be evidence of magnetic accretion. In addition, previous studies using UV spectrum point to an accretion disk truncated in its inner parts in an IP-like configuration (ZELLEM et al., 2009).

6.2.5 LS Peg

LS Peg was observed over 7 nights between 2010 and 2019 in the V and R_C bands showing mean magnitudes of 11.9 mag and 11.7 mag, respectively.

The time series analysis of LS Peg was very thorough: we obtained periodograms combining all observed bands, combining data by filters, and the individual nights. All these results are shown in Table 5 in Lima et al. (2021). The photometric power spectrum of LS Peg exhibits a peak at 21.0 ± 1.2 min when the mean magnitude from the photometric data set of each night was subtracted and the low-frequency modulations removed. The phase diagram folded at 21 min shows a sinusoidal variation with a semi-amplitude of 0.02 mag. However, the polarization curves did not show modulation. Other strong periods found in our photometry are 19 min and 16 min, which were also previously detected by Garnavich and Szkody (1992) and Szkody et al. (2001). The 21 min signal, within the uncertainties, was interpreted by us as the beat period between the WD spin period and the orbital period. From circular and linear polarimetric data, we found the periods of 18.8 ± 0.005 and 11.5 ± 0.1 min, respectively. The folded light curves at 18.8 min show the circular polarimetric data with positive and negative variations with semi-amplitudes of 0.05% (see the blue line in the third panel in Figure 6.5). However, the photometric and linear polarimetric data did not display a clear modulation (see first and fourth panels). The period of linear polarimetric data was half that of the circular. This could be interpreted as the reflection (scattering) of the PSR region emission in the inner regions of the disk. We interpreted the period of 18.8 min as WD spin period.

Figure 6.4 - Photometry of V380 Oph in the B and V bands from SOS/SAS and OPD observatories, respectively. The power spectra show periods at 12.4 min at B band and 47.4 min at V band. The phase diagram folded at these periods in flux, P_C, and P are shown in the second, third, and fourth panels.

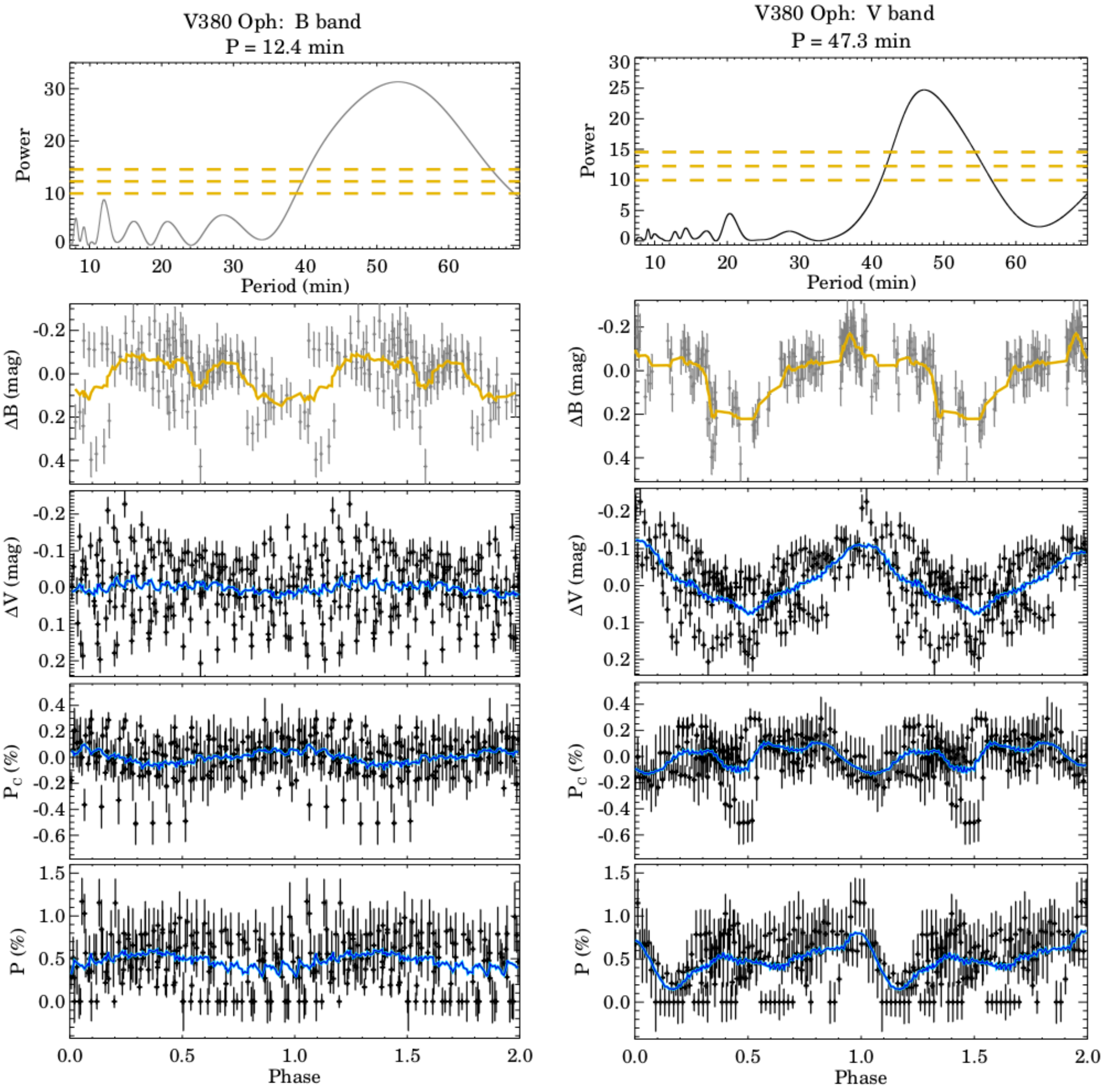

SOURCE: Lima et al. (2021).

Figure 6.5 - Circular polarimetry of LS Peg. The power spectrum is located in the top panel indicating the period at 18.8 min, folded diagram with this period of magnitude, P_C and P are shown in the second, third, and fourth panels.

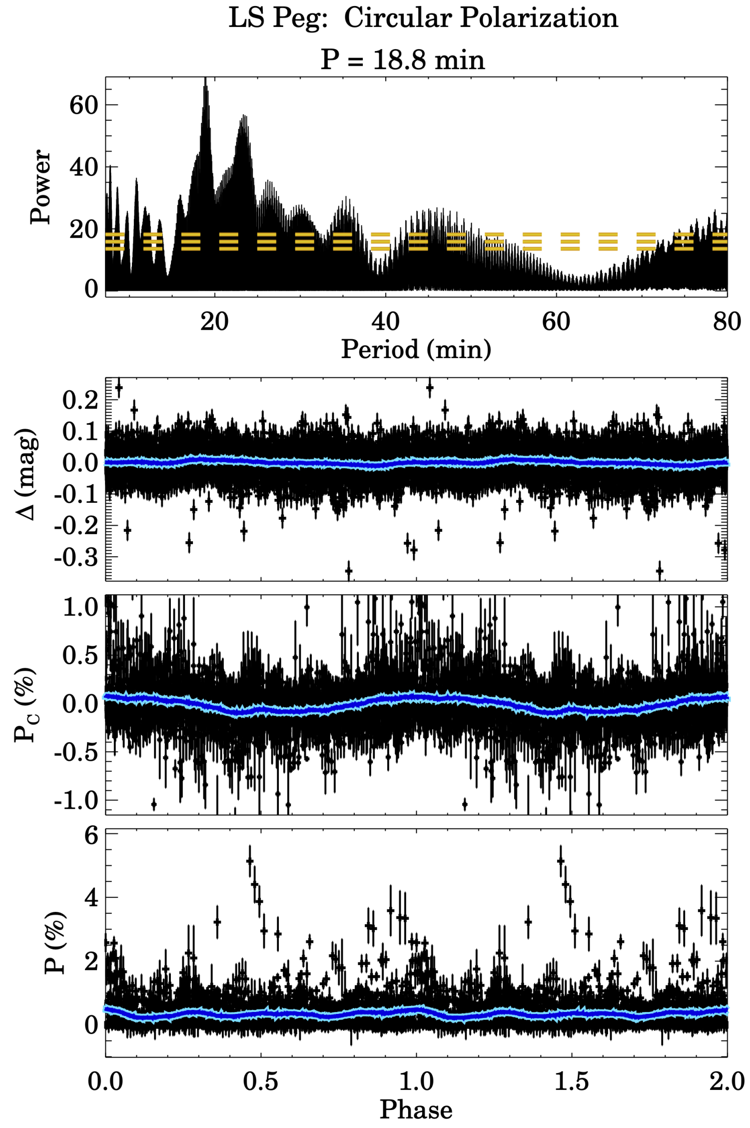

SOURCE: Lima et al. (2021).

6.2.6 UU Aqr

We observed UU Aqr in August and October 2009 over 5 nights in the V band showing a magnitude of ≈13 mag.

The photometry power spectrum shows a strong peak at 54.4 ± 0.5 min. The phase diagrams folded at this period display a sinusoidal pattern for the photometry with an amplitude of around 0.4 mag. The circular polarimetry periodogram exhibits a prominent peak at 25.7 ± 0.23 min (see Figure 6.6). The phase diagram of the circular polarimetric data shows a modulation with peak-to-peak amplitude of 0.1% (the blue line in the third panel). The ∼26 min is half the period of the photometry, which favored the interpretation of this polarimetric period as the spin period of a magnetic WD. In fact, Robertson et al. (2018) hitherto suggested that UU Aqr could have magnetic accretion.

6.3 Discussion

Our photometric and polarimetric data were used to search for evidence of magnetic accretion in a sample of six SW Sextantis stars: BO Cet, SW Sex, V442 Oph, V380 Oph, LS Peg, and UU Aqr. Assuming that periodicities found in circular polarization are related to the spin period of a magnetic WD, because the polarized flux came from cyclotron emission of the PSR region, our analysis revealed three objects with probable magnetic accretion: BO Cet presents spin period at 11.1 min, SW Sex at 41.2 min , and UU Aqr at 25.7 min. We also found two SW Sex stars with possible magnetic accretion: V442 Oph, whose tentative period of 19.4 min is below the FAP level of 1% as well as V380 Oph which shows an uncertain period at 22.0 min. We confirmed the detection of circular polarization in LS Peg, previously reported by Rodríguez-Gil et al. (2001). However, unlike these authors, we found a period of 18.8 min, which we assumed as the probable period of the WD rotation. Based on these results, we conclude that 15% (11/73) of SW Sex stars have direct evidence of magnetic accretion from circular polarimetric data. We also contributed to the number of objects whose circular polarization is uncertain, around 30% of the objects.

Figure 6.6 - Circular polarimetry of UU Aqr. The power spectrum is located on the top panel indicating the period at 25.7 min, folded diagram with this period of magnitude, P_C and P are showed in the second, third, and fourth panels.

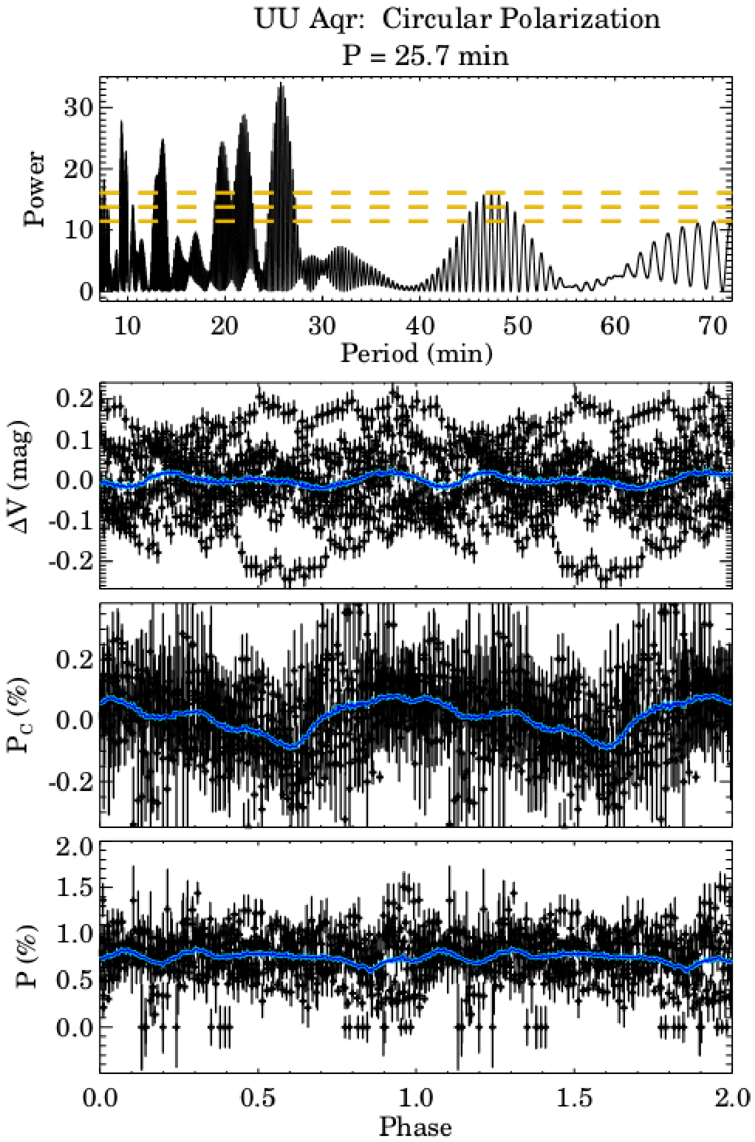

SOURCE: Lima et al. (2021).

We noticed that flaring modulation in the emission lines, usually present in some IPs and associated with the WD spin or the beat between the WD spin and the orbital period, seems to be twice the polarimetric period. In BO Cet, the flaring period proposed by Rodríguez-Gil et al. (2007) is approximately 20 min and we found a circular polarization period of 11 min. V380 Oph also presents a flaring period of ∼47 min found by Rodríguez-Gil et al. (2007), which is twice our value of 22 min, considering the error bar. It should be pointed out that both spectroscopic flaring periods are also present in our photometric data. In UU Aqr, no flaring was reported in the literature, but we found this same relationship between the photometric and polarimetric periods.

Another point we highlighted is the relationship between the inclination and the circular polarization. We verified that 73% of 11 SW Sex stars with possible circular polarization are non-eclipsing systems. If we considered only the objects with confirmed detection, ∼57% (4/7) are non-eclipsing. The disk from high-inclination systems could be the responsible for obstructing the PSR emission, and consequently resulting in undetectable circular polarization.

As mentioned in Section 1.1.3, SW Sex stars occupy a specific position in the diagram of the number distribution of objects by orbital period, which is between 3 to 4.5 hr, immediately before the orbital period gap in terms of CVs time evolution. Therefore, SW Sex systems deserve special attention to understand the evolution of CVs, in particular the magnetic ones. Indeed, Pala et al. (2020) found that 36% of the CVs in a volume-limited sample from GAIA host a magnetic WD. This fraction is numerically consistent with SW Sex stars forming the magnetic portion of the nova-like CVs. In this context, a theory for the evolution of CVs should also explain the formation of all magnetic CVs including the SW Sex systems clustered just above the orbital period gap (BELLONI et al., 2021).

6.3.1 BO Cet: an SW Sex star?

In this section, I will present the discussion concerning the nature of BO Cet recently proposed by Kato et al. (2021). The authors suggest that BO Cet is not a nova-like SW Sex type, but a unique dwarf novae member with properties of SU UMa-type and IW And-type. The features of IW And class are: (i) brightening during the final of (quasi-)standstills; (ii) typical recurrence time of ∼30 – 100 d; (iii) deep dips are sometimes seen following brightening.

The observations of Kato et al. (2021) occurred over eight nights between June 2020 and March 2021. BO Cet was in a bright state with g = 13.6 mag and accompanied by superhumps and superoutbursts. These types of behavior are not expected for a SW Sex star. Kato et al. (2021) did not find our periods of 11.1 min or 19.7 min, which is not surprising, because the system was brighter by around 0.6 mag in their observations and the bright disk can dilute the cyclotron emission. Although the authors consider our results as QPOs, the stability of the period from circular polarimetry observations during 2010 and 2016 is a good argument maintaining BO Cet as a magnetic WD. This discussion is important for the development of CV comprehension, and it shows that there is a lot to be learned about these objects. In particular, more time series concerning BO Cet would be very useful in order to confirm its real nature.

7 CONCLUSIONS AND PERSPECTIVES

In this PhD thesis, we applied for the first time the CYCLOPS code to model the structure of an IP. This code was previously used only for polars. We selected V405 Aur, which is considered the IP with the highest magnetic field, as our first attempt. UU Col is also another good candidate. Both candidates have previous studies proposing non-successful geometries that simultaneously explains the optical and X-ray emissions. In this context, we tried to model V405 Aur using X-ray spectrum and light curve data and photometric and circular polarimetric light curves at UBVRI bands using a new version of the CYCLOPS code that solves the shock structure and provides a more realistic approach.

We performed the modeling in parts using X-ray and optical data separately and looked for parameters that could be fixed and that belonged to a same model family. From X-ray data, we noted that it is possible to break the degeneracy problem by fitting absolute spectrum together with the light curve as mentioned in Belloni et al. (2021). We also determined a mass accretion rate interval in the range of 10^{-9} – 10^{-10} $M_{\odot}$ year^{-1}, which is consistent with the results obtained by Suleimanov et al. (2005) and Suleimanov et al. (2019). The modeling of optical data proved to be very complex. We only found a good model using photometry and circular polarimetry for one band. When we tested other bands in order to obtain simultaneous UBVRI bands results and included X-ray data, we were not able to find a good model despite using one and two accretion columns originating from the same threading region. That shows that IPs have a very complex accretion geometry. A possible solution is to have different threading regions for different PSRs. To solve this problem, we recently realized that the accretion of V405 Aur may be different for the two poles. CYCLOPS currently only considers one threading region, which is consistent with polars, perhaps this might not be correct in the case of IPs. In this sense, we propose a new implementation in the code of a second threading region. After this, we expect to unveil the magnetic accretion geometry of V405 Aur and in the future apply the CYCLOPS code to UU Col as well.

In Lima et al. (2021), we searched for direct evidence of magnetic accretion in definitive members of SW Sex type: BO Cet, SW Sex, V442 Oph, V380 Oph, LS Peg, and UU Aqr. If SW Sex stars have IP behavior, multi-periodicity may be a typical feature of these systems as the WD spins asynchronously with the orbital period. Therefore, we looked for periodic signals from photometric and polarimetric data, which could be related to WD spin period. Polarized cyclotron emission is a distinguishing signal of magnetic accretion. Hence, emission processes that involve simultaneous regions with different rotations can be observed to vary with the beat period. The emission processes related solely to the WD must have a coherent and stable variability.

The results of this study identified 15% of SW Sex stars with some evidence of non-null circular polarization of 73 systems classified as definite, possible, and probable SW Sex stars (HOARD et al., 2003). If we consider only the definite SW Sex members, we obtain 33% (10/30) of possible polarized objects. From the circular polarimetric data, we found a period of 41.2 min at SW Sex, the prototype of the class, 11.1 min at BO Cet, 25.7 min at UU Aqr. Also, we found 22 min at V380 Oph and 19.4 min at V442 Oph, although they are below the FAP level of 1%. LS Peg, also one of our targets, is the first SW Sex star with circular polarization detected with a period associated to WD rotation at ∼29 min by Rodríguez-Gil et al. (2001). However, we found a period of 18.8 min, which we consider to be the true spin period. We are aware that additional polarimetric observations which have a longer time span would be useful to confirm these results and an increase in the sample is needed. In this context, we performed observations with other SW Sex stars, such as AO Psc and VZ Scl, the data analysis is in progress.

In addition to the study of SW Sex stars and IPs (described in Caps. 5 and 6), we have also participated in efforts to discover new CVs and MCVs. In Oliveira et al. (2020), we performed an exploratory search for MCVs in the CRTS survey followed by spectroscopic snapshot observations, which yielded a discovery of one intermediate polar and seven polars. Two polars were observed in a low accretion state, revealing photospheric features of the secondary star thereby allowing the estimation of their spectral type. In Szkody et al. (2020), we also found CV candidates using the ZTF survey. Our results indicate 207 systems with variability behavior similar to CVs of which 30 are possibly CVs and one system is likely to be an intermediate polar.

REFERENCES

AIZU, K. X-ray emission region of a white dwarf with accretion. **Progress of Theoretical Physics**, v. 49, p. 1184–1194, 1973. 14, 16, 18, 39

ALLAN, A.; HORNE, K.; HELLIER, C.; MUKAI, K.; BARWIG, H.; BENNIE, P. J.; HILDITCH, R. W. The spin period of the intermediate polar RX J0558+53. **Monthly Notices of the Royal Astronomical Society**, v. 279, n. 4, p. 1345–1348, 1996. 61, 62, 77

ANZOLIN, G.; MARTINO, D. de; BONNET-BIDAUD, J.-M.; MOUCHET, M.; GÄNSICKE, B. T.; MATT, G.; MUKAI, K. Two new intermediate polars with a soft x-ray component. **Astronomy and Astrophysics**, v. 489, p. 1243–1254, 2008. 19

ARNAUD, K.; SMITH, R.; SIEMIGINOWSKA, A. **Handbook of X-ray astronomy**. United Kingdom: Cambridge University Press, 2011. 48

ARNAUD, K. A. XSPEC: The first ten years. In: JACOBY, G. H.; BARNES, J. (Ed.). **Astronomical data analysis software and systems V**. [S.l.: s.n.], 1996. (Astronomical Society of the Pacific Conference Series, v. 101), p. 17. 47, 48, 49

BAILER-JONES, C. A. L.; RYBIZKI, J.; FOUESNEAU, M.; DEMLEITNER, M.; ANDRAE, R. Estimating distances from parallaxes. V. Geometric and photogeometric distances to 1.47 billion stars in Gaia early data release 3. **The Astronomical Journal**, v. 161, n. 3, p. 147, mar. 2021. 57, 69

BALBUS, S. A.; HAWLEY, J. F. A powerful local shear instability in weakly magnetized disks. I - linear analysis. II - nonlinear evolution. **Astrophysical Journal**, v. 376, p. 214–233, 1991. 6

BARLOW, E. J.; KNIGGE, C.; BIRD, A. J.; DEAN, A. J.; CLARK, D. J.; HILL, A. B.; MOLINA, M.; SGUERA, V. 20-100 keV properties of cataclysmic variables detected in the INTEGRAL/IBIS survey. **Monthly Notices of the Royal Astronomical Society**, v. 372, n. 1, p. 224–232, out. 2006. 11

BAUMGARTNER, W. H.; TUELLER, J.; MARKWARDT, C. B.; SKINNER, G. K.; BARTHELMY, S.; MUSHOTZKY, R. F.; EVANS, P. A.; GEHRELS, N. The 70 month Swift-BAT all-sky hard X-ray survey. **The Astrophysical Journal Supplement Series**, v. 207, n. 2, p. 19, ago. 2013. 11

BEARDMORE, A. P.; OSBORNE, J. P.; HELLIER, C. The multi-temperature x-ray spectrum of the intermediate polar V1223 Sagittarii. **Monthly Notices of the Royal Astronomical Society**, v. 315, p. 307–315, 2000. 18

BELLONI, D.; RODRIGUES, C. V.; SCHREIBER, M. R.; CASTRO, M.; COSTA, J. E. R.; HAYASHI, T.; LIMA, I. J.; LUNA, G. J. M.; MARTINS, M.; OLIVEIRA, A. S.; PARSONS, S. G.; SILVA, K. M. G.; STECCHINI, P. E.; STUCHI, T. J.; ZOROTOVIC, M. Breaking the degeneracy in magnetic cataclysmic variable X-ray spectral modeling using X-ray light curves. **The Astrophysical Journal Supplement Series**, v. 256, n. 2, p. 45, out. 2021. 12, 13, 17, 18, 19, 25, 39, 44, 50, 52, 53, 78, 93, 113

BELLONI, D.; SCHREIBER, M. R.; PALA, A. F.; GÄNSICKE, B. T.; ZOROTOVIC, M.; RODRIGUES, C. V. Evidence for reduced magnetic braking in polars from binary population models. **Monthly Notices of the Royal Astronomical Society**, v. 491, n. 4, p. 5717–5731, fev. 2020. 11, 82, 84, 96

BELLONI, D.; SCHREIBER, M. R.; SALARIS, M.; MACCARONE, T. J.; ZOROTOVIC, M. Magnetic dynamos in white dwarfs - I. explaining the dearth of bright intermediate polars in globular clusters. **Monthly Notices of the Royal Astronomical Society**, v. 505, n. 1, p. L74–L78, jul. 2021. 111

BESSELL, M. S. UBVRI photometry. II - the cousins VRI system, its temperature and absolute flux calibration, and relevance for two-dimensional photometry. **Astronomical Society of the Pacific**, v. 91, p. 589–607, 1979. 68

BEUERMANN, K. Magnetic cataclysmic variables: the state of the art after ROSAT. In: ASCHENBACH, B.; FREYBERG, M. J. (Ed.). **Highlights in X-ray astronomy**. [S.l.: s.n.], 1999. v. 272, p. 410. 11

BLOEMEN, S.; MARSH, T. R.; STEEGHS, D.; ØSTENSEN, R. H. Spin-resolved spectroscopy of the intermediate polar DQ Her. **Monthly Notices of the Royal Astronomical Society**, v. 407, n. 3, p. 1903–1912, set. 2010. 11

BRYANS, P.; LANDI, E.; SAVIN, D. W. A new approach to analyzing solar coronal spectra and updated collisional ionization equilibrium calculations. II. updated ionization rate coefficients. **The Astrophysical Journal**, v. 691, n. 2, p. 1540–1559, fev. 2009. 54

BUAT-MÉNARD, V.; HAMEURY, J. M.; LASOTA, J. P. The nature of dwarf nova outbursts. **Astronomy & Astrophysics**, v. 366, p. 612–622, fev. 2001. 2

BURWITZ, V.; REINSCH, K.; BEUERMANN, K.; THOMAS, H.-C. X-ray and optical observations of a new x-ray soft intermediate polar: RX J0512.2-3241. In: SCHIELICKE, R. E. (Ed.). **Astronomische gesellschaft abstract series**. [S.l.: s.n.], 1996. (Astronomische gesellschaft abstract series, v. 12), p. 188. 58

BUTTERS, O. W.; NORTON, A. J.; MUKAI, K.; BARLOW, E. J. RXTE confirmation of the intermediate polar status of IGR J15094-6649. **Astronomy and Astrophysics**, v. 498, p. L17–L19, 2009. 14

BUTTERS, O. W.; NORTON, A. J.; MUKAI, K.; TOMSICK, J. A. RXTE and XMM observations of intermediate polar candidates. **Astronomy and Astrophysics**, v. 526, p. A77, 2011. 19

CANALLE, J. B. G.; SAXTON, C. J.; WU, K.; CROPPER, M.; RAMSAY, G. Accretion in dipole magnetic fields: flow structure and x-ray emission of accreting white dwarfs. **Astronomy and Astrophysics**, v. 440, p. 185–198, 2005. 16, 18, 38

CARDELLI, J. A.; CLAYTON, G. C.; MATHIS, J. S. The relationship between infrared, optical, and ultraviolet extinction. **Astronomy and Astrophysics**, v. 345, p. 245–256, 1989. 34, 35

CASARES, J.; MARTINEZ-PAIS, I. G.; MARSH, T. R.; CHARLES, P. A.; LAZARO, C. V795 Her: an SW Sex star in the period gap? **Monthly Notices of the Royal Astronomical Society**, v. 278, n. 1, p. 219–235, jan. 1996. 8

CHARBONNEAU, P. Genetic algorithms in astronomy and astrophysics. **Astrophysical Journal Supplement**, v. 101, p. 309, 1995. 31

COSTA, J. E. R.; RODRIGUES, C. V. Stokes imaging of AM Her systems using 3D inhomogeneous models - I. description of the code and an application to V834 Cen. **Monthly Notices of the Royal Astronomical Society**, v. 398, p. 240–248, 2009. 25, 26, 28, 45

CROPPER, M. The polars. **Space Science Reviews**, v. 54, p. 195, 1990. 3, 42

CROPPER, M.; WU, K.; RAMSAY, G. Continuum and line emission from post-shock flows. In: HELLIER, C.; MUKAI, K. (Ed.). **Annapolis workshop on magnetic cataclysmic variables**. [S.l.: s.n.], 1999. (Astronomical Society of the Pacific Conference Series, v. 157), p. 325. 15, 18

CUMMING, A. Magnetic field evolution in accreting white dwarfs. **Astronomical Society of the Pacific Conference Series**, v. 315, p. 58, 2004. 14

DHILLON, V. S.; SMITH, D. A.; MARSH, T. R. The SW Sex enigma. **Monthly Notices of the Royal Astronomical Society**, v. 428, n. 4, p. 3559–3568, fev. 2013. 8

DONE, C.; MAGDZIARZ, P. Complex absorption and reflection of a multitemperature cyclotron-bremsstrahlung X-ray cooling shock in BY Cam. **Monthly Notices of the Royal Astronomical Society**, v. 298, p. 737, 1998. 20

DORMAN, B.; ARNAUD, K. A. Redesign and Reimplementation of XSPEC. In: HARNDEN F. R., J.; PRIMINI, F. A.; PAYNE, H. E. (Ed.). **Astronomical Data Analysis Software and Systems X**. [S.l.: s.n.], 2001. (Astronomical Society of the Pacific Conference Series, v. 238), p. 415. 47, 48

ESA, E. S. A. 2021. (Available from: `https://www.cosmos.esa.int/web/xmm-newton/sas-threads`). 73

EVANS, P. A.; HELLIER, C. Why does the intermediate polar V405 Aurigae show a double-peaked spin pulse? **Monthly Notices of the Royal Astronomical Society**, v. 353, p. 447–452, 2004. xvi, 61, 62, 63, 64, 67, 72, 74, 75, 77, 80, 85, 93, 95

______. Why do some intermediate polars show soft X-ray emission? A survey of XMM-Newton spectra. **The Astrophysical Journal**, v. 663, p. 1277–1284, 2007. 12, 58, 60

EZUKA, H.; ISHIDA, M. Iron line diagnostics of the postshock hot plasma in magnetic cataclysmic variables observed with ASCA. **The Astrophysical Journal Supplement Series**, v. 120, p. 277–298, 1999. 16, 20

______. Iron line diagnostics of the postshock hot plasma in magneticcataclysmic variables observed with asca. **The Astrophysical Journal Supplement Series**, v. 120, p. 277, 1999. 17

FABIAN, A. C.; PRINGLE, J. E.; REES, M. J. X-ray emission from accretion on to white dwarfs. **Monthly Notices of the Royal Astronomical Society**, v. 175, p. 43–60, abr. 1976. 39

FERRARIO, L.; MARTINO, D. de; GANSICKE, B. T. Magnetic white dwarfs. **Space Science Reviews**, v. 191, p. 111–169, 2015. 11, 14

FRANK, J.; KING, A.; RAINE, D. J. **Accretion power in astrophysics**. United Kingdom: Cambridge Astrophysics Series, 2002. 2, 3, 4, 6

GARNAVICH, P. M.; SZKODY, P. The unusual cataclysmic variable S193. **Journal of the American Association of Variable Star Observers (JAAVSO)**, v. 21, p. 81–85, out. 1992. 106

GROOT, P. J.; RUTTEN, R. G. M.; PARADIJS, J. van. SW Sextantis in an excited, low state. **Astronomy & Astrophysics**, v. 368, p. 183–196, mar. 2001. 101

HABERL, F.; THROSTENSEN, J. R.; MOTCH, C.; SCHWARZENBERG-CZERNY, A.; PAKULL, M.; SHAMBROOK, A.; PIETSCH, W. Discovery of the new intermediate polar RX J0558.0+5353. **Astronomy and Astrophysics**, v. 291, p. 171–180, 1994. 61

HAYASHI, T.; ISHIDA, M. A new comprehensive X-ray spectral model from the post-shock accretion column in intermediate polars. **Monthly Notices of the Royal Astronomical Society**, v. 438, n. 3, p. 2267–2277, mar. 2014. 17, 18, 38, 42, 93

_____. Application of the new comprehensive X-ray spectral model to the two brightest intermediate polars EX Hydrae and V1223 Sagittarii. **Monthly Notices of the Royal Astronomical Society**, v. 438, p. 3718, 2014. 39

HELLIER, C. Disc-overflow accretion in the intermediate polar FO Aquarii. **Monthly Notices of the Royal Astronomical Society**, v. 265, p. L35–L39, 1993. 11

_____. V1315 Aquilae and the nature of SW Sextantis Stars. **The Astrophysical Journal**, v. 471, p. 949, nov. 1996. 8

_____. Recent results on intermediate polars. **Astronomical Society of the Pacific Conference Series**, v. 157, p. 1, 1999. 12, 19

_____. **Cataclysmic variable stars**: how and why they vary? United Kingdom: UK: Springer, 2001. 1, 5, 6, 10, 11

_____. The magnetospheric boundary in cataclysmic variables. In: BOZZO, E.; KRETSCHMAR, P.; AUDARD, M.; FALANGA, M.; FERRIGNO, C. (Ed.). **European Physical Journal Web of Conferences**. [S.l.: s.n.], 2014. (EPJ Web of Conferences, v. 64). 3

HELLIER, C.; BEARDMORE, A. P. The accretion flow in the discless intermediate polar V2400 Ophiuchi. **Monthly Notices of the Royal Astronomical Society**, v. 331, n. 2, p. 407–416, mar. 2002. 12

HERDER, J. W. den; BRINKMAN, A. C.; KAHN, S. M.; BRANDUARDI-RAYMONT, G.; THOMSEN, K.; AARTS, H.; AUDARD, M.; BIXLER, J. V.; BOGGENDE, A. J. den; COTTAM, J.; DECKER, T.; DUBBELDAM, L.; ERD, C.; GOULOOZE, H.; GÜDEL, M.; GUTTRIDGE, P.; HAILEY, C. J.; JANABI, K. A.; KAASTRA, J. S.; KORTE, P. A. J. de; LEEUWEN, B. J. van; MAUCHE, C.; MCCALDEN, A. J.; MEWE, R.; NABER, A.; PAERELS, F. B.; PETERSON, J. R.; RASMUSSEN, A. P.; REES, K.; SAKELLIOU, I.; SAKO, M.; SPODEK, J.; STERN, M.; TAMURA, T.; TANDY, J.; VRIES, C. P. de; WELCH, S.; ZEHNDER, A. The reflection grating spectrometer on board XMM-Newton. **Astronomy & Astrophysics**, v. 365, p. L7–L17, jan. 2001. 70

HILL, C. A.; WATSON, C. A.; STEEGHS, D.; DHILLON, V. S.; SHAHBAZ, T. Roche tomography of cataclysmic variables - VII. the long-term magnetic activity of AE Aqr. **Monthly Notices of the Royal Astronomical Society**, v. 459, n. 2, p. 1858–1874, jun. 2016. 14

HOARD, D. W.; SZKODY, P.; FRONING, C. S.; LONG, K. S.; KNIGGE, C. Observations of the SW Sextantis star DW Ursae Majoris with the far ultraviolet spectroscopic explorer. **The Astronomical Journal**, v. 126, p. 2473–2486, nov. 2003. 7, 8, 99, 114

HOFFMAN, J.; DRAINE, B. T. Accurate modeling of X-ray extinction by interstellar grains. **The Astrophysical Journal**, v. 817, p. 139, 2016. 34

HONEYCUTT, R. K.; SCHLEGEL, E. M.; KAITCHUCK, R. H. Evidence for a bipolar wind in the cataclysmic variable PG 1012-029. **The Astrophysical Journal**, v. 302, p. 388–402, mar. 1986. 8

ISHIDA, T.; TAKEUTI, M. Shock phenomena in a hydrodynamic model of a classical cepheid. **Publications of the Astronomical Society of Japan** , v. 43, p. 795–807, dez. 1991. 13, 16

ITOH, N.; SAKAMOTO, T.; KUSANO, S.; NOZAWA, S.; KOHYAMA, Y. Relativistic thermal bremsstrahlung Gaunt factor for the intracluster plasma. II. analytic fitting formulae. **The Astrophysical Journal Supplement Series**, v. 128, n. 1, p. 125–138, maio 2000. 54, 55

JANSEN, F.; LUMB, D.; ALTIERI, B.; CLAVEL, J.; EHLE, M.; ERD, C.; GABRIEL, C.; GUAINAZZI, M.; GONDOIN, P.; MUCH, R.; MUNOZ, R.; SANTOS, M.; SCHARTEL, N.; TEXIER, D.; VACANTI, G. XMM-Newton observatory. I. the spacecraft and operations. **Astronomy and Astrophysics**, v. 365, p. L1–L6, 2001. 70

KAASTRA, J. S. **An X-ray spectral code for optically thin plasmas**. United Kingdom: Internal SRON-Leiden Report, Updated Version 2.0, 1992. 48, 74

KARZAS, W. J.; LATTER, R. Electron radiative transitions in a Coulomb field. **The Astrophysical Journal Supplement Series**, v. 6, p. 167, maio 1961. 50

KASHYAP, V.; DRAKE, J. J. PINTofALE: package for the interactive analysis of line emission. **Bulletin of the Astronomical Society of India**, v. 28, p. 475–476, jun. 2000. 27, 34, 53

KATAJAINEN, S.; BUTTERS, O.; NORTON, A. J.; LEHTO, H. J.; PIIROLA, V.; BERDYUGIN, A. Discovery of polarized emission from two soft X-ray-emitting intermediate polars: UU Col and NY Lup. **The Astrophysical Journal**, v. 724, p. 165–170, 2010. 60

KATO, T.; TAMPO, Y.; KOJIGUCHI, N.; SHIBATA, M.; ITO, J.; ISOGAI, K.; ITOH, H.; HAMBSCH, F.-J.; MONARD, B.; KIYOTA, S.; VANMUNSTER, T.; SOSNOVSKIJ, A. A.; PAVLENKO, E. P.; DUBOVSKY, P. A.; KUDZEJ, I.; MEDULKA, T. BO Ceti: Dwarf nova showing both IW And-type and SU UMa-Type features. **Publications of the Astronomical Society of Japan** , jul. 2021. 111, 112

KELLOGG, E.; BALDWIN, J. R.; KOCH, D. Studies of cluster X-ray sources. energy spectra for the Perseus, Virgo, and Coma clusters. **The Astrophysical Journal**, v. 199, p. 299–306, jul. 1975. 50

KENNEDY, M. R.; GARNAVICH, P. M.; LITTLEFIELD, C.; CALLANAN, P.; MUKAI, K.; AADLAND, E.; KOTZE, M. M.; KOTZE, E. J. X-ray observations of FO Aqr during the 2016 low state. **Monthly Notices of the Royal Astronomical Society**, v. 469, n. 1, p. 956–967, jul. 2017. 14

KIM, Y.; BEUERMANN, K. Spin-modulated radiation of intermediate polars. I. X-ray spectrum and light curves. **Astronomy and Astrophysics**, v. 298, p. 165, 1995. 61

KING, A. R.; LASOTA, J. P. Accretion on to highly magnetized white dwarfs. **Monthly Notices of the Royal Astronomical Society**, v. 188, p. 653, 1979. 14, 39

KING, A. R.; LASOTA, J.-P. Spin evolution and magnetic fields in cataclysmic variables. **Astrophysical Journal**, v. 378, p. 674–681, 1991. 5

KNIGGE, C.; BARAFFE, I.; PATTERSON, J. Evolution of cataclysmic variables as revealed by their donor stars. **The Astrophysical Journal Supplement**, v. 194, p. 48, 2011. 6

LAMB, D. Q. DQ Herculis - weak sister to HZ Herculis. **The Astronomical Journal**, v. 192, p. L129–L133, 1974. 10

LAMB, D. Q.; MASTERS, A. R. X and UV radiation from accreting magnetic degenerate dwarfs. **Astrophysical Journal**, v. 234, p. L117, 1979. 2, 14, 39

LARSON, K. A.; WHITTET, D. C. B. Reddening and the extinction law at high galactic latitude. **The Astrophysical Journal**, v. 623, p. 897–910, 2005. 33

LIEDAHL, D. A.; OSTERHELD, A. L.; GOLDSTEIN, W. H. New calculations of Fe L-shell X-ray spectra in high-temperature plasmas. **Astrophysical Journal, Part 2 - Letters**, v. 438, n. 2, p. L115–L118, 1995. 48, 74

LIMA, I. J. **Busca por acreção magnética em objetos do tipo SW Sextantis**. Tese (Doutorado) — em Astrofísica. Instituto Nacional de Pesquisas Espaciais, São José dos Campos, 2016. Disponível em: <`http://www.inpe.br/posgraduacao/ast/arquivos/dissertacoes/dissertacao_isabel_jesus_2016.pdf,pages={135p},`>. 100

LIMA, I. J.; RODRIGUES, C. V.; LOPES, C. E. F.; SZKODY, P.; JABLONSKI, F. J.; OLIVEIRA, A. S.; SILVA, K. M. G.; BELLONI, D.; PALHARES, M. S.; SHUGAROV, S.; BAPTISTA, R.; ALMEIDA, L. A. Search for magnetic accretion in SW Sextantis systems. **The Astronomical Journal**, v. 161, n. 5, p. 225, maio 2021. 22, 99, 100, 102, 103, 105, 106, 107, 108, 110, 113

LOMB, N. R. Least-squares frequency analysis of unequally spaced data. **Astrophysics & Space Science**, v. 39, p. 447–462, fev. 1976. 100

LUNA, G. J. M.; RAYMOND, J. C.; BRICKHOUSE N. S.AND MAUCHE, C. W.; SULEIMANOV, V. Testing the cooling flow model in the intermediate polar EX Hydrae. **Astronomy and Astrophysics**, v. 578, p. 15L, 2015. 12, 18

LUTOVINOV, A.; SULEIMANOV, V.; LUNA, G. J. M.; SAZONOV, S.; MARTINO, D. de; DUCCI, L.; DOROSHENKO, V.; FALANGA, M. INTEGRAL view on cataclysmic variables and symbiotic binaries. , v. 91, p. 101547, dez. 2020. 11

MAGALHÃES, A. M.; RODRIGUES, C. V.; MARGONINER, V. E.; PEREYRA, A.; HEATHCOTE, S. High precision ccd imaging polarimetry. In: ROBERGE, W. G.; WHITTET, D. C. B. (Ed.). **Polarimetry of the interstellar medium**. [S.l.: s.n.], 1996. (Astronomical Society of the Pacific Conference Series, v. 97), p. 17. 100

MARSH, T. R.; DUCK, S. R. Stroboscopic Doppler tomography of FO Aqr. **New Astronomy**, v. 1, n. 2, p. 97–119, out. 1996. 11

MARTINO, D. de; MATT, G.; MUKAI, K.; BONNET-BIDAUD, J.-M.; BURWITZ, V.; GÄNSICKE, B. T.; HABERL, F.; MOUCHET, M. The X-ray properties of the magnetic cataclysmic variable UU Columbae. **Astronomy and Astrophysics**, v. 454, p. 287–294, 2006. 58, 59

MASON, K. O.; BREEVELD, A.; MUCH, R.; CARTER, M.; CORDOVA, F. A.; CROPPER, M. S.; FORDHAM, J.; HUCKLE, H.; HO, C.; KAWAKAMI, H.; KENNEA, J.; KENNEDY, T.; MITTAZ, J.; PANDEL, D.; PRIEDHORSKY, W. C.; SASSEEN, T.; SHIREY, R.; SMITH, P.; VREUX, J.-M. The XMM-Newton optical/UV monitor telescope. **Astronomy and Astrophysics**, v. 365, p. L36–L44, 2001. 70

MEGGITT, M. A.; WICKRAMASINGHE, D. T. The polarization properties of magnetic accretion columns. **Monthly Notices of the Royal Astronomical Society**, v. 198, p. 71, 1982. 27

MEGGITT, S. M. A.; WICKRAMASINGHE, D. T. The polarization properties of magnetic accretion columns. **Monthly Notices of the Royal Astronomical Society**, v. 198, p. 71–82, jan. 1982. 9

MEWE, R.; GRONENSCHILD, E. H. B. M.; OORD, G. H. J. van den. Calculated X-radiation from optically thin plasmas. v. **Astronomy and Astrophysics Supplement Series**, v. 62, n. 3, p. 197–254, 1985. 48, 74

MEWE, R.; LEMEN, J. R.; OORD, G. H. J. van den. Calculated X-radiation from optically thin plasmas. VI - Improved calculations for continuum emission and approximation formulae for nonrelativistic average Gaunt actors. **Astronomy & Astrophysics Supplement Series**, v. 65, p. 511–536, set. 1986. 54, 55

_____. Calculated X-radiation from optically thin plasmas. VI - improved calculations for continuum emission and approximation formulae for nonrelativistic average Gaunt factors. **Astronomy and Astrophysics Supplement Series**, v. 65, n. 3, p. 511–536, 1986. 48

MUKAI, K. The X-ray emission of magnetic cataclysmic variables. **"The X-ray Universe 2011"**, A, p. 011, 2011. 18

______. **The catalog of IPs and IP candidates by right ascension**. 2014. (Available from: `http://asd.gsfc.nasa.gov/Koji.Mukai/iphome/catalog/alpha.html`). 57

______. X-ray emissions from accreting white dwarfs: a review. **Publications of the Astronomical Society of Pacific**, v. 129, n. 6, p. 062001, 2017. 16, 18, 21, 22

MUKAI, K.; KINKHABWALA, A.; PETERSON, J. R.; KAHN, S. M.; PAERELS, F. Two types of X-ray spectra in cataclysmic variables. **The Astrophysical Journal Supplement Series**, v. 586, p. L77, 2003. 18

MUKAI, K.; RANA, V.; BERNARDINI, F.; MARTINO, D. de. Unambiguous detection of reflection in magnetic cataclysmic variables: joint NuSTAR-XMM-Newton observations of three intermediate polars. **The Astrophysical Journal**, v. 807, p. L30, 2015. 13

NASA, N. A. S. A. **Introduction to Cataclysmic Variables (CVs)**. 2006. (Available from: `https://heasarc.gsfc.nasa.gov/docs/objects/cvs/cvstext.html`). 3

NAUENBERG, M. Analytic approximations to the mass-radius relation and energy of zero-temperature stars. **The Astrophysical Journal**, v. 175, p. 417, jul. 1972. 40

NELDER, J. A.; MEAD, R. A simplex method for function minimization. **The Computer Journal**, v. 7, p. 308–313, 1965. 31

NORTON, A. J.; HELLIER, C.; BEARDMORE, A. P.; WHEATLEY, P. J.; OSBORNE, J. P.; TAYLOR, P. Stream-fed and disc-fed accretion in TX Columbae. **Monthly Notices of the Royal Astronomical Society**, v. 289, n. 2, p. 362–370, ago. 1997. 12

NORTON, A. J.; MUKAI, K. A precessing accretion disc in the intermediate polar XY Arietis? **Astronomy and Astrophysics**, v. 472, p. 225–232, 2007. 61

NORTON, A. J.; WATSON, M. G. Spin modulated X-ray emission from intermediate polars. **Monthly Notices of the Royal Astronomical Society**, v. 237, p. 853–874, 1989. 18

NORTON, A. J.; WYNN, G. A.; SOMERSCALES, R. V. The spin periods and magnetic moments of white dwarfs in magnetic cataclysmic variables. **Astrophysical Journal**, v. 614, p. 349–357, 2004. 10, 11

OLIVEIRA, A. S.; RODRIGUES, C. V.; CIESLINSKI, D.; JABLONSKI, F. J.; SILVA, K. M. G.; ALMEIDA, L. A.; RODRÍGUEZ-ARDILA, A.; PALHARES, M. S. Exploratory spectroscopy of magnetic cataclysmic variables candidates and other variable objects. **The Astronomical Journal**, v. 153, n. 4, p. 144, abr. 2017. 11

OLIVEIRA, A. S.; RODRIGUES, C. V.; MARTINS, M.; PALHARES, M. S.; SILVA, K. M. G.; LIMA, I. J.; JABLONSKI, F. J. Exploratory spectroscopy of magnetic cataclysmic variables candidates and other variable objects. II. **The Astronomical Journal**, v. 159, n. 3, p. 114, mar. 2020. 11, 57, 114

OSAKI, Y. Dwarf-nova outbursts. **Publications of the Astronomical Society of the Pacific**, v. 108, p. 39, 1996. 1, 2

PACHOLCZYK, A. G.; SWIHART, T. L. Polarization of radio sources. VI. an oscillatory behavior of the intensity in a general solution of the radiation transfer problem in a plasma. **The Astrophysical Journal**, v. 196, p. 125–127, fev. 1975. 27

PALA, A. F.; GÄNSICKE, B. T.; BREEDT, E.; KNIGGE, C.; HERMES, J. J.; FUSILLO, N. P. G.; HOLLANDS, M. A.; NAYLOR, T.; PELISOLI, I.; SCHREIBER, M. R.; TOONEN, S.; AUNGWEROJWIT, A.; CUKANOVAITE, E.; DENNIHY, E.; MANSER, C. J.; PRETORIUS, M. L.; SCARINGI, S.; TOLOZA, O. A volume-limited sample of cataclysmic variables from Gaia DR2: space density and population properties. **Monthly Notices of the Royal Astronomical Society**, v. 494, n. 3, p. 3799–3827, abr. 2020. 11, 111

PARKER, T. L.; NORTON, A. J.; MUKAI, K. X-ray orbital modulations in intermediate polars. **Astronomy and Astrophysics**, v. 439, p. 213–225, 2005. 61

PATTERSON, J. A rapidly rotating white dwarf in AE Aquarii. In: HORN, H. M. van; WEIDEMANN, V.; SAVEDOFF, M. P. (Ed.). **IAU Colloq. 53: White Dwarfs and Variable Degenerate Stars**. [S.l.: s.n.], 1979. p. 519. 10

_____. The DQ Herculis stars. **Publications of the Astronomical Society of the Pacific**, v. 106, n. 697, p. 209–238, 1994. 11, 14

PATTERSON, J.; BEUERMANN, K.; AFRICANO, J. The optical and X-ray pulsation of AE Aquarii. **Bulletin of the American Astronomical Society**, v. 20, p. 1099, 1988. 14

PATTERSON, J.; BRANCH, D.; CHINCARINI, G.; ROBINSON, E. L. 33 second X-ray pulsations in AE Aquarii. **Astrophysical Journal**, v. 240, p. L133–L136, 1980. 61

PATTERSON, J.; FENTON, W. H.; THORSTENSEN, J. R.; HARVEY, D. A.; SKILLMAN, D. R.; FRIED, R. E.; MONARD, B.; O'DONOGHUE, D.; BESHORE, E.; MARTIN, B.; NIARCHOS, P.; VANMUNSTER, T.; FOOTE, J.; BOLT, G.; REA, R.; COOK, L. M.; BUTTERWORTH, N.; WOOD, M. Superhumps in cataclysmic binaries. XXIII. V442 Ophiuchi and RX J1643.7+3402. **Publications of the Astronomical Society of the Pacific** , v. 114, p. 1364–1381, dez. 2002. 7, 9, 100, 101, 104

PIIROLA, V. A double image chopping polarimeter. **Astronomy and Astrophysics**, v. 27, p. 383–338, 1973. 68

______. Simultaneous five-colour (UBVRI) photopolarimeter. In: COYNE, G. V.; MAGALHÃES, A. M.; MOFFAT, A. F.; SCHULTE-LADBECK, R. E.; TAPIA, S. (Ed.). **Polarized radiation of circumstellar Origin**. [S.l.: s.n.], 1988. p. 735–746. 68, 69

PIIROLA, V.; VORNANEN, T.; BERDYUGIN, A.; COYNE, G. V. S. J. V405 Aurigae: a high magnetic field intermediate polar. **The Astrophysical Journal**, v. 684, p. 558–568, 2008. xvi, 62, 63, 64, 65, 66, 67, 70, 84, 85, 86, 91, 94, 95

PRESS, W. H.; TEUKOLSKY, S. A.; VETTERLING, W. T.; FLANNERY, B. P. **Numerical recipes in FORTRAN. the art of scientific computing**. United Kingdom, 2.ed.: Cambridge: University Pres, 1992. 31

RITTER, H.; KOLB, U. Catalogue of cataclysmic binaries, low-mass X-ray binaries and related objects (seventh edition). **Astronomy and Astrophysics**, v. 404, p. 301–303, 2003. 7, 11

ROBERTS, D. H.; LEHAR, J.; DREHER, J. W. Time series analysis with CLEAN. I. derivation of a spectrum. **The Astronomical Journal**, v. 93, p. 968–989, abr. 1987. 104

ROBERTSON, J. W.; HONEYCUTT, R. K.; HENDEN, A. A.; CAMPBELL, R. T. Orbital light curves of UU Aquarii in stunted outburst. **The Astronomical Journal**, v. 155, n. 2, p. 61, fev. 2018. 109

RODRIGUES, C. V.; CIESLINSKI, D.; STEINER, J. E. Polarimetry and spectroscopy of the polar RX J1141.3-6410. **Astronomy and Astrophysics**, v. 335, p. 979–984, 1998. 100

RODRÍGUEZ-GIL, P.; CASARES, J.; MARTÍNEZ-PAIS, I. G.; HAKALA, P.; STEEGHS, D. Evidence of magnetic accretion in an SW Sextantis Star: discovery of variable circular polarization in LS Pegasi. **The Astrophysical Journal Letters**, v. 548, n. 1, p. L49–L52, fev. 2001. 9, 99, 109, 114

RODRÍGUEZ-GIL, P.; GÄNSICKE, B. T.; HAGEN, H.-J.; ARAUJO-BETANCOR, S.; AUNGWEROJWIT, A.; PRIETO, C. A.; BOYD, D.; CASARES, J.; ENGELS, D.; GIANNAKIS, O.; HARLAFTIS, E. T.; KUBE, J.; LEHTO, H.; MARTÍNEZ-PAIS, I. G.; SCHWARZ, R.; SKIDMORE, W.; STAUDE, A.; TORRES, M. A. P. SW Sextantis stars: the dominant population of cataclysmic variables with orbital periods between 3 and 4h. **Monthly Notices of the Royal Astronomical Society**, v. 377, p. 1747–1762, jun. 2007. 8, 111

RODRÍGUEZ-GIL, P.; MARTÍNEZ-PAIS, I. G. V533 Herculis: the second SW Sex old nova displaying emission-line flaring. **Monthly Notices of the Royal Astronomical Society**, v. 337, p. 209–215, nov. 2002. 9

RODRÍGUEZ-GIL, P.; SCHMIDTOBREICK, L.; GÄNSICKE, B. T. Spectroscopic search for new SW Sextantis stars in the 3-4 h orbital period range - I. **Monthly Notices of the Royal Astronomical Society**, v. 374, p. 1359–1376, fev. 2007. 101, 104, 111

RYBICKI, G. B. G.; LIGHTMAN, A. P. **Radiative processes in astrophysics**. New York: Wiley-Interscience, 1979. 37

SANAD, M. R. Ultraviolet spectroscopy of PQ Gem and V405 Aur from the HST and IUE satellites. **The Astrophysical Journal**, v. 812, p. 97, 2015. 61

SAXTON, C. J.; WU, K.; CANALLE, J. B. G.; CROPPER, M.; RAMSAY, G. X-ray emissions from two-temperature accretion flows within a dipole magnetic funnel. **Monthly Notices of the Royal Astronomical Society**, v. 379, n. 2, p. 779–790, ago. 2007. 17

SCARGLE, J. D. Studies in astronomical time series analysis. II - statistical aspects of spectral analysis of unevenly spaced data. **The Astrophysical Journal**, v. 263, p. 835–853, dez. 1982. 100

SCHLAFLY, E. F.; FINKBEINER, D. P. Measuring reddening with Sloan Digital Sky Survey stellar spectra and recalibrating SFD. **The Astrophysical Journal**, v. 737, p. 103, 2011. 34

SCHLEGEL, D. J.; FINKBEINER, D. P.; DAVIS, M. Maps of dust infrared emission for use in estimation of reddening and cosmic microwave background radiation foregrounds. **The Astrophysical Journal**, v. 500, p. 525–553, 1998. 69

SCHMIDT, G. D.; SZKODY, P.; SMITH, P. S.; SILBER, A.; TOVMASSIAN, G.; HOARD, D. W.; GÄNSICKE, B. T.; MARTINO, D. de. AR Ursae Majoris: the first high-field magnetic cataclysmic variable. **The Astrophysical Journal**, v. 473, p. 483, dez. 1996. 3

SCHWOPE, A. D.; THOMAS, H.-C.; BEUERMANN, K.; BURWITZ, V.; JORDAN, S.; HAEFNER, R. Two-pole accretion in the high-field polar RX J1938.6-4612. **Astronomy and Astrophysics**, v. 293, p. 764–776, 1995. 38

SHAKHOVSKOJ, N. M.; KOLESNIKOV, S. V. RX J0558.0+5353. **IAU Circular**, v. 6760, out. 1997. 68

SHAKURA, N. I.; SUNYAEV, R. A. Black holes in binary systems. observational appearance. **Astronomy and Astrophysics**, v. 24, p. 337–355, 1973. 6

SHUGAROV, S.; GOLYSHEVA, P.; SOKOLOVSKY, K.; CHOCHOL, D. Photometric variability of the novalike object V380 Oph in 1976 - 2016. In: **Proceedings of Astro plate**. [S.l.: s.n.], 2016. p. 59–62. 104

SILVA, K. M. G. **Modelagem multiespectral da região de acréscimo de polares**. 73 p p. Tese (Doutorado) — em Astrofísica. Instituto Nacional de Pesquisas Espaciais, São José dos Campos, 2013. Disponível em: <`http://mtc-m19.sid.inpe.br/col/sid.inpe.br/mtc-m19/2013/03.14.14.13/doc/publicacao.pdf`>. 25, 50

SILVA, K. M. G.; RODRIGUES, C. V.; COSTA, J. E. R.; SOUZA, C. A. d.; CIESLINSKI, D.; HICKEL, G. R. Stokes imaging of AM Her systems using 3D inhomogeneous models- II. modelling x-ray and optical data of CP Tucanae. **Monthly Notices of the Royal Astronomical Society**, v. 432, p. 1587–1599, 2013. 25, 27, 34, 37, 45

SILVA, K. M. G.; RODRIGUES, C. V.; OLIVEIRA, A. S.; ALMEIDA, L. A.; CIESLINSKI, D.; COSTA, J. E. R.; JABLONSKI, F. J. MLS110213:022733+130617: a new eclipsing polar above the period gap. **Monthly Notices of the Royal Astronomical Society**, v. 451, p. 4183–4192, 2015. 25, 26

SING, D. K.; HOWELL, S. B.; SZKODY, P.; CORDOVA, F. A. Far ultraviolet spectroscopic explorer spectroscopy of the transitional magnetic cataclysmic variable V405 Aurigae. **The Publications of the Astronomical Society of the Pacific**, v. 116, p. 1056–1060, 2004. 64

SINGH, K. P. X-ray emission from magnetic cataclysmic variables. In: NANDI (Ed.). **Astronomische gesellschaft abstract series**. [S.l.: s.n.], 2013. (Astronomical Society of India Conference Series, v. 8). 1

SKILLMAN, D. R. Photometry of the new dq her star, rx j0558.0+5353. **Publications of the Astronomical Society of the Pacific**, v. 108, p. 130, 1996. 61

SMITH, R. K.; BRICKHOUSE, N. S.; LIEDAHL, D. A.; RAYMOND, J. C. Collisional plasma models with APEC/APED: emission-line diagnostics of hydrogen-like and Helium-like ions. **The Astrophysical Journal Letters**, v. 556, n. 2, p. L91–L95, ago. 2001. 48, 74

SOM, L. V. B.; FALIZE, É.; BONNET-BIDAUD, J. M.; MOUCHET, M.; BUSSCHAERT, C.; CIARDI, A. Numerical simulations of high-energy flows in accreting magnetic white dwarfs. **Monthly Notices of the Royal Astronomical Society**, v. 473, n. 3, p. 3158–3168, jan. 2018. 15, 17, 18, 39, 40, 42

STOCKMAN, H. S.; SCHMIDT, G. D.; BERRIMAN, G.; LIEBERT, J.; MOORE, R. L.; WICKRAMASINGHE, D. T. A search for circular polarization in cataclysmic variables. **Astrophysical Journal**, v. 401, n. 2, p. 629–641, 1992. 99

SULEIMANOV, V.; DOROSHENKO, V.; DUCCI, L.; ZHUKOV, G. V.; WERNER, K. GK Persei and EX Hydrae: intermediate polars with small magnetospheres. **Astronomy & Astrophysics**, v. 591, p. A35, jun. 2016. 93

SULEIMANOV, V.; POUTANEN, J.; FALANGA, M.; WERNER, K. Influence of compton scattering on the broad-band X-ray spectra of intermediate polars. **Astronomy and Astrophysics**, v. 491, p. 525–529, 2008. 18, 20

SULEIMANOV, V.; REVNIVTSEV, M.; RITTER, H. RXTE broadband X-ray spectra of intermediate polars and white dwarf mass estimates. **Astronomy &**

Astrophysics, v. 443, n. 1, p. 291–291, nov. 2005. 13, 16, 41, 79, 80, 82, 93, 94, 96, 113

SULEIMANOV, V. F.; DOROSHENKO, V.; WERNER, K. Hard X-ray view on intermediate polars in the Gaia era. **Monthly Notices of the Royal Astronomical Society**, v. 482, n. 3, p. 3622–3635, jan. 2019. 79, 80, 82, 84, 93, 94, 113

SUTHERLAND, R. S. Accurate free-free Gaunt factors for astrophysical plasmas. **Monthly Notices of the Royal Astronomical Society**, v. 300, n. 2, p. 321–330, out. 1998. 54, 55

SZKODY, P.; ANDERSON, S. F.; AGÜEROS, M.; COVARRUBIAS, R.; BENTZ, M.; HAWLEY, S.; MARGON, B.; VOGES, W.; HENDEN, A.; KNAPP, G. R.; BERK, D. E. V.; REST, A.; MIKNAITIS, G.; MAGNIER, E.; BRINKMANN, J.; CSABAI, I.; HARVANEK, M.; HINDSLEY, R.; HENNESSY, G.; IVEZIC, Z.; KLEINMAN, S. J.; LAMB, D. Q.; LONG, D.; NEWMAN, P. R.; NEILSEN, E. H.; NICHOL, R. C.; NITTA, A.; SCHNEIDER, D. P.; SNEDDEN, S. A.; YORK, D. G. Cataclysmic variables from the Sloan Digital Sky Survey. I. the first results. **The Astronomical Journal**, v. 123, p. 430–442, 2002. 11

SZKODY, P.; ANDERSON, S. F.; BROOKS, K.; GÄNSICKE, B. T.; KRONBERG, M.; RIECKEN, T.; ROSS, N. P.; SCHMIDT, G. D.; SCHNEIDER, D. P.; AGÜEROS, M. A.; GOMEZ-MORAN, A. N.; KNAPP, G. R.; SCHREIBER, M. R.; SCHWOPE, A. D. Cataclysmic variables from the Sloan Digital Sky Survey. VIII. the final year (2007-2008). **The Astronomical Journal**, v. 142, p. 181, 2011. 11

SZKODY, P.; ANDERSON, S. F.; HAYDEN, M.; KRONBERG, M.; MCGURK, R.; RIECKEN, T.; SCHMIDT, G. D.; WEST, A. A.; GÄNSICKE, B. T.; GOMEZ-MORAN, A. N.; SCHNEIDER, D. P.; SCHREIBER, M. R.; SCHWOPE, A. D. Cataclysmic variables from SDSS. VII. the seventh year (2006). **The Astronomical Journal**, v. 137, p. 4011–4019, 2009. 11

SZKODY, P.; DICENZO, B.; HO, A. Y. Q.; HILLENBRAND, L. A.; ROESTEL, J. van; RIDDER, M.; LIMA, I. D.; GRAHAM, M. L.; BELLM, E. C.; BURDGE, K.; KUPFER, T.; PRINCE, T. A.; MASCI, F. J.; MRÓZ, P. J.; GOLKHOU, V. Z.; COUGHLIN, M.; CUNNINGHAM, V. A.; DEKANY, R.; GRAHAM, M. J.; HALE, D.; KAPLAN, D.; KASLIWAL, M. M.; MILLER, A. A.; NEILL, J. D.; PATTERSON, M. T.; RIDDLE, R.; SMITH, R.; SOUMAGNAC, M. T.

Cataclysmic variables in the first year of the Zwicky transient facility. **The Astronomical Journal**, v. 159, n. 5, p. 198, maio 2020. 11, 114

SZKODY, P.; EVERETT, M. E.; DAI, Z.; SERNA-GREY, D. Follow-up observations of SDSS and CRTS candidate cataclysmic variables II. **The Astronomical Journal**, v. 155, p. 28, 2018. 11

SZKODY, P.; FRASER, O.; SILVESTRI, N.; HENDEN, A.; ANDERSON, S. F.; FRITH, J.; LAWTON, B.; OWENS, E.; RAYMOND, S.; SCHMIDT, G.; WOLFE, M.; BOCHANSKI, J.; COVEY, K.; HARRIS, H.; HAWLEY, S.; KNAPP, G. R.; MARGON, B.; VOGES, W.; WALKOWICZ, L.; BRINKMANN, J.; LAMB, D. Q. Cataclysmic variables from the Sloan Digital Sky Survey. II. the second year. **The Astronomical Journal**, v. 126, p. 1499–1514, 2003. 11

SZKODY, P.; HENDEN, A.; AGÜEROS, M.; ANDERSON, S. F.; BOCHANSKI, J. J.; KNAPP, G. R.; MANNIKKO, L.; MUKADAM, A.; SILVESTRI, N. M.; SCHMIDT, G. D.; STEPHANIK, B.; WATSON, T. K.; WEST, A. A.; WINGET, D.; WOLFE, M. A.; BARENTINE, J. C.; BRINKMANN, J.; BREWINGTON, H. J.; DOWNES, R. A.; HARVANEK, M.; KLEINMAN, S. J.; KRZESINSKI, J.; LONG, D.; NEILSEN, E. H.; NITTA, A.; SCHNEIDER, D. P.; SNEDDEN, S. A.; VOGES, W. Cataclysmic variables from Sloan Digital Sky Survey. V. the fifth year (2004). **The Astronomical Journal**, v. 131, p. 973–983, 2006. 11

SZKODY, P.; HENDEN, A.; FRASER, O.; SILVESTRI, N.; BOCHANSKI, J.; WOLFE, M. A.; AGÜEROS, M.; WARNER, B.; WOUDT, P.; TRAMPOSCH, J.; HOMER, L.; SCHMIDT, G.; KNAPP, G. R.; ANDERSON, S. F.; COVEY, K.; HARRIS, H.; HAWLEY, S.; SCHNEIDER, D. P.; VOGES, W.; BRINKMANN, J. Cataclysmic variables from the Sloan Digital Sky Survey. III. the third year. **The Astronomical Journal**, v. 128, p. 1882–1893, 2004. 11

SZKODY, P.; HENDEN, A.; FRASER, O. J.; SILVESTRI, N. M.; SCHMIDT, G. D.; BOCHANSKI, J. J.; WOLFE, M. A.; AGÜEROS, M.; ANDERSON, S. F.; MANNIKKO, L.; DOWNES, R. A.; SCHNEIDER, D. P.; BRINKMANN, J. Cataclysmic variables from Sloan Digital Sky Survey. IV. the fourth year (2003). **The Astronomical Journal**, v. 129, p. 12386–2399, 2005. 11

SZKODY, P.; HENDEN, A.; MANNIKKO, L.; MUKADAM, A.; SCHMIDT, G. D.; BOCHANSKI, J. J.; AGÜEROS, M.; ANDERSON, S. F.; SILVESTRI, N. M.; DAHAB, W. E.; OGURI, M.; SCHNEIDER, D. P.; SHIN, M.-S.; STRAUSS, M. A.; KNAPP, G. R.; WEST, A. A. Cataclysmic variables from Sloan

Digital Sky Survey. VI. the sixth year (2005). **The Astronomical Journal**, v. 134, p. 185–194, 2007. 11

SZKODY, P.; NISHIKIDA, K.; LONG, K. S.; FRIED, R. X-Ray and optical spectra of the unusual cataclysmic variables LS Pegasi and T Leonis. **The Astronomical Journal**, v. 121, p. 2761–2768, maio 2001. 106

SZKODY, P.; PICHE, F. The phase 0.5 absorption in V1315 Aquilae, SW Sextantis, and DW Ursae Majoris. **The Astrophysical Journal**, v. 361, p. 235–243, sep 1990. 8

THORSTENSEN, J. R.; RINGWALD, F. A.; WADE, R. A.; SCHMIDT, G. D.; NORSWORTHY, J. E. PG0027 + 260 - an example of a class of cataclysmic binaries with mysterious, but consistent, behavior. **The Astronomical Journal**, v. 102, p. 272–283, jul. 1991. 8

TOVMASSIAN, G.; HERNANDEZ, M. S.; GONZÁLEZ-BUITRAGO, D.; ZHARIKOV, S.; GARCÍA-DÍAZ, M. T. On the SW Sex-type eclipsing cataclysmic variable SDSS0756+0858. **The Astronomical Journal**, v. 147, p. 68, mar. 2014. 8

TURNER, M. J. L.; ABBEY, A.; ARNAUD, M. The european photon imaging camera on XMM-Newton: The MOS cameras. **Astronomy and Astrophysics**, v. 365, p. L27–L35, 2001. 70

WALKER, M. F. Elements of the short-period eclipsing binary nova DQ Hercules. **Proceedings of the Astronomical Society of Pacific**, v. 67, p. 262, 1955. 10

WARNER, B. **Cataclysmic variable stars**. United Kingdom: Cambridge Astrophysics Series, 1995. 1

WEST, S. C.; BERRIMAN, G.; SCHMIDT, G. D. The discovery of near-infrared polarized cyclotron emission in the intermediate polar BG Canis Minoris. **The Astrophysical Journal**, v. 322, p. L35–L39, 1987. 37

WHITTET, D. C. B. **Dust in the galactic environment**. 2.ed., Bristol, Philadelphia: Institute of Physics Publishing, 1992. 34

WICKRAMASINGHE, D. T.; FERRARIO, L. Magnetism in isolated and binary white dwarfs. **Publications of the Astronomical Society of the Pacific** , v. 112, n. 773, p. 873–924, jul. 2000. 11

WICKRAMASINGHE, D. T.; MEGGITT, S. M. A. The polarization properties of magnetic accretion columns. III - a grid of uniform temperature and shock front models. **Monthly Notices of the Royal Astronomical Society**, v. 605-618, p. 214, 1985. 64

WILLIAMS, R. E. Eclipse line profiles in cataclysmic variables - evidence for absence of accretion disks. **The Astronomical Journal**, v. 97, p. 1752–1758, jun. 1989. 8

WU, K. Structure of inhomogeneous accretion shocks. **Proceedings of the Astronomical Society of Australia**, v. 11, n. 1, p. 61–64, 1994. 15

WU, K.; CHANMUGAM, G.; SHAVIV, G. Structure of steady state accretion shocks with several cooling functions: closed integral-form solution. **Astrophysical Journal**, v. 426, n. 2, p. 664–668, 1994. 15, 18, 38, 39

YUASA, T.; NAKAZAWA, K.; MAKISHIMA, K.; SAITOU, K.; ISHIDA, M.; EBISAWA, K.; MORI, H.; YAMADA, S. White dwarf masses in intermediate polars observed with the Suzaku satellite. **Astronomy & Astrophysics**, v. 520, p. A25, set. 2010. 17, 18, 42, 84

ZAZNOBIN, I.; SAZONOV, S.; BURENIN, R.; USKOV, G.; SEMENA, A.; GILFANOV, M.; MEDVEDEV, P.; SUNYAEV, R.; ESELEVICH, M. Identification of 3 cataclysmic variables detected by the ART-XC and eROSITA telescopes aboard SRG during the all-sky X-ray survey. **arXiv e-prints**, p. arXiv:2107.05611, jul. 2021. 11

ZELLEM, R.; HOLLON, N.; BALLOUZ, R.-L.; SION, E. M.; GODON, P.; GÄNSICKE, B. T.; LONG, K. Hubble Space Telescope STIS spectroscopy of the peculiar nova-like variables BK Lyn, V751 Cygni, and V380 Oph. **Publications of the Astronomical Society of the Pacific** , v. 121, n. 883, p. 942, set. 2009. 106

ZHU, H.; TIAN, W.; LI, A.; ZHANG, M. The gas-to-extinction ratio and the gas distribution in the Galaxy. **Monthly Notices of the Royal Astronomical Society**, v. 471, n. 3, p. 3494–3528, nov. 2017. 34

ZUHONE, J. A.; BIFFI, V.; HALLMAN, E. J.; RANDALL, S. W.; FOSTER, A. R.; SCHMID, C. Simulating X-ray observations with Python. **arXiv e-prints**, p. arXiv:1407.1783, jul. 2014. 31

APPENDIX A

PAPER: SEARCH FOR MAGNETIC ACCRETION IN SW SEXTANTIS SYSTEMS

Draft version February 19, 2021
Typeset using LATEX **twocolumn** style in AASTeX63

Search for magnetic accretion in SW Sextantis systems

I. J. Lima,[1,2] C. V. Rodrigues,[1] C. E. Ferreira Lopes,[1] P. Szkody,[2] F. J. Jablonski,[1]
A. S. Oliveira,[3] K. M. G. Silva,[4] D. Belloni,[1] M. S. Palhares,[3] S. Shugarov,[5,6] R. Baptista,[7] and
L. A. Almeida[8]

[1] *Instituto Nacional de Pesquisas Espaciais (INPE/MCTI), Av. dos Astronautas, 1758, São José dos Campos, SP, Brazil*
[2] *Department of Astronomy, University of Washington, Box 351580, Seattle, WA 98195, USA*
[3] *IP&D, Universidade do Vale do Paraíba, 12244-000, São José dos Campos, SP, Brazil*
[4] *Gemini Observatory Southern Operations Center - c/o AURA, Casilla 603, La Serena, Chile*
[5] *Astronomical Institute of the Slovak Academy of Sciences, Tatranská Lomnica, Slovakia*
[6] *Sternberg Astronomical Institute, M.V. Lomonosov Moscow State University, Moscow, Russia*
[7] *Departamento de Física, Universidade Federal de Santa Catarina, Trindade, 88040-900, Florianópolis, SC, Brazil*
[8] *Universidade Federal do Rio Grande do Norte, UFRN, Departamento de Física, CP 1641, Natal, RN, 59072-970, Brazil*

(Received; Revised; Accepted)

Submitted to AJ

ABSTRACT

SW Sextantis systems are nova-like cataclysmic variables that have unusual spectroscopic properties, which are thought to be caused by an accretion geometry having part of the mass flux trajectory out of the orbital plane. Accretion onto a magnetic white dwarf is one of the proposed scenarios for these systems. To verify this possibility, we analysed photometric and polarimetric time-series data for a sample of six SW Sex stars. We report possible modulated circular polarization in BO Cet, SW Sex, and UU Aqr with periods of 11.1, 41.2 and 25.7 min, respectively, and less significant periodicities for V380 Oph at 22 min and V442 Oph at 19.4 min. We confirm previous results that LS Peg shows variable circular polarization. However, we determine a period of 18.8 min, which is different from the earlier reported value. We interpret these periods as the spin periods of the white dwarfs. Our polarimetric results indicate that 15% of the SW Sex systems have direct evidence of magnetic accretion. We also discuss SW Sex objects within the perspective of being magnetic systems, considering the latest findings about cataclysmic variables demography, formation and evolution.

Keywords: binaries: close — novae, cataclysmic variables — stars: dwarf novae — stars: variables: general — techniques: polarimetric

1. INTRODUCTION

SW Sextantis systems are a class of nova-like cataclysmic variables (CVs). CVs are compact binary systems containing a late-type main-sequence star that is transferring matter onto a white dwarf (WD) via Roche lobe overflow. Nova-like variables spend most of the time in a "high state" mode, which is characterized by high mass-transfer rates, $\dot{M}$, producing steady and bright accretion disks. Thorstensen et al. (1991) coined the classification SW Sex for a small group of nova-like variables based on their own observations and previous works (e.g. Szkody & Piche 1990). The SW Sex systems are identified by their spectroscopic characteristics (see below), which challenge explanation within the standard accretion model of CVs.

Initially, SW Sex objects were associated with eclipsing nova-like variables despite showing single-peaked emission lines, an unexpected property for high-inclination disks, which normally produce double-peaked lines (e.g. Horne & Marsh 1986). Currently, the SW Sex phenomenon is understood as independent of the system inclination (Rodríguez-Gil et al. 2007a). Additional observational properties of SW Sex systems are

Corresponding author: I. J. Lima
isabel.lima@inpe.br, isabellima01@gmail.com

described by Hoard et al. (2003) and summarized below. These systems can exhibit absorption in the central part of the Balmer and He I emission line profiles around orbital phase 0.5 (superior conjunction of the secondary star). They also show high-ionization emission lines, such as He II 4686 Å. The emission line radial velocities are shifted in phase compared to expectations from a simple model of the binary system. The emission lines of SW Sex systems also show high-velocity S-waves extending up to 4000 km/s, with maximum blueshift near phase 0.5. Interestingly, their orbital periods are typically around 3 to 4 h, just above the period gap. More importantly, a large number of CVs in this orbital period range are SW Sex objects (Rodríguez-Gil et al. 2007b). This grants SW Sex objects an important role in the comprehension of CV evolution. An effort to concatenate information about SW Sex systems is the "The Big List of SW Sextantis Stars"[1] ("The Big List" hereinafter), which is updated until 2016.

Some SW Sex systems show low states, when their brightness drops by a few magnitudes. This behavior is the defining characteristic of the VY Scl nova-like systems (Warner 1995). Due to those episodic reductions in brightness, they were originally termed anti-dwarf nova systems. The recurrence of those low states is irregular and probably associated with a variation of $\dot{M}$. In a high state, the average $\dot{M}$ in SW Sex systems is $\approx 5 \times 10^{-9}\,\mathrm{M}_{\odot}\,\mathrm{yr}^{-1}$ and not statistically different from the values found for other nova-like systems (Puebla et al. 2007; Ballouz & Sion 2009).

Some of the spectroscopic features of SW Sex systems can be explained by the presence of material out of the orbital plane. Several scenarios with this property have been proposed to explain the SW Sex phenomena (e.g. Hellier 1996; Hoard et al. 2003): an accretion disk wind (e.g. Honeycutt et al. 1986); a gas stream produced by disk overflow; a bright/extended hot spot and a flared accretion disk (e.g. Dhillon et al. 2013; Tovmassian et al. 2014); and magnetic accretion (e.g. Williams 1989; Casares et al. 1996; Rodríguez-Gil et al. 2001; Hoard et al. 2003). Those ideas are not mutually exclusive.

Nova-like systems are commonly classified as non-magnetic CVs (e.g. Dhillon 1996). However, there are claims that the magnetic scenario is more appropriate to explain the SW Sex systems (see, for instance, Hoard et al. 2003). The detection of variable circular polarization in some SW Sex systems is very strong evidence that magnetic accretion occurs in a fraction of these systems. In Appendix A, we present a compilation of all polarimetric measurements of SW Sex systems to date, which are discussed in Section 5.1.

In magnetic CVs, the accretion flow leaves the binary orbital plane to follow the WD magnetic-field lines creating one or two accretion magnetic structures that direct matter onto the WD surface. Close to the WD, the matter reaches supersonic velocities due to a quasi-freefall regime and a shock develops. An increase in the density and temperature in the region between the shock front and the WD surface forms the so-called postshock region (PSR). Optical polarized cyclotron emission from the PSR region is a defining characteristic of the CVs termed polars, for which the magnetic-field intensities of the WDs are in the range 10 − 250 MG. In these systems, the percentage of circularly polarized light in optical wavelengths is typically 10 − 30%. Such high values of polarization are reached because the PSR region emission is not diluted by any accretion disk emission, since in polars the balistic mass-transfer stream goes directly to the magnetic accretion column and no accretion disk is formed. Intermediate polars (IPs), with magnetic fields in the range 1 − 10 MG, can also exhibit circular polarization, but at much smaller levels, less than a few percent, since they have truncated accretion disks that are an important contribution to the optical emission. A compendium of the search for circular polarization in IPs is presented by Butters et al. (2009). The presence of a very bright accretion disk in SW Sex systems may result in even smaller values of optical polarization compared to IPs.

Other observational properties of the SW Sex systems are also related to magnetic accretion in CVs: a flux modulation associated with the WD rotation (e.g. Avilés et al. 2020; Rodríguez-Gil et al. 2020); flux oscillations in the optical emission-line wings — usually referred as emission-line flaring (e.g. Rodríguez-Gil & Martínez-Pais 2002); and kilosecond quasi-periodic oscillations (QPOs) (Patterson et al. 2002). A review of these properties is given by Hoard et al. (2003).

Patterson et al. (2002) suggested that SW Sex systems could also be classified as magnetic CVs. In a diagram of magnetic momentum, μ, and $\dot{M}$, the SW Sex systems could be located in the upper right portion with high μ and high $\dot{M}$. The polars would have similar μ, but smaller $\dot{M}$ and IPs would have smaller μ (see their Fig. 16). The large values of $\dot{M}$ in SW Sex systems would result in small magnetospheres even for intense magnetic fields. In this interpretation, SW Sex stars, which are located mainly above the period gap, would

---

[1] D. W. Hoard's Big List of SW Sextantis Stars at https://www.dwhoard.com/biglist. See also Hoard et al. (2003).

evolve towards smaller periods, and hence smaller $\dot{M}$, becoming polars below the period gap.

In this paper, we present an observational search for evidence of magnetic accretion in six objects of the SW Sex class: BO Cet, SW Sex, V442 Oph, V380 Oph, LS Peg, and UU Aqr. Specifically, we look for periodic variability of flux or polarization that can be associated with the rotation of the WD. Our targets are assigned to the "Definite" SW Sex membership status in "The Big List". The observations and reduction procedure are described in Section 2. The adopted methodology for searching for periodicities is presented in Section 3. A brief literature review and the results for each object are shown in Section 4. Section 5 discusses our results in the general scenario of SW Sex objects as CVs. Finally, the conclusions are given in Section 6.

2. DATA DESCRIPTION

We obtained simultaneous photometric and polarimetric time series for a sample of 6 SW Sex systems. Table 1 presents a summary of these observations. The observations were performed using the 1.6 m Perkin-Elmer telescope of the Observatório do Pico dos Dias (OPD) coupled with the IAGPOL polarimeter (Magalhães et al. 1996), which was equipped with a quarter-wave retarder plate and a Savart plate (Rodrigues et al. 1998). This instrument splits the incident beam of each object in the field of view (FoV) into two orthogonally polarized beams, the so-called ordinary and extraordinary beams. The observer can use the counts from those beams to obtain differential photometry and/or the polarimetry, as described below. Bias frames and dome flat-field images were collected to correct for the systematic effects from CCD data. The data reduction was carried out using IRAF[2] and the PCCDPACK package (Pereyra 2000; Pereyra et al. 2018).

To perform photometry using these polarimetric observations, the total counts from each object were obtained by summing the counts of the ordinary and extraordinary beams. Then, differential photometry was performed by the calculation of the flux ratio between the target objects and a reference star in the FoV that was assumed to be non variable. The adopted reference stars are shown in Table 2. When possible, we used reference stars previously proposed in the literature: Semena et al. (2013) (LS Peg) and Henden & Honeycutt (1995, HH95). We calibrated the instrumental magnitudes using the magnitudes in the NOMAD and USNO-A2.0 catalogues, which are also given in Table 2. The estimated accuracy of the conversion from instrumental magnitudes to the calibrated values is around 0.3 mag (Monet et al. 2003).

The polarization was calculated using a differential technique in which the Stokes parameters are estimated from the modulation of the ratio of the ordinary beam and extraordinary beam counts (Rodrigues et al. 1998). Specifically, the modulation curve is a function of the Stokes parameters Q, U, and V normalized by the total flux. The images were acquired in 16 positions of the quarter-wave retarder plate, which are separated by 22.5°. To obtain our time series, the waveplate position was continuously increased by this amount. One polarization measurement corresponds to a set of 8 images. We opted for increasing the time resolution at the expense of non-redundant measurements, i.e. to obtain the polarimetric time series we performed a redundant combination of images. Specifically, the first polarimetric point of a series corresponds to the images $1-8$, the second point corresponds to the images $2-9$, and so on. The polarization error was calculated based on the data dispersion around the modulation curve obtained using the estimated Stokes parameters. To evaluate the quality of our polarimetry, we compared this error with the expected value considering the Poisson noise of the source and of the sky, and the detector's gain and read-out noise. The ratio of these two error values varies from 0.5 to 2.0. Therefore, our observational setup provides high-quality data, in the limit of what can be obtained considering the photon and detector noises.

In SW Sex systems, we expect very low circular polarization values due to the dilution of the PSR region flux by the disk emission. Indeed, the observed circular polarization in SW Sex systems is, with few exceptions, around tenths of a percent (see table in Appendix A). An example is V1084 Her, whose circular polarization varies between -0.5 and $+0.5\%$ (Rodríguez-Gil et al. 2009). Hence, any improvement in the polarization estimate is worthwhile. With this aim, we implemented an iterative procedure that takes into account the expected value of the sum of the ordinary (and extraordinary) counts in all images used to calculate one polarization point. The method is described in Appendix B.

We obtained negligible values for the instrumental polarization, which was estimated using measurements of unpolarized standard stars. Table 3 shows the average values of the percentage of circular polarization per object and per observational run. Given the small values and no clear trend in the data, no correction was applied.

---

[2] IRAF (Image Reduction and Analysis Facility) is distributed by the National Optical Astronomy which are operated by the Association of Universities for Research in Astronomy, Inc., under cooperative agreement with the National Science Foundation (Tody 1986, 1993).

Table 1. Summary of the observations.

Object	Date Obs.	Filter	Mean magnitude (mag)	Exp. time (s)	Time span (h)	Detector	Telescope	Used in this analysis
BO Cet	2010 Oct 05	R_C	14.29 ± 0.09	60	1.34	IkonL	OPD	N
	2010 Oct 06	V	14.16 ± 0.08	10	3.17	IkonL	OPD	Y
	2010 Oct 11	V	15.13 ± 0.07	30	1.94	IkonL	OPD	Y
	2010 Oct 12	R_C	14.47 ± 0.10	30	1.94	IkonL	OPD	Y
	2016 Oct 19	V	14.53 ± 0.15	10	1.50	IkonL	OPD	Y
	2016 Oct 25	V	14.39 ± 0.12	10	3.87	IkonL	OPD	N
	2019 Sep 12	R_C	14.51 ± 0.07	30	1.19	Ixon	OPD	N
SW Sex	2014 Mar 29	R_C	14.58 ± 0.65	40	3.29	IkonL	OPD	Y
V442 Oph	2014 Mar 29	R_C	13.37 ± 0.06	20	1.44	IkonL	OPD	Y
	2014 Jul 20	V	13.60 ± 0.05	30	2.62	IkonL	OPD	Y
V380 Oph	2014 Jul 19	V	14.51 ± 0.01	40	2.75	IkonL	OPD	Y[a]
	2002 – 2016	V	14.88 ± 0.16	···	···	···	SOS/SAS	Y
	2002 – 2016	B	14.86 ± 0.14	···	···	···	SOS/SAS	Y
	2002 – 2016	R_C (high state)	15.05 ± 0.23	···	···	···	SOS/SAS	Y
	2002 – 2016	R_C (low state)	18.78 ± 0.14	···	···	···	SOS/SAS	Y
LS Peg	2010 Oct 06	V	11.82 ± 0.06	0.9	2.26	IkonL	OPD	Y
	2010 Oct 12	R_C	11.79 ± 0.08	5	2.35	IkonL	OPD	Y
	2016 Oct 19	V	11.95 ± 0.39	2	3.65	IkonL	OPD	Y
	2016 Oct 25	V	11.93 ± 0.04	2	0.54	IkonL	OPD	N
	2019 Sep 09	V	11.87 ± 0.05	5	1.17	Ixon	OPD	N
	2019 Sep 10	R_C	11.72 ± 0.10	5	1.42	Ixon	OPD	Y
	2019 Sep 12	R_C	11.54 ± 0.44	15	2.10	Ixon	OPD	Y
UU Aqr	2009 Aug 21	V	12.90 ± 0.14	4	6.44	S800	OPD	N
	2009 Aug 22	V	12.87 ± 0.09	15	2.05	S800	OPD	N
	2009 Oct 23	V	13.09 ± 0.10	15	3.02	S800	OPD	Y
	2009 Oct 24	V	13.17 ± 0.32	15	3.18	S800	OPD	N
	2009 Oct 25	V	13.04 ± 0.08	14	3.83	S800	OPD	Y

[a] Except linear polarization data.

Table 2. Reference stars used in the magnitude calibration of the targets.

Target	Reference star					
	Name	HH95	R.A. (2000.0)	DEC. (2000.0)	V (mag)	R (mag)
BO Cet	USNO-A2.0 0825-00488714	···	02:06:32.13	−02:04:00.3	15.1	14.1
SW Sex	USNO-A2.0 0825-07140676	SW Sex-2	10:15:18.00	−03:07:21.0	···	12.93
V442 Oph	USNO-A2.0 0737-0410665	V442 Oph-20	17:32:18.03	−16:15:41.2	13.97	14.53
V380 Oph	USNO-A2.0 0960-0317152	V380 Oph-13	17:50:07.14	+06:05:13.8	13.9	···
LS Peg	TYC 1134-178-1	···	21:52:04.92	+14:05:02.3	10.82	9.8
UU Aqr	USNO-A2.0 0825-19566061	UU Aqr-5	22:09:04.93	−03:46:42.2	13.80	···

Table 3. Circular polarization measurements of unpolarized standard stars.

Run	Object	P_c (%)	Number of observations
2009 Aug	HD 154892	-0.026 ± 0.127	1
2009 Oct	HD 64299	0.007 ± 0.037	1
2010 Oct	HD 12021	0.01 ± 0.02	6
	HD 14069	0.02 ± 0.01	3
2014 Mar	HD 94851	-0.01 ± 0.04	4
	HD 98161	0.12 ± 0.08	4
2014 Jul	WD 1620-391	-0.04 ± 0.01	5
	WD 2007-303	-0.02 ± 0.03	5
2016 Oct	HD 14069	-0.06 ± 0.023	1
2019 Sep	HD 154892	-0.014 ± 0.022	1

To convert the position angle of the linear polarization from the instrumental to the equatorial reference frame, we used observations of polarized standard stars. We also corrected all linear polarization measurements for their positive bias as described by Vaillancourt (2006).

In addition to the OPD observations described above, we also reanalysed the V380 Oph photometry presented in Shugarov et al. (2016) that was taken in BVR$_C$ filters and obtained with different telescopes of the Southern Observatory Station (SOS) of Moscow State University and Slovak Academy of Sciences (SAS). The mean magnitude of these data in each filter is presented in Table 1.

3. DATA ANALYSIS STRATEGY

The most characteristic signatures of magnetic accretion in CVs are circularly polarized emission and coherent photometric and/or polarimetric variability associated with the rotation of the WD. Therefore, we performed a search for periodicities in the magnitude, circular polarization, and linear polarization time series of all objects in our sample. This search was performed separately for the polarimetric and photometric data because the flux may show other periodicities that are not related to the WD rotation. In this section, we describe the common procedures in the data analysis of all objects.

The Lomb-Scargle (LS) method (Lomb 1976; Scargle 1982) was used to search for periodicities. We adopted a maximum frequency of 240 d^{-1} (6 min), while the minimum frequency was adjusted for each star, having typical values around 14 d^{-1} (100 min). The adopted frequency grid is composed of at least 10^5 elements, which is adequate to recover the correct period as discussed by, e.g. Ferreira Lopes et al. (2018).

To minimize spurious peaks in the power spectra of the photometric data, the LS method was applied after the subtraction of the mean magnitude of each night. This procedure also removed possible long-term modulations present in the time series. Since the mean polarization is very small, no mean level was removed from the linear and circular polarization data. For some objects, we filtered low-frequency signals, such as the orbital period or any other known/detected low-frequency period of the system.

To have a realistic estimate of the uncertainty of a signal detected with the LS periodogram, we scrambled the y-coordinates of the correspondent time series, without repetition. Then we injected a signal centered at the detected frequency, but randomly distributed around a few frequency resolution elements and with a random reference epoch between $0 - 2\pi$. The amplitude of the injected signal was the amplitude derived from the LS periodogram. We ran this simulation 1,000 times. For each realization, it was calculated the difference between injected and recovered periods. The standard deviation of the difference, obtained from the median absolute deviation (MAD), is quoted as the uncertainty of the periods found in our analysis.

We compared the errors provided by the above simulations with two analytical estimates. From eq. 2 of Dorn-Wallenstein et al. (2020) (see also Lucy & Sweeney 1971), the period error, σ_P, is:

$$\sigma_P = \frac{\sigma P^2}{\pi T A}\sqrt{\frac{6}{N}}, \tag{1}$$

where P is the period, σ is the standard deviation of the data, T is the temporal baseline of the time series, A is the amplitude of signal at P, and N is the number of points in the time series. This error estimate is a good approximation for time series in which the counting of the cycles is not lost, as in a continuous time series. However, when the data collected are on different nights, which can be years apart, there is an additional error source and it can be shown that a more adequate estimate is:

$$\sigma_P = \frac{\sigma P}{2\pi A}\sqrt{\frac{2}{N}}. \tag{2}$$

In this expression, the cycle uncertainty was expressed by considering $T = P$. The uncertainty of the phase, corresponding to a factor equals to 1/12 in a uniform distribution, was not considered in Equation 2 in spite of being considered in Equation 1. The period errors from the simulation are of the same order of magnitude as the values obtained using Equation 2 for data spanning one or more nights. Therefore, this equation can be used as a quick estimate of period errors.

The emission from a likely magnetic accretion structure would be strongly diluted by the very bright accretion disk of SW Sex systems. Therefore, if present, the circular polarization and the amplitude of the spin-modulated emission must be very small, as is indeed observed in the known polarized SW Sex systems (see Appendix A). In order to avoid the detection of spurious signals but not lose real features, we adopted a set of criteria to check the reliability of the data sets, as described below.

We verified if the magnitude and polarization time series of our targets are correlated with those of the field stars. Correlations can be caused by instrumental effects, such as the usage of a rotating optical element in the observation procedure, that could cause some artificial modulation in the observed counts. To evaluate the presence of such a correlation, we initially calculated the Pearson correlation coefficient (PCC) between target and field-stars time series. Fig. 1 shows the PCC as a function of the ratio of the standard deviations of the field-star time series to those of the target stars. For most targets, we tested the data using more than one field star. Hence, Fig. 1 can have more than one point with a given symbol and colour. The points inside the light grey region have $|PCC| < 0.32$ and are considered as non-correlated data sets, while the dark grey bands indicate possible correlations ($0.32 < |PCC| < 0.70$). The limit of $|PCC| = 0.32$ was not an *a priori* assumed value. It results instead from the complete analysis of the correlation between the flux and polarization of field stars and target systems, which were inspected individually. Only a fraction of the data sets in the dark grey region were removed from the analysis.

The significance of a period was also assessed through the comparison of the science object power spectrum with those of field stars on a nightly basis. We removed from the analysis the data sets that showed similar peaks in science and field-stars periodograms. The last column of Table 1 states if a given data set was included in the analysis as a result of the procedure just described.

The small number of targets allow us to perform an individual and careful analysis of each source to take into account its peculiarities. Therefore, some adjustments to the above procedure were performed when required. The detailed analysis and results for each source are described in Section 4.

4. RESULTS AND ANALYSIS

In the following sections, we present an overview of previous findings, our results on a period search, and our analysis of the presence of magnetic accretion in each object of our sample. Table 4 presents the main periods found in the literature as well as those found in this paper.

4.1. *BO Cet*

BO Cet was first classified as a nova-like CV with $V \approx 14 - 15$ mag by Downes et al. (2005). Its spectrum displays the typical single-peaked H I emission lines of SW Sex systems, along with double-peaked He I and relatively strong He II 4686 Å emission lines (Zwitter & Munari 1995). BO Cet was classified as a non-eclipsing SW Sex star by Rodríguez-Gil et al. (2007a), who published a spectroscopic study of this source. The Hα trailed spectra show an S-wave with an amplitude of $\sim$300 km s^{-1}, with the bluest velocity and minimum intensity both occurring at phase 0.5, as well as a high-velocity S-wave component reaching $\sim$2000 km s^{-1}. This high-velocity component exhibits periodic emission-line flaring at a period of 19.9 ± 0.9 min, which is interpreted as the spin period of a magnetic WD. Its orbital period is estimated as 0.13983 d by Bruch (2017) based on the Center for Backyard Astrophysics (CBA) data. The only hitherto formally published photometric time series of BO Cet is by Bruch (2017). His data sets show strong flickering, and the orbital modulation is not always discernible. AAVSO[3] data taken over 2020 show an interesting variability pattern: BO Cet magnitudes oscillate between 13.6 and 16.2 mag in an approximate cadence of 2 weeks. This behavior suggests a possible Z Cam classification as already mentioned by Taichi (2018).

We observed BO Cet in the V and R$_C$ bands during three runs in 2010, 2016 and 2019 (see Table 1) with exposure times between 10 and 60 s. Our data do not show any significant variation in the average magnitude in the R$_C$ band, but the V band average varied by around 1 mag (see Table 1).

Our data are not suitable to refine the orbital period, since the individual data sets span time intervals comparable to or smaller than the suggested orbital period, and the long term data sampling introduces a huge aliasing structure in the power spectrum. Moreover, Bruch (2017) shows that an orbital modulation is not always clearly present in BO Cet photometry.

The following analysis includes only data from 2010 October 6, 11, 12, and 2016 October 19 (see Table 1),

---

[3] See https://www.aavso.org/LCGv2/

Table 4. Claimed periods from the literature and from our analysis. We indicate our periods having small confidence levels with a trailing question mark.

Object	Period	Data type	Interpretation	Reference
BO Cet	3.36 h	Photometry	$P_{\rm orb}$	1
	19.9 ± 0.9 min	Spectroscopy (Hα RV)	$P_{\rm spin}$	2
	19.6 ± 0.9 min	Spectroscopy (Hα EW)	$P_{\rm spin}$	2
	50.9 ± 0.5 min	Photometry	—	This work
	19.7 min	Photometry	—	This work
	15.3 min	Photometry	—	This work
	11.1 ± 0.08 min	Circular Pol.	$P_{\rm spin}$	This work
	9 min	Circular Pol.	$P_{\rm beat}$ (50.9 - 11.1)	This work
	14 min	Circular Pol.	$P_{\rm beat}$ (50.9 - 11.1)	This work
SW Sex	3.24 h	Photometry	$P_{\rm orb}$	3
	22.6 ± 1.4 min	Photometry	$P_{\rm spin}/2$	This work
	41.2 ± 8.5 min	Circular Pol.	$P_{\rm spin}$	This work
V442 Oph	2.98 h	Spectroscopy (RV)	$P_{\rm orb}$	4
	4.37 d	Photometry	P_W	5
	2.90 h	Photometry	$P_{\rm SH-}$	5
	16.66 min	Photometry	QPOs	5
	16.0 min	Photometry	QPOs?	5
	19.5 min	Photometry	QPOs?	5
	12.4 ± 0.09 min	Photometry	—	This work
	19.4 ± 0.4 min (?)	Circular Pol.	$P_{\rm spin}$	This work
	18.3 ± 1.1 min (?)	Linear Pol.	$P_{\rm spin}$	This work
V380 Oph	3.70 h	Spectroscopy (Hα RV)	$P_{\rm orb}$	2
	4.51 d	Photometry	P_W	6
	3.56 h	Photometry	$P_{\rm SH-}$	6
	46.7 ± 0.1 min	Spectroscopy (Hα EW)	$P_{\rm spin}$	2
	47.4 ± 4.9 min	Photometry (V band)	—	This work
	12.4 ±0.66 min	Photometry (B band)	$P_{\rm spin}$?	This work
	22.0 ± 1.2 min (?)	Circular Pol.	$P_{\rm spin}$?	This work
	12.7 ± 0.4 min (?)	Circular Pol.	$P_{\rm spin}$?	This work
LS Peg	4.2 h	Spectroscopy (Hα RV)	$P_{\rm orb}$	7,8
	20.7 ± 0.3 min	Photometry	QPOs	7
	19 min	Photometry	$P_{\rm spin}$?	9
	16.5 ± 2 min	Photometry	—	10
	19 min	Photometry	QPOs	11
	∼20 min	Spectroscopy	QPOs	12
	33.5 ± 2.2 min min	Spectroscopy	$P_{\rm beat}$	13
	29.6 ± 1.8 min	Circular Pol.	$P_{\rm spin}$	13
	30.9 ± 0.3 min[a]	X-rays	$P_{\rm spin}$	14
	21.0 ± 1.2 min	Photometry	$P_{\rm beat}$ ($P_{\rm orb}$ - $P_{\rm spin}$)	This work
	16.8 min	Photometry	—	This work
	19.3 min	Photometry	—	This work
	24.2 min	Photometry	—	This work
	18.8 ± 0.005 min	Circular Pol.	$P_{\rm spin}$	This work
	11.5 ± 0.1 min	Linear Pol.	$P_{\rm spin}/2$	This work
UU Aqr	3.9 h	Photometry	$P_{\rm orb}$	15
	4.2 h	Photometry	$P_{\rm SH+}$	16
	4 d	Photometry	—	17
	54.4 ± 0.5 min	Photometry	2 $P_{\rm spin}$	This work
	25.7 ± 0.23 min	Circular Pol.	$P_{\rm spin}$	This work

[a] This X-ray periodicity was not confirmed by later XMM observations (Ramsay et al. 2008).

Note—Symbols and acronyms used in this table are as follows. $P_{\rm orb}$: orbital period; $P_{\rm spin}$: spin period; $P_{\rm beat}$: beat period (the two periods causing the beat are presented between brackets); $P_{\rm SH+}$: positive superhump period; $P_{\rm SH-}$: negative superhump period; P_W: Disk wobble period; RV: Radial velocity; EW: Equivalent width.

References—(1) Bruch (2017), (2) Rodríguez-Gil et al. (2007b), (3) Groot et al. (2001), (4) Hoard et al. (2000), (5) Patterson et al. (2002), (6) Shugarov et al. (2005), (7) Taylor et al. (1999), (8) Martínez-Pais et al. (1999), (9) Garnavich & Szkody (1992), (10) Szkody et al. (1994a), (11) Szkody et al. (2001), (12) Szkody et al. (1997), (13) Rodríguez-Gil et al. (2001), (14) Baskill et al. (2005), (15) Baptista et al. (1996), (16) Patterson et al. (2005), (17) Bruch (2019)

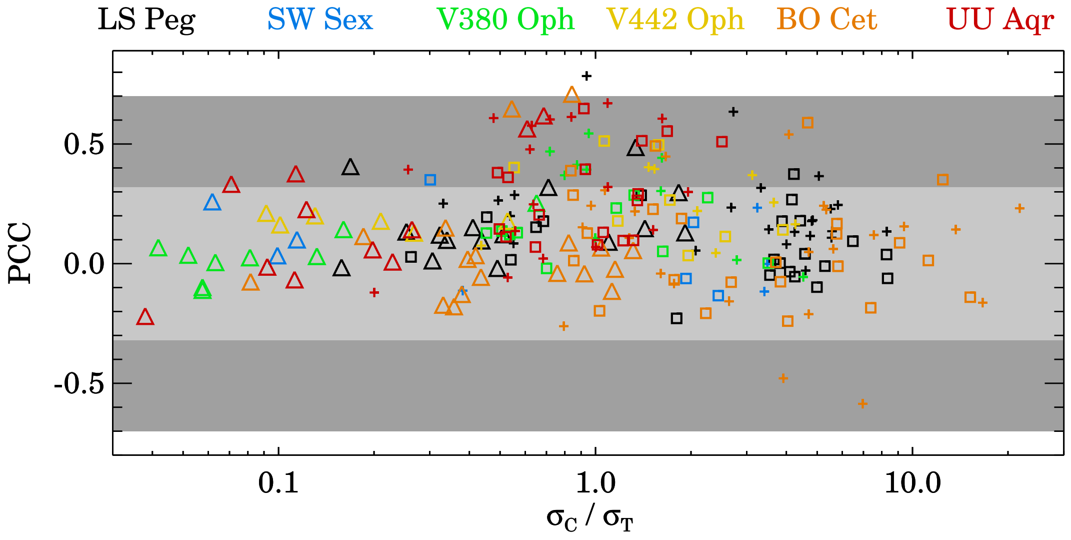

Figure 1. The Pearson correlation coefficient (PCC) as a function of the ratio of the standard deviation of the measurements of a given comparison star (σ_C) relative to the value of the target (σ_T). The triangles represent the photometric data, the plus signs refer to the circular polarimetry, and the squares denote linear polarimetry data. Different colours are used to distinguish each SW Sex star of our sample. We compare each target with more than one field star. This procedure results in a number of points having the same color and symbol. The points inside the light grey region do not present correlation, as explained in the text. The dark grey region contains data sets that should be inspected individually to verify the presence of correlation.

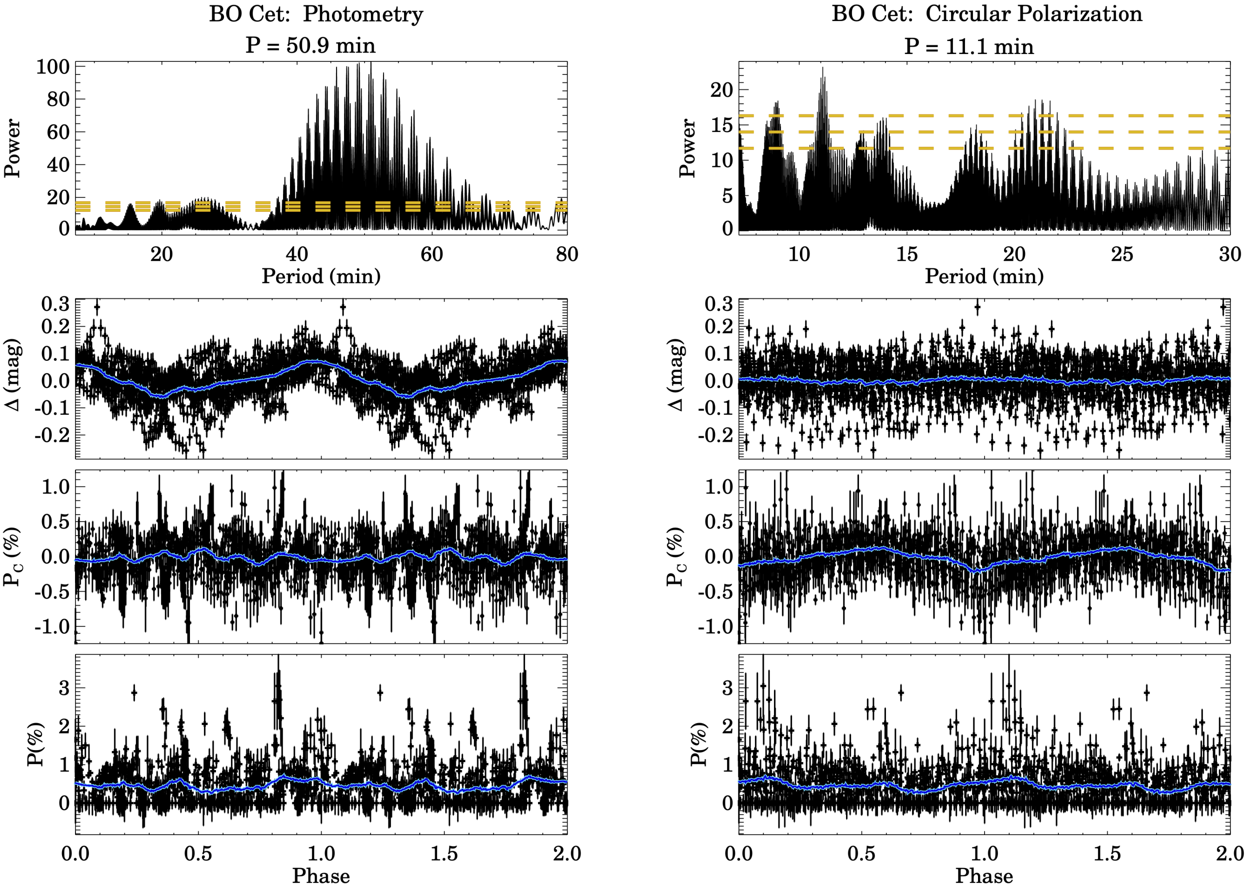
BO Cet: Photometry

P = 50.9 min

BO Cet: Circular Polarization

P = 11.1 min

Figure 2. Time-series analysis of BO Cet. First column: (Top panel) LS periodogram of the photometric data. The second, third, and fourth panels (from top to bottom) exhibit the magnitude, the percentage of circular polazation (P_C) and the percentage of linear polarization (P) data, folded with the 50.9 min period and an arbitrary zero phase. The second column follows the same structure of the first one, but the periodogram corresponds to the circular polarimetry data, and the curves are folded with the 11.1 min period. The dashed orange lines represent the FAP levels of 1%, 0.1%, and 0.01%, calculated according to Scargle (1982). The blue lines correspond to a central-moving average considering the points inside an interval of 0.05 in phase.

which do not show significant correlation with the measurements of the field stars, as described in Sec. 3. The photometric data were pre-whitened at the orbital period before the computation of the LS periodograms. The power spectrum peaks at P = 50.9 ± 0.5 min (Fig. 2). The strong 1-day aliasing structure hinders the determination of the exact value of this periodicity. But it is most likely real since it is well above the 0.01% false-alarm probability (FAP) line and is consistently present in the individual nights (not shown here) that are spread over a 6-years range. This peak is also present in the periodogram with no pre-whitening. The magnitude phase diagram shows a clear modulation with a semi-amplitude of around 0.05 mag (Fig. 2, second panel from top to bottom). A harmonic at around 25 min is present in the periodogram. Other peaks are seen at 19.7 min and 15.3 min.

The (no pre-whitened) circular polarimetric data show a periodic signal at 11.1 ± 0.08 min, as shown in the power spectrum of Fig. 2 (see top panel of the second column). This period is not present in the field stars, which gives us some confidence that it is not an artefact. The circular polarization data folded with the 11.1 min period reveals a sinusoidal modulation having both negative and positive polarization excursions and a semi-amplitude of around 0.1% (see the solid blue line).

Linear polarization measurements do not follow a normal probability distribution and are intrinsically biased (Clarke et al. 1983). In the case of BO Cet, the bias correction applied to the linear polarization data results in many points of null polarization. Even so, we performed the LS analysis. The power spectrum shows a variety of peaks in the region of 50 min, the same region of the strong signal in the photometry periodogram. The power of those peaks is slightly higher than the level of 0.01% of FAP. The curve folded using the strongest peak, at 54.4 ± 0.9 min, does not show any coherent variation, therefore we do not show any figure related to the linear polarization data.

The main circular polarization peak at 11.1 min has adjacent structures centered at about 9 min and 14 min (Table 4), which are consistent with the positive and negative beats of the main peak with the 50.9 min photometric main period. The presence of the beat periods between the main photometric and polarimetric peaks supports the reality of these periods. The periodicity of 11.1 min found in circular polarization corroborates that BO Cet could harbour magnetic accretion, as suggested by Rodríguez-Gil et al. (2007a). In this IP scenario, the photometric signal at ∼51 min could be associated with a continuum radiation source located in the inner disk region. In particular, this region could be at the magnetosphere radius, where the mass flow starts to follow the magnetic field lines and leaves the orbital plane.

Rodríguez-Gil et al. (2007a) found a period of 19.9 min from the radial velocities of the Hα line wings, consistent with a 19.6 min period from the equivalent widths of the Hα blue wing. They suggested this to be associated with the WD rotation period. As the origin of the circular polarization is more directly connected with the WD rotation, we suggest that the WD spin period is 11.1 min. Interestingly, our photometric power spectrum also shows a peak at around 19.7 min, which could be related to the line-emission source detected by Rodríguez-Gil et al. (2007a) diluted by continuum emission.

4.2. *SW Sex*

SW Sex, the prototype of the class, was discovered in the Palomar-Green survey by Green et al. (1982). Follow-up spectroscopy and photometry (Penning et al. 1984) showed high-excitation emission lines, a deep eclipse of 1.9 mag, and an orbital period of 3.24 h. A refined orbital period, 0.1349384411(10) d, was obtained by Groot et al. (2001). SW Sex has been observed in two brightness states considering its magnitude out of eclipse, which has mean values of ∼14.2 (high state) and ∼15.1 (low state) in unfiltered observations calibrated with Johnson V band zeropoint, according to observations available in the American Association of Variable Star Observers website (AAVSO). Spectroscopy performed in the bright state showed the typical central absorption in the Balmer emission lines between phases 0.4 and 0.6 (e.g. Szkody & Piche 1990). Spectrophotometric observations during the faint state of the system did not exhibit the absorption feature and emission-line flaring was not detected (Dhillon et al. 2013). No periodicity other than that due to the eclipses in broad band photometry is reported for this system. Circular polarimetric observations by Stockman et al. (1992) revealed no significant circular polarization in the 3200 – 8600 Å range, with values as low as 0.05 ± 0.14% in a single 8 min integration and -0.03 ± 0.05% in 16 min. However, in a paper about the detection of circular polarization in LS Peg, Rodríguez-Gil et al. (2001) made a side note about a period of 28 min detected in the B band circular polarization of SW Sex.

SW Sex was observed by us on one single night (March 29, 2014). A time series of R_C measurements was made during 3.9 h covering one complete orbital cycle and one total eclipse. The mean magnitude out of eclipse in our photometric data is R_C= 14.66 mag, indicating that the system was in a high brightness state. The folded light curve shows a deep eclipse with amplitude of 1.6 mag, as expected (Fig. 3, first column).

The folded polarization data reveal an increase in the absolute values of circular and linear polarizations during the eclipse (Fig. 3, bottom panels). This could be interpreted as a polarized emission component that is diluted by an unpolarized light source out of eclipse. During the eclipse, part of the unpolarized component is occulted, thus reducing the dilution and making the net polarization of the system larger. Reasonable guesses as to the origin of the polarized and unpolarized components are the PSR region of a magnetic accretion column and the accretion disk, respectively. The eclipse of the PSR region could also occur. It would last less than the disk eclipse, because the PSR region is much smaller. In the polars FL Cet and MLS110213 J022733+130617, the PSR region is eclipsed during an interval of about 0.05 in the orbital cycle (O'Donoghue et al. 2006; Silva et al. 2015, respectively). In this case, the polarization should drop to zero around the middle of the eclipse, producing an "M" shaped polarization pattern. As it is not observed, we can conclude that the PSR region is not eclipsed in SW Sex.

To perform the period search, we removed the points associated with the eclipse from the dataset and then subtracted the orbital modulation using a third-order polynomial fit to the photometric data (e.g. Basri et al. 2011; Ferreira Lopes et al. 2015). The resulting power spectrum has one significant peak at 22.6 ± 1.4 min (see Fig. 3). This peak is also present, but with a lower power, if we do not subtract the orbital modulation. The light curve folded at this period displays a modulation with an amplitude of about 0.11 mag.

The period search in the polarimetric data was also performed removing the eclipse points. The periodogram of circular polarization shows a peak at 41.2 ± 8.5 min. The mean polarization in the phase diagram ranges between -0.2% and 0.2% (blue line in circular polarization panel of the last column of Fig. 3). Interestingly, the photometric period (22.6 min) is consistent with the first harmonic of the period found in polarimetry (41.2 min), considering the uncertainties in the peak positions. The phase diagrams of the photometry using these two periods in Fig. 3 illustrate this. The linear polarization folded with the 41.2 min period shows a relatively well organized phase diagram. However, the highest peak in linear polarization occurs at 12.7 ± 0.7 min (below the adopted FAP levels) and the corresponding phase diagram is very noisy. Hence, we do not discuss it here. Probably, the time-series analysis of the linear polarimetry is affected by the large number of measurements consistent with zero, due to the large errorbars.

Some IPs (e.g. V405 Aur and UU Col, Piirola et al. 2008; Katajainen et al. 2010, respectively) show two maxima in the flux phase diagram, associated with positive and negative circular polarization. Our data suggest that this can also be true for SW Sex. This finding and the increase in the polarization during the eclipse support the presence of a magnetic WD rotating at around 41 min in SW Sex. Additional polarimetric observations having a longer time span would be useful to confirm these results.

4.3. *V442 Oph*

V442 Oph was identified as a CV by Szkody & Wade (1980). The typical V band brightness of V442 Oph fluctuates between around 13.2 and 14.2 mag (Szkody & Wade 1980; Szkody & Shafter 1983; Patterson et al. 2002). However, AAVSO data show that it can be as faint as 15.5 mag. This is somewhat confirmed by Patterson et al. (2002), who affirmed that the 14 mag state corresponds to a high state. However, those authors do not mention the maximum magnitude of V442 Oph in their data. Some spectral features point to a classification as a low-inclination SW Sex star (Hoard et al. 2000): single-peaked emission lines, strong He II 4686 Å emission line, a transient absorption at 0.5 phase in the Balmer and He I lines, and a high-velocity component in Hα at $\approx \pm 1900$ km s^{-1}. Their spectroscopic dataset settled the orbital period as 0.12433 d (2.98 h). Long photometric campaigns show persistent modulations with periods at 4.37(15) d and 0.12090(8) d, which are interpreted as the wobble period of the disk and a negative superhump, respectively (Patterson et al. 2002). At higher frequencies, the system displays rapid flickering and periodicities around 1000 s, interpreted as QPOs. In the QPO structure of the periodogram of the best quality data, there are two distinguishable peaks at 74.0 and 89.9 cycles per day (19.5 and 16.0 min). Circular polarimetry obtained in two nights provided 0.01% ± 0.05% and -0.03% ± 0.08% with 16 min and 8 min of total integration times, respectively (Stockman et al. 1992). These values are consistent with no net circular polarization averaged over the time interval of the measurements.

We observed V442 Oph for a total of 4.06 h spread over two nights: 2014, March 29 and 2014, July 20 (Table 1). Light curves in R_C and V filters were obtained using exposure times of 20 s and 30 s, respectively. The time series has some gaps repeating on time scales of half an hour, so we limit our analysis to a maximum period of 30 min. The mean magnitudes during each day of our observations are quite similar, $R_C = 13.37$ mag and $V = 13.60$ mag. Such values indicate that we observed V442 Oph in its typical high state.

We performed a period search in the R_C and V photometric time series independently and found a period of around 12 min in both cases. No pre-whitening or detrending was applied to the data. Finding the same period in two independent data sets, obtained about four months apart, suggests the presence of a stable periodicity in V442 Oph. The power spectrum of the combined photometry has a prominent peak located at 12.4 ±0.09 min (see first column of Fig. 4). The data folded using this period and an arbitrary epoch at HJD 2456859.4033 show a near sinusoidal profile with a semi-amplitude around 0.04 mag (second panel). The folded circular polarimetric curve also shows a slight modulation with an amplitude of around 0.1% (blue line in the third panel). A peak at 19.9 min with 0.1% false-alarm probability merits attention, since it also appears in the circular and linear power spectra — see below.

The power spectra of the circular and linear polarization show peaks at 19.4 ± 0.4 and 18.3 ± 1.1 min, respectively, which are below the FAP lines of 0.1% (Fig. 4, middle and right columns). The data folded at these periods do not show clear modulations, but we suggest that there could be a real periodicity of the system around 19 min. Besides being present in the periodograms of flux, circular and linear polarizations - even though with a weak signal - a similar period is also found by Patterson et al. (2002, see Table 4). They commented that the modulation semi-amplitude at this frequency is around 0.01 mag and that it is not easily detectable among other

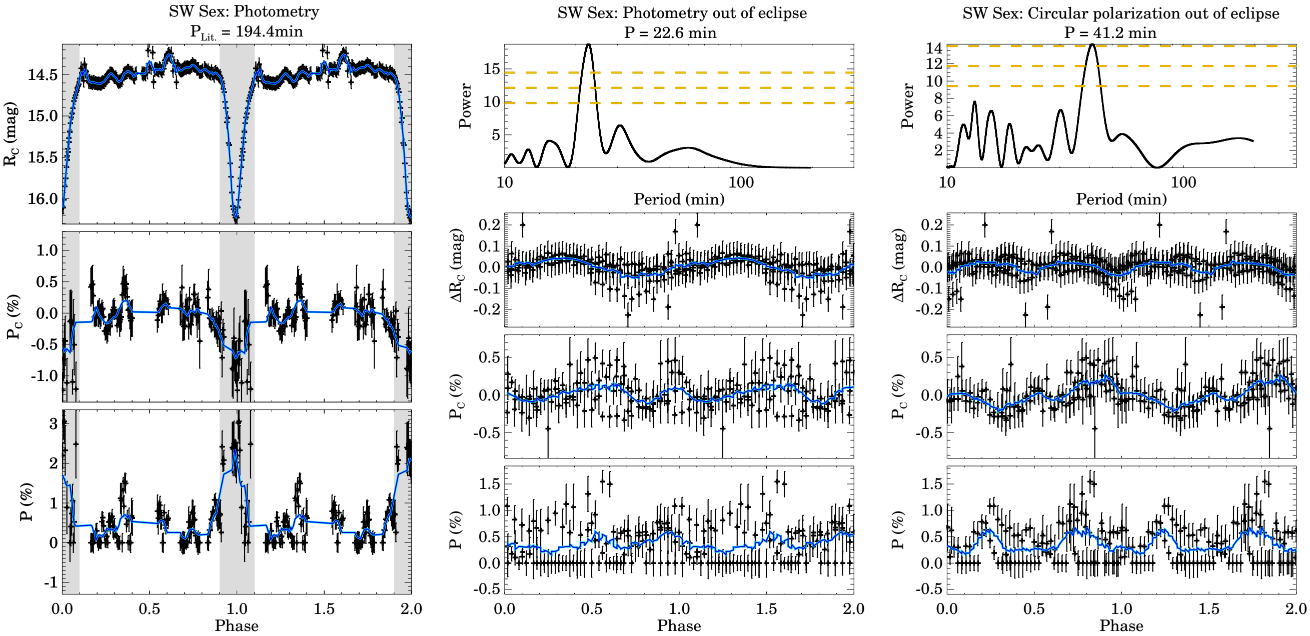

Figure 3. Time-series analysis of SW Sex. First column: Phase diagrams of the photometry, circular polarimetry (P_C) and linear polarimetry (P) data, folded with the orbital period and T_0 = 2456746.704430 HJD. The eclipse phases are highlighted by the gray bar. The points in this region were not considered in the analysis presented in the following columns. Second column: the top panel shows the LS periodogram of the photometry, after subtracting the orbital modulation (see text). The panel below presents the phase diagram of the magnitude folded with P = 22.6 min and arbitrary zero phase. The third and fourth panels from top to bottom show the folded circular and linear polarization, respectively. The last column follows the same structure of the second column, but for circular polarization. The lines are colour-coded as in Figure 2.

variability also present in the light curves, features which are consistent with our folded curves. As this period is present in our polarimetric data, its natural explanation is the WD rotation.

In spite of the low signal, we suggest that the 19.4 min modulation found in V442 Oph is due to the WD rotation. However, we have no explanation for the 12 min modulation seen in the total flux. In particular, we could not explain this modulation as a beat between other periodicities of the system.

4.4. *V380 Oph*

V380 Oph was reported as a nova-like CV with orbital period of 3.8 h based on spectroscopic observations (Shafter 1985). Using archival data and new photometric observations, Shugarov et al. (2005) showed that V380 Oph is usually at 14.5 mag, but underwent a faint state (around 17 mag) in 1979. Hence, they suggested that the system can be classified as a VY Scl object. Indeed, the VY Scl behaviour of V380 Oph is confirmed by additional data presented by Shugarov et al. (2016) and the light curves available at AAVSO. Shugarov et al. (2005) also found two photometric periods, 3.56 h and 4.51 d, interpreted as due to negative superhumps and an eccentric wobbling accretion disk, respectively. Time-resolved spectra obtained by Rodríguez-Gil et al. (2007a) show the standard characteristics of the SW Sex class, single-peaked emission lines and a high-velocity S-wave in the Hα trailed spectra. Their radial-velocity curve provided an orbital period of 3.69857(2) h, consistent with the period obtained by Shafter (1985). They also suggest the presence of rapid flaring in the line wings with a periodicity of 46.7 ± 0.1 min, which they proposed as the rotation of a magnetic WD. Optical photometry of V380 Oph performed by Bruch (2017) is consistent with an orbital modulation and reveals a flickering activity that is compatible with those of VY Scl systems. White-light circular polarimetry was performed by Stockman et al. (1992), who obtained a signal consistent with zero, P_C = -0.12 ± 0.16%, in a short 8 minute integration.

V380 Oph is the only object of our sample for which we have additional data obtained from observatories other than OPD (see Section 2 and Table 1). We reanalyzed the SOS/SAS V380 Oph photometric data (Shugarov et al. 2016) obtained from 2002 to 2016 searching for short periods possibly associated with the WD rotation.

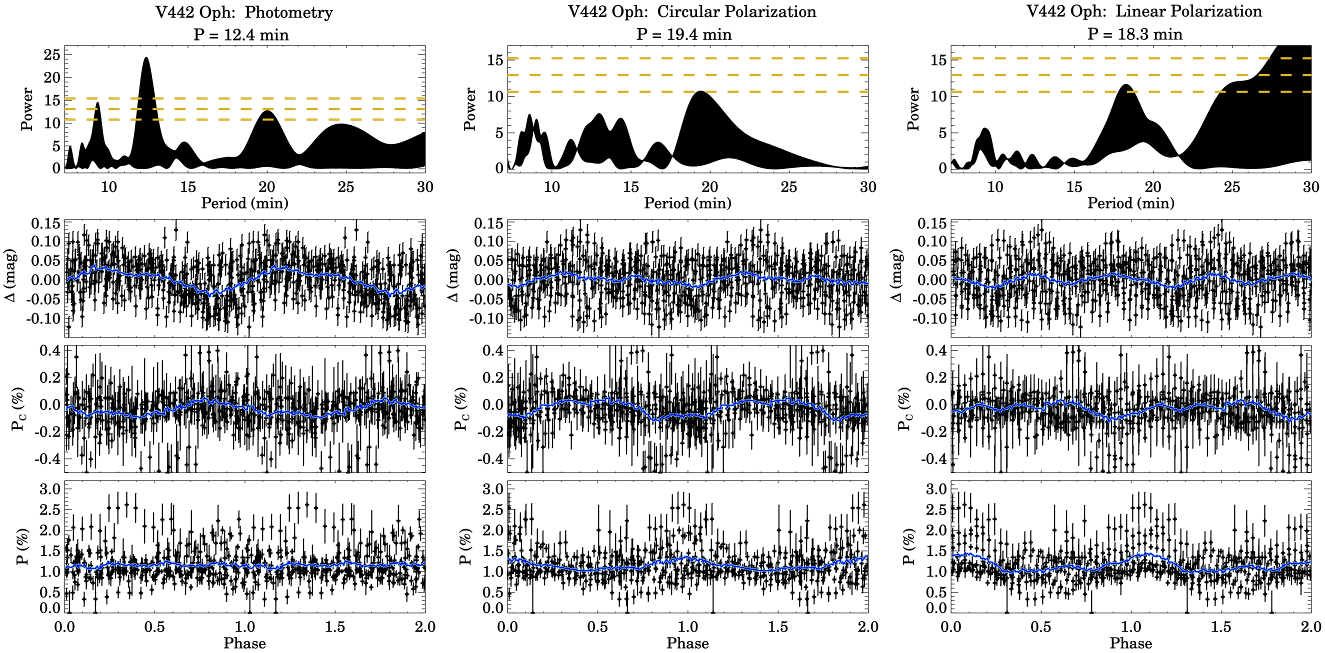

Figure 4. Time-series analysis of V442 Oph. First column, from top to bottom: the LS periodogram from photometry; the phase diagram of the magnitude folded with 12.4 min and an arbitrary zero phase; the same as above for the circular polarization; and the phase diagram of the linear polarization using the same period. The second and third columns follow the same structure of the first column, but the periodograms are done using the circular and linear polarization data, respectively. The orange and blue lines follow the definition of previous figures.

Typically, V380 Oph has a mean magnitude of approximately 15 mag (high state). During three nights on 2015 July 15 to 22, a low state was detected in the R_C band with an average brightness of 18.8 mag.

Initially, we present the periodicity analysis of the time series obtained at SOS/SAS observatories. The V band data were obtained over many years and are characterized by data blocks with time spans from around 1 to 4 h. The LS power spectrum (not shown here) is very complex. It shows a clear signal at around 4.5 d, as previously reported. The peak is broad and highly structured. A stronger and narrower peak at around 1.3 d is also present. We have filtered the time series using the main peaks relative to periods on a timescale of days. The periodograms remain very complex with many peaks on timescales of hours and days. No clear signal on a minutes timescale could be found. We also studied the data sets on a daily basis and no clear signal appears. We applied the CLEAN technique (Roberts et al. 1987) in order to verify if we could obtain a better understanding of the photometric variability, but the results are essentially the same as those obtained using the LS method. The R_C data in the bright state are sparser and have shorter daily data blocks compared to the V band. The results are essentially the same for both bands. The R_C data set in the low state is composed of 3 daily blocks: no clear periodicity is found. The *B* band periodogram has a very broad feature at around 55 min, which is badly constrained by the short time span of about 2 h. Similar features are present in some power spectra of the V and R_C daily data blocks. A peak at 12.4 ± 0.66 min is present below a FAP of 1%. Fig. 5 (left column) shows the power spectrum and the B band data folded on 12.4 min. There seems to be a coherent modulation of the circular polarization at this period. After removing the orbital modulation, only the 12 min peak remains, yet below the 1% FAP.

Our OPD observations were performed in the V band on a single night, 2014 July 19, having a total time span of ~2.7 h with 40 s of exposure time. The system was in the usual high state at around 14.5 mag. The power spectrum of the photometry shows a periodicity at 47.4 ± 4.9 min (Fig. 5, middle column). This period is in the upper limit of the range of reliable periods due to the total time span of the observation. However, it is consistent with the ~47 min flaring period reported by Rodríguez-Gil et al. (2007a).

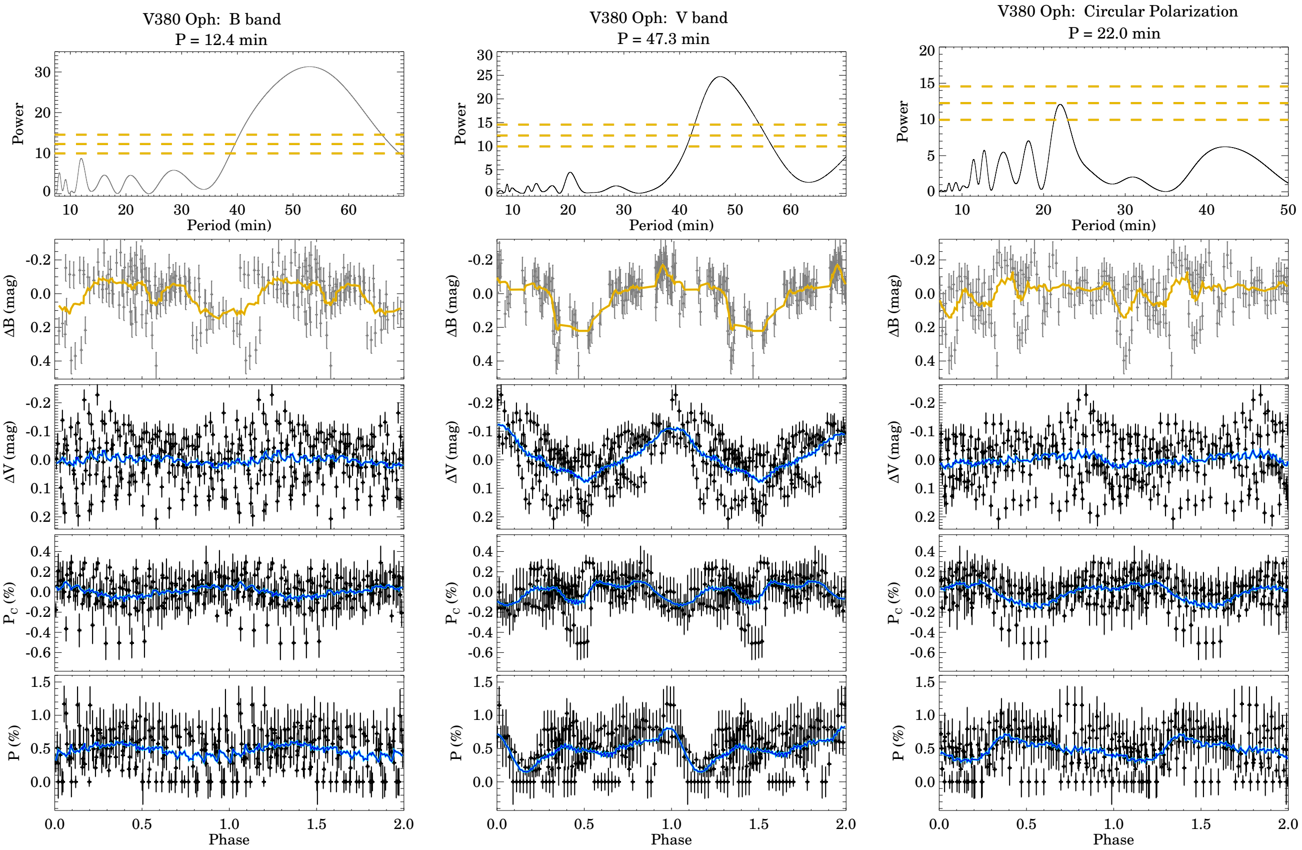

Figure 5. Time-series analysis of V380 Oph. First column: B band photometric data from SOS/SAS observatories. Second column: V band photometric data from OPD observatory. Third column: V band circular polarimetric data from OPD observatory. From top to bottom: the power spectrum; the phase diagrams of B band and V band photometry, and circular and linear polarizations. The coloured lines are as defined in Figure 2.

The circular polarimetry periodogram shows a peak at 22.0 ± 1.2 min with a level similar to the 0.1% FAP (Fig. 5, right column). After removing the orbital modulation, we obtained a period at 12.7 ± 0.4 min above the 0.01% FAP (not shown), which is similar to that found in the B band data obtained at the SOS/SAS observatories. In this case, the modulation in circular polarization is similar to that shown in Fig. 5, left column, therefore we do not present a figure with exactly this period. In the linear polarimetry data, we found 17.7 ± 1.5 min. However, the same period is also found in one field star, consequently this period can be related to instrumental effects and is suspicious.

In addition to its complex photometric behaviour, V380 Oph also shows variation in the measured values of the radial velocity amplitude depending on its brightness state (see Szkody et al. 2018, and references therein), which could be related to the variation of the accretion-disk size. Zellem et al. (2009) obtained the UV spectrum of V380 Oph, which is too red to be fitted with an optically-thick accretion-disk model. A possible interpretation is an accretion disk truncated in its inner parts in an IP-like configuration. These facts together with the presence of line flaring (Table 4) and a possible periodicity in circular polarimetry may indicate magnetic accretion. But, we consider additional polarimetric and spectroscopic observations are important to corroborate these findings.

4.5. *LS Peg*

LS Peg was classified as a CV by Downes & Keyes (1988). It has high and low states ranging from V = 12 to 14 mag (Garnavich & Szkody 1992). UV spectra at the high state led Szkody et al. (1997) to propose LS Peg as a non-eclipsing SW Sex object. Taylor et al. (1999) estimate an orbital period of 0.174774(3) d based on radial velocity curves. The same orbital period was almost simultaneously reported by Martínez-Pais et al. (1999). The first detection of modulated circular polarization in an SW Sex system was obtained for LS Peg: the circular polarization values were the result of the integration in the 3900 – 5070 Å range of spectropolarimetric data and are consistent with a periodicity of 29.6 ± 1.8 min and amplitude of $\sim 0.3\%$ (Rodríguez-Gil et al. 2001). Those authors suggested that this modulation corresponds to the WD spin. That paper also shows the presence of flaring in the Hβ emission line with a period of 33.5 ± 2.2 min, which the authors interpreted as the beat period between the WD spin period (29.6 min) and the orbital period. Baskill & Wheatley (2006) reported a detection of a period at 30.9 ± 0.3 min in X-ray data obtained by ASCA SISO (2 – 8 keV). However, this modulation was not confirmed by the XMM-Newton observations of LS Peg in the 0.1 – 12 keV energy range (Ramsay et al. 2008). These authors mentioned that the X-ray spectrum of LS Peg is similar to those of IPs. Later, Szkody et al. (2018) suggested that LS Peg may be a magnetic CV with a WD rotation period around 20 min due to a conspicuous photometric modulation. However, it is uncertain if this period is stable in time. Examples of periods cited in the literature are: 19 min, 16.5 ± 2 min, and 20.7 ± 0.3 min (Garnavich et al. 1988; Garnavich & Szkody 1992; Szkody et al. 1994b; Taylor et al. 1999; Szkody et al. 2001).

Our data on LS Peg were obtained on 7 nights between 2010 and 2019 in the V and R_C bands (Table 1). The photometric light curves show a mean magnitude of 11.9 mag and 11.7 mag in the V and R_C bands, respectively. Data from two nights were removed from the periodicity analysis (see Sect. 3) that was performed combining the data in three ways: all observed bands, combining data by filters, and the individual nights.

The mean magnitude was subtracted from the photometric data set of each night, which were also filtered to remove low-frequency modulations. The resulting power spectrum exhibits the strongest peak at 21.0 ± 1.2 min (see top of the first column of Fig. 6). This period is consistent night-by-night, except for two of them (see Table 5). However, these nights do have a secondary peak around 20 min. The light curve folded on the 21 min periodicity shows a sinusoidal modulation with a semi-amplitude of 0.02 mag. Circular and linear polarization combining the two bands and folded on the same period do not show a coherent variability (see first column of Fig. 6). The other "high-frequency" peaks seen in the power spectra are 16.8 and 24.2 min. A peak at 19.3 min superimposed on the main peak is also present. Taylor et al. (1999) found a photometric period of 20.7 min in a photometric time series collected on 12 nights spread over 18 days. The modulation was not stable in phase. Modulations around 19 min and 16 min have already been reported by Garnavich & Szkody (1992) and Szkody et al. (2001).

Table 5. Periods found in the LS Peg data set.

Data type	Date Obs.	Period (min)
Photometry	All nights	21.0 ± 1.2
	2010 Oct 06	21.4 ± 4.0
	2010 Oct 12	19.7 ± 1.7
	2016 Oct 19	40.3 ± 6.7
	2019 Sep 10	23.3 ± 3.7
	2019 Sep 12	13.9 ± 1.4
Circular polarimetry	All nights	18.8 ± 0.005
	2010 Oct 06	19.0 ± 1.6
	2010 Oct 12	18.6 ± 1.2
	2016 Oct 19	44.4 ± 5.8
	2019 Sep 10	18.4 ± 3.4
	2019 Sep 12	17.8 ± 2.1

Circular polarization data were not prewhitened. The periodogram of the entire data set shows a sharp peak centred at 18.8 ± 0.005 min (see top of the second column of Fig. 6). This same period is also seen if we combine all 2010 data or all 2019 data. This suggests that LS Peg has a stable periodicity in circular polarization along a baseline of 9 years. As in photometry, the main peak in the periodogram of 2016 October 19 occurs at around 40 min (see Table 5). The circular polarization curves folded on 18.8 min exhibit positive and negative excursions with semi-amplitudes of 0.05% (blue line in third panel of second column of Fig. 6). The photometry and linear polarization do not show clear modulations at this period (see last panel).

The periodograms of the linear polarization data show strong signals at low frequencies. Hence, we prewhitened the data and found a peak at 11.5 ± 0.1 min, which could be related to half of the photometric 21 min period. A possible origin of this modulation could be the reflection (scattering) of the PSR region emission in the inner regions of the disk.

As stated above, Rodríguez-Gil et al. (2001) also detected modulated circular polarization. They found a period of 29.6 min using 19 circular polarimetry spectra with a time resolution of about 10 minutes, which results in a Nyquist frequency of around 20 min. Therefore, their data were not adequate to search for periodicities of the order of those previously found in photometry.

The periodic signals found in LS Peg (Table 4) can be interpreted in terms of WD spin, QPOs, orbital period, or the combination of those as beat periods. Since the best explanation for the presence of circular polarization is cyclotron emission from a PSR region on the

WD surface, the circular polarization modulation must be attributed to the rotation of a magnetic WD. Hence, our results indicate that the period of ∼19 min is the spin period of the WD, consistent with previous suggestions (e.g. Szkody et al. 2018). In such a scenario, the photometric 21 min can be, within the uncertainties, the beat period between the WD spin period and the orbital period. This interpretation is in line with the linear polarization modulation at around 11 min being caused by internal scattering, since beat periodicities are usually associated with reflection of internal sources on the accretion structures.

V795 Her has spectroscopic properties very similar to LS Peg (Taylor et al. 1999; Martínez-Pais et al. 1999), indicating a similar mass accretion configuration. This object has non-null circular polarization modulated at a period of 19.54 min (Rodríguez-Gil et al. 2002), close to the periodicity attributed to QPOs in LS Peg. So, in a comparative way, this reinforces the presence of a magnetic WD in LS Peg.

4.6. *UU Aqr*

The variability of UU Aqr was discovered by Beljawsky (1926). More than half a century later, Berger & Fringant (1984) found that the object has a strong UV excess. Photometric monitoring performed by Volkov et al. (1986) and Volkov & Volkova (2003) confirmed the UV excess and revealed that UU Aqr has deep eclipses up to 2 mag and strong flickering outside the eclipse, establishing UU Aqr as a CV. Using multiwavelength eclipse mapping, Baptista et al. (1996) suggested that UU Aqr is an SW Sex object. This was confirmed by Hoard et al. (1998) based on spectroscopic features, even though the He II 4686 Å emission line is weak in comparison with Hβ and the line absorption is deepest at orbital phase ∼0.8. UU Aqr has an average magnitude outside the eclipse of 13.5 mag with an eclipse depth around 1.4 mag (see Fig. 1 in Baptista & Bortoletto 2008). In the high state, a bright spot on the outer edge of the disk changes the shape of the eclipse profile. Its orbital period is 0.163580487(2) d (Borges B. & Baptista R., private communication). Using data collected in 2000, Patterson et al. (2005) found a period of 4.2 h that is attributed to the superhump phenomenon. However, Bruch (2019) did not detect superhumps in data obtained in 2018 September, only regular variations with a period of about 4 days.

UU Aqr was observed during five nights distributed between August and October 2009 (see Table 1). The V filter was used in all observations and the exposure times range between 4 s and 15 s. The magnitude was stable during those nights with an average value of V ≈ 13 mag. The magnitude dispersion in our data is around 0.1 mag for most nights. We found a large correlation between the photometry and polarimetry of UU Aqr and those of the field stars on some nights, so they were not considered in the analysis (see Table 1). We also removed the observations obtained during the eclipses.

The power spectrum of the photometric data applying no filtering shows a strong peak at 54.4 ± 0.5 min (Fig. 7). The peak is also present if we subtract the orbital modulation from the data. The folded light curve displays a clear modulation with a semi-amplitude of around 0.2 mag. The large dispersion around the average is due to the orbital flux modulation. The average folded polarimetric data suggests a regular pattern (see the blue line in the third panel of the first column of Fig. 7).

We did not subtract the low frequencies from the circular polarimetric data. The periodogram shows the strongest peak at 25.7 ± 0.23 min (see second column of Fig. 7). This peak is also present in the periodograms of the individual nights, supporting the persistent nature of this periodicity. The phase diagram of the circular polarimetry shows a modulation with peak-to-peak amplitude of 0.1% (blue line). We did not find any statistically significant periods in the linear polarimetry.

As already discussed for the other objects, the only possible explanation for a periodic variability in circular polarization is the presence of a PSR region near the WD surface. Hence, the 26 min periodicity could be associated with the spin period of a magnetic WD. An argument in favour of this is the presence of a modulation with nearly twice this period in the photometry (Table 4). Another indirect evidence of a magnetic WD in UU Aqr comes from the observation of variability on timescales of 0.5 − 5 days during stunted outbursts (Robertson et al. 2018) who suggested it to be caused by “blobby” accretion associated with the fragmentation of the stream by the WD magnetic field.

In order to confirm the stability of the 26 min period and consequently the magnetic nature of the WD in UU Aqr, it is necessary to obtain additional polarimetric data. It is important to mention that the strong flickering of UU Aqr makes it difficult to search for real periodic variabilities. The flickering is not polarized but, being a variable emission that dilutes the polarization, it can introduce noise in the polarization signal. It can also produce fake peaks in the total flux periodogram.

5. DISCUSSION

5.1. *Present status of circular polarization measurements of SW Sex systems*

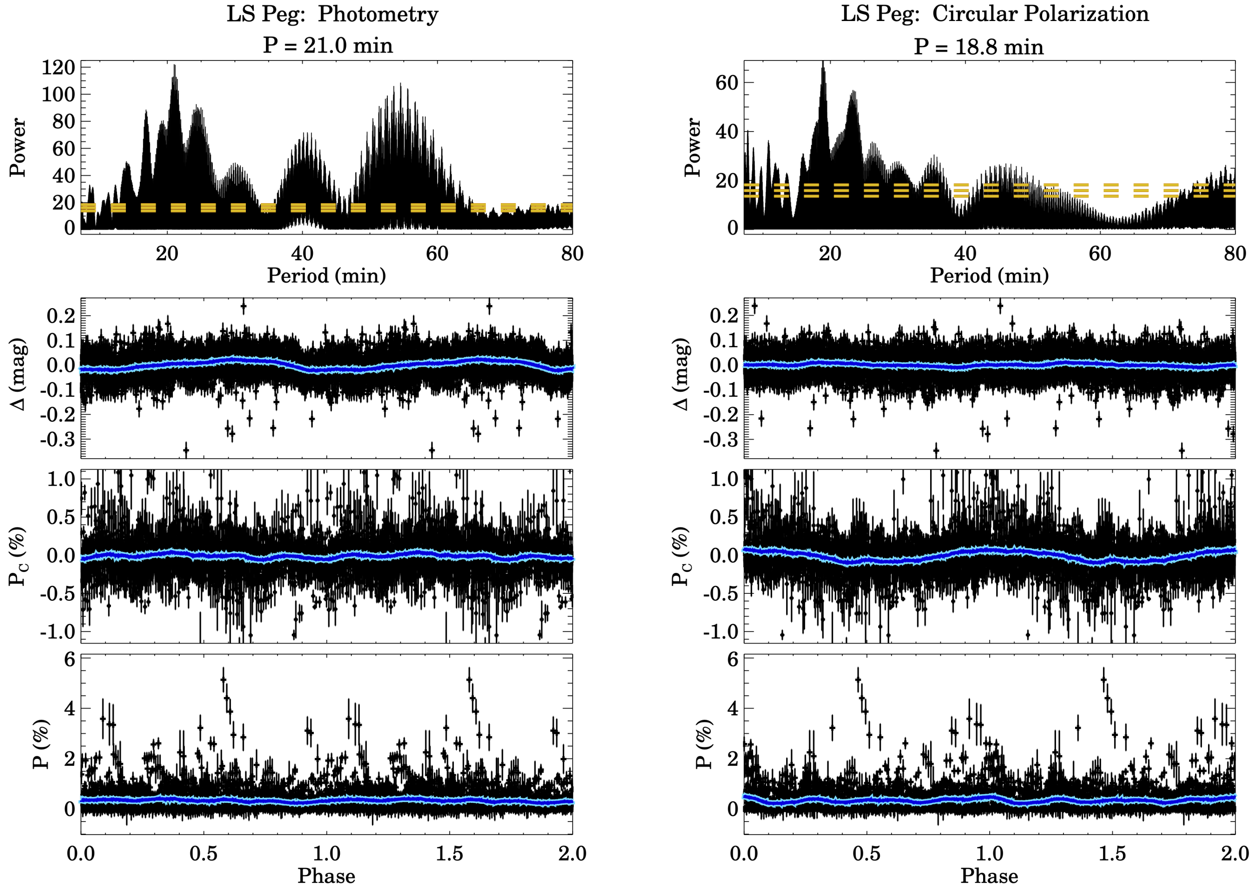

Figure 6. Time-series analysis of LS Peg. The first column shows, from top to bottom, the power spectrum of the photometric data in the V and R_C bands and the phase diagrams of photometry, circular and linear polarimetric data, folded on the period P = 21 min and arbitrary zero phase. The second column has the same structure of the first one, but the power spectrum is calculated for the circular polarization and has a peak at 18.8 min. The lines are colour-coded as in Figure 2.

We have performed polarimetry of 6 definite SW Sex systems. In four of them (BO Cet, SW Sex, LS Peg, and UU Aqr), we have found evidence of modulated circular polarization. For V442 Oph and V380 Oph, the detection of circular polarization is uncertain.

Table 8 summarises all circular polarization measurements of SW Sex systems. This table is strongly based on information presented in The Big List of SW Sex Systems of Hoard et al. (2003). We included the results of this paper and made some other changes, as follows. RR Pic is quoted as polarized in The Big List, but this measurement refers to linear polarization, which could originate from other mechanisms than emission from the PSR region. Therefore, it is not evidence of magnetic accretion and, hence, it is not included in Table 8. We have also changed the "polarized" classification of AO Psc from "N?" to "Y?", since it has some evidence of modulation in circular polarization, but the errors are not small enough to confirm it. This object is also classified as an IP (e.g. Butters et al. 2009)[4]. As a result, our table lists 27 systems, including BO Cet and UU Aqr for which the first measurements are presented here. The first lines of the table group the objects having confirmed or possible non-null circular polarization.

A large fraction of the polarimetric observations of SW Sex systems was performed by Stockman et al. (1992). Their observations consist of a single or a few measurements. Each measurement is the result of data taken over an interval of 8 min (or even longer), which is inadequate to detect the circular polarization in these objects because the timescale of the modulation is usually of this same order, causing the smearing of an in-

---

[4] There are other objects in The Big List that are also classified as IPs. Some of them will be cited later in this discussion.

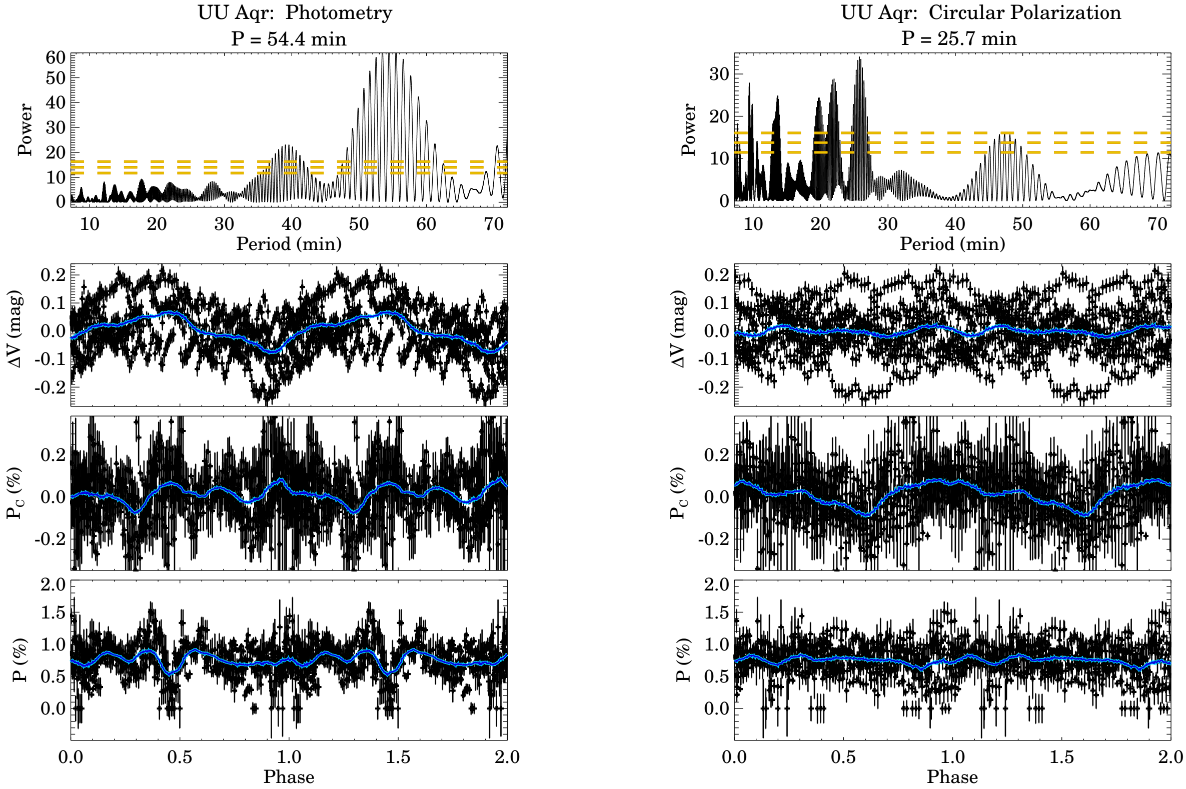

Figure 7. Time-series analysis of UU Aqr. From top to bottom, the power spectrum of the photometry and the phase diagrams of photometry, circular and linear polarization. The first column shows the photometric results and the second column presents the period search in circular polarization data. The coloured lines are as defined in Figure 2.

trinsically low polarization signal, when present. Hence, their negative detections are unreliable. Some other measurements in Table 8 classified as "polarized = N?" refer to long integrations with the same caveat of Stockman et al. (1992)'s measurements. High signal-to-noise ratio (polarization error smaller than 0.1%) and time-resolution of around 1 min are necessary to detect circular polarization in SW Sex systems.

According to The Big List, there are 73 objects classified as SW Sex. They are divided into 30 definite, 18 probable, and 25 possible candidates. Table 8 lists 11 objects with some evidence of non-null circular polarization: this results in 15% of SW Sex systems with evidence of magnetic accretion from polarimetry. This is a non-negligible fraction since few objects have been observed with enough sensitivity and time resolution. If we consider only the definite SW Sex members, we obtain 33% (10/30) of possible polarized objects. Taking into account only objects with confirmed modulated circular polarization, this fraction decreases to 23% (7/30).

The above numbers may reveal the presence of magnetic WDs in a considerable fraction of SW Sex stars. More polarimetric observations like the ones presented in this paper are in demand to confirm previous measurements and expand the sample of observed SW Sex objects.

5.2. *Periodicities in asynchronous magnetic CVs*

In this section, we discuss the main findings related to rapid variability in SW Sex and compare them with what is observed in IPs.

SW Sex systems usually show complex photometric variability. In some systems, periodicities related to the WD rotation, orbital cycle, or sidebands have been found, similar to what is observed in some IP systems (e.g. Warner 1986; Norton et al. 1996). Superhumps, with periods slightly longer or shorter than the orbital period, are also present in some systems and are attributed to the precession of an eccentric accretion disk or disk warping. Another photometric variability common in the SW Sex class is quasi-periodic oscillations with time scales of 1000 s. Patterson et al. (2002) present a review of these different kinds of variability and propose that some of them can be explained by a magnetic WD.

Non-orbital emission line periodicities are found in IPs as well as in SW Sex stars. They can be observed as a modulation of the total emission line flux or as "flares" in the line wings. In IPs, they are associated with the WD spin or the beat of the WD spin and orbital period. Examples of detailed studies of spin-phase resolved spectroscopy of IPs are Marsh & Duck (1996, FO Aqr) and Bloemen et al. (2010, DQ Her). Doppler tomography phased on the spin cycle of seven IPs is presented by Hellier (1999). V1025 Cen is an example of the complex variability behaviour in IPs (Buckley et al. 1998), for which the interpretation of the observed periods and the relation between values found in photometry and spectroscopy are not straightforward. Rapid spectroscopic variability has been found in 8 definite and 2 possible SW Sex systems: EX Hya (Kaitchuck et al. 1987), which is classified as a possible SW Sex system by Hoard et al. (2003); LS Cam (Dobrzycka et al. 1998); BT Mon (Smith et al. 1998); LS Peg (Rodríguez-Gil et al. 2001); V533 Her (Rodríguez-Gil & Martínez-Pais 2002); BO Cet and V380 Oph (Rodríguez-Gil et al. 2007a); V1084 Her (Rodríguez-Gil et al. 2009); DW UMa (Dhillon et al. 2013); and SDSS J075653.11+085831.8, in which the flaring is visible but no periodicity was found (Tovmassian et al. 2014). The periods range from 16 to 50 min. Some authors suggested that these periods could be associated with the WD spin rotation, as in IPs.

The literature has several examples of modulated circular polarization in IPs (e.g. Piirola et al. 2008 - V405 Aur - and Katajainen et al. 2010 - UU Col). The periods are the spin period or half this value. The last case is in fact explained by two maxima per spin cycle, hence the modulation of the polarization in IPs is always on the WD rotation. PQ Gem, for instance, presents both behaviours (one or two polarization peaks per cycle), depending on the band (Potter et al. 1997). Moreover, the total flux and the polarization do not necessarily vary in the same way. NY Lup and IGR J15094−6649 have their polarization modulated with the spin period. However, the photometry of NY Lup shows sideband periods in some bands, while the flux of IGR J15094−6649 modulates with the WD spin (Potter et al. 2012).

The SW Sex systems with periodic modulation in emission-line flaring and circular polarization are V1084 Her, LS Peg, BO Cet, and V380 Oph (the last two considering circular polarization from this work). Rodríguez-Gil et al. (2009) detected a period of 19.4 ± 0.4 min in the circular polarization of V1084 Her (RX J1643.7+3402) and twice this period in the radial velocity and equivalent width of the Balmer and He II 4686 Å emission lines. The authors discussed that these observations can be understood in two ways: (1) ∼19 min is half of the beat between the spin and orbital periods and ∼39 min is the beat period itself or (2) ∼19 min is half the spin period and ∼39 min is the spin period. They favoured the first explanation. Patterson et al. (2002) obtained a long photometric time series on more than 50 nights. The power spectrum shows a QPO broad bump with a superimposed narrow peak at 17.38 min, which is consistent with the beat of 19 min and the orbital period. X-ray observations show a clear orbital modulation and a possible periodicity of around 26 min (Worpel et al. 2020), at odds with any previously reported period in this range.

LS Peg is one of the objects included in this work. The periods already claimed in the literature for this object as well as those found in this work are presented in Table 4. We could not confirm the previous claim of circular polarization modulated at 29.6 ± 1.8 min (Rodríguez-Gil et al. 2001). Instead, we detected a modulation with a period of 18.8 ± 0.005 min, which is consistent with the periods systematically found in photometry (see Table 4). We also found photometric periods in the interval between 16.8 and 24.2 min. The main photometric period in our data is 21.0 ± 1.2 min, consistent with the 20.7 ± 0.3 min from Taylor et al. (1999), and also consistent with the beat between our polarimetric period and the orbital period. For V1084 Her, the photometric period is also consistent with the beat of the polarization and orbital periods, but it is larger than the polarimetric period, inversely to what is observed in LS Peg. The spectroscopic period of 33.5 ± 2.2 min (Rodríguez-Gil et al. 2001) is around twice the polarimetric period, analogous to V1084 Cen.

The results for V1084 Her and LS Peg suggest a possible relation between the periods of the emission-line flaring and circular polarization, with the latter half the value of the former. BO Cet follows the same trend: a spectroscopic period of approximately 20 min (Rodríguez-Gil et al. 2007b) and a circular polarization period of 11.1 ± 0.08 min. For V380 Oph, a similar situation happens. We raised two questionable periods of 22 and 12 min. Considering the first one, the same relation between circular polarization and spectroscopic flaring (46.7 ± 0.1 min, Rodríguez-Gil et al. 2007a) would be present. In both cases, the period found for spectroscopic flaring is also present in our photometric data, i.e. they have photometric periods of twice the polarimetric period. The same approximate relation is seen for UU Aqr, for which no flaring was reported in the literature.

Table 6. Relations of orbital period and spin period considering our results.

Object	P_{orb} (min)	P_{spin} (min)	P_{spin}/P_{orb}	f (R_{L_1})
BO Cet	201.36	11.1	0.06	0.32
SW Sex	194.31	41.2	0.21	0.78
V442 Oph	179.07	19.4	0.11	0.50
V380 Oph	221.91	12.7	0.06	0.32
LS Peg	251.67	18.8	0.07	0.39
UU Aqr	235.56	25.7	0.11	0.50

On the other hand, SW Sex and V442 Oph have polarimetric periods (uncertain for V442 Oph) of approximately twice the photometric periods. Rapid spectroscopic variability was not reported for these two objects.

Magnetic WDs in spin-rate equilibrium can have different types of accretion flow depending on the ratio between the WD rotation period, P_{spin}, and the orbital period, P_{orb} (Norton et al. 2008). Considering a mass ratio of 0.5, the conditions for the different accretion geometries are the following: if $P_{spin}/P_{orb} \lesssim 0.1$, the geometry will be disk-like; if $0.1 \lesssim P_{spin}/P_{orb} \lesssim 0.6$, it will be stream-like, and if $P_{spin}/P_{orb} \sim 0.6$, it will be ring-like. In all cases, the material is propelled in order to maintain angular momentum balance. The magnetic scenario for SW Sex stars proposed by Rodríguez-Gil et al. (2001) has a magnetosphere radius extending up to the corotation radius with a corresponding relation between P_{spin} and P_{orb} given by:

$$P_{\rm spin} \approx 0.31 f^{3/2} P_{\rm orb}, \tag{3}$$

where f is the corotation radius in units of R_{L_1}, which is the distance between the inner Lagrangian point L_1 and the WD. In this model, the gas stream from the secondary star overflows the disk and hits the magnetosphere of the primary.

Table 6 shows the results of the relation P_{spin}/P_{orb} and f for our sample of objects, considering the periodicities found in this paper and interpreted as the P_{spin}. BO Cet, V442 Oph, V380 Oph, LS Peg and UU Aqr can be classified as disk-like and their f values are consistent with the interval of $0.4 - 0.6$ R_{L_1} (Groot et al. 2001). Only SW Sex itself exhibits the accretion flow as stream-like, and a corotation radius of 0.7 R_{L_1}, slightly larger than the value measured by Groot et al. (2001).

5.3. *Inclination versus polarization*

The SW Sex class was initially supposed to be composed only of eclipsing systems. In spite of the discovery of an increasing number of non-eclipsing systems, more than a half of the SW Sex systems are eclipsing, which is not consistent with a homogeneous distribution of inclinations. This high incidence of eclipsing systems allows us to verify if the detection of polarization in SW Sex objects is correlated with their inclination. For the present discussion, it is not relevant if this is an observational or historical bias or a physical characteristic of the SW Sex phenomenon.

Notwithstanding the small number of objects, Table 8 shows that 73% (8/11) of SW Sex stars with possible circular polarization are non-eclipsing systems. If we focus only on objects with confirmed circular polarization, 4 out of 7 are non-eclipsing. Therefore, there is a higher incidence of polarized objects among non-eclipsing systems.

A possible origin for such a correlation could be the following. In the magnetic accretion scenario, the cyclotron emission is produced very near the WD surface and is responsible for the observed polarization. The accretion disks of SW Sex systems could block the direct view of the PSR region in high-inclination systems, which would prevent us from observing the polarized component in the total system emission at all phases. Such occultation is favoured by geometrically thick or flared disks, which could explain some spectroscopic features of SW Sex systems (see Dhillon et al. 2013, and references therein). In fact, models of the vertical structure of accretion disks predict an increase of the disk thickness with $\dot{M}$ (Meyer & Meyer-Hofmeister 1982). On the other hand, the flux from the disk increases with its projected area, which makes the dilution of a possible PSR region emission larger for lower inclinations. Hence, there should be an optimal inclination where the detection of the polarization would be most favoured. This inclination is likely near the maximum inclination for which no eclipse is seen.

5.4. *SW Sex stars in X-rays*

In addition to the optical cyclotron emission, the material in the postshock region also cools by bremsstrahlung emission in X-rays. Hence, models of the optical and X-ray emission of magnetic CVs can be used to constrain their physical and geometrical properties (e.g. Silva et al. 2013; Oliveira et al. 2019). The X-ray flux is usually modulated with the WD rotation due to variable absorption with the viewing angle or occultation of the emitting region by the WD. Mukai (2017) presents a comprehensive review on X-ray emission from accreting WDs. In this section, we briefly overview the X-ray emission of SW Sex objects.

Table 7 shows the SW Sex objects that have X-ray counterparts. They add up to 10 objects, corresponding to ∼14% of the 73 systems of The Big List. Five of them have reported X-ray periodicity and two of them are also classified as IPs: EX Hya (Hellier et al. 2000) and AO Psc (Hellier & van Zyl 2005). The IP systems are not discussed here.

Three SW Sex systems are X-ray sources and have positive circular polarization detection (see Table 8): LS Peg, V533 Her, and V1084 Her. Baskill & Wheatley (2006) claimed a period of 30.9 min in the X-ray emission of LS Peg, which is consistent with the circular polarization period of 29.6 min reported by Rodríguez-Gil et al. (2001). However, Ramsay et al. (2008) did not find any periodicity in further X-ray data and we did not confirm the period of 29.6 min in circular polarization either (see also Section 4.5). V533 Her and V1084 Her have been recently studied by Worpel et al. (2020) using XMM-Newton. V533 Her has low X-ray luminosity and its light curve exhibits an uncertain periodicity of 22.48 min, which is close to (but inconsistent with) the 23.33 min periodicity detected in the equivalent width of emission lines by Rodríguez-Gil & Martínez-Pais (2002). The relation between these two periods cannot be explained by a beat with the orbital period. There is only one measurement of the optical circular polarization of V533 Her, which corresponds to a marginal 3-sigma detection (Stockman et al. 1992). Worpel et al. (2020) reported an X-ray periodicity of around 26 min for V1084 Her, which does not correspond to the optical circular polarization period of 19.4 min reported by Rodríguez-Gil et al. (2009) or to any other periodicity reported from optical photometry or spectroscopy.

From the above discussion, there is no clear evidence of magnetic accretion from the X-ray light curves of SW Sex systems. In particular, the modulations observed in X-rays are not seen in optical measurements. Patterson et al. (2002) discussed if the absence/small levels of X-ray emission is inconsistent with the magnetic scenario. They proposed that the high density in the accretion column could prevent the production of a shock, which hinders the gas to reach keV temperatures. However, the subject is far from being settled. Hopefully, forthcoming X-ray surveys (e.g. e-Rosita) will shed light on this topic.

5.5. *CV demography and SW Sex systems*

Schwope (2018) and Pala et al. (2020) have provided volume-limited studies of CVs, considering distances from the *Gaia* second data release. The latter authors provide 42 systems within a distance of 150 pc. This sample is dominated by systems with low mass-transfer rate: it contains only three nova-like CVs including one SW Sex object (EX Hya, which is compiled in that work as an IP). They found that 36% of the objects host a magnetic WD. The sample is dominated by objects below the period gap (83%), but the fractions of magnetic systems below and above the gap are around the same, 37% and 28% respectively, considering the small number of objects. If the fraction of magnetic CVs does not depend on the mass-transfer rate or the orbital period, we would expect that around 36% of the nova-like CVs would harbor a magnetic WD. Here, nova-like variables stand for high mass-transfer rate CVs that are not polars or IPs. The fraction of SW Sex systems among the nova-like systems in the Ritter & Kolb (2003) catalog (version 7.24) is 46%, which is numerically consistent with the assumption that SW Sex systems are the missing magnetic nova-like CVs.

Table 7. SW Sex stars detected in X-rays. If a periodic modulation is present in the data, the period, P, is shown in the second column. A question mark indicates uncertainty in the period.

Object	P (min)	Reference
LS Peg	30.9 ± 0.3	Baskill & Wheatley (2006)
LS Peg	–	Ramsay et al. (2008)
V533 Her	22.48 (?)	Worpel et al. (2020)
V1084 Her	25.82 (?)	Worpel et al. (2020)
AO Psc	13.4 ($P_{\rm spin}$)	Johnson et al. (2006)
AH Men	–	White et al. (2000)
EX Hya	67 ($P_{\rm spin}$)	Heise et al. (1987)
DW UMa	–	Hoard et al. (2010)
WX Ari	–	White et al. (2000)
PX And	–	White et al. (2000)
UX UMa	–	Pratt et al. (2004)

5.6. *SW Sex stars in the context of the evolution of cataclysmic variables*

The CVs in the orbital period range between 3 and 4 hours that have sufficient observations show at least some SW Sex characteristics. A possible interpretation is that all long-period CVs have to evolve through this SW Sex regime before entering the period gap (e.g. Rodríguez-Gil et al. 2007b; Schmidtobreick et al. 2012). In fact, the number of dwarf novae around 4 h decreases in comparison with the number of SW Sex stars. In this scenario, the SW Sex stars represent an important stage in CV evolution.

CVs evolve towards shorter orbital periods driven by angular momentum loss through magnetic braking and gravitational radiation (e.g. Paczyński 1967; Verbunt & Zwaan 1981). In addition to these mechanisms, there is additional angular momentum losses due to mass transfer itself, usually called consequential angular momentum loss (CAML, e.g. King & Kolb 1995). Reasonable candidates for this sort of angular momentum loss include nova eruptions and circumbinary disks, among others. In the last couple of years, evidence supporting the importance of CAML in CV evolution has been growing (e.g. Schreiber et al. 2016; Nelemans et al. 2016; Liu & Li 2016), especially regarding stability for dynamical mass transfer and the required extra angular momentum loss below the orbital period gap (Knigge et al. 2011; Pala et al. 2017). In particular, the empirical formulation by Schreiber et al. (2016) provides an explanation for the paucity of helium-core WDs among the CV population (Zorotovic et al. 2011; McAllister et al. 2019), as well as the space density and the fractions of short- and long-period systems consistent with observations (Belloni et al. 2020; Pala et al. 2020). In addition, it can also explain the properties of detached CVs crossing the orbital period gap (Zorotovic et al. 2016), the existence of single helium-core WDs (Zorotovic & Schreiber 2017), and the mass density of CVs in globular clusters (Belloni et al. 2019).

CAML might solve several problems of the CV evolution model, but not all of them. There are some inconsistencies between predictions and observations that are most likely connected to our ignorance of magnetic braking. One prescription widely used in CV investigations is that proposed by Rappaport, Verbunt, & Joss (1983).

A well-known problem of this prescription, which is directly related to this work, is the contradiction between the expected mass-transfer rates among SW Sex stars (given the brightness of such systems) and the predicted ones (e.g. Rodríguez-Gil et al. 2007b). Indeed, SW Sex stars cluster at the upper edge of the orbital period gap, between ~ 3 and ~ 4 h. According to the prescription by Rappaport, Verbunt, & Joss (1983), the mass-transfer rate drops as a CV ages, which means that just above the orbital period gap, this prescription provides the lowest mass-transfer rates. On the other hand, the mass-transfer rates expected from the characteristics of SW Sex stars are supposed to be the highest among all CVs.

Other evidence that the magnetic braking prescription should be different were recently provided by Belloni et al. (2020) and Pala et al. (2020), who showed that the observed and predicted fractions of period-bouncers are in serious disagreement, with those predicted being much larger than observed. In addition, these authors showed that the evolutionary trend in the WD effective temperature above the period gap, which is directly connected with the mean mass-transfer rate, is opposite to the observed one. Finally, Fuentes-Morales et al. (2020) showed that the predicted fraction of old novae just above the orbital period gap is much smaller than the observed fraction. These four pieces of evidence point towards a needed revision of the magnetic braking prescription. SW Sex stars are therefore important objects in this context, which can provide significant constraints on the CV evolution model, especially considering that they are more abundant than period bouncers and long-period CVs having WDs with measured effective temperatures.

We note, however, that there is some progress in this regard. Knigge et al. (2011) provide a list of magnetic braking recipes, which are illustrated in their Fig. 2. Among them, the formulation developed by Kawaler (1988) clearly predicts an increase in the angular momentum loss rate when the CV evolves towards shorter orbital periods, which would, in turn, provide the largest mass-transfer rates just at the upper edge of the orbital period gap. This could potentially explain the expected mass-transfer rates of SW Sex stars, which could make SW Sex stars a natural stage in the long-period CV pathway. Additionally, the observed distribution of WD effective temperatures versus orbital period could be reproduced. Belloni et al. (in preparation) upgrade the prescription by Kawaler (1988) and show these and other issues related to magnetic braking might be solved.

5.7. *Origin of magnetic cataclysmic variables*

There are currently two main scenarios that could account for the formation of magnetic WDs in close binaries. In the first one, during common-envelope evolution, a dynamo driven by shear due to differential rotation in the hot outer layers of the degenerate core (Wickramasinghe et al. 2014) would be responsible for the magnetic field generation. This idea was originally designed for single WDs, but was generalized by Briggs et al. (2018), who extended the model to the case in which the binary survives the common-envelope evolution. However, Belloni & Schreiber (2020) detected several flaws in this model. One of them is the difficulty in explaining the complete absence of hot and young WDs among the population of post-common-envelope WD + late-type main-sequence stars (e.g. Parsons et al. 2021, and references therein). In addition, the predicted fractions of magnetic WDs in the different populations of close binaries are much higher than the observed ones.

An alternative scenario for the origin of single low-field magnetic WDs was proposed by Isern et al. (2017), who argued that a dynamo similar to those operating in planets could be responsible for weak magnetic field generation in WDs. This is possible because, once the WD temperature becomes low enough, its interior starts to crystallize, which, in turn, allows the generation of a magnetic field through a dynamo. This scenario, if applied to close binaries, could help to explain the low-temperature WDs in the population of detached magnetic post-common-envelope binaries. However, the magnetic fields predicted by Isern et al. (2017) are much weaker than those observed in magnetic WDs among the different population of close binaries.

If all or part of SW Sex systems have high-magnetic moment (e.g. Patterson et al. 2002), any theory aiming to explain the origin of high-field magnetic WDs would need to account for their properties. That said, SW Sex stars are important pieces to constrain evolutionary models of CVs, and understanding whether they are predominantly magnetic or not, should provide useful constraints to any model aiming to explain the origin and evolution of magnetic WDs in close binaries.

6. CONCLUSIONS

We reported time-series analyses of photometric and polarimetric data of six SW Sex stars: BO Cet, SW Sex, V442 Oph, V380 Oph, LS Peg, and UU Aqr. We associated the periodicities found in circular polarization with the spin period of a magnetic WD, based on the assumption that the polarized flux is related to cyclotron emission from a PSR region. We found the following tentative periods from circular polarimetry: 11.1 min in BO Cet, 41.2 min in SW Sex, and 25.7 min in UU Aqr. We also found uncertain periodicities (below the FAP level of 1%) of 22.0 min and 19.4 min for V380 Oph and V442 Oph, respectively. We confirmed the detection of circular polarization in LS Peg, previously reported by Rodríguez-Gil et al. (2001). However, differently from these authors, we found a period of 18.8 min, which we assumed as the probable period of the WD rotation. Considering these new possible detections, 15% of all SW Sex in Hoard's Big List of SW Sextantis Stars (which contains 73 objects) have direct evidence of magnetic accretion from circular polarimetric data.

There is a weak indication that the circular polarimetric period is half of the emission-line flaring period. There is also a tendency of detection of circular polarization in non-eclipsing SW Sex systems: 73% of objects with detected polarization are non-eclipsing, contrasting with the trend of SW Sex systems to show eclipses.

The recent finding that 36% of the CVs in a volume-limited sample are magnetic (Pala et al. 2020) agrees with an interpretation that SW Sex systems are the magnetic portion of the nova-like systems. If this is really true, the formation of magnetic CVs should also explain the SW Sex systems, and not only polars and IPs. In fact, any model for the origin and evolution of CVs should also reproduce the tendency of SW Sex systems to cluster just above the orbital period gap.

Additional time-resolved and high signal-to-noise ratio circular polarimetric measurements of SW Sex systems are necessary to confirm the suggested periods and to search for magnetic accretion in those objects.

ACKNOWLEDGMENTS

The authors thank the referee for corrections and suggestions to the manuscript. This study was supported by grants #2018/05420-1, #2015/24383-7, #2013/26258-4, Fundação de Amparo à Pesquisa do Estado de São Paulo (FAPESP). C.V.R. is also grateful to the support of Conselho Nacional de Desenvolvimento Científico e Tecnológico - CNPq (grant #303444/2018-5). C.E.F.L. acknowledges a PCI/CNPQ/MCTI post-doctoral support. P.S. acknowledges support from NSF AST-1514737. A.S.O. acknowledges São Paulo Research Foundation (FAPESP) for financial support under grant #2017/20309-7. D.B. was supported by the grant #2017/14289-3, São Paulo Research Foundation (FAPESP). S.S. was supported by the Slovak Research and Development Agency under the contract No. APVV-15-0458, by the Slovak Academy of Sciences grant VEGA No. 2/0008/17 and was partially supported by the Program of Development of M. V. Lomonosov Moscow State University "Leading Scientific Schools", project "Physics of Stars, Relativistic Objects and Galaxies". The authors thank the MCTI/FINEP (CT-INFRA grant 0112052700) and the Embrace Space Weather Program for the computing facilities at INPE. This work was based on observations made at Observatório do Picos dos Dias managed by the Laboratório Nacional de Astrofísica/MCTI, Brazil. We acknowledge the use of observations from the AAVSO International Database contributed by observers worldwide and used in this research. The authors also acknowledge Deonísio Cieslinski, for his help in the beginning of the project, and Matthias Schreiber, for his comments on aspects of CV evolution.

Facilities: LNA:1.6m, SOS/SAS, AAVSO

Software: IRAF (Tody 1986, 1993)

APPENDIX

A. POLARIMETRIC MEASUREMENTS OF SW SEX SYSTEMS

In this section, we present a table with a compilation of polarization measurements of SW Sex systems from the literature. The table also includes the measurements presented in this work and is strongly based on the information presented in The Big List of SW Sex Systems (Hoard et al. 2003).

Table 8. Summary of previous circular polarization measurements of SW Sex systems listed in Hoard et al. (2003). The first objects are those having confirmed non-null polarization.

Object	SW Sex status	Eclipse	Polarized	P_c (%)	Wavelength range	Period (min)	Reference
UU Aqr	Definite	Deep	Y	-0.1 – +0.1	V	25.7 ± 0.23	This paper
BO Cet	Definite	None	Y	-0.1 – +0.1	V, R$_C$	11.1 ± 0.08	This paper
RR Cha	Definite	Deep	Y	5 – 10	3500–9000 Å	· · ·	Rodríguez-Gil & Potter (2003)
V533 Her	Definite	None	Y?	-0.38(11) and 0.00(7)	3200–8600 Å	· · ·	Stockman et al. (1992)
V795 Her	Definite	None	Y	0.1 – 0.22	U	19.54	Rodríguez-Gil et al. (2002)
V1084 Her	Definite	None	Y	-0.5 – +0.5	3600–5350 Å	19.4 ± 0.4	Rodríguez-Gil et al. (2009)
V380 Oph	Definite	None	Y?	-0.1 – +0.1	V	22.0 ± 1.2	This paper
			N?	+0.12(16)	3200–8600 Å	· · ·	Stockman et al. (1992)
V442 Oph	Definite	None	Y?	-0.1 – +0.1	V, R$_C$	19.4 ± 0.4	This paper
			N?	+0.01(5) and -0.03(8)	3200–8600 Å	· · ·	Stockman et al. (1992)
LS Peg	Definite	None	Y	0.05 – +0.05	V, R$_C$	18.8 ± 0.005	This paper
			Y	0.0 – -0.3	3720–5070 Å	29.6 ± 1.8	Rodríguez-Gil et al. (2001)
AO Psc	Possible	None	Y?	1.3 ± 0.5	I	13.42	Butters et al. (2009)
SW Sex	Definite	Deep	Y	-0.2 – +0.2	R$_C$	41.2 ± 8.5	This paper
			N?	+0.05(14) and -0.03(5)	3200–8600 Å	· · ·	Stockman et al. (1992)
PX And	Definite	Shallow	N?	-0.02(9) and +0.06(4)	3200-8600 Å		Stockman et al. (1992)
TT Ari	Definite	None	N?	-0.01(2) and -0.02(2)	3200–8600 Å		Stockman et al. (1992)
OZ Dra	Definite	Deep	N?	<0.24(17)	4000–8000 Å		Wolfe et al. (2003)
EV Lyn	Possible	Shallow	N?	<0.1–0.4	–		Szkody et al. (2006)
EX Hya	Possible	Shallow	N?	-0.02(4) and +0.01(2)	5700–9200 Å		Stockman et al. (1992)
BT Mon	Definite	Deep	N?	0.10(17), 0.04(6) and 0.21(12)	3200–8600 Å		Stockman et al. (1992)
V Per	Probable	Deep	N?	-0.81(82)	3200–8600 Å		Stockman et al. (1992)
V347 Pup	Probable	Deep	N?	<0.5	0.34–1.6 μm		Buckley et al. (1990)
V348 Pup	Definite	Deep	N?	-0.09(11) and +0.14(13)	5500–8400 Å		Tuohy et al. (1990)
VZ Scl	Possible	Deep	N?	+0.18(8)	3500–9200 Å		Cropper (1986)
LX Ser	Probable	Deep	N?	+0.04(7)	3200–8600 Å		Stockman et al. (1992)
WY Sge	Possible	Deep	N?	+0.32(46)	3200–8600 Å		Stockman et al. (1992)
DW UMa	Definite	Deep	N?	+0.06(14)	3200–8600 Å		Stockman et al. (1992)
UX UMa	Probable	Deep	N?	-0.06(4)	3200–8600 Å		Stockman et al. (1992)
1RXS J064434.5+334451	Probable	Deep	N	+0.003(3)	4200–8400 Å		Sing et al. (2007)
SDSS J210131.26+105251.5	Possible	None?	N?	<0.4	V		Homer et al. (2006)

NOTE—Column 5 shows the measured percentage of circular polarization. Errors are shown in parentheses, when available.

B. IMPROVING THE DATA REDUCTION OF THE IAGPOL CIRCULAR POLARIZATION MODE

This section explains a procedure for the data reduction of the circular polarimetric mode of IAGPOL (Magalhães et al. 1996). The procedure takes into account the expected value of the ratio of the sum of the ordinary counts of all images used to calculate one polarization point relative to the sum of the extraordinary counts. The ratio is designated by k and is expressed as (Magalhães et al. 1984):

$$k = \frac{\sum_i C_o(W_i)}{\sum_i C_e(W_i)}, \tag{B1}$$

where $C_o(W_i)$ is the value of the ordinary counts in an image obtained with the retarder waveplate in the position W_i and $C_e(W_i)$ is the equivalent for the extraordinary counts. A polarization measurement corresponds to 8 images, therefore i runs from 1 to 8. The difference between the angular waveplate positions in two subsequent images is 22.5°.

The k value can be understood as a correction for possible different efficiencies in the detection of the ordinary and extraordinary fluxes. A value of k different from the expected theoretical value can occur, for instance, if the detector sensitivity depends on the polarization of the incident beam, since the polarization of the ordinary beam is perpendicular to the polarization of the extraordinary beam.

In the linear polarization mode of IAGPOL, the theoretical expected value of k is 1, due to the use of a half-wave retarder plate (see Magalhães et al. 1984). Hence, in that case, the correction is implemented by simply multiplying the measured extraordinary counts by the k value obtained from the observations. On the other hand, the quarter-wave plate is used to measure the circular and linear polarizations. For that case, the expressions for the counts in the ordinary and extraordinary beams given by Rodrigues et al. (1998) can be used to demonstrate that the theoretical value of k is a function of the Stokes parameter Q (eq. B2).

$$k = \frac{1 + 0.5Q}{1 - 0.5Q}. \tag{B2}$$

Therefore, we initially calculated the Stokes parameters considering $k = 1$. Then we recalculated the polarization taking into account the estimated Stokes parameter Q and the resulting k value was used as a multiplicative factor to the extraordinary counts. This iteration was repeated until a negligible difference in subsequent values of all Stokes parameters was achieved. An example of the application of this procedure is an absolute reduction of 0.07% in the mean polarization error of the SW Sex object itself.

The above expression is valid for IAGPOL. The expression for k for other polarimeters depends on the optical configuration of the retarders and analysers of the instrument.

REFERENCES

Avilés, A., Arias, I., Chávez, C. E., et al. 2020, RMxAA, 56, 11, doi: 10.22201/ia.01851101p.2020.56.01.03

Ballouz, R.-L., & Sion, E. M. 2009, ApJ, 697, 1717, doi: 10.1088/0004-637X/697/2/1717

Baptista, R., & Bortoletto, A. 2008, ApJ, 676, 1240, doi: 10.1086/528706

Baptista, R., Steiner, J. E., & Horne, K. 1996, MNRAS, 282, 99, doi: 10.1093/mnras/282.1.99

Baskill, D. S., & Wheatley, P. J. 2006, in ESA Special Publication, Vol. 604, The X-ray Universe 2005, ed. A. Wilson, 239

Baskill, D. S., Wheatley, P. J., & Osborne, J. P. 2005, Monthly Notices of the Royal Astronomical Society, 357, 626

Basri, G., Walkowicz, L. M., Batalha, N., et al. 2011, AJ, 141, 20, doi: 10.1088/0004-6256/141/1/20

Beljawsky, P. R. 1926, Beobachtungs-Zircular der Astron. Nachr., 6, 38

Belloni, D., Giersz, M., Rivera Sandoval, L. E., Askar, A., & Ciecielag, P. 2019, MNRAS, 483, 315, doi: 10.1093/mnras/sty3097

Belloni, D., & Schreiber, M. R. 2020, MNRAS, 492, 1523, doi: 10.1093/mnras/stz3601

Belloni, D., Schreiber, M. R., Pala, A. F., et al. 2020, MNRAS, 491, 5717, doi: 10.1093/mnras/stz3413

Berger, J., & Fringant, A. M. 1984, A&AS, 58, 565

Bloemen, S., Marsh, T. R., Steeghs, D., & Østensen, R. H. 2010, MNRAS, 407, 1903, doi: 10.1111/j.1365-2966.2010.17035.x

Briggs, G. P., Ferrario, L., Tout, C. A., & Wickramasinghe, D. T. 2018, MNRAS, 478, 899, doi: 10.1093/mnras/sty1150

Bruch, A. 2017, NewA, 52, 112, doi: 10.1016/j.newast.2016.10.013

—. 2019, Information Bulletin on Variable Stars, 6257, doi: 10.22444/IBVS.6257

Buckley, D. A. H., Cropper, M., Ramsay, G., & Wickramasinghe, D. T. 1998, MNRAS, 299, 83, doi: 10.1046/j.1365-8711.1998.01744.x

Buckley, D. A. H., Sullivan, D. J., Remillard, R. A., Tuohy, I. R., & Clark, M. 1990, ApJ, 355, 617, doi: 10.1086/168794

Butters, O. W., Katajainen, S., Norton, A. J., Lehto, H. J., & Piirola, V. 2009, A&A, 496, 891, doi: 10.1051/0004-6361/200811058

Casares, J., Martinez-Pais, I. G., Marsh, T. R., Charles, P. A., & Lazaro, C. 1996, MNRAS, 278, 219, doi: 10.1093/mnras/278.1.219

Clarke, D., Stewart, B. G., Schwarz, H. E., & Brooks, A. 1983, A&A, 126, 260

Cropper, M. 1986, MNRAS, 222, 225, doi: 10.1093/mnras/222.2.225

Dhillon, V. S. 1996, in Astrophysics and Space Science Library, Vol. 208, IAU Colloq. 158: Cataclysmic Variables and Related Objects, ed. A. Evans & J. H. Wood (Kluwer Academic Publisher), 3, doi: 10.1007/978-94-009-0325-8_1

Dhillon, V. S., Smith, D. A., & Marsh, T. R. 2013, MNRAS, 428, 3559, doi: 10.1093/mnras/sts294

Dobrzycka, D., Dobrzycki, A., Engels, D., & Hagen, H.-J. 1998, AJ, 115, 1634, doi: 10.1086/300281

Dorn-Wallenstein, T. Z., Levesque, E. M., Neugent, K. F., et al. 2020, ApJ, 902, 24, doi: 10.3847/1538-4357/abb318

Downes, R. A., & Keyes, C. D. 1988, AJ, 96, 777, doi: 10.1086/114846

Downes, R. A., Webbink, R. F., Shara, M. M., et al. 2005, Journal of Astronomical Data, 11

Ferreira Lopes, C. E., Cross, N. J. G., & Jablonski, F. 2018, MNRAS, 481, 3083, doi: 10.1093/mnras/sty2469

Ferreira Lopes, C. E., Leão, I. C., de Freitas, D. B., et al. 2015, A&A, 583, A134, doi: 10.1051/0004-6361/201424900

Fuentes-Morales, I., Tappert, C., Zorotovic, M., et al. 2020, MNRAS, doi: 10.1093/mnras/staa3482

Garnavich, P. M., & Szkody, P. 1992, Journal of the American Association of Variable Star Observers (JAAVSO), 21, 81

Garnavich, P. M., Szkody, P., & Goldader, J. 1988, in BAAS, Vol. 20, Bulletin of the American Astronomical Society, 1020

Green, R. F., Ferguson, D. H., Liebert, J., & Schmidt, M. 1982, PASP, 94, 560, doi: 10.1086/131022

Groot, P. J., Rutten, R. G. M., & van Paradijs, J. 2001, A&A, 368, 183, doi: 10.1051/0004-6361:20000483

Heise, J., Mewe, R., Kruszewski, A., & Chlebowski, T. 1987, A&A, 183, 73

Hellier, C. 1996, ApJ, 471, 949, doi: 10.1086/178021

—. 1999, ApJ, 519, 324, doi: 10.1086/307345

Hellier, C., Kemp, J., Naylor, T., et al. 2000, MNRAS, 313, 703, doi: 10.1046/j.1365-8711.2000.03301.x

Hellier, C., & van Zyl, L. 2005, ApJ, 626, 1028, doi: 10.1086/430123

Henden, A. A., & Honeycutt, R. K. 1995, PASP, 107, 324, doi: 10.1086/133557

Hoard, D. W., Szkody, P., Froning, C. S., Long, K. S., & Knigge, C. 2003, AJ, 126, 2473, doi: 10.1086/378605

Hoard, D. W., Szkody, P., Still, M. D., Smith, R. C., & Buckley, D. A. H. 1998, MNRAS, 294, 689, doi: 10.1046/j.1365-8711.1998.01321.x

Hoard, D. W., Thorstensen, J. R., & Szkody, P. 2000, ApJ, 537, 936, doi: 10.1086/309074

Hoard, D. W., Lu, T.-N., Knigge, C., et al. 2010, AJ, 140, 1313, doi: 10.1088/0004-6256/140/5/1313

Homer, L., Szkody, P., Henden, A., et al. 2006, AJ, 132, 2743, doi: 10.1086/508928

Honeycutt, R. K., Schlegel, E. M., & Kaitchuck, R. H. 1986, ApJ, 302, 388, doi: 10.1086/163997

Horne, K., & Marsh, T. R. 1986, MNRAS, 218, 761, doi: 10.1093/mnras/218.4.761

Isern, J., García-Berro, E., Külebi, B., & Lorén-Aguilar, P. 2017, ApJL, 836, L28, doi: 10.3847/2041-8213/aa5eae

Johnson, E. M., Imamura, J. N., & Steiman-Cameron, T. Y. 2006, PASP, 118, 797, doi: 10.1086/505334

Kaitchuck, R. H., Hantzios, P. A., Kakaletris, P., Honeycutt, R. K., & Schlegel, E. M. 1987, ApJ, 317, 765, doi: 10.1086/165325

Katajainen, S., Butters, O., Norton, A. J., et al. 2010, ApJ, 724, 165, doi: 10.1088/0004-637X/724/1/165

Kawaler, S. D. 1988, ApJ, 333, 236, doi: 10.1086/166740

King, A. R., & Kolb, U. 1995, ApJ, 439, 330, doi: 10.1086/175176

Knigge, C., Baraffe, I., & Patterson, J. 2011, ApJS, 194, 28, doi: 10.1088/0067-0049/194/2/28

Liu, W.-M., & Li, X.-D. 2016, ApJ, 832, 80, doi: 10.3847/0004-637X/832/1/80

Lomb, N. R. 1976, Ap&SS, 39, 447, doi: 10.1007/BF00648343

Lucy, L. B., & Sweeney, M. A. 1971, AJ, 76, 544, doi: 10.1086/111159

Magalhães, A. M., Benedetti, E., & Roland, E. H. 1984, PASP, 96, 383, doi: 10.1086/131351

Magalhães, A. M., Rodrigues, C. V., Margoniner, V. E., Pereyra, A., & Heathcote, S. 1996, in Astronomical Society of the Pacific Conference Series, Vol. 97, Polarimetry of the Interstellar Medium, ed. W. G. Roberge & D. C. B. Whittet, 118

Marsh, T. R., & Duck, S. R. 1996, NewA, 1, 97, doi: 10.1016/S1384-1076(96)00008-5

Martínez-Pais, I. G., Rodríguez-Gil, P., & Casares, J. 1999, MNRAS, 305, 661, doi: 10.1046/j.1365-8711.1999.02483.x

McAllister, M., Littlefair, S. P., Parsons, S. G., et al. 2019, MNRAS, 486, 5535, doi: 10.1093/mnras/stz976

Meyer, F., & Meyer-Hofmeister, E. 1982, A&A, 106, 34

Monet, D. G., Levine, S. E., Canzian, B., et al. 2003, AJ, 125, 984, doi: 10.1086/345888

Mukai, K. 2017, PASP, 129, 062001, doi: 10.1088/1538-3873/aa6736

Nelemans, G., Siess, L., Repetto, S., Toonen, S., & Phinney, E. S. 2016, ApJ, 817, 69, doi: 10.3847/0004-637X/817/1/69

Norton, A. J., Beardmore, A. P., & Taylor, P. 1996, MNRAS, 280, 937, doi: 10.1093/mnras/280.3.937

Norton, A. J., Butters, O. W., Parker, T. L., & Wynn, G. A. 2008, ApJ, 672, 524, doi: 10.1086/523932

O'Donoghue, D., Buckley, D. A. H., Balona, L. A., et al. 2006, MNRAS, 372, 151, doi: 10.1111/j.1365-2966.2006.10834.x

Oliveira, A. S., Rodrigues, C. V., Palhares, M. S., et al. 2019, MNRAS, 489, 4032, doi: 10.1093/mnras/stz2445

Paczyński, B. 1967, AcA, 17, 287

Pala, A. F., Gänsicke, B. T., Townsley, D., et al. 2017, MNRAS, 466, 2855, doi: 10.1093/mnras/stw3293

Pala, A. F., Gänsicke, B. T., Breedt, E., et al. 2020, MNRAS, 494, 3799, doi: 10.1093/mnras/staa764

Parsons, S. G., Gänsicke, B. T., Schreiber, M. R., et al. 2021, MNRAS, doi: 10.1093/mnras/stab284

Patterson, J., Fenton, W. H., Thorstensen, J. R., et al. 2002, PASP, 114, 1364, doi: 10.1086/344587

Patterson, J., Kemp, J., Harvey, D. A., et al. 2005, PASP, 117, 1204, doi: 10.1086/447771

Penning, W. R., Ferguson, D. H., McGraw, J. T., Liebert, J., & Green, R. F. 1984, ApJ, 276, 233, doi: 10.1086/161607

Pereyra, A. 2000, Thesis, Instituto Astronômico e Geofísico (USP), São Paulo

Pereyra, A., Magalhães, A. M., Rodrigues, C., & Carciofi, A. 2018, PCCDPACK: Polarimetry with CCD. http://ascl.net/1809.002

Piirola, V., Vornanen, T., Berdyugin, A., Coyne, G. V., & J., S. 2008, ApJ, 684, 558, doi: 10.1086/590144

Potter, S. B., Cropper, M., Mason, K. O., Hough, J. H., & Bailey, J. A. 1997, MNRAS, 285, 82, doi: 10.1093/mnras/285.1.82

Potter, S. B., Romero-Colmenero, E., Kotze, M., et al. 2012, MNRAS, 420, 2596, doi: 10.1111/j.1365-2966.2011.20232.x

Pratt, G. W., Mukai, K., Hassall, B. J. M., Naylor, T., & Wood, J. H. 2004, MNRAS, 348, L49, doi: 10.1111/j.1365-2966.2004.07574.x

Puebla, R. E., Diaz, M. P., & Hubeny, I. 2007, AJ, 134, 1923, doi: 10.1086/522112

Ramsay, G., Wheatley, P. J., Norton, A. J., Hakala, P., & Baskill, D. 2008, MNRAS, 387, 1157, doi: 10.1111/j.1365-2966.2008.13299.x

Rappaport, S., Verbunt, F., & Joss, P. C. 1983, ApJ, 275, 713, doi: 10.1086/161569

Ritter, H., & Kolb, U. 2003, A&A, 404, 301, doi: 10.1051/0004-6361:20030330

Roberts, D. H., Lehar, J., & Dreher, J. W. 1987, AJ, 93, 968, doi: 10.1086/114383

Robertson, J. W., Honeycutt, R. K., Henden, A. A., & Campbell, R. T. 2018, AJ, 155, 61, doi: 10.3847/1538-3881/aaa1a8

Rodrigues, C. V., Cieslinski, D., & Steiner, J. E. 1998, A&A, 335, 979. https://arxiv.org/abs/astro-ph/9805193

Rodríguez-Gil, P., Casares, J., Martínez-Pais, I. G., Hakala, P., & Steeghs, D. 2001, ApJL, 548, L49, doi: 10.1086/318922

Rodríguez-Gil, P., Casares, J., Martínez-Pais, I. G., & Hakala, P. J. 2002, in Astronomical Society of the Pacific Conference Series, Vol. 261, The Physics of Cataclysmic Variables and Related Objects, ed. B. T. Gänsicke, K. Beuermann, & K. Reinsch, 533

Rodríguez-Gil, P., & Martínez-Pais, I. G. 2002, MNRAS, 337, 209, doi: 10.1046/j.1365-8711.2002.05904.x

Rodríguez-Gil, P., Martínez-Pais, I. G., & de la Cruz Rodríguez, J. 2009, MNRAS, 395, 973, doi: 10.1111/j.1365-2966.2009.14585.x

Rodríguez-Gil, P., & Potter, S. B. 2003, MNRAS, 342, L1, doi: 10.1046/j.1365-8711.2003.06617.x

Rodríguez-Gil, P., Schmidtobreick, L., & Gänsicke, B. T. 2007a, MNRAS, 374, 1359, doi: 10.1111/j.1365-2966.2006.11245.x

Rodríguez-Gil, P., Gänsicke, B. T., Hagen, H.-J., et al. 2007b, MNRAS, 377, 1747, doi: 10.1111/j.1365-2966.2007.11743.x

Rodríguez-Gil, P., Shahbaz, T., Torres, M. A. P., et al. 2020, MNRAS, 494, 425, doi: 10.1093/mnras/staa612

Scargle, J. D. 1982, ApJ, 263, 835, doi: 10.1086/160554

Schmidtobreick, L., Rodríguez-Gil, P., & Gänsicke, B. T. 2012, Mem. Soc. Astron. Italiana, 83, 610. https://arxiv.org/abs/1111.6678

Schreiber, M. R., Zorotovic, M., & Wijnen, T. P. G. 2016, MNRAS, 455, L16, doi: 10.1093/mnrasl/slv144

Schwope, A. D. 2018, A&A, 619, A62, doi: 10.1051/0004-6361/201833723

Semena, A. N., Revnivtsev, M. G., Khamitov, I. M., et al. 2013, Astronomy Letters, 39, 227, doi: 10.1134/S1063773713040051

Shafter, A. W. 1985, AJ, 90, 643, doi: 10.1086/113769

Shugarov, S., Golysheva, P., Sokolovsky, K., & Chochol, D. 2016, in Proceedings of Astro plate, 59–62. https://arxiv.org/abs/1605.01162

Shugarov, S. Y., Katysheva, N. A., Seregina, T. M., Volkov, I. M., & Kroll, P. 2005, in Astronomical Society of the Pacific Conference Series, Vol. 330, The Astrophysics of Cataclysmic Variables and Related Objects, ed. J.-M. Hameury & J.-P. Lasota, 495

Silva, K. M. G., Rodrigues, C. V., Costa, J. E. R., et al. 2013, MNRAS, 432, 1587, doi: 10.1093/mnras/stt578

Silva, K. M. G., Rodrigues, C. V., Oliveira, A. S., et al. 2015, MNRAS, 451, 4183, doi: 10.1093/mnras/stv1105

Sing, D. K., Green, E. M., Howell, S. B., et al. 2007, A&A, 474, 951, doi: 10.1051/0004-6361:20078026

Smith, D. A., Dhillon, V. S., & Marsh, T. R. 1998, MNRAS, 296, 465, doi: 10.1046/j.1365-8711.1998.00743.x

Stockman, H. S., Schmidt, G. D., Berriman, G., et al. 1992, ApJ, 401, 628, doi: 10.1086/172091

Szkody, P., Everett, M. E., Dai, Z., & Serna-Grey, D. 2018, AJ, 155, 28, doi: 10.3847/1538-3881/aa9ede

Szkody, P., Garnavich, P., Castelaz, M., & Makino, F. 1994a, PASP, 106, 616, doi: 10.1086/133421

Szkody, P., Garnavich, P., Holberg, J., Silber, A., & Pastwick, L. 1997, AJ, 113, 2276, doi: 10.1086/118438

Szkody, P., Hoard, D. W., Patterson, J., et al. 1994b, in Astronomical Society of the Pacific Conference Series, Vol. 56, Interacting Binary Stars, ed. A. W. Shafter, 350

Szkody, P., Nishikida, K., Long, K. S., & Fried, R. 2001, AJ, 121, 2761, doi: 10.1086/320382

Szkody, P., & Piche, F. 1990, ApJ, 361, 235, doi: 10.1086/169188

Szkody, P., & Shafter, A. W. 1983, PASP, 95, 509, doi: 10.1086/131200

Szkody, P., & Wade, R. A. 1980, PASP, 92, 806, doi: 10.1086/130754

Szkody, P., Henden, A., Agüeros, M., et al. 2006, AJ, 131, 973, doi: 10.1086/499308

Taichi, K. 2018, JST

Taylor, C. J., Thorstensen, J. R., & Patterson, J. 1999, PASP, 111, 184, doi: 10.1086/316316

Thorstensen, J. R., Ringwald, F. A., Wade, R. A., Schmidt, G. D., & Norsworthy, J. E. 1991, AJ, 102, 272, doi: 10.1086/115874

Tody, D. 1986, in Proc. SPIE, Vol. 627, Instrumentation in astronomy VI, ed. D. L. Crawford, 733, doi: 10.1117/12.968154

Tody, D. 1993, in Astronomical Society of the Pacific Conference Series, Vol. 52, Astronomical Data Analysis Software and Systems II, ed. R. J. Hanisch, R. J. V. Brissenden, & J. Barnes, 173

Tovmassian, G., Stephania Hernandez, M., González-Buitrago, D., Zharikov, S., & García-Díaz, M. T. 2014, AJ, 147, 68, doi: 10.1088/0004-6256/147/3/68

Tuohy, I. R., Remillard, R. A., Brissenden, R. J. V., & Bradt, H. V. 1990, ApJ, 359, 204, doi: 10.1086/169050

Vaillancourt, J. E. 2006, PASP, 118, 1340, doi: 10.1086/507472

Verbunt, F., & Zwaan, C. 1981, A&A, 100, L7

Volkov, I. M., Shugarov, S. Y., & Seregina, T. M. 1986, Astronomicheskij Tsirkulyar, 1418, 3

Volkov, I. M., & Volkova, N. S. 2003, in Stellar Variability, 121–126

Warner, B. 1986, MNRAS, 219, 347, doi: 10.1093/mnras/219.2.347

—. 1995, Cambridge Astrophysics Series, 28

White, N. E., Giommi, P., & Angelini, L. 2000, VizieR Online Data Catalog, IX/31

Wickramasinghe, D. T., Tout, C. A., & Ferrario, L. 2014, MNRAS, 437, 675, doi: 10.1093/mnras/stt1910

Williams, R. E. 1989, AJ, 97, 1752, doi: 10.1086/115115

Wolfe, M. A., Szkody, P., Fraser, O. J., et al. 2003, PASP, 115, 1118, doi: 10.1086/377013

Worpel, H., Schwope, A. D., Traulsen, I., Mukai, K., & Ok, S. 2020, A&A, 639, A17, doi: 10.1051/0004-6361/202038038

Zellem, R., Hollon, N., Ballouz, R.-L., et al. 2009, PASP, 121, 942, doi: 10.1086/605547

Zorotovic, M., & Schreiber, M. R. 2017, MNRAS, 466, L63, doi: 10.1093/mnrasl/slw236

Zorotovic, M., Schreiber, M. R., & Gänsicke, B. T. 2011, A&A, 536, A42, doi: 10.1051/0004-6361/201116626

Zorotovic, M., Schreiber, M. R., Parsons, S. G., et al. 2016, MNRAS, 457, 3867, doi: 10.1093/mnras/stw246

Zwitter, T., & Munari, U. 1995, A&AS, 114, 575

PUBLICAÇÕES TÉCNICO-CIENTÍFICAS EDITADAS PELO INPE

Teses e Dissertações (TDI)

Teses e Dissertações apresentadas nos Cursos de Pós-Graduação do INPE.

Notas Técnico-Científicas (NTC)

Incluem resultados preliminares de pesquisa, descrição de equipamentos, descrição e ou documentação de programas de computador, descrição de sistemas e experimentos, apresentação de testes, dados, atlas, e documentação de projetos de engenharia.

Propostas e Relatórios de Projetos (PRP)

São propostas de projetos técnico-científicos e relatórios de acompanhamento de projetos, atividades e convênios.

Publicações Seriadas

São os seriados técnico-científicos: boletins, periódicos, anuários e anais de eventos (simpósios e congressos). Constam destas publicações o Internacional Standard Serial Number (ISSN), que é um código único e definitivo para identificação de títulos de seriados.

Pré-publicações (PRE)

Todos os artigos publicados em periódicos, anais e como capítulos de livros.

Manuais Técnicos (MAN)

São publicações de caráter técnico que incluem normas, procedimentos, instruções e orientações.

Relatórios de Pesquisa (RPQ)

Reportam resultados ou progressos de pesquisas tanto de natureza técnica quanto científica, cujo nível seja compatível com o de uma publicação em periódico nacional ou internacional.

Publicações Didáticas (PUD)

Incluem apostilas, notas de aula e manuais didáticos.

Programas de Computador (PDC)

São a seqüência de instruções ou códigos, expressos em uma linguagem de programação compilada ou interpretada, a ser executada por um computador para alcançar um determinado objetivo. Aceitam-se tanto programas fonte quanto os executáveis.